Dwarf Galaxies as Probes of the Nature and Distribution of Dark Matter

ANNA GENINA

GENINA, ANNA (2020) Dwarf Galaxies as Probes of the Nature and Distribution of Dark Matter. Doctoral thesis, Durham University.

Dwarf Galaxies as Probes of the Nature and Distribution of Dark Matter

Anna Genina

Abstract

ΛCDM is presently the most successful, and simplest, model of our Universe. The model consists of two main ingredients. The first is dark energy, Λ, causing our Universe to expand. The second is cold dark matter (CDM), an unknown substance that makes up most of the matter content of our Universe. Despite the numerous successes of ΛCDM on large scales, problems persist on small scales – the scales of dwarf galaxies. ΛCDM predicts that galaxies should reside in "haloes" of dark matter, in which the central density distribution should follow a steep power-law "cusp". This is contrary to observations, which instead suggest a constant density "core". This discrepancy became known as the "core-cusp problem". In this thesis, I focus on the possible solutions to this problem. I first examine a particular kind of dwarf galaxies, which contain two spatially and chemo-dynamically distinct stellar populations. These can provide independent constraints on the dark matter density distribution. I show that various formation mechanisms of the two populations sometimes result in them exhibiting varying degrees of asphericity and spatial misalignment. These phenomena complicate dynamical analyses, resulting in a false inference of a core. I then move on to test various Jeans equation-based approaches on a sample of fully cosmological simulated dwarf galaxies in Cold and Self-interacting dark matter models. I show that the line-of-sight data alone is, at present, insufficient to distinguish between cores and cusps, even when constraints from higher-order moments of the velocity distribution are available. Finally, I look at the evidence for a core in the Fornax dwarf galaxy, suggested by its low inferred central dark matter density. I show that, within the ΛCDM framework, Fornax is consistent with having a cuspy halo the density of which has been reduced by Galactic tides.

Supervisors: Prof. Carlos Frenk, Prof. Shaun Cole and Dr. Alejandro Benítez-Llambay

Dwarf Galaxies as Probes of the Nature and Distribution of Dark Matter

Anna Genina

A thesis presented for the degree of
Doctor of Philosophy

Institute for Computational Cosmology
Department of Physics
Durham University
United Kingdom
August 2020

Contents

1 Introduction 1

Declaration

The work in this thesis is based on research carried out by the author between 2016 and 2020 at the Institute for Computational Cosmology, Department of Physics, Durham University. During this time the author had been supervised by Prof. Carlos Frenk, Prof. Shaun Cole and Dr. Alejandro Benítez-Llambay. No part of this thesis has been submitted elsewhere for any other degree or qualification, and it is the sole work of the author unless referenced to the contrary in the text.

Some of the work presented in this thesis has been published in academic journals. The relevant publications are listed below.

Publications

Genina, A., Frenk, C. S., Benítez-Llambay, A., Cole, S., Navarro, J. F., Oman, K. A.,and Fattahi, A. (2019). The distinct stellar metallicity populations of simulated Local Group dwarfs. MNRAS, 488(2):2312–2331 (Chapter 2)

Genina, A., Benítez-Llambay, A., Frenk, C. S., Cole, S., Fattahi, A., Navarro, J. F., Oman,K. A., Sawala, T., and Theuns, T. (2018). The core-cusp problem: a matter of perspective. MNRAS, 474:1398–1411 (Chapter 3)

Genina, A., Read, J. I., Frenk, C. S., Cole, S., Benítez-Llambay, A., Ludlow, A. D., Navarro, J. F., Oman, K. A., and Robertson, A. (2020). To β or not to β: can higher-order Jeans analysis break the mass–anisotropy degeneracy in simulated dwarfs? MNRAS, staa2352. (Chapter 4)

List of Figures

List of Tables

Acknowledgements

I certainly did not get through this "experience" (i.e. a fight with impostor syndrome that will probably get worse during my postdoc) completely alone, so thanks to:

My parents and my grandma for being extremely supportive, despite still not knowing what I actually do. No, not black holes. Yes, "Anna is good student".

My boyfriend Chris for teaching me how to take a break. I would have struggled to get through this without his love and support, especially in the last few months.

Carlos & Shaun for being the best supervisory team I could have asked for. To Carlos, who is probably my biggest fan and who has believed in me and reassured me from day one. To Shaun, for being the smartest person in the room and for keeping me, Carlos and Alejandro in check.

Alejandro for being Alejandro. I have done some of my best work trying to prove you wrong.

Justin for putting up with me and my e-mails, even though I have seemingly made it my life mission to scrutinize everything he's ever done.

Alis & Adrian, my annual review team, for getting things done. Particular thanks to Alis for making me part of the 'Deason group'.

César for being the best office mate ever (not just because he never showed up). I have enjoyed the bits of moral support you've given me and I'm excited to be sharing my postdoc experience with you for another three years!

Malcolm, Chris and Eugene, who gave me the greatest possible start to my academic career when they definitely didn't have to.

Mo and Emily for being my best friends throughout the years and someone I could always talk to about anything. I miss you two every day. Emily, I hope we can resume our yearly beach/nuclear wasteland holidays soon.

Pgjammers: for getting me through my undergraduate years and for keeping in touch. Particularly big thanks to Parid, who always believed I was a “strong candidate”.

Louise for being a great friend and teaching me how to recycle.

Behzad, James, Josh, Stuart, Matthieu, Oliver, Stefan, Piotr, Stu, Sownak, Alex Smith, Jaime, Aaron, Mathilde, Andrew, Will & Steve, Calvin, Ra’ad, Victor, Tilly, Jake, Jack, Ed, Carol, Joaquin (not Arnau), Arnau, Ellen, Giorgio, Aidan, double Tom and Alex for all the banter.

Chapter 1

Introduction

1.1 ΛCDM as the standard cosmological model

It is fairly standard to attribute the emergence of the dark matter hypothesis to Fritz Zwicky and his work measuring redshifts of the 9 galaxies belonging to the Coma cluster in as early as 1933 (Zwicky, 1933). Zwicky found that the velocity distribution of the galaxies had a dispersion of ~ 1000 kms^{-1}. This suggested that the mass of Coma must be $\gtrsim 400$ times that of the inferred baryonic mass (i.e. the stars in the member galaxies). In his paper, Zwicky refers to this missing matter as “dunkle Materie", or dark matter. A similar analysis was later carried out by Sinclair Smith in 1936, with a larger sample, consisting of 32 members in the Virgo cluster (Smith, 1936). The work had confirmed the presence of ‘missing mass’ in this cluster. In 1959, Kahn and Woltjer used the speed with which the Milky Way’s nearest neighbour M31, or Andromeda, approaches our Galaxy to point out that this motion must require a total Local Group mass of $> 2 \times 10^{12} M_{\odot}$, which could not be explained by the observed matter alone (Kahn and Woltjer, 1959). More evidence for dark matter came from the simulations of Ostriker and Peebles (1973), where it was pointed out that a self-gravitating disk will form a bar unless embedded in a halo of matter, stabilizing the disk. This halo of matter needed to be at least as massive as the disk.

It was not, however, until the late 1970s that the existence of haloes of matter around galaxies began to be taken seriously. This came about from numerous measurements of galaxy rotation curves, which were shown to be flat (van de Hulst et al., 1957; Rubin and Ford, 1970; Roberts and Whitehurst, 1975; Rubin et al., 1976a,b; Bosma, 1978; Rubin et al., 1980). This implied the presence of an unseen mass that transforms the expected Keplerian curve into a flat shape. Note, however, that even throughout the 1980s it was still argued that the rotation curves of Rubin and Ford (1970) did not extend far enough to be interpreted as being due to a massive halo, rather than a galactic bulge (Kalnajs, 1983; Kent, 1986, 1987, 1988; Athanassoula et al., 1987). It was, instead, the disk stability arguments from Ostriker and Peebles (1973) and the works of Ostriker et al. (1974), looking at various estimates of the masses of spiral galaxies, and Einasto et al. (1974a,b), who examined galaxy companions, that had strengthened the case for massive dark haloes in galaxies. In a review by Faber and Gallagher (1979), the authors note that *"...it is our opinion that the case for invisible mass in the Universe is very strong and getting stronger"* and *"...we think it likely that the discovery of invisible matter will endure as one of the major conclusions of modern astronomy"*.

In the 1980s, motivated by the recent measurement of the electron neutrino mass by Lyubimov et al. 1980 (which was then hypothesized to be the missing matter in galaxies), Frenk et al. (1983) and White et al. (1983) have shown, using N-body simulations, that the clustering of matter in a universe where dark matter is a relativistic particle, such as a neutrino, was incompatible with the results of the CfA redshift survey (Davis et al., 1982) and, further, Davis et al. (1985) established that the clustering could only be reproduced if dark matter was 'cold' (i.e. having a small free-streaming length). This result showed that if dark matter is indeed an elementary particle, it is likely to be outside the standard model of particle physics. This became the birth of the 'Cold Dark Matter' (CDM) paradigm.

During the 1990s it became quite evident from the Big Bang Nucleosynthesis arguments, the need for cosmological inflation and from cluster dynamical mass estimates, that baryons make up only a fraction of all matter in the Universe (White et al., 1993). Nevertheless, the strongest evidence for dark matter came from the measurements of the cosmic microwave background (CMB) temperature fluctuations (Melchiorri et al., 2000; Hanany et al., 2000; Spergel et al., 2003; Komatsu et al., 2011; Planck Collaboration, 2018). The angular scale of the peaks and peak heights of the power spectrum of CMB temperature fluctuations are extremely sensitive to cosmological parameters. The CMB shows that our Universe is approximately flat in its curvature, that it is fairly isotropic, and that dark matter must make up $\sim 85\%$ of the matter density. Further, measurements of distances and redshifts of Type 1a supernovae (Riess et al., 1998; Perlmutter et al., 1999) show that our Universe is slowly expanding and that this expansion is accelerating, driven by the mysterious 'dark energy'. An independent source of evidence for dark energy came from galaxy clustering measurements (Maddox et al., 1990; Efstathiou et al., 1990). Dark energy is assumed to be an additional component of the total energy density of the Universe. This is represented by the 'cosmological constant', Λ. Originally proposed by Einstein to allow a static Universe in the framework of General Relativity (GR), Λ is today the key component in the standard cosmological model.

1.2 Predictions of ΛCDM

From the establishment of CDM as the leading model for dark matter, N-body simulations became an important tool for evaluating the predictions of this model, from the large scale structure of the Universe to individual dark matter haloes (White et al., 1987a,b; Frenk et al., 1985, 1988; Jenkins et al., 1998; Navarro et al., 1995; Navarro et al., 1996a, 1997). In the early 2000s, the cosmological parameters were being measured with very high precision from CMB experiments (Melchiorri et al., 2000; Hanany et al., 2000; Spergel et al., 2003). Simultaneously, large supercomputers were becoming available for the running of cosmological simulations. The MILLENNIUM simulation (Springel et al., 2005) marked the start of what would now be almost two decades of large volume, high-resolution cosmological simulations (see the review by Vogelsberger et al. 2020). This allowed detailed investigations of structure formation, which had shown that structure assembles hierarchically in ΛCDM, with small dark matter haloes collapsing first. Larger haloes form from the aggregation of smaller dark matter clumps (Springel et al., 2006). Eventually, larger and larger structures are built up, with haloes linked through a "cosmic web" of sheets and filaments.

The development of semi-analytical models of galaxy formation (White and Frenk, 1991; Kauffmann et al., 1993; Cole et al., 2000), where the luminous component is tracked and evolved in dark matter-only simulations through a series of physically-motivated prescriptions, allowed direct comparison of simulations like MILLENNIUM (Croton et al., 2006; Springel et al., 2006) with structures observed in galaxy redshift surveys (York et al., 2000; Colless et al., 2001). This has revealed staggering compatibility between the clustering of luminous matter in our Universe and in ΛCDM. The model made other successful predictions, like the baryon acoustic oscillation feature in the matter power spectrum (Eisenstein et al., 2005; Cole et al., 2005).

While investigations of individual dark matter haloes were already underway in the 1990s (Dubinski and Carlberg, 1991; Navarro et al., 1997), the fully cosmological simulations that span multiple orders of magnitude in halo mass, from dwarf to Milky Way-like galaxies, became possible in the late 2000s with the use of the "zoom-in" technique (Katz and White, 1993; Tormen et al., 1997; Frenk et al., 1999; Bertschinger, 2001; Gao et al., 2005; Hahn and Abel, 2011; Jenkins, 2013). The AQUARIUS and VIA LACTEA simulations (Springel et al., 2008b; Diemand et al., 2008) marked the start of the 'zoom' era, where the inner structure of haloes could be studied with high resolution (Navarro et al., 2009). These simulations showed that dark matter haloes – from the smallest resolved haloes, to galactic haloes, to galaxy clusters – have a self-similar Navarro-Frenk-White (hereafter NFW) form (Navarro et al., 1996b, 1997):

$$\rho(r) = \frac{\rho_s}{\frac{r}{r_s}\left(1 + \frac{r}{r_s}\right)^2}, \tag{1.1}$$

where r_s and ρ_s are the scale radius and density. Today this result is confirmed with 'zoom' simulations in over 20 orders of magnitude in halo mass (Wang et al., 2019a).

1.3 The small-scale challenges to ΛCDM

Despite the successes of ΛCDM on the large scales, there exist a number of problems on small scales – scales of galactic haloes and their satellite dwarf galaxies. I will briefly highlight these issues here, however, one should see the work of Bullock and Boylan-Kolchin (2017) for a detailed review.

1.3.1 The missing satellites problem

Simulations in ΛCDM cosmology make predictions on the mass function of subhaloes for a halo of a given mass. This means that above some smallest resolved dark matter halo mass in simulations the model predicts how many subhaloes are expected in each mass bin, with some halo-to-halo variance (Klypin et al., 1999; Moore et al., 1999). For a galaxy like the Milky Way, simulations predict $\sim 10^5$ subhaloes with masses above $\sim 10^5 M_\odot$ (Springel et al., 2008b). If one, however, compares this with the number of observed satellite dwarf galaxies of the Milky Way ($\sim$ 50 galaxies) (Adelman-McCarthy et al., 2007; Bechtol et al., 2015; Drlica-Wagner et al., 2015; Koposov et al., 2015), it is clear that there is a large discrepancy. Some fraction of the missing satellites could perhaps be attributed to survey magnitude limits (i.e. the difficulty in observing very faint dwarfs), although it seems unlikely that this could account for all the ‘missing’ dwarfs (Koposov and Belokurov, 2008; Tollerud et al., 2008; Hargis et al., 2014; Kim et al., 2018; Newton et al., 2018). A comparison between dark subhaloes and luminous galaxies may, however, be inappropriate, as it is not clear that all haloes should host a galaxy.

1.3.2 The “too-big-to-fail” problem

Since the subhalo mass function in dark-matter-only simulations is fairly well known, one can make predictions for the dynamical masses of Milky Way satellites. These predicted masses can then be compared to those inferred from observations. Specifically, with abundance matching arguments (where larger galaxies form in larger haloes), one could attempt to map Milky Way dwarfs to simulated dark matter haloes. This procedure leads to another problem: it would appear, from the kinematics of dwarf spheroidals, that the most massive subhaloes in ΛCDM *do not* host the largest galaxies and the mapping is not one-to-one (Boylan-Kolchin et al., 2011, 2012). The problem could be more specifically described by the number of subhaloes with $V_{\text{max}} > 30$ kms^{-1} that host galaxies*. In the Milky Way, there are three dwarfs which match these criteria, whereas ΛCDM predicts 2-3 times that number (Sawala et al., 2016). Perhaps an even more concerning issue is that the problem appears to exist for field Local Group dwarfs and isolated dwarf galaxies (Kirby et al., 2014; Ferrero et al., 2012), making solutions that have to do with satellite-host interactions unlikely.

1.3.3 The plane-of-satellites problem

It was known in the 1970s, before the advent of the standard cosmological model, that a number of satellites of the Milky Way appear to form a thin plane that is approximately perpendicular to the Galactic disk (Lynden-Bell, 1976; Kunkel and Demers, 1976). Moreover, it was shown by Metz et al. (2008) and Pawlowski and Kroupa (2013) that these satellites also have aligned orbital poles. This phenomenon is problematic not only for ΛCDM, but, in general, for the theory of hierarchical structure formation, where one might naively expect isotropic or prolate satellite configurations (Kroupa et al., 2005; Metz et al., 2007). In fact, satellite accretion is expected to be in groups, via the cosmic filaments, introducing a degree of anisotropy (Libeskind et al., 2014, 2015). Although the configuration is still possible to observe in ΛCDM simulations, the probability is very small (< 1%) (Shao et al., 2019; Pawlowski and McGaugh, 2014; Pawlowski and Kroupa, 2020) and is seemingly in disagreement with the fact that planes of satellites have been observed in *both* Milky Way and Andromeda (Ibata et al., 2013); however, the work of Cautun et al. (2015), shows that this discrepancy is lifted once the diversity of the satellite planes is considered and the "look elsewhere" effect is taken into account. This has led some authors to hypothesize

---

*V_{max} is defined as the maximum of the $V = \sqrt{\frac{GM(<r)}{r}}$ curve, where G is the gravitational constant and $M(<r)$ is the enclosed mass at radius r

that dwarf galaxies in the Milky Way may, in fact, be tidal dwarfs (Metz and Kroupa, 2007; Pawlowski et al., 2012), although this scenario implies a lack of dark matter content in these galaxies, which would be at odds with the measurements of their dynamical mass-to-light ratios (Mateo, 1998).

1.3.4 The core-cusp problem

As pointed out in the previous section, simulations in ΛCDM make a prediction on the inner structure of haloes. To better than $\sim 10\%$, these follow an NFW profile (Wang et al., 2019a), where the dark matter density in the centre has a "cusp" ($\rho \propto r^{-1}$). On the other hand, the inferred HI rotation curves in nearby isolated dwarfs suggest that dark matter in the inner regions of these galaxies has a core ($\rho \propto r^{0}$) (Moore, 1994; Kuzio de Naray et al., 2006; Oh et al., 2008; Adams et al., 2014; Oh et al., 2015; Zhu et al., 2016; Read et al., 2017). This discrepancy was first pointed out in 1994 in the works of Moore (1994) and Flores and Primack (1994) and was later dubbed the "core-cusp problem" (de Blok, 2010). The problem persists for satellite dwarfs of the Milky Way, where cores have been inferred from stellar kinematics, although different analyses often arrive at conflicting results for each dwarf (Battaglia et al., 2008; Walker and Peñarrubia, 2011; Amorisco and Evans, 2012b; Breddels et al., 2013; Strigari et al., 2014; Richardson and Fairbairn, 2014).

1.4 ΛCDM with baryonic physics

In our discussion on ΛCDM and its challenges so far, I have been careful to speak of dark-matter-only simulations. For a meaningful comparison between the predictions of the standard cosmological model with observations of nearby galaxies, one must include the physics of galaxy formation consistently within a simulation. We must understand *how* galaxies form and *in which* dark matter haloes and, further, how is the structure of dark matter haloes affected by baryonic physics.

1.4.1 Cosmological simulations of galaxy formation

Although baryons make up only ~16% of all the matter in the Universe (~5% of all the energy content), they constitute its only observable component (Planck Collaboration, 2018). To understand how this component might affect the dark matter, one must understand the physics of galaxy formation. For example, one must accurately model the cooling of gas, star formation and energy from supernovae.

Cosmological simulations are limited in their spatial and mass resolution. This means that astrophysical processes must be modelled in the 'subgrid' (i.e. below the resolution limit of the simulations). For example, simulations must be able to model the different phases of the interstellar medium, gas cooling, the formation of molecular clouds and their fragmentation into individual stars (Vogelsberger et al., 2020). Simulating the details of these processes is extremely computationally challenging for a large cosmological volume. For instance, the densities reached in the molecular clouds are much higher than one can obtain in simulations. This means that one has to impose an artificial density threshold for star formation (Schaye, 2004; Hopkins et al., 2013), $n_{\rm th} \sim 0.1$ atoms cm^{-3} (average density in a star-forming disk) or $\sim$ 100 atoms cm^{-3} (average density of a molecular cloud). Since one cannot resolve individual stars, one also has to model the energy injection from supernovae and stellar winds in the 'subgrid'.

Despite the numerical limitations, large cosmological simulations of galaxy formation have been able to reproduce a number of observed galaxy properties. For example, the galaxy stellar mass function, stellar mass - star formation rate relation, mass - metallicity relation, gas content, black hole masses and the morphology of galaxies – from ellipticals to grand-design spirals – have been succesfully recovered in recent, high-resolution cosmological simulations (Vogelsberger et al., 2014a,b; Dubois et al., 2014; Schaye et al., 2015; Crain et al., 2015; Khandai et al., 2014; Feng et al., 2015; Bocquet et al., 2015; Davé et al., 2016; McCarthy et al., 2016; Tremmel et al., 2016; Springel et al., 2018; Davé et al., 2019).

1.4.1.1 Zoom-in simulations of Milky Way analogues

Of particular interest in this thesis are the Milky Way galaxy and the dwarf galaxies surrounding it. As mentioned previously, one may use the ‘zoom-in’ technique to simulate smaller cosmological volumes of interest (Katz and White, 1993; Tormen et al., 1997; Frenk et al., 1999; Bertschinger, 2001; Gao et al., 2005; Hahn and Abel, 2011; Jenkins, 2013). These could be isolated dwarfs, Local Group and Virgo cluster-like environments and large galaxy clusters. The procedure involves looking at very large cosmological volumes and selecting the region of interest, as in Fattahi et al. (2016a). The particles within the region are then tracked back to their ‘Lagrangian region’ in the initial conditions of the simulations. This could make up a very large region of the initial conditions (Borrow et al., 2020). Regions around the selected one are simulated at a lower resolution to preserve a realistic tidal field. An alternative method for generating initial conditions which will produce a cosmological volume of interest is through “constrained realizations” (Hoffman and Ribak, 1991; Klypin et al., 2003; Gottlöber et al., 2010; Jasche and Wandelt, 2013). This method uses present-day observations of a given volume, such as the Virgo cluster, to constrain the initial conditions of a simulation. It is thus possible to simulate structure and galaxy formation in environments that closely resemble the one of interest (like the Local Group). This allows for a direct comparison of simulated and observed properties of member galaxies, including dwarf galaxies. It also provides an excellent test of our understanding of the physics of galaxy formation and evolution as the properties of nearby objects are particularly well resolved with current instruments.

1.4.2 Baryonic solutions to small-scale challenges in ΛCDM

By now we have seen that state-of-the-art cosmological simulations are able to implement baryonic processes, the effects of which can be modelled down to classical dwarf galaxy scales. Taking this into consideration, we now revise the aforementioned small-scale problems, taking into account results from ‘zoom-in’ simulations.

1.4.2.1 The effects of reionization

After the formation of the first stars in the Universe, the intergalactic medium is reionized (i.e its temperature is increased to approximately 10^4 K). This prevents the gas from falling into dark matter haloes and allowing star formation to occur (Efstathiou, 1992; Thoul and Weinberg, 1996). Some more massive haloes will be able to accrete more gas in the future, but some lower-mass haloes are expected to remain completely dark. Recently, this was looked at in detail by Beǹitez-Llambay and Frenk (2020), who found that haloes with virial masses below $M_{200} \sim 3 \times 10^8 M_\odot$ never form stars. This can explain the low number of luminous satellites observed in the Milky Way compared to the predicted number of dark subhaloes.

1.4.2.2 The effects of supernova feedback

Supernovae feedback is responsible for regulating star formation in galaxies. The energy associated with supernovae is able to blow out the gas from a galaxy and prevents the gas from cooling and condensing to form stars. Baryonic outflows may transport binding energy from the centre of the halo outwards, causing the dark matter also to move outwards. This process can occur intermittently and is able to permanently change an existing dark matter cusp into a core (Navarro et al., 1996a; Read and Gilmore, 2005; Pontzen and Governato, 2012; Madau et al., 2014; Read et al., 2016). The requirement for such a transition is that the gas must dominate the gravitational potential in the galactic centre prior to the blow-out (Benítez-Llambay et al., 2019). As the blow-out occurs, the potential is significantly perturbed and the dark matter moves to higher-energy orbits. A cusp may be restored if the gas is allowed to accumulate in the galactic centre, causing an adiabatic contraction of the halo. Alternative methods of core creation could involve energy transfer to the outer halo by infalling clamps through dynamical friction (El-Zant et al., 2001; Sánchez-Salcedo et al., 2006; Mashchenko et al., 2008; del Popolo and Kroupa, 2009; Cole et al., 2011), or through resonant effects induced by a central stellar bar (Weinberg and Katz, 2002). These processes may be able to simultaneously explain the core-cusp problem (particularly in the star-forming dwarf irregulars) (Read et al., 2016, 2019) and the "too-big-to-fail" problem (by lowering the central density of CDM haloes), but only if dwarf spheroidals are also able to form cores (Zolotov et al., 2012).

Another important consequence of supernova feedback and reionization is their impact on the growth rate of dark matter haloes (Sawala et al., 2016; Zhu et al., 2016). Feedback blows out gas supplies available for star formation at early times and thus reduces the total halo mass, compared to a dark-matter-only halo. This leads to a reduction in the halo growth rate and, consequently, lower $V_{\rm max}$, thereby solving the "too-big-to-fail" problem. The work of Sawala et al. (2016) shows that $V_{\rm max}$ of subhaloes, including those with $V_{\rm max} > 30$ kms^{-1} is reduced by up to 15% in simulations with baryon physics, compared to dark-matter-only, thus solving the problem.

1.4.2.3 Environmental effects

Satellite dwarf galaxies are susceptible to interactions with their hosts. When a satellite gets close to the centre of the host galaxy, it will undergo tidal stripping, halo shocking and disk shocking. These processes result in the reduction of the central dark matter density, providing another possible solution to the "too-big-to-fail" problem (Zolotov et al., 2012; Arraki et al., 2014; Brooks and Zolotov, 2014; Zhu et al., 2016; Sawala et al., 2016; Wetzel et al., 2016; Dutton et al., 2016; Garrison-Kimmel et al., 2019). Disk shocking, in particular, is an effect that is not taken into account in dark-matter-only simulations (D'Onghia et al., 2010a). Moreover, the accumulation of baryons in the halo of the host would cause an adiabatic contraction (i.e a slow steepening of the potential). A stronger central cusp in the host galaxy will enhance the stripping and shocking of approaching satellites (Peñarrubia et al., 2010). These processes could also lead to the enhanced disruption of subhaloes (Sawala et al., 2017; Garrison-Kimmel et al., 2017; Richings et al., 2020).

We have previously noted that the "too-big-to-fail" problem may also exist for isolated dwarf galaxies. Fattahi et al. (2020) have shown that the number of massive dwarfs with peak circular velocities $V_{\rm peak} > 30$ kms^{-1} is actually proportional to the total mass of the

Local Group. Moreover, the number of such dwarfs is greatly reduced in hydrodynamic simulations compared to dark-matter-only, somewhat easing the problem. In fact, two of their Local Group-like volumes have ~10 dwarfs with $V_{\mathrm{peak}} > 30\ \mathrm{kms}^{-1}$, consistent with the Local Group. It is also possible that the "too-big-to-fail" problem in the field could instead be a consequence of observational biases. For example, the gas in these galaxies may not be probing the peak of the rotational velocity curve (Benson et al., 2002; Macciò et al., 2016).

Observational biases may also be partly responsible for the apparent plane of satellites in the Milky Way. Sky surveys do not point along the Galactic plane and are thus focused on the regions perpendicular to it (where the plane of satellites is). Nevertheless, the co-rotation of the satellites and the thinness of the planes in the Milky Way and Andromeda still remains an intriguing feature of the satellite distribution (Cautun et al., 2015; Pawlowski, 2016; Shao et al., 2019).

1.4.2.4 Modelling bias

There may also exist modelling biases, resulting in a false inference of a dark matter core, when in reality the is a cusp. In Hɪ rotation curve measurements this could be, for instance, due to the presence of non-circular motions that are not taken into account. Additionally, the possible inclination angles of these galaxies with respect to the observer also need to be accounted for (Oman et al., 2016, 2019; Pineda et al., 2017). For dwarf spheroidals, common assumptions are the absence of internal rotation, spherical symmetry and dynamical equilibrium of the system (Wolf et al., 2010). These assumptions are known to be violated in satellite dwarf spheroidals in the Milky Way (McConnachie, 2012; del Pino et al., 2017a) and ignoring these may lead to an incorrect inference of a core.

1.4.3 Solutions to small-scale problems using CDM alternatives

The small scale problems to CDM, in the absence of baryonic physics, have inspired exploration of more exotic models of dark matter capable of resolving these issues. In particular, in Warm Dark Matter (WDM) models there exists a cut-off in the power spectrum due to the increased free-streaming length of the dark matter particles. Haloes less massive than a characteristic mass for a given free-streaming length of a dark matter particle (related to a particle's mass) cannot form (Bode et al., 2001; Avila-Reese et al., 2001; Schneider et al., 2012; Lovell et al., 2012). This could in part solve the missing satellites problem. Moreover, the absence of small substructure also tends to affect halo growth, such that haloes assemble later. This would lead to smaller $V_{\max}$ in luminous dark matter galaxies and, thus, also solve the "too-big-to-fail" problem (Anderhalden et al., 2013; Lovell et al., 2016; Newton et al., 2019). Haloes in warm dark matter do not, however, form large cores (Shao et al., 2013).

Self-interacting dark matter models (SIDM) also have been proposed (Spergel and Steinhardt, 2000). In these models, instead of being a collisionless fluid, dark matter can interact with itself with an interaction cross-section, $\langle \sigma m \rangle$. For sufficiently large cross-sections dark matter is able to scatter to an extent that a dark matter core is produced in the central regions. This simultaneously lowers the central density compared to CDM, solving the "too-big-to-fail" problem (Vogelsberger et al., 2012; Elbert et al., 2015). However, the power spectrum resembles that of CDM and thus does not on its own solve the missing satellites problem (Rocha et al., 2013). Moreover, the window of cross-sections that produce dark matter cores is in tension with the cross-sections required to mimic the high central densities in large galaxy clusters (Kaplinghat et al., 2016; Robertson et al., 2019). It is then possible to have a velocity-dependent self-interacting dark matter particle, which will scatter differently on different orders of magnitude in halo mass.

1.5 Dwarf galaxies as dark matter probes

So far I have shown that a number of challenges to the ΛCDM model have been identified on the small scales. With the advent of high-resolution 'zoom-in' simulations including baryonic physics, a number of those problems appear to be solved within the "ΛCDM + baryons" framework. Still, some challenges persist. One is the plane-of-satellites problem, the solution to which likely lies in the statistical significance of the planes in Local Group-like environments (Cautun et al., 2015). Another persisting problem is the core-cusp problem, where disagreements exist in competing simulations due to their mass resolution and subgrid physics implementations (Benítez-Llambay et al., 2019). Moreover, an important aspect of the problem is the reliability of kinematic tracers in the inference of the shape of the underlying gravitational potential (Strigari et al., 2010). I focus on the core-cusp problem in this thesis.

Dwarf spheroidal galaxies are some of the best places to study dark matter for several reasons. Firstly, these objects have particularly high dynamical mass-to-light ratios (i.e. the kinematics of their stars imply much larger enclosed masses than those that could be attributed to stars alone) (Mateo, 1998; McConnachie, 2012). In fact, dwarf galaxies are some of the most dark matter-dominated objects found in the Universe (Pryor and Kormendy, 1990). Secondly, a number of dwarf galaxies reside sufficiently close to Earth such that individual stars can be resolved in these objects. This allows for precise kinematic, photometric and proper motion measurements. Finally, dwarf galaxies are also excellent places to look for the by-products of dark matter self-annihilation (Springel et al., 2008a). Their location away from the Galactic disk and relative proximity implies more signal and smaller background/foreground contamination (Gaskins, 2016; Strigari, 2018).

One way to infer the shape of the gravitational potential (core or cusp) in a dwarf galaxy is to study the motions of a set of kinematic tracers. In satellite dwarfs, where gas is typically absent as a tracer due to effects of star formation, tidal and ram-pressure stripping (McConnachie, 2012; Spekkens et al., 2014), one must rely on the measured kinematics of individual stars. While proper motions for a number of dwarf spheroidals have recently become available with *Gaia* DR2, the distances for the majority of dwarfs are too large to obtain small proper motion errors on individual stars (Gaia Collaboration et al., 2016, 2018). This means that the dynamical modelling at present relies on the line-of-sight spectroscopic measurements only. This introduces significant errors in the measurements due to the so-called mass-anisotropy degeneracy, where the enclosed mass of the system cannot be fully constrained unless one has full 3D tracer motions.

As reliable proper motions for individual stars cannot be presently obtained, one must rely on line-of-sight measurements and seek additional, independent constraints. Some studies have focused on the use of the fourth line-of-sight velocity moment (the kurtosis of the velocity distribution). This can be related to the enclosed mass via higher orders of the spherical Jeans equation or the virial theorem (Merrifield and Kent, 1990; Łokas and Mamon, 2003; Łokas, 2002, 2009; Richardson and Fairbairn, 2013a; Mamon et al., 2013; Read and Steger, 2017). Another possibility is the use of multiple tracers of the gravitational potential. In particular, it turns out that a number of Local Group dwarfs contain spatially and chemo-dynamically distinct stellar populations (Tolstoy et al., 2004; Battaglia et al., 2008, 2006, 2011; Ho et al., 2012; Battaglia et al., 2012). These populations may serve as independent tracers, providing a corresponding number of constraints that could, in principle, break the degeneracy. Finally, in models where cores form in initially cuspy dark matter haloes due to gas blowouts, a core could be distinguished from a cusp based on the lower enclosed density compared to ΛCDM predictions (Read et al., 2019), provided this density was not reduced for other reasons (for example, due to tidal shocks). Some works also consider the present-day distributions of globular clusters as an indicator of an underlying core or a cusp (Goerdt et al., 2006; Cole et al., 2012; Contenta et al., 2018; Orkney et al., 2019).

1.6 An outline of this thesis

In this thesis, I explore the various methods of constraining the shape of the dark matter density distribution. I first focus on the dwarf galaxies that exhibit two stellar metallicity populations. In Chapter 2, I explore the various paths that lead to the formation of two populations, their observational characteristics and whether these paths are imprinted in the kinematics of individual populations. In Chapter 3, I test a method for using the two populations to obtain two independent measurements of the enclosed mass at two different radii and how these can be used to deduce the slope of the mass profile, related to that of the density profile. I discuss the limitations of this method, some of which are related to the formation paths of the two populations, as identified in Chapter 2. This concludes the discussion on two metallicity populations as independent tracers of the potential.

In Chapter 4, I introduce the pyGravSphere code, a python implementation of the GravSphere method, developed in Read and Steger (2017), which uses both the second and fourth-order moments of the velocity distribution to place additional constraints on the gravitational potential. I test the method on simulated dwarfs comparable to the Fornax dwarf spheroidal in ΛCDM and SIDM cosmologies (which have cusps and cores, respectively) and identify sources of bias and uncertainty. I suggest a statistic to weed out biased models and suggest cosmologically-motivated priors for future dynamical analyses.

In Chapter 5, I explore the origins of the low dark matter density in the Fornax dwarf spheroidal galaxy in the context of the ΛCDM cosmology. The low density in Fornax is hypothesised to be due to core formation. I evaluate how likely this density is considering the present-day orbit of Fornax and its star formation history.

Finally, in Chapter 6, I summarize the results presented in this thesis and outline some possible directions for future work.

CHAPTER 2

The distinct stellar metallicity populations in simulated Local Group dwarfs

2.1 Introduction

Dwarf galaxies in the Local Group show a diversity of star formation histories: some form the majority of their stars in a short burst early on, while others continue to form stars over their lifetime at varying rates (Dolphin et al., 2005; Tolstoy et al., 2009; Weisz et al., 2014; Gallart et al., 2015). Some also exhibit signs of peculiar kinematics and stellar substructure, suggesting a history of accretion (Amorisco and Evans, 2012a; del Pino et al., 2015; del Pino et al., 2017a,b; Cicuéndez and Battaglia, 2018). A number of satellites of the Milky Way and Andromeda, including Sculptor, Fornax, Sextans, Andromeda II and Carina display evidence of distinct stellar metallicity and age populations (Tolstoy et al., 2004; Battaglia et al., 2008, 2006, 2011; Ho et al., 2012; Battaglia et al., 2012). The younger and metal-rich stars are typically centrally concentrated; the older and metal-poor stars are more spatially extended. In certain cases the two populations exhibit different kinematics. This feature has been widely used for dynamical mass modelling of these galaxies (Battaglia et al., 2008; Walker and Peñarrubia, 2011; Amorisco and Evans, 2012b;

Hayashi et al., 2018) and we shall return to it in the next chapter.

A number of possible scenarios for the formation of two metallicity populations have been proposed. The simplest suggest gas reaccretion or recycling, whereby the feedback from the first episode of star formation empties the gas reservoir and the second population is not formed until the gas returns and cools (Dong et al., 2003; Tolstoy et al., 2004). These highly idealised models do not explain why the two metallicity populations should exhibit spatial segregation.

The work of El-Badry et al. (2016) suggests baryon inflows and outflows associated with bursts of star formation as a driving force behind stellar radial migration. The gravitational potential fluctuations that are also responsible for the formation of inner dark matter cores in these simulations tend to heat the orbits of the stars over long timescales. Thus, the older and more metal-poor stars migrate to systematically larger distances than younger ones, creating a metallicity and an age gradient. This mechanism would explain the presence of gradients in some dwarf galaxies. However, unless this mechanism is coupled to another process triggering two well separated episodes of star formation activity, it is unclear how it can lead to large spatial segregations such as that observed in, for example, Sculptor, where the effective radius of the metal-rich population is ~ 0.55 that of the metal-poor population (Battaglia et al., 2008; Walker and Peñarrubia, 2011).

The works of Benítez-Llambay et al. (2015, 2016) suggest gas-rich mergers as a mechanism for forming two stellar populations that are distinct in age and spatial extent. Using the CLUES simulations (Gottlöber et al., 2010), these authors find that some haloes, ranging in stellar mass from 9×10^6 to 6×10^7 $M_\odot$, are able to form stars before reionization but, due to star formation feedback and a low virial mass, they are not able to reaccrete gas until a late time merger takes place and funnels gas to the centre, resulting in a second burst of star formation. A merger increases the velocity dispersion of the old stars. This scenario can explain both why the stellar populations are distinct in age and also why the younger population is more centrally concentrated than the older population.

In their zoom-in simulations of isolated dwarfs using the chemo-dynamical N-body code

GEAR (Revaz and Jablonka, 2012), Revaz and Jablonka (2018) find no such late accretion events that result in the formation of two metallicity populations. However, they do find that the dwarf galaxies with significantly steeper metallicity gradients than others appear in systems which have assembled *early on* from metal-poor galaxy progenitors, resulting in a very extended distribution of metal-poor stars. N-body simulations show that dwarf-dwarf mergers are not uncommon in a ΛCDM universe (Deason et al., 2014). Furthermore, these would help explain photometric and kinematic anomalies present in dwarfs such as Andromeda II and Fornax (Amorisco et al., 2014a; Łokas et al., 2014; del Pino et al., 2017a).

Another plausible formation path has been suggested by Wright et al. (2019). These authors identified ram pressure as a mechanism for the reignition of star formation in field dwarf galaxies of stellar mass in the range 9.2×10^8 - 8.4×10^9 $M_\odot$, and in which the star formation history has a prolonged gap. They find that star formation may be reignited by ram pressure due to, for example, gas blown out by intense star formation activity from a nearby galaxy. Given sufficiently low velocity relative to the surrounding medium, the hot gas in the outer regions of the halo may be stripped while the gas in the inner regions may be compressed and cooled resulting in a new star formation episode and the formation of metal-rich stars.

Kawata et al. (2006), on the other hand, argue that the two metallicity populations observed in Sculptor may, in fact, be a single stellar population. These authors were able to reproduce Sculptor's steep metallicity gradient in a simulated galaxy that undergoes a single star formation episode at z = 13 - 20. The star formation in their simulated dwarf is powered by smooth accretion, where the gas is primarily enriched in the denser central regions, while supernovae feedback prevents star formation in the outermost regions. This mechanism creates a metallicity gradient that is sufficiently steep, such that the system appears to contain two chemo-dynamically and spatially distinct populations.

A successful scenario for the formation of dwarfs with two stellar metallicity populations would need to explain both the difference in the age/metallicity of the two populations as well as the difference in their spatial extent. Whilst the works of Benítez-Llambay et al. (2016) and Wright et al. (2019) have been able to achieve this, neither have con-

Table 2.1: Dark matter, gas and the ranges of stellar particle masses for the five L1 volumes of APOSTLE used in this work. The gravitational softening at $z = 0$ is 134 pc.

Volume	$m_{DM}h^{-1}$ [$M_{\odot}$]	$m_{gas}h^{-1}$ [$M_{\odot}$]	$m_{star}h^{-1}$ [$M_{\odot}$]
AP-1	3.5×10^4	7.0×10^3	$0.4\text{-}1.4 \times 10^4$
AP-4	1.7×10^4	3.5×10^3	$0.2\text{-}1.0 \times 10^4$
AP-6	3.7×10^4	7.5×10^3	$0.4\text{-}2.5 \times 10^4$
AP-10	3.6×10^4	7.2×10^3	$0.4\text{-}1.2 \times 10^4$
AP-11	3.5×10^4	7.1×10^3	$0.4\text{-}1.6 \times 10^4$

sidered satellite dwarfs in a Local Group-like environment. In this work, we analyse the assembly histories of both field and satellite dwarf galaxies with stellar masses spanning the range 10^6 - 10^9 $M_{\odot}$ in five high-resolution hydrodynamical simulations of environments resembling that of the Local Group. We will identify two-metallicity population dwarf galaxies and examine their formation paths. We will further discuss how these histories are imprinted in the observable properties of the dwarfs.

The details of the simulations and the galaxy sample are discussed in Section 2.2. In Section 2.3 we examine the formation histories of field dwarfs with two metallicity populations and analyse the satellites in Section 2.4. Section 2.6 explores the stellar mass dependence of these mechanisms. In Section 2.7 we look at the properties of the individual stellar populations. Section 2.8 examines the conditions necessary to observe bimodality in metallicity distributions and in Section 2.9 we summarise our conclusions. Readers who are particularly interested in dwarf satellites (for which we have uncovered a new physical process) may wish to skip directly to Section 2.4.

2.2 Simulations

2.2.1 APOSTLE simulations

A Project Of Simulating The Local Environment (APOSTLE) consists of a suite of hydrodynamical zoom simulations of 12 cosmological volumes; volumes AP-(1-12) were simulated at medium and low levels of resolution (L2 and L3) while five volumes (AP-1, AP-4, AP-6, AP-10 and AP-11) were simulated at high resolution (L1). In this work, we

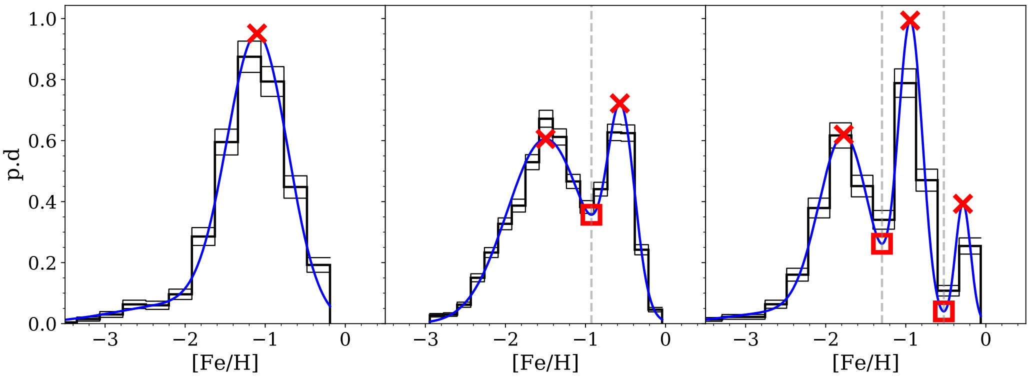

Figure 2.1: Metallicity probability density (p.d) for examples of galaxies with one (left), two (middle) and three (right) distinct stellar populations as determined by the method described in Section 2.2.4. The black lines show binned data and corresponding Poisson errors. The blue line shows the best fitting Gaussian Mixture Model. The red crosses show the location of peaks; their number is equal to the number of identified populations. The red squares show the local minima and mark the locations where populations are split (also shown with a vertical dashed grey line).

use only the five L1 volumes. The gas, dark matter and stellar particle masses for each of these may be found in Table 2.1. The Milky Way and Andromeda analogues were selected from the DOVE simulation (Jenkins, 2013). The separations, masses, radial and tangential velocities of the halo pairs, as well as the broad kinematics of other members of the Local Group analogues were chosen to satisfy observational constraints (Fattahi et al., 2016a). The simulations are described in detail in that paper and in Sawala et al. (2016).

APOSTLE was run with the EAGLE code (Schaye et al., 2015; Crain et al., 2015), which is a modified version of the TreePM smoothed particle hydrodynamics (SPH) code GADGET 3 (Springel, 2005). EAGLE was calibrated to reproduce the stellar mass function at $z = 0.1$ in the resolved range of $10^8 - 10^{11}$ $M_\odot$, as well as galaxy sizes and colours.

Radiative cooling and photoheating prescriptions in EAGLE follow Wiersma et al. (2008). Star formation is stochastic and follows a pressure law described by Schaye and Dalla Vecchia (2008). The star formation threshold is dependent on both the number density of hydrogen and the gas metallicity, following the prescription of Schaye (2004). Each stellar particle represents a stellar population with masses between 0.1 - 100 $M_\odot$, following a Chabrier (2003) initial mass function. Newly formed stellar particles inherit their parent gas kernel smoothed abundances. Altogether eleven chemical elements are tracked: H, He, C, N, O, Ne, Mg, Si, S, Ca and Fe. Nine of these are tracked individually, while Ca and S are assumed to have fixed mass ratios relative to Si. Stellar evolution and mass loss follows the model of Wiersma et al. (2009) and includes winds from AGB, massive stars and SNe Type II. The rate of SNe Type Ia follows a time-delayed exponential distribution function. Their yields are taken from Thielemann et al. (2003). Lost stellar mass is distributed through an SPH kernel to 48 gas particle neighbours. Stochastic thermal feedback from star formation is implemented following Dalla Vecchia and Schaye (2012). Hydrogen reionization is modelled by a spatially-uniform and time-dependent ionizing background, which is turned on instantaneously at $z = 11.5$ (Haardt and Madau, 2001; Schaye et al., 2015).

2.2.2 Constructing merger trees

We constructed merger trees using the HBT+ halo finder (Han et al., 2018). Each halo in the simulation is assigned a 'track ID' which is used to follow the main progenitor across time. Thus, the position and velocity of the main progenitor at every snapshot in the simulation may be determined. We calculate the centres of subhaloes using the "shrinking spheres" algorithm (Power et al., 2003) on at least 100 stellar particles, if present, or on the bound dark matter particles if not.

2.2.3 Calculating V-band luminosities

The V-band luminosities for our simulated dwarfs are calculated following the GALAXEV population synthesis model of Bruzual and Charlot (2003). The model provides absolute AB magnitudes of a stellar population with mass $\mathrm{M}_{\odot}$, age t_* and metallicity Z_*, assuming a Chabrier (2003) initial mass function. The magnitudes are tabulated on a grid of metallicity ($1\times10^{-4} < Z_* < 5\times10^{-2}$) and age ($0.1 < t_*/\mathrm{Myr} < 2\times10^{4}$). For each simulated stellar particle, described by its initial mass, age and metallicity, we thus perform a 2-dimensional interpolation over the age-metallicity grid and obtain its absolute magnitude in the V-band. If the simulated stellar particle falls outside the metallicity range of interpolation, we assume that its metallicity is either the minimum or maximum value of the tables (i.e. we do not perform an extrapolation).

In this work, we will use these luminosities to calculate quantities that are compared to observations (such as the half-light radius).

2.2.4 Defining stellar metallicity populations in galaxies

We now define what we mean by galaxies with two metallicity populations.

We use [Fe/H] as the measure of metallicity, as is common in observational work[*]. For each stellar particle, kernel-smoothed metallicity abundances are used. In order to identify the number of stellar metallicity populations in dwarf galaxies, we employ a peak finding algorithm. We fit the [Fe/H] distribution with a Gaussian Mixture Model (GMM) (Hastie et al., 2001) in order to eliminate the effects of noise in the distribution. We exclude extremely metal-poor stellar particles ([Fe/H] < -4) from the fit as these lie in a long tail of the distribution that may bias the fit. We have verified that this choice indeed removes the extremely low-metallicity tail and does not discriminate against identifying the more metal-poor subpopulations[†].

To identify the best performing GMM, we evaluate χ^2 for the binned data, with the optimal number of bins determined by Doane's formula for non-normal distributions (Doane, 1976). We test n components for the GMM, where $n < m/3$, m being the number of bins, and evaluate their quality in representing the data using the Akaike Information Criterion corrected for sample size (AICc; Akaike, 1998). The model with the smallest AICc is selected and a peak finding algorithm is run on the resultant metallicity distribution function. A peak location is defined as a point, i, where the function, f, has a local maximum, such that $f_{i-1} < f_i > f_{i+1}$. The number of identified peaks in the distribution of [Fe/H] is the number of unique stellar populations in the galaxy. Once the peaks have been found, in cases where the number of populations is greater than one, we split the

---

[*] The adopted mass fractions are $0.0014\mathrm{M}_\odot$ for iron and $0.7381\mathrm{M}_\odot$ for hydrogen.

[†] Extremely metal-poor stars typically make up 0.5 per cent of [Fe/H] distributions and we assign these stars to the metal-poor population in further analysis.

stellar particles into their respective populations by applying a hard cut at the positions of the local minima between the peaks.

By definition, our method identifies galaxies with two or more peaks in their stellar metallicity distributions. However, in some cases, the size of a subdominant population may be negligible, such that the galaxy effectively consists of a single stellar population. We thus consider dwarfs in which the mass ratio of the smaller to the larger population is less than 10 per cent as single population galaxies. We additionally limit our sample to galaxies where any stellar population contains at least 100 stellar particles. At this limit sampling noise becomes important, although some galaxy properties can be measured with 20 per cent accuracy (see Section A of the Appendix) and, provided that the metallicity distribution exhibits distinguishable peaks, it is still possible to separate different stellar populations.

In Fig. 2.1, we show [Fe/H] distributions for examples of galaxies with one, two and three identified stellar populations. The EAGLE model produces a wide range of stellar metallicity distributions and it is clear that the method works well in identifying populations of varying sizes in the distributions of [Fe/H]. We note that the metallicity distributions may be sensitive to the specifics of subgrid physics. In particular, metal mixing is not properly accounted for in our simulations, although the use of SPH-smoothed metallicities does somewhat mitigate this issue (Starkenburg et al., 2017). Nevertheless, the origin of the metallicity distribution bimodality (see Section 2.5), spatial segregation and, thus, the main results of this work should not be affected.

The resulting sample consists of 290 galaxies with ~ 43 per cent containing two metallicity populations (61 field and 64 satellite dwarfs), 10 per cent containing three (16 field and 14 satellites) and 47 per cent containing a single stellar component (66 field and 69 satellites). According to these statistics, nearly half of all simulated dwarfs above $\sim 10^6$ $L_\odot$ exhibit metallicity bimodality in their [Fe/H] distributions. We find these ratios to be approximately constant across the range of luminosities above $\sim 4\times 10^6$ $L_\odot$. Below this value, the fraction of two-population dwarfs decreases steadily down to 20 per cent, but this is due to the imposed minimum number of stellar particles for a given metallicity population. We will discuss the observational implications of this in Section 2.8.

In what follows we consider only the dwarfs that contain two stellar populations, with a particular emphasis on the formation mechanisms responsible for the *spatial segregation* within these galaxies. We leave the three-population galaxies for future work. These may be interesting in the context of the dynamical method of Walker and Peñarrubia (2011) and may allow additional constraints to be placed on the slope of the dark matter density profiles.

2.2.4.1 Properties of our galaxy sample

We first demonstrate that the dwarfs in our sample have basic structural properties that resemble those of real field and satellite dwarfs. In Fig. 2.2 we show the projected half-light radii, $\mathrm{R_{hl}}$, line-of-sight velocity dispersion, σ_{los}, and the mean mass-weighted stellar metallicities, $\langle[\mathrm{Fe/H}]\rangle$, as a function of V-band magnitude, $\mathrm{M_V}$. We compare the values for our sample of galaxies with observed Local Group dwarfs. The Local Group data have been taken from McConnachie (2012) and includes all dwarfs for which measurements of half-light radius, line-of-sight velocity dispersion and metallicity are available. Note that some of these measurements do not have error bars. The Milky Way and Andromeda satellites (red and blue symbols, respectively) as well as other Local Volume dwarfs (green symbols) shown in Fig. 2.2 are the same across the three panels. The velocity dispersion and half-light radii for the simulated dwarfs are shown with error bars representing the 16^{th} and the 84^{th} percentiles found by generating 1536 isotropically distributed lines of sight (Górski et al., 2005). The error bars for mass-weighted mean stellar metallicities are calculated by taking 1000 samples of stellar particles with the number of particles within each sample, $N_{*,\mathrm{sample}} \sim N_{*,\mathrm{total}}/10$. We exclude stellar particles with [Fe/H] > -4 from the mean metallicity calculation, as these metallicities are sensitive to the mass resolution of our simulations (Schaye et al., 2015; Starkenburg et al., 2017). The two-population galaxies are shown in blue, satellites are represented with circles and field dwarfs with squares. It can be seen that the two-population galaxies occur within a wide range of luminosities and galaxy sizes.

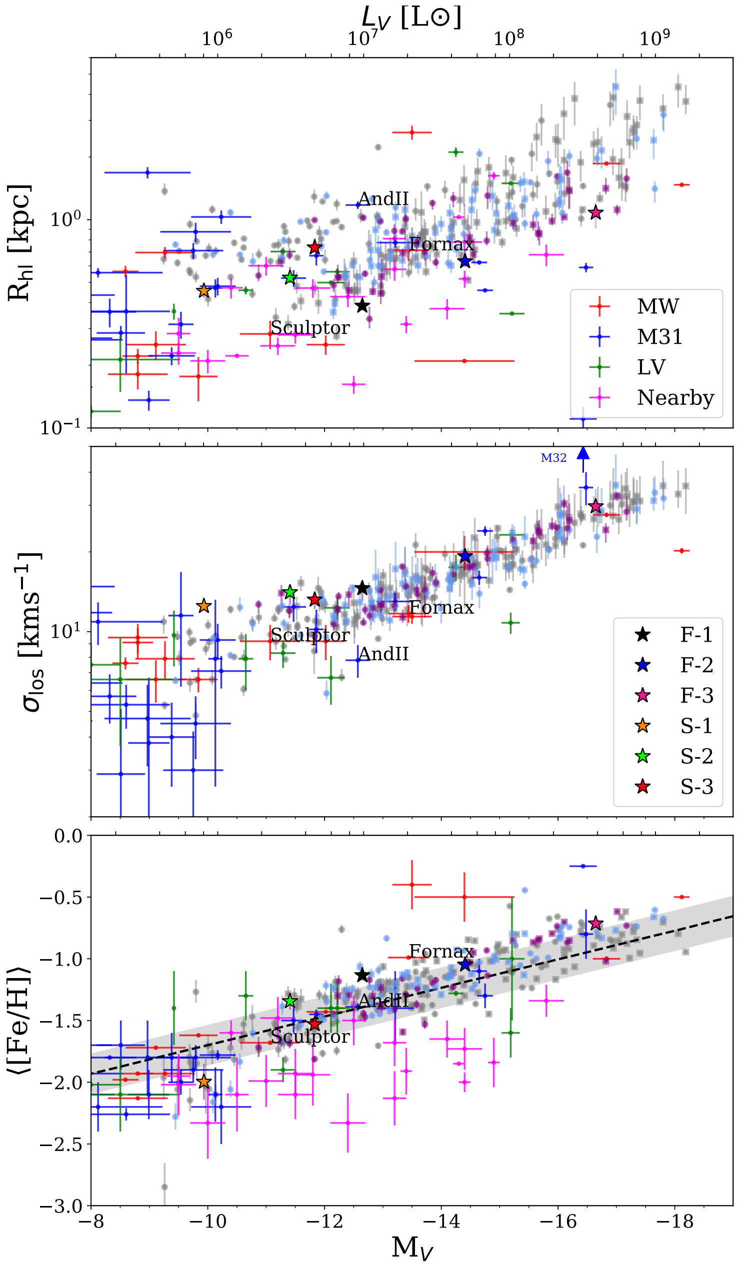

Figure 2.2: *Top:* projected half-light radii for our sample of dwarfs as a function of M_V, with error bars representing the 16th and the 84th percentiles. Model galaxies with two metallicity populations are shown with blue symbols, with satellites and field dwarfs represented by circles and squares, respectively. The remainder of the sample is shown with grey symbols. The data for the Local Volume and nearby galaxies from McConnachie (2012) is shown with symbols identified in the legend. Corresponding V-band luminosities are shown in the upper horizontal axis. *Middle:* the V - band luminosity-weighted line-of-sight velocity dispersion for galaxies in our sample as a function of M_V. *Bottom:* mean luminosity-weighted stellar metallicity as a function of M_V for our sample of dwarfs. The black dashed line shows the relation derived by Kirby et al. (2013). The specific examples of field and satellite galaxies that will be discussed later on are marked across the three panels with stars, as identified in the middle panel.

As a result of the imposed minimum number of stellar particles, our simulated galaxies are only comparable to some of the brightest, or classical, Local Group dwarfs. The black dashed line in the bottom panel of Fig. 2.2 displays the mean-metallicity – luminosity relation derived by Kirby et al. (2013), extrapolated to higher luminosities. The grey bands represent the scatter. Our simulated dwarfs trace this relation.

Sculptor, Fornax and Andromeda II, particularly well-studied examples of two-population dwarfs, are identified on the plot. It can be seen that our sample contains galaxies of comparable luminosities to these three dwarfs. A number of simulated galaxies match the size and velocity dispersion measurements for Fornax, although its mean metallicity is above the locus traced by our galaxy sample. The sample contains matches for Sculptor in velocity dispersion and mean metallicity, although the half-light radius of Sculptor is below those seen in our simulations at comparable luminosities. The size-luminosity relation in our simulations flattens at low luminosities ($\lesssim 10^6 L_\odot$). As discussed in more detail in Campbell et al. (2017), the galaxy sizes are sensitive to spatial resolution and are typically larger than 2.8 times the Plummer-equivalent softening of our simulations (i.e. $\sim$ 0.4 kpc), which is the radius above which the forces are Newtonian. We have also explicitly checked that the luminosities derived from the stellar synthesis models are not responsible for the apparently large sizes of these galaxies, as their half-mass and half-number radii have comparable values. The sizes of these low-luminosity dwarfs and those of their subpopulations should be taken with caution in the rest of this work, but should not affect our ability to identify spatial segregation and its origin.

We now identify a subsample of these simulated dwarfs that also exhibit significant spatial segregation, comparable to that derived for Sculptor and Fornax, and examine their formation mechanisms.

2.3 Assembly history of field dwarfs

It has previously been suggested by Benítez-Llambay et al. (2016) and Revaz and Jablonka (2018) that mergers play a significant role in the formation of two-population systems.

A merger provides a natural explanation for both the large spatial extent of the metal-poor stellar population and the reignition of star formation activity that results in the formation of a more metal-rich population. If this is indeed the case, simulated systems with strong spatial segregation between two populations should also exhibit larger fractions of accreted material. Fig. 2.3 shows the fraction of stellar particles that have formed outside $\sim 0.15 \times R_{200}$ of the main progenitor* (i.e that have been accreted), $f_{accr,*}$, as a function of r_{mr}/r_{mp}, the ratio of the metal-rich to the metal-poor half-mass radii, with the colours representing the median of the line-of-sight velocity dispersion in these systems as a tracer of mass. It is evident that the two-population dwarfs make up two subsets: those that accrete a significant fraction of their stars, typically $f_{accr,*} > 0.05$, and in which the spatial segregation is large ($r_{mr}/r_{mp} \lesssim 0.65$) and those where both the amount of accretion and the spatial segregation are small. This separation does not appear to be dependent on the mass of these systems as large spatial segregation is seen in both high ($\sigma_{los} \sim 25$ kms^{-1}) and low velocity dispersion systems ($\sigma_{los} \sim 10$ kms^{-1}). We thus select dwarfs with $r_{mr}/r_{mp} < 0.65$ as our subsample of galaxies that have two spatially segregated populations, which are the main focus of this work.

The top panel of Fig. 2.4 shows the distribution of the metallicities of accreted particles for all field dwarfs with two spatially segregated populations, with each galaxy given equal weight. The subset of accreted stellar particles that belong to the metal-rich population of their host galaxy is shown by the red histogram. It is evident that only a very small fraction of the accreted stars belong to the metal-rich population (typically ~6 per cent). We thus conclude that the metal-rich population in these dwarfs is primarily formed *in-situ*. The bottom panel shows the distribution of all particles in galaxies with two well-segregated populations (blue), with equal weight per galaxy. It appears that the field dwarfs show a preference for a more dominant metal-rich population. The grey histogram shows a subset of particles that were accreted. These particles are partly responsible for the metal-poor bump seen in two-metallicity population galaxies, though typically only ~ 0.13 of the

---

*We define R_{200} as the radius enclosing a mean density of 200 times the critical density of the Universe. We find the $0.15 \times R_{200}$ cut to be a reliable tracer of the accreted stellar particles since the merging galaxies tend to form a large fraction of stars during the merging process itself, i.e. within R_{200}. In practice, we vary this factor between (0.1-0.4)$\times R_{200}$ to better suit the stellar halo size of each system.

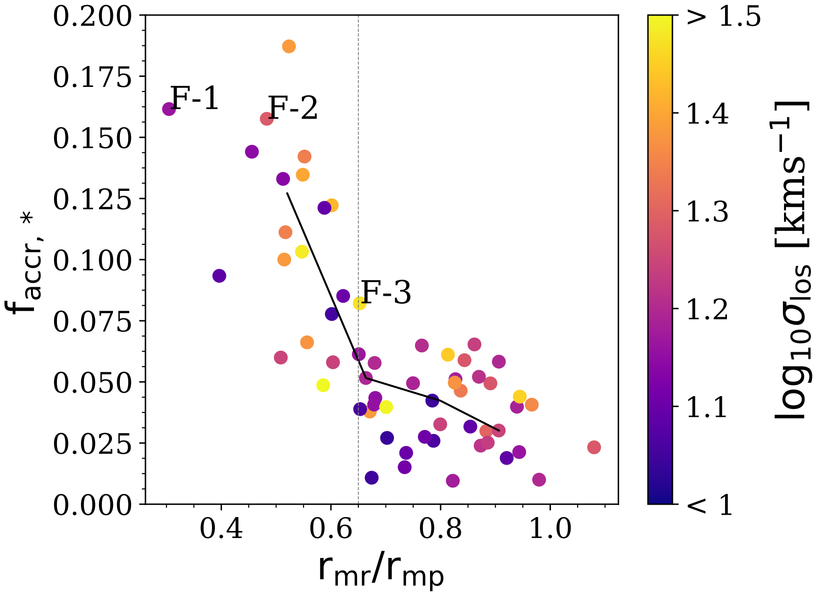

Figure 2.3: The fraction of the accreted stellar particles, $f_{\mathrm{accr},*}$, as a function of spatial segregation for galaxies with two metallicity populations. The points are coloured by the median of the line-of-sight velocity dispersion. The grey vertical dashed line separates dwarfs with low and high $r_{\mathrm{mr}}/r_{\mathrm{mp}}$. The galaxies on the left of this line are selected as our subsample of well spatially segregated galaxies. The black solid line shows the median relation in four bins of equal galaxy numbers. Three galaxies that will be studied in particular detail are labelled F-(1-3).

total stellar mass is made up of the stars that were accreted. Nonetheless, a large accretion fraction suggests prior merger activity; processes associated with these mergers are capable of inducing spatial segregation, as we now discuss.

2.3.1 Spatial segregation through mergers

We now investigate how mergers influence the spatial extent of the two metallicity populations. In Fig. 2.5 we illustrate this by tracking the evolution of the half-mass radii of three individual galaxies, ranging from the largest spatial segregation ($r_{\mathrm{mr}}/r_{\mathrm{mp}} = 0.30$) to the segregation at which we cut to select our subsample ($r_{\mathrm{mr}}/r_{\mathrm{mp}} = 0.65$). In the top row, the blue line represents the stars belonging to the metal-poor population formed *in-situ* and the red line shows the metal-rich population. The black line is the *total* half-mass radius. The half-mass radii are tracked from the moment when 50 stellar particles are present within the virial radius of the dwarf. We exclude the accreted stars as these make up a small fraction

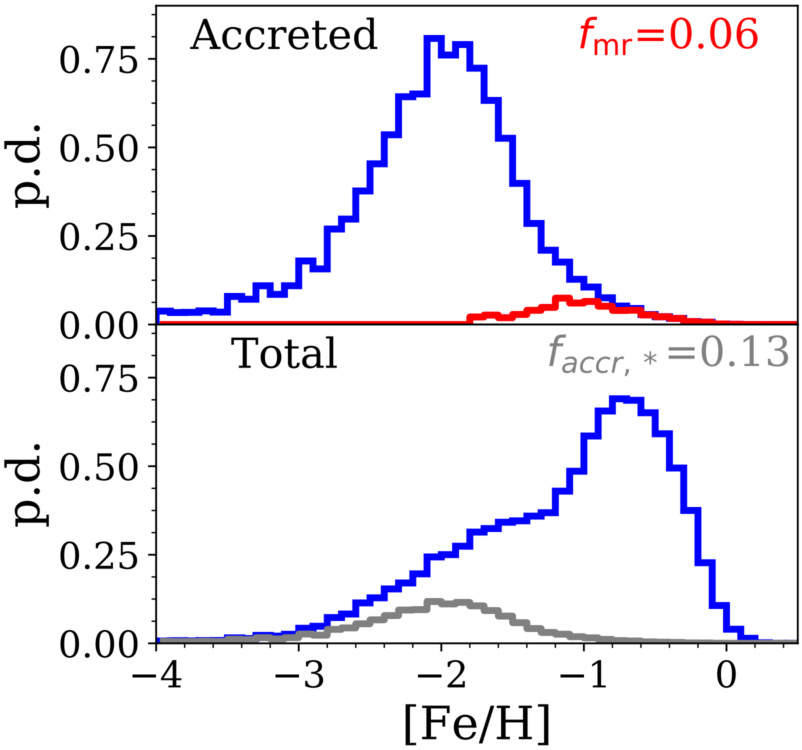

Figure 2.4: *Top:* the histogram of metallicities of accreted particles in field galaxies with $r_{mr}/r_{mp} < 0.65$ (blue). The red histogram corresponds to the subset of accreted particles that belong to the metal-rich population. *Bottom:* the histogram of all stellar particles in blue. The subset of particles that are accreted are shown in grey. The histograms give equal weight to each galaxy.

of the overall stellar population and their half-mass radii, throughout a dwarf's history, are not easily defined. The middle row shows the evolution of dark matter (black), gas (red) and stars (blue) bound mass*, normalized by their maximum mass throughout the history of the dwarf, M/M_{max}. The logarithmic maximum masses are shown in the upper left of each plot. The presence of mergers is evident as a sudden increase in dark matter mass. The metallicity-age distribution is shown in the bottom row for stellar particles present within the galaxy at $z = 0$. The black dashed line displays the value of the metallicity at which we split the two populations.

It can be seen that the mergers at early times are associated with a large increase in the half-mass radius of the system. The metal-poor particles that were formed *in-situ* prior to

---

*Bound mass is determined via a core-averaged unbinding procedure, as implemented in Han et al. (2012); Han et al. (2018).

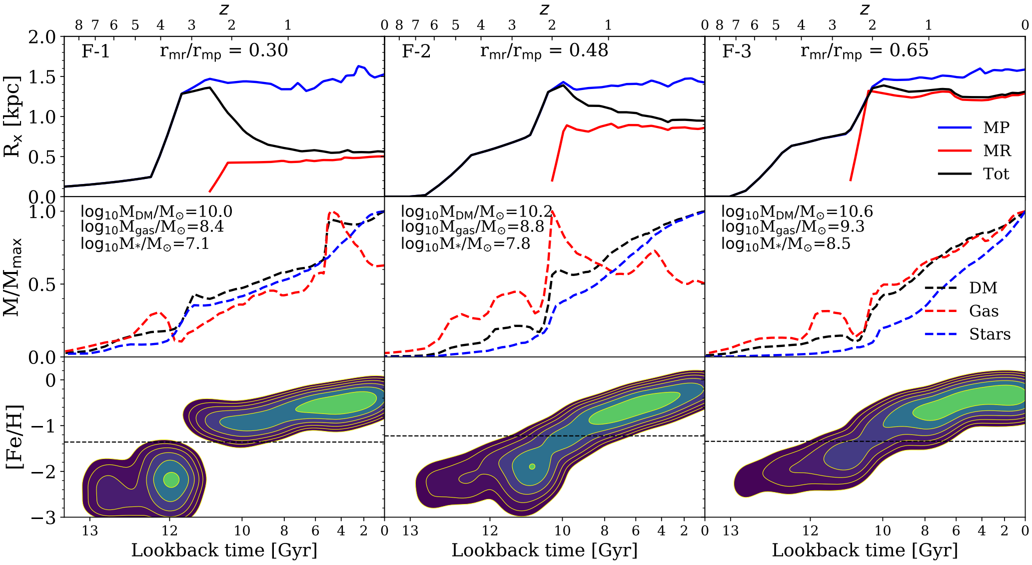

Figure 2.5: *Top:* the evolution of the half-mass radius of the metal-poor stars formed *in-situ* (blue), the metal-rich stars (red) and the entire set of stellar particles formed *in-situ* (black). The lookback time is shown on the bottom axis and the redshift on the top. The subpopulations are tracked from the time when they first contain at least 50 stellar particles. From left to right are three examples of galaxies with progressively poorer spatial segregation. *Middle:* the evolution of mass for the dark matter (black), gas (red) and stars (blue). Sudden increases in dark matter mass correspond to mergers. The mass is normalised by the maximum component mass, shown by the labels in the upper left corners. Note that galaxy F-2 merges with two haloes at approximately the same time. *Bottom:* the metallicity-age relation for the three example galaxies. The rise in metallicity is seen to occur following a merger. The contours in probability density are spaced geometrically by factors of 2 and are consistent for the three galaxies.

the merger move to larger characteristic radii. This is likely due to redistribution of particle energies as a result of a rapidly changing gravitational potential. This effect is particularly evident in dwarf F-1, where the half-mass radius almost quadruples in size. Dwarf F-1 undergoes a second major merger at ∼ 5 Gyr lookback time, with a secondary-to-primary halo mass ratio of $\mu \sim 0.3$. This mass ratio is far smaller than that at ∼ 12 Gyr ($\mu \sim 1$) and has little effect on the spatial segregation of the two populations.

The early mergers in the three systems coincide with an increase in the number of stars formed and are followed by a significant increase in the stellar metallicity. As we demonstrate in Section 2.5.2, these mergers are associated with a rise in star formation activity followed by a steep drop, as large fractions of gas are expelled in winds. The enrichment of the interstellar medium from the newly formed stars continues during this period of low star formation activity and the metal-rich stars are consequently formed at systematically higher metallicities. The metal-rich population proceeds to form gradually until late times, creating a significant gap between the peak metallicities of the two populations (see Section 2.5.1). We examine the origin of the metallicity distribution bimodality and where the gas particle enrichment occurs in greater detail in Section 2.5.

It can be seen in Fig. 2.5 that the half-mass radius of the metal-poor population increases to ~ 1.5 kpc in all three dwarfs following the merger and the characteristic radii at which the metal-rich stars form appears to determine the extent of spatial segregation between two metallicity populations in these systems. From left to right of Fig. 2.5 the dwarfs increase in stellar and halo mass and the size of the metal-rich population in these galaxies likely follows a mass-size relation (see the top panel of Fig. 2.2). For instance, like F-2, dwarf F-3 undergoes an early merger; yet the spatial segregation between its two populations is smaller. This galaxy retains a larger fraction of gas following the merger, as well as accreting new gas, such that star formation continues during and immediately after the merger. This results in continuous enrichment of the stellar particles and a less pronounced gap in the distribution of metallicities. For a more massive halo, new stars are forming at correspondingly larger radii, limiting the spatial segregation. Nonetheless, the merger that this galaxy experienced increased the extent of the metal-poor population sufficiently that the final spatial segregation between the two populations is significant.

Nonetheless, as previously seen in Fig. 2.3, the spatial segregation is not determined by the final mass of the system, represented by velocity dispersion in that figure, and the radii at which the metal-rich stars form are additionally affected by halo assembly history, gas supply and environment.

2.3.2 Merger-induced formation of two metallicity populations

We have seen that the spatial segregation between two metallicity populations in field dwarfs is related to mergers and their effect on the size of the metal-poor population as well

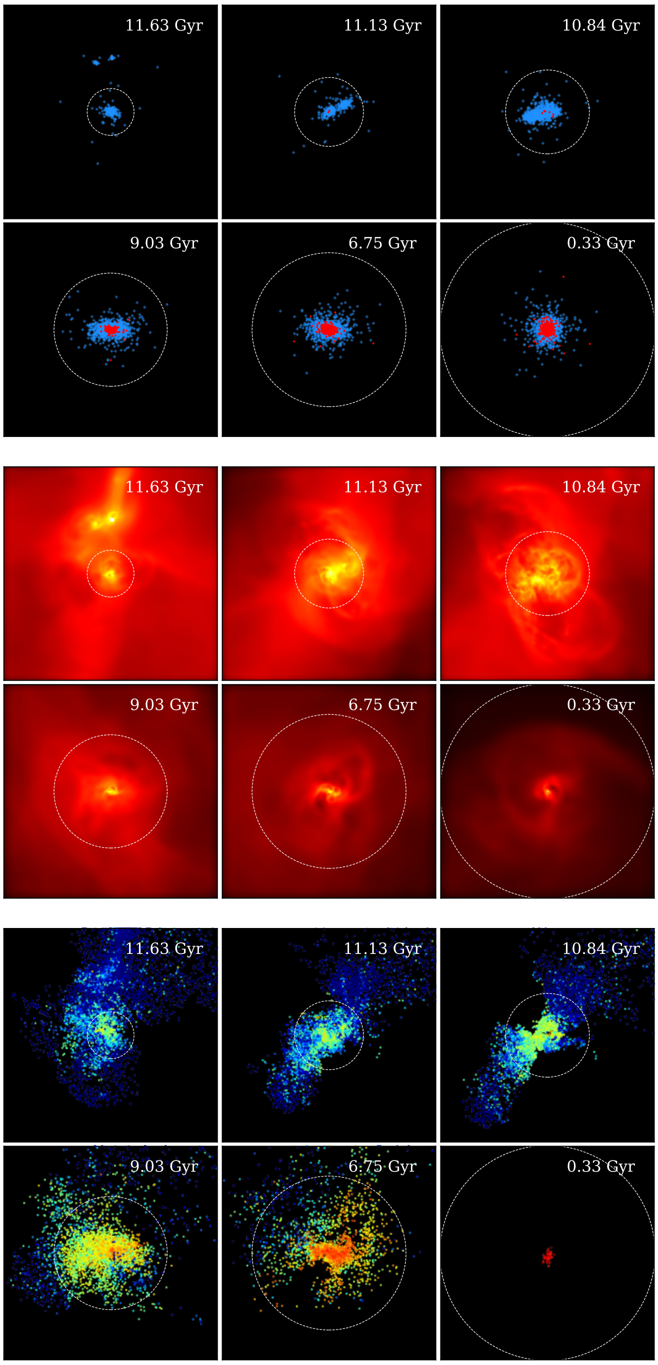

Figure 2.6: A field dwarf (labelled F-2) at 6 stages of its evolution. Lookback time is shown in the top right of each image. The images cover a cube of 50 kpc on a side. The galaxy is shown from a direction perpendicular to its angular momentum vector at each time. The white circles show the virial radius. *Top:* stellar particles with metal-poor particles in blue and metal-rich ones in red. *Middle:* the gas content of the dwarf. The kernel smoothed gas density varies from low density (dark red) to high density (yellow). *Bottom:* gas particles destined to form stars, coloured by their metallicity from lowest (blue) to highest (red).

as on the radii at which the metal-rich stars form. We now investigate the role that mergers play in the formation of two metallicity populations further.

In Fig. 2.6 we show the evolution of one particular two-population field dwarf with a strong spatial segregation ($r_{mr}/r_{mp} = 0.48$), previously labelled as F-2. The top panel shows the stellar particles in the galaxy; the metal-poor stars are coloured blue and the metal-rich stars red. The middle panel displays the corresponding gas densities on a logarithmic scale, with black indicating the lowest densities and yellow the highest. The bottom panel shows the gas particles destined to form a star within the galaxy, coloured by their metallicity at that time, with blue the most metal-poor and red the most metal-rich.

At the lookback time of 11.63 Gyr the main progenitor is approached by two gas-rich haloes. These haloes will supply some of the gas that will form stars within the galaxy. By 11.13 Gyr those haloes have combined into a single halo that merges with the main progenitor at around 10.84 Gyr. The mass ratio in dark matter is $\mu \sim 1$, making this a major merger. The virial radius of the system, R_{200} (indicated by a white dashed circle), has visibly increased following the merger as has the extent of the metal-poor stellar population. During the merger, at 10.84 Gyr, one can see gas bubbles extending beyond the virial radius. This is the result of a wind powered by large amounts of energy released in supernovae from stars that formed as a result of the merger. This gas is expelled beyond the virial radius and the majority will never return to form stars. The first metal-rich stars have been formed in this burst of star formation. A small fraction of gas remains at 9.03 Gyr and down to very late times this gas reservoir is enriched within the galaxy and continuously depleted by further formation of metal-rich stars.

Dwarfs F-1 and F-3 follow a similar formation history with the key differences being the halo masses and the ability to retain gas immediately after the merger. It is thus evident that two-population systems that end up with small values of r_{mr}/r_{mp} follow a well-defined formation mechanism. Dwarfs with $r_{mr}/r_{mp} < 0.65$ can form within a wide range of halo and stellar mass. In these galaxies the peak of star formation occurs simultaneously with the merger, typically between 9-12 Gyr in lookback time. The associated burst of star formation leads to the expulsion of large amounts of gas, with only the most strongly

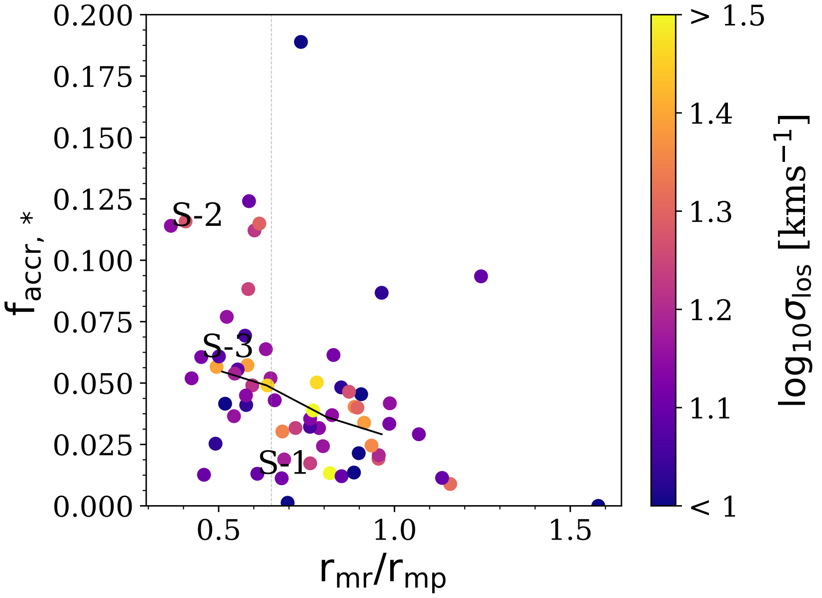

Figure 2.7: Similar to Fig. 2.3, but for satellite dwarfs: the stellar accretion fraction for satellite dwarfs. The two-population satellites are shown with blue circles. The vertical grey line separates well- and poorly spatially segregated metallicity populations. The black line shows the median of the relation. Three dwarfs that will be later discussed in particular detail are labelled S-(1-3).

bound gas remaining. The gas expulsion causes a decrease in star formation activity and, therefore, a drop in the number of metal-poor stars formed. The stars formed during the merger proceed to enrich the interstellar medium from which the metal-rich stars form, giving rise to a gap in the metallicity distribution. The dwarfs that do not follow these conditions typically end up with weaker spatial segregation and less clear bimodality in the metallicity distribution.

2.4 The formation of two populations in satellite dwarfs

We now focus on the satellite dwarfs in the APOSTLE simulations. Unlike isolated dwarfs, these may be subject to tidal and ram pressure stripping, as well as other interactions with their hosts. As a result, the origin of the two metallicity populations is different from isolated galaxies.

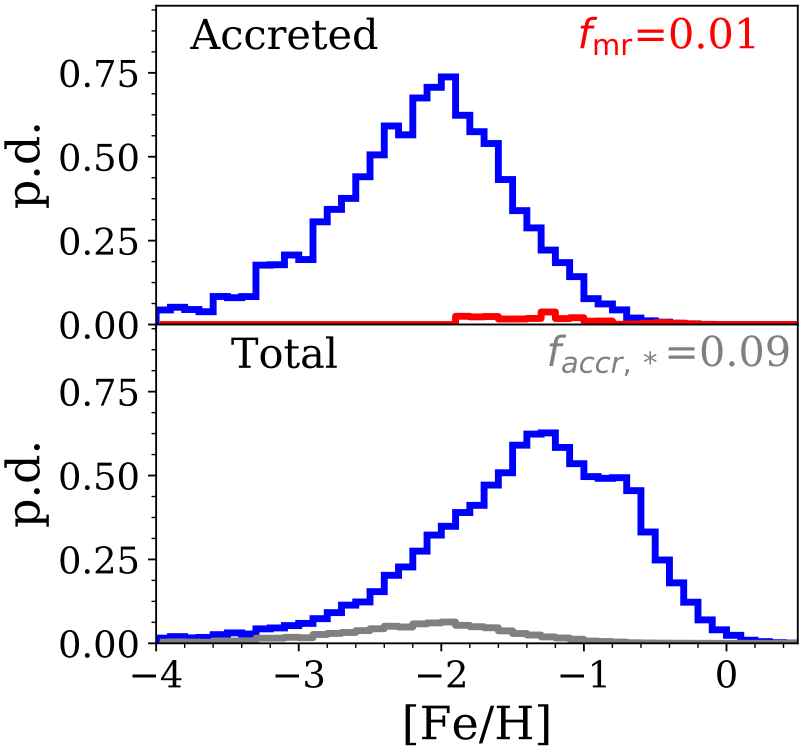

Figure 2.8: Similar to Fig. 2.4, but for satellite dwarfs with $r_{mr}/r_{mp} < 0.65$: histograms of metallicity for stars that have been accreted (upper figure) and for the total stellar population (bottom figure).

2.4.1 Halo assembly in satellites

Following our discussion of field dwarfs, we now investigate the role of mergers in the formation of two metallicity populations in satellites. Similarly to Fig. 2.3 and Fig. 2.4, Fig. 2.7 shows the fraction of accreted stars and Fig. 2.8 the distribution of metallicities for the accreted and total stellar populations in the satellites.

A pattern similar to that in Fig. 2.3 may be seen, although with larger scatter. The galaxies with greater spatial segregation do indeed accrete larger fractions of their stars, though to a lesser extent than field dwarfs. As shown at the top of Fig. 2.8, approximately 1 per cent of the metal-rich population typically comes from outside the galaxy and thus, as in field dwarfs, the metal-rich population is predominantly formed *in-situ*. Unlike for field dwarfs, however, the total metallicity distribution displays a more dominant metal-poor population. For similar accretion fractions to those of field dwarfs, this would suggest that either the

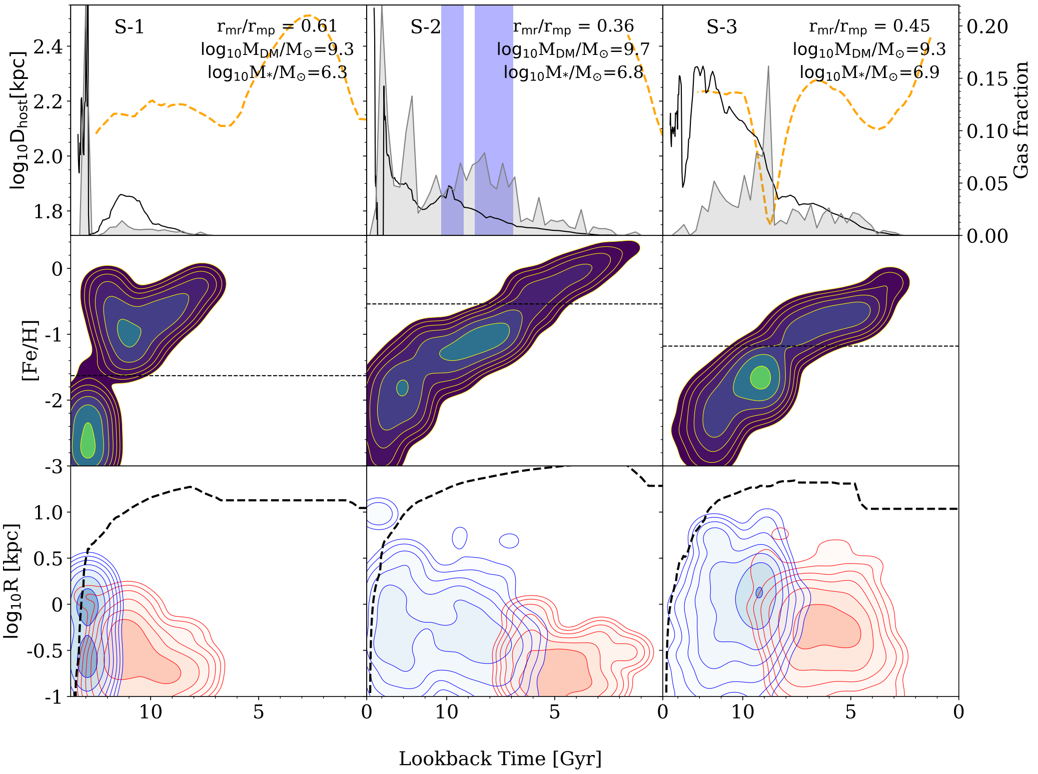

Figure 2.9: Properties of three example satellites in order of increasing stellar mass. *Top:* grey shaded areas show the SFH of the dwarfs in arbitrary units. The black solid lines show the gas fraction of the satellites (the bound gas mass divided by the dark matter mass), with the corresponding scale displayed on the right. The yellow dashed lines show distance to the host galaxy. For dwarf S-2, the blue bands show the times of interaction with cosmic filaments, as will be illustrated in Fig. 2.10. *Middle:* the metallicity-age distribution for the three galaxies. The dashed line shows the metallicity value at which our method splits the two populations. The probability density contours are geometrically spaced with a ratio of 2 and are consistent for the three dwarfs. *Bottom:* the radii at which the metal-rich (red) and the metal-poor (blue) particles form. The black dashed line is the evolution of the virial radius, which becomes the tidal radius after infall. The width of the smoothing kernel of the density estimate is consistent for the three galaxies across the middle and bottom panels.

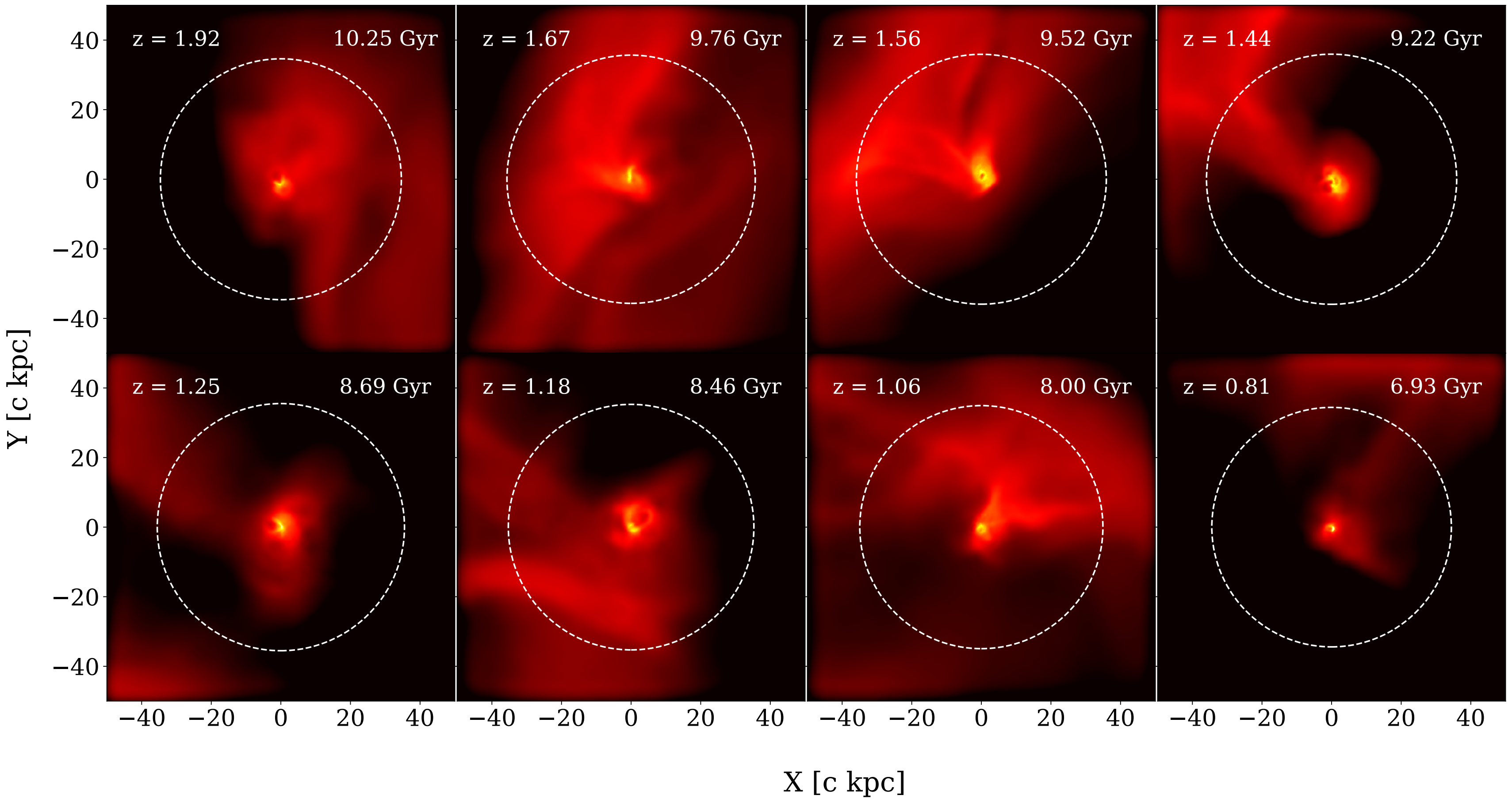

Figure 2.10: Gas density of dwarf S-2 as it passes through two cosmic filaments (top and bottom panels, respectively), which enhances star formation activity. The redshift and lookback times are given in the upper corners and the white circle represents the virial radius. The high-density regions are shown in yellow and the low-density regions in black.

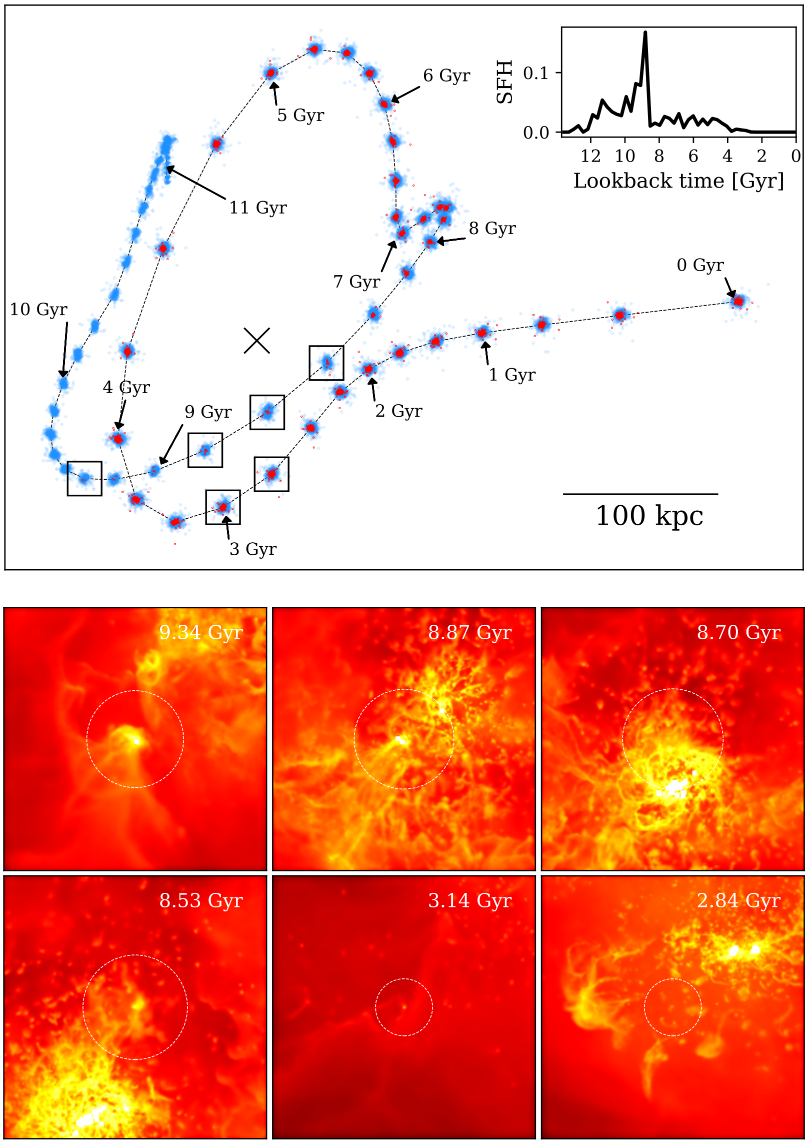

Figure 2.11: *Top panel*: the evolution of the satellite (labelled S-3) since its first stars formed just before a lookback time of 11 Gyr. The thin dotted line tracks the orbit of the satellite in the reference frame of the host halo. The black cross shows the position of the host halo. The squares mark important stages of the satellite's evolution. Between 9 and 8 Gyr in lookback time the satellite passes though the pericentre. At ~3 Gyr it encounters a larger, more massive, satellite. The inset at the top right displays the star formation history. The abrupt changes in the orbit between 8 and 6 Gyr, are caused by a fluctuation in the centre of potential of the host halo as it merges with a massive object. *Bottom panel:* the evolution of the gas distribution during the six stages of the satellite's evolution, as shown with squares in the upper figure. Yellow shows high density and black shows low density regions. The circle indicates the virial radius before infall (~9.5 Gyr) and the tidal radius thereafter. The images show a cube of 50 kpc on a side.

mergers tend to occur later in satellites, allowing less time for the metal-rich population to form, or that processes other than mergers are at play that shut off star formation, resulting in a smaller fraction of metal-rich stars.

We can conclude that mergers may play some role in the formation of satellite dwarfs with two spatially segregated metallicity populations, yet lower accretion fractions and differences in the typical metallicity distribution compared to field dwarfs suggest that the precise mechanism may be more complex than in field galaxies.

We select the objects with $\mathrm{r_{mr}/r_{mp}} < 0.65$ as our subsample of satellite dwarfs with two well spatially segregated populations. We will now examine the mechanisms by which the metal-rich population forms in these galaxies.

2.4.2 Satellites with two metallicity populations and their environment

We have seen some evidence that the satellites tend to have smaller fractions of metal-rich stars than the field dwarfs. The process of infall into the host halo limits the gas available to form the second population of stars and thus may be responsible for the formation of a smaller metal-rich population. We now examine three examples of well spatially segregated satellite dwarfs in the context of their environment.

Fig. 2.9 shows the three example dwarfs in order of their stellar mass. The top panel shows the distance to the host galaxy (yellow line), the evolution of the gas fraction (black) and the star formation history (grey). The middle panel displays the metallicity-age distribution for these galaxies and the lower panel shows the radii at which the metal-rich (red) and the metal-poor (blue) stars form.

2.4.2.1 Two populations through mergers in satellites

Dwarf S-1 has the lowest stellar mass of the two-population galaxies in our sample. At $\sim$13 Gyr in lookback time, it merges with a gas-rich halo and forms its entire metal-poor population in a quick burst of star formation that consumes all of the available gas, expelling the rest from the halo through star formation feedback. This is evident in the evolution of the gas fraction seen for this dwarf in Fig. 2.9. Following the burst, the galaxy smoothly accretes more gas that is used up over the next ~5 Gyr in the formation of a metal-rich population. Note the peculiar shape of the metallicity-age distribution for this dwarf (middle panel). Some of the more metal-rich stars form first in this galaxy after the merger. This is because the first gas to return to the galaxy comes pre-enriched with metals expelled in the original outflow. The remainder of the accreted gas is slowly enriched as it sinks to the centre of the dwarf, with more metal-rich stars forming near the centre (bottom panel of Fig. 2.9). Further accretion of gas in S-1 is prevented as the galaxy falls into its host halo with the first pericentre at ∼ 7 Gyr in lookback time.

2.4.2.2 Ram pressure-induced star formation

As can be seen in Fig. 2.9, dwarf S-2 does not reach the pericentre of its orbit by $z = 0$ and only falls in within the last 1 Gyr. At lookback times of ∼ 13 Gyr and ∼ 12 Gyr it undergoes two accretion events, where its star formation peaks and the new stars are consequently formed with higher metallicities. Nonetheless, the metal-rich stars in this galaxy, as determined by our method, only begin forming at ∼ 9 Gyr, when the satellite passes through a gaseous cosmic filament (blue band), triggering an increase in the star formation rate. At ∼ 8 Gyr this galaxy passes through another gaseous filament. The metal-rich stars continue forming until the gas is depleted in this galaxy. Such interactions have been previously noted by Benítez-Llambay et al. (2013) and Wright et al. (2019). We show this passage through the cosmic filaments in greater detail in Fig. 2.10. This displays the gas distribution of the dwarf and its surroundings as it approaches the cosmic filaments (the first filament is seen coming from the bottom right corner at 10.25 Gyr and the second filament in the bottom left corner at ~8.69 Gyr) and passes through the overdense regions. Following passage through each filament, the dwarf develops a tail of stripped gas. It is at these times that S-2 undergoes the intense star formation activity that enriches the interstellar medium and triggers the formation of metal-rich stars. Additionally, the stripping of the gas results in the preferential formation of these stars in the central regions, where the gas still remains bound (see bottom panel of Fig. 2.9).

A small fraction of dwarfs form their two populations through interactions with other dwarf galaxies. The two dwarfs pass by each other without a merger, but with interacting dark matter haloes and gas, which results in the compression of the gas in the centre and its stripping in the outer regions. Note that these two mechanisms are also applicable to field dwarfs.

2.4.2.3 Induced star formation by pericentric passage

For dwarf S-3, the most intense episode of star formation activity is seen to align with the first pericentric passage in Fig. 2.9. In the metallicity-age distribution (middle panel) this is visible as a density peak associated with the metal-poor population, followed by a tail of metal-rich stars.

In Fig. 2.11 we examine galaxy S-3 in particular detail. The top panel displays the orbit of the satellite and the formation of its stars. The star formation history is shown in the inset. The lower panel displays the gas distribution, with the white circles representing the virial radius at times prior to infall and the tidal radius after infall[*].

This satellite falls into the host halo at ~ 9.34 Gyr. As can be seen in the bottom panel, it still retains some amount of gas at infall. Between 8.87-8.53 Gyr the satellite passes the pericentre of its orbit and encounters the gaseous halo of its host, losing a significant fraction of its gas through ram pressure stripping, as shown by the tails in the gas distribution. However, during this time, star formation in the satellite peaks and, by approximately 8 Gyr, the first metal-rich stars begin to form. By ~ 3 Gyr the satellite has turned most of its gas into stars and the remainder is further stripped by an encounter with a larger subhalo, as seen in the bottom right panel (at 2.84 Gyr). The abrupt changes in the satellite's orbit between 8 and 6 Gyr in lookback time are a consequence of the host galaxy undergoing a merger, resulting in a noticeable shift of its centre of potential whilst the merger is ongoing.

---

[*] We define the tidal radius as the radius where the enclosed subhalo density is 3 times that of the host halo at that distance.

We have verified that the orbit of the satellite is, in fact, smooth in a different reference frame.

The example of dwarf S-3 suggests a new mechanism for the formation of two metallicity populations, whereby near pericentre the satellite's innermost gas is compressed in the centre of the dwarf triggering a starburst. This gives rise to significant enrichment of the interstellar medium over a short period of time and to the formation of a metal-rich population at the centre. Furthermore, due to ram pressure stripping, a large portion of the remaining gas is subsequently lost and star formation is shut off.

2.4.3 Summary

We have identified three processes by which satellites can form their two metallicity populations. The first, as in the example of dwarf S-1, is consistent with a scenario we previously found for field dwarfs, with an extra caveat of an interaction with a host galaxy, where further growth of the metal-rich population is prevented by ram pressure stripping.

In galaxies S-2 and S-3 ram pressure and tidal interactions act to enhance the star formation activity and to enrich the interstellar medium, provided there is a pre-existing supply of gas. Furthermore, gas stripping allows only the innermost bound gas to remain to form stars, resulting in a high spatial segregation as well as a smaller fraction of metal-rich stars. The degree of spatial segregation achieved through this mechanism is expected to be limited by the size of the metal-poor population (in particular by whether or not it had been expanded by earlier merger activity) and the amount of gas available for star formation. Note that the Small and Large Magellanic Clouds have long been speculated to have episodes of enhanced star formation activity due to interactions with each other and the Milky Way (Weisz et al., 2013).

We note that merger activity or accretion is not uncommon in satellite dwarfs (see Fig. 2.7). This plays a significant role in increasing the extent of the metal-poor population, thus enhancing the spatial segregation, although these events do not appear to be the cause of the formation of the metal-rich population in the majority of our sample.

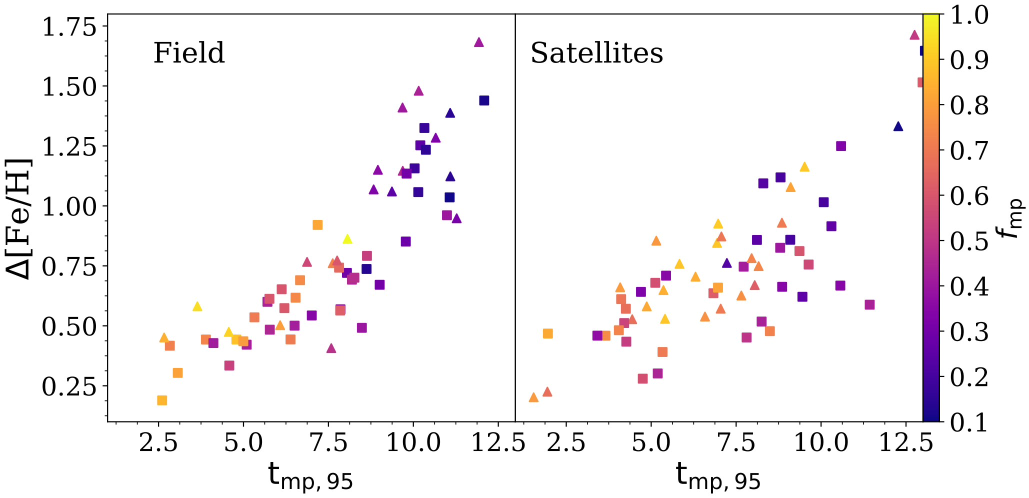

Figure 2.12: The ‘gap’ between the peak metallicities of the metal-rich and metal-poor populations as a function of the lookback time to when the metal-poor population stopped forming, $t_{mp,95}$. The points are coloured by the fraction of metal-poor stellar mass. Field galaxies are shown on the left and satellites on the right. The galaxies that have a particularly large spatial segregation are shown with triangles. It is clear that these are not dependent on the size of the metallicity peak separation.

Whether these scenarios are applicable to Local Group satellite galaxies is, of course, dependent on the realism of star formation histories exhibited by simulated dwarfs. For APOSTLE dwarfs, this has been recently investigated by Digby et al. (2019), who find general agreement with Local Group galaxies for which the photometry reaches the main sequence turnoff.

The efficiency of gas stripping when a satellite falls into the halo of its host is one of the key aspects that determines whether it may continue to form stars. In Appendix B we show the mass in HI to light ratio for our dwarfs as a function of distance to the nearest host galaxy at $z = 0$. These values agree well with the current measurements. In light of this, the scenarios described above are certainly plausible in Milky Way and Andromeda satellites.

2.5 The origin of the metallicity distribution bimodality

In this section, we discuss the origin of the bimodality in the metallicity distribution that allows our method to identify two metallicity populations. In particular, we focus on the creation of a ‘gap’, or the separation, between the two metallicity peaks and of the ‘dip’ in the distribution (i.e the minimum between the two metallicity peaks). We note that the ‘dip’ can be a feature of the Gaussian mixture fit, rather than of the metallicity distribution itself. In fact, the region where the metallicity cut is placed can be rather flat in certain cases. This region between the two metallicity peaks does, however, play a role in determining the optimal number of Gaussian mixtures in the fit to the distribution and therefore our ability to identify two peaks.

2.5.1 The gap between the two metallicity peaks and spatial segregation

Given a supply of gas available for star formation, a galaxy will gradually self-enrich as the newly produced stars pollute the interstellar medium with metals through mass loss and supernovae winds. In this simplistic assumption, the spread of a metallicity distribution for a single population should be related to the time taken to produce that population. Consequently, the ‘gap’ between peak metallicities of the two populations should be related to the difference in their formation times.

In the left panel of Fig. 2.12 we show the separation between the metal-rich and the metal-poor population peaks, $\Delta\,[\mathrm{Fe/H}]$, as a function of the approximate time when the metal-poor stars stopped forming, defined as the 95th percentile of the metal-poor stellar particle formation lookback times, $\mathrm{t_{mp,95}}$. The points are coloured by the fraction of metal-poor stars within the galaxy. The left panel displays the field galaxies and the right panel shows the satellite dwarfs. In case of the field galaxies a very clear trend is seen, where higher metallicity separations occur in galaxies that form their metal-poor population quickly, thus allowing the metal-rich population to build up whilst star formation is ongoing. This trend is also seen for satellite dwarfs, but with significant scatter. It appears that the metal-poor population in satellites forms later than in field dwarfs, typically around ~7 Gyr in lookback time. However, for the same metal-poor population formation time we now see a wide range of fractions of metal-poor stars. The mechanism responsible for the formation of the two populations in these galaxies must then also cause star formation to stall so that only relatively few metal-rich stars are able to form. We have established that the infall of

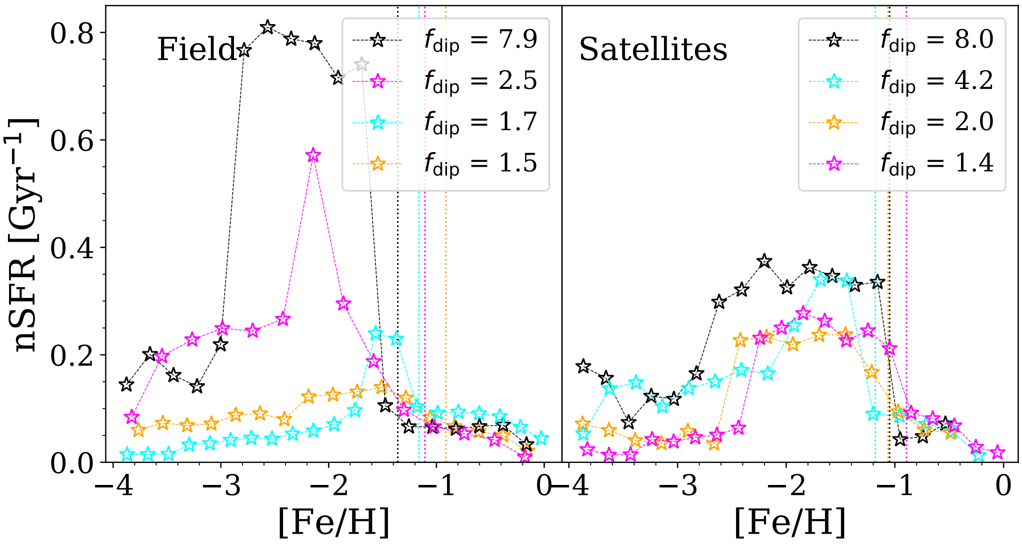

Figure 2.13: The median star formation rate in bins of stellar metallicity, normalised by the stellar mass of the galaxy, shown for four example galaxies with metal-poor peak to ‘dip’ ratio, $f_{\rm dip}$, given in the legend. The values represent how quickly the stars in each metallicity bin form.

the satellite into the host halo and the stripping of its available gas is capable of providing these conditions.

The triangles mark the galaxies which are spatially segregated. It is evident that spatial segregation may occur for any metallicity peak separation. However, in the limit where the metal-poor population is strongly dominant by mass or the metal-rich stars have little time to form, one might also expect to see strong spatial segregation due to the first metal-rich stars preferentially forming in central high-density regions. This is evident in the case of satellite galaxies, where the majority of galaxies with two well-segregated populations have very large fractions of metal-poor stars and are clearly distinct from the rest of the sample.

2.5.2 The transition between the metal-poor and the metal-rich population

What causes the ‘dip’ in the metallicity distribution that allows us to define a boundary between two populations?

In Fig. 2.13 we investigate four field and four satellite galaxies with well defined ‘dips’.

We define f_{dip} as the ratio of the height of the metal-poor population peak to the height of the distribution at which the metallicity cut is placed in a normalised [Fe/H] histogram. We show the median star formation rate normalised by the total stellar mass, nSFR, for bins in metallicity. The dotted vertical lines show the metallicity at which we place the cut between the two populations. It is evident that larger ‘dips’ correspond to larger drops in star formation rate near the boundary between the two populations. The metal-poor stars appear to have formed at a larger than average rate, while for the metal-rich population formation, the star formation rate drops significantly. Note that after the drop in star formation the stars form at an approximately constant rate for field dwarfs, such that the metal-rich population takes a long time to complete its formation, which is consistent with the origin of the metallicity ‘gap’ proposed earlier. For the satellite galaxies, one can see a gradual decrease in the star formation rate following the drop. This gradual decrease in star formation activity is consistent with the rapid removal of gas following infall in satellites. (Simpson et al., 2018).

2.5.3 Where is the gas enriched?

One may now ask whether it is gas enriched within the galaxy or elsewhere that causes the formation of the metal-rich stars. In order to investigate this, we track all gas particles that have spawned a stellar particle and the evolution of their metallicity. We find the position of these particles when they first cross the metallicity threshold that would allow them to be classified as metal-rich particles. In the left panel of Fig. 2.14, for field galaxies, we show a stacked histogram of these positions, together with the 16^{th} and the 84^{th} percentiles, normalised by the virial radius of the halo at that time. The black dashed line shows the location of the virial radius. It can be seen that almost all particles reach the metallicity required to form a metal-rich star within the virial radius of the halo and only ~ 1.5 per cent are enriched outside the halo. In a merger, each of the merger partners can carry on forming stars, until the stellar components have also merged into a single stellar halo. The purple dashed line shows the typical galaxy stellar size, $0.15\times$ R_{200}. Approximately 65.5 per cent of gas particles are enriched within the stellar halo of the galaxy and only

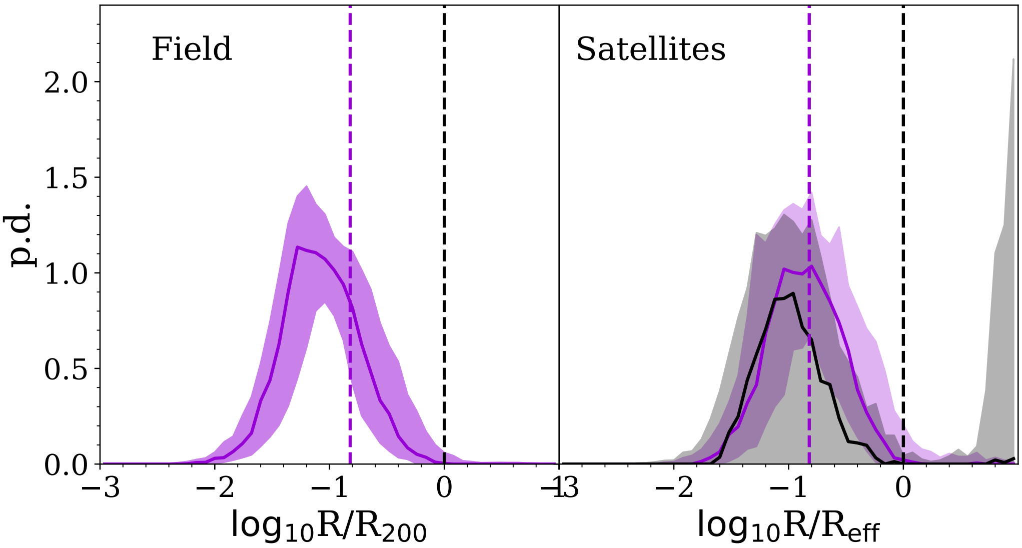

Figure 2.14: The position of the gas particles destined to form a metal-rich star at the time when they crossed the metal-rich metallicity threshold, normalised by the virial radius of the halo. The median histogram shape is shown with a purple line and the bands represent the 16th and the 84th percentiles. The black and purple dashed lines represent the virial radius and the typical galaxy stellar halo size ($0.15\times R_{200}$), respectively.

33 per cent are enriched outside and within the virial radius. We thus conclude that the enrichment necessary to form a metal-rich population is mostly self-enrichment within the galaxy whether it is in the process of merging or not.

In the right panel of Fig. 2.14, we show the corresponding distributions for satellite dwarfs. The positions are normalised by a radius, $R_{\rm eff}$, which is the virial radius pre-infall (purple stacked histogram) or the tidal radius of the satellite after infall (black stacked histogram). As in the case of field dwarfs, it is clear that prior to infall enrichment occurs within the galaxy, with only ~3 per cent of the gas being enriched elsewhere. After infall, the individual histories for each satellite vary significantly, with some undergoing no further enrichment at all and others showing evidence of further self-enrichment, as displayed by the grey shaded region. A significant fraction of galaxies appear to accrete some of their gas after infall (see the 84th percentile peak outside of the virial radius). A satellite may be able to accrete some of its host's enriched gas if it is moving at a sufficiently low relative velocity. We conclude that the formation of the metal-rich particles in satellites is triggered primarily by star formation activity and by self-enrichment of gas within the satellite itself.

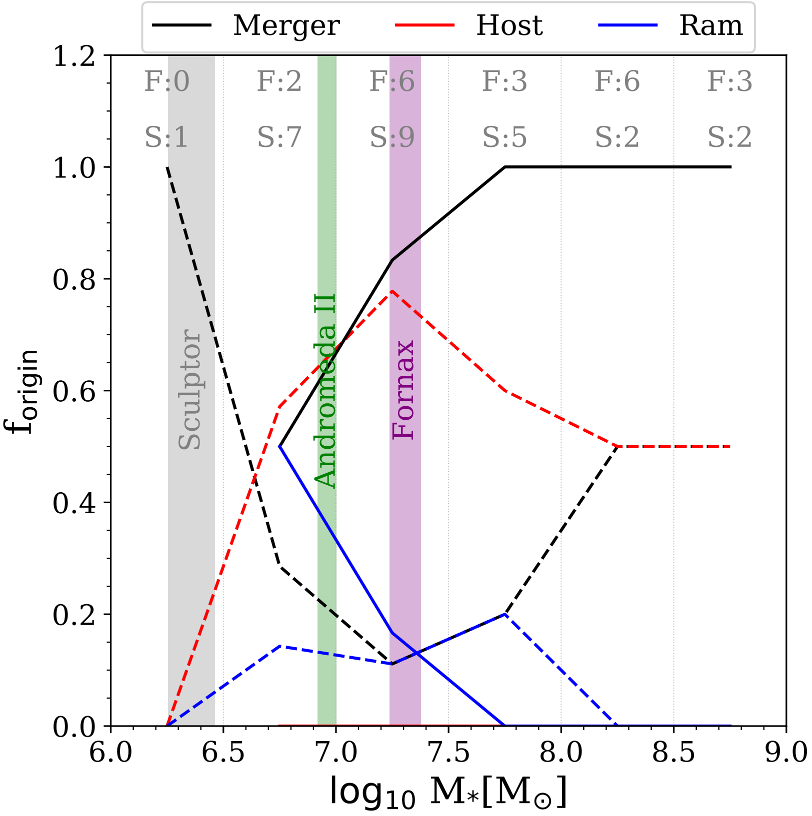

Figure 2.15: The fraction of field (solid lines) and satellite (dashed lines) dwarfs forming through each mechanism: mergers (black), interaction with a host galaxy (red, for satellites only) and ram pressure and tidal interactions with cosmic filaments or other galaxies (blue). Bins in stellar mass are separated with grey dashed lines. At the top, we show the number of field and satellite dwarfs within each bin. The stellar masses (assuming the stellar mass-to-light ratio of 1) for Sculptor, Fornax, and Andromeda II are shown with coloured bands.

2.6 Mass dependence of the formation mechanisms

In this section, we explore how the formation mechanisms described for field and satellite dwarfs with two spatially segregated populations operate for different bins in stellar mass. For each dwarf in this sample, we determine the primary cause of formation of the metal-rich population through analysis of the metallicity-age relation, as well as merger and environmental histories. In particular, we note the event responsible for sufficient gas enrichment that results in the formation of metal-rich stars. The results are shown in Fig. 2.15, where we explore 6 stellar mass bins, $\log_{10}M_*/M_\odot$ = [6, 6.5, 7, 7.5, 8, 8.5, 9], highlighted with grey dashed lines.

For field dwarfs with $r_{mr}/r_{mp} < 0.65$ (solid lines) we find that ~90 per cent form their two populations through mergers (black), with the remainder forming through interactions with cosmic filaments and other dwarfs (blue). We find that the probability of formation through mergers steadily increases with stellar mass, as expected for more massive haloes.

We find that ~60 per cent of the satellites with $r_{mr}/r_{mp} < 0.65$ (dashed lines) form their metal-rich population by passing through pericentre (red), ~30 per cent form through mergers (red) and ~10 per cent through interaction with filaments or nearby galaxies (blue). The pericentre mechanism for satellites dominates at all stellar masses above $\log_{10}M_*/M_\odot = 6.5$, remaining consistently at above ~50 per cent. Above $\log_{10}M_*/M_\odot = 7.5$ the fraction formed through mergers increases from ~10 per cent to 50 per cent. Below $\log_{10}M_*/M_\odot = 6.5$ only S-1 is present in our sample, which formed through a merger. There is some evidence for an increase in the formation of a metal-rich population through mergers below $\log_{10}M_*/M_\odot = 7$. It is difficult to say whether in this mass range the merger scenario would dominate, given the sample size, although these lower-mass objects are certainly less likely to maintain sufficient amounts of gas to form a metal-rich population at pericentre.

The grey, green and purple bands show the mass ranges for Sculptor, Andromeda II and Fornax, respectively (assuming the stellar mass-to-light ratio equal to 1) (McConnachie, 2012). As satellites, Andromeda II and Fornax are most likely to have formed their metal-rich populations during their pericentric passages; however, this scenario is dependent on these dwarfs passing through the pericentre while retaining a sufficient supply of star-forming gas. Otherwise, mergers and interactions with other subhalos or filaments are likely to play the main role. The analyses of dwarf star formation histories and proper motions, in light of results from *Gaia* (Gaia Collaboration et al., 2018), should shed light on the applicability of the pericentre scenario to individual dwarfs.

2.7 Properties of two-metallicity population dwarfs

In this section, we explore properties of two-population satellites and field dwarfs. Of particular interest are the ellipticities of the individual populations, the significance of rotation, velocity anisotropy, metallicity gradients and the velocity dispersion ratio of the two populations. We investigate whether these properties contain information about the formation paths of these galaxies. We show these properties in Fig. 2.16, which displays satellite and field dwarfs with $\mathrm{r_{mr}/r_{mp}} < 0.65$ with coloured symbols, with the rest of dwarfs that show bimodality in their metallicity distributions shown in grey. The size of the symbols reflects the logarithm of the stellar mass of the dwarfs.

We define sphericity as the ratio, $s = c/a$, where c^2 and a^2 are the eigenvalues of the reduced inertia tensor corresponding to the minor and major axes of a 3D ellipsoid (Bett et al., 2007). An isotropic distribution would have $s = 1$. The upper panels of Fig. 2.16 show the individual sphericities of the metal-rich (horizontal axis) and the metal-poor populations (vertical axis). Field dwarfs are shown in the left-hand panel and satellites in the right. The black circles represent dwarfs with two spatially segregated metallicity populations, where the formation of the metal-rich-population has occurred as a result of a merger, while the red circles show satellites where the metal-rich population has formed as a result of the first pericentric passage. The blue circles show objects where the metal-rich population is the result of a galaxy's interaction with a cosmic filament or a nearby galaxy. It is clear that satellites tend, on average, to be more spherical than field galaxies. Additionally, the subset of satellites whose star formation peaks near the first pericentre also tends to be more spherical than the rest of the sample. The field dwarfs with high spatial segregation tend to have more spherical metal-rich populations. This could be a reflection of the effects that the mergers responsible for the creation of a metal-rich population have on the shape of these galaxies.

We characterize the rotation of individual subpopulations by the fraction of stars within that subpopulation that are rotating in the same direction. In the second row of Fig. 2.16 we show these fractions for the metal-rich, $\mathrm{f_{mr}}$, and the metal-poor, $\mathrm{f_{mp}}$, populations. The

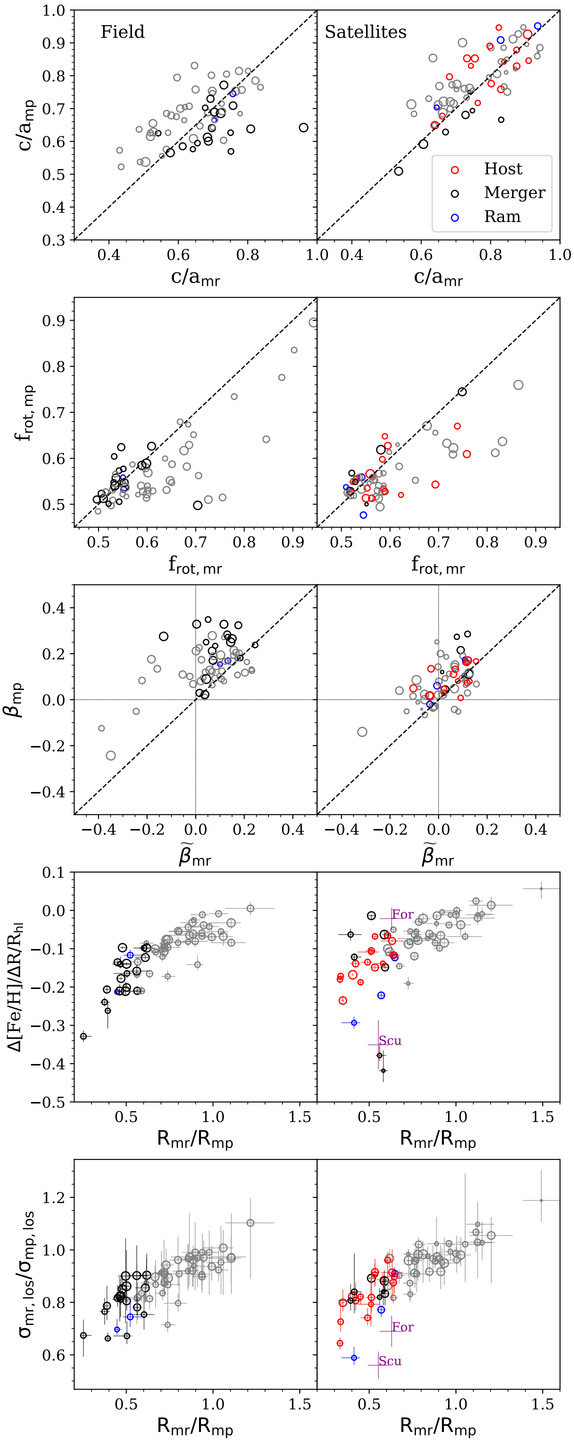

Figure 2.16: Properties of individual subpopulations. Colours denote formation mechanisms (see legend). Symbol sizes indicate the logarithm of stellar mass. The black dashed lines are one-to-one relations. *First row:* the sphericity of the two populations, c/a. *Second row:* the fraction of stellar particles in ordered rotation, $\mathrm{f_{rot}}$. *Third row:* velocity anisotropy, $\widetilde{\beta}$. *Fourth row:* the metallicity gradient, $\Delta\,[\mathrm{Fe/H}]/\Delta \mathrm{R}/\mathrm{R_{hl}}$, as a function of the ratio of the projected half-mass radii, $\mathrm{R_{mr}}/\mathrm{R_{mp}}$. *Fifth row:* the ratio of the line-of-sight velocity dispersions as a function of $\mathrm{R_{mr}}/\mathrm{R_{mp}}$.

metal-rich populations tend to exhibit stronger rotation than the metal-poor populations, in both satellites and field dwarfs. Field dwarfs with high spatial segregation appear closer to the one-to-one relation, whilst satellites with star formation peaking near pericentre show a small bias towards more rapidly rotating metal-rich populations. Evidence of rotation has been found in real two-population Local Group dwarfs (Battaglia et al., 2008; Ho et al., 2012; del Pino et al., 2017a).

We define the orbital anisotropy as $\beta = 1 - \sigma_t^2/(2\sigma_r^2)$, where σ_t and σ_r are the tangential and radial velocity dispersion components respectively. In the third row of Fig. 2.16 we plot the anisotropy, normalised to lie between 1 (radial) and -1 (tangential), $\widetilde{\beta} = \beta/(2-\beta)$ (Read and Steger, 2017). These values are averaged in bins of equal particle number. The dotted lines indicate isotropy. It is clear that stars in field dwarfs have preferentially radially-biased motions that are stronger in the metal-poor population. This behaviour is less extreme in satellites perhaps reflecting preferential stripping of radially-biased orbits.

The fourth row of Fig. 2.16 shows the projected metallicity gradients of our satellite and field dwarfs as a function of $\mathrm{R_{mr}/R_{mp}}$. The uncertainties were derived by calculating these quantities along 1536 evenly distributed lines of sight (Górski et al., 2005). The metallicity gradients are characterized by the slope of the least-squares fit to [Fe/H] and $\mathrm{R/R_{hl}}$, where $\mathrm{R_{hl}}$ is the projected half-light radius. In this fit, we exclude the extremely metal-poor stellar particles ([Fe/H] < -4) as these are unreliable given the mass resolution of our simulations (Schaye et al., 2015). We also only include the stars within $\mathrm{5R_{hl}}$, which excludes the outer halo stars that would be difficult to differentiate from background in observations. Galaxies with strong spatial segregation exhibit particularly steep gradients, in some cases, more than twice as steep as the typical value for the sample ($\Delta\mathrm{[Fe/H]}/\Delta(\mathrm{R/R_{hl}}) \sim -0.1$). This is consistent with the metal-poor halo assembly through early mergers seen in the simulations of Revaz and Jablonka (2018). The purple symbols show the metallicity gradients in Sculptor and Fornax, respectively, obtained from Kirby et al. (2010), where we take the $\Delta\mathrm{[Fe/H]}/\Delta\mathrm{r}$ values and multiply by the half-light radii from McConnachie (2012), carrying the errors, for better comparison with what we measure in our simulations. These observations are consistent with the steep metallicity gradients present in satellites in our simulations with well spatially segregated populations. In particular, note that Sculptor overlaps within 1σ with two satellite dwarfs that has formed via a merger (black points). One of these galaxies is dwarf S-1 and anther follows a similar formation history.

Finally, the bottom panel of Fig. 2.16 shows the ratio of the line-of-sight velocity dispersions of the two populations, $\sigma_{\rm mr,los}/\sigma_{\rm mp,los}$, plotted against the ratio of the projected half-mass radii. These quantities are of particular interest in the application of the Walker and Peñarrubia (2011) method for the determination of the inner dark matter density slopes (which we shall discuss in the next chapter). The two quantities follow a very clear relation. This is not surprising, as the velocity dispersion is expected to scale with enclosed mass. Satellites appear to have a less significant kinematic difference between the two populations than field dwarfs. Sales et al. (2010) show that this may be due to the effects of tidal stripping. We have investigated this and found only a weak trend, which may be due to star formation at pericentre, which Sales et al. (2010) do not include in their analysis. The values for Sculptor and Fornax, taken from Walker and Peñarrubia (2011), are plotted in the figure. These values lie well below our relation even after taking into account the effects of projection. The origin of this discrepancy is unclear and might be due to the differences in the way in which the two metallcity populations are defined in the simulations and in the data; in particular, metallicity mixing between the two populations may have an effect. Additionally, the larger typical sizes of our sample of dwarfs compared to real dwarfs may contribute to this discrepancy, in particular by increasing the velocity dispersion of the metal-rich population, although the effect of the larger overall sizes on $\rm R_{mr}/R_{mp}$ is not entirely clear.

From these considerations we conclude that the spatial and kinematic properties of individual subpopulations do not provide sufficient information on the formation paths of the two subpopulations; many of the observed differences are primarily due to environmental effects (satellites or isolated dwarfs) and seem to be independent of stellar mass. Nonetheless, we have seen that satellites tend to have a smaller number of metal-rich stars relative to metal-poor stars than field dwarfs. This is almost certainly due to the smaller gas supply available to form the metal-rich stars due to tidal and ram pressure stripping of gas as the satellite falls in. In this case, the constraints on the stellar ages, metallicities and the satellite orbit should allow one to distinguish between the merger or pericentric passage origin of the metal-rich population.

2.8 Metallicity bimodality in Local Group dwarfs

In this work, we have identified a sample of dwarf galaxies within the APOSTLE suite of simulations that exhibit a bimodality in their [Fe/H] distribution, which we define as an indicator of the presence of two metallicity populations. These galaxies make up nearly half of our overall sample in the stellar mass range 3×10^6 - 1×10^9 $M_\odot$. Whilst signs of bimodality have been seen in the metallicity distributions of Sculptor (Kirby et al., 2009) and Fornax (Battaglia et al., 2006), the shapes of the distributions also tend to change with different or updated samples of stars (Kirby et al., 2013). In fact, the work of Walker et al. (2009a), with data for over 1000 stars in both Sculptor and Fornax, shows no trace of two metallicity peaks*. We thus aim to establish to what extent does the sampling of stars and the spatial extent of the observed region affect the effectiveness of our method, described in Section 2.2.4, in determining the number of populations in a given dwarf.

We begin by considering our entire sample of two-population dwarfs. For each of these dwarfs, we select 192 evenly spaced lines of sight with the method of Górski et al. (2005) and change the size of the “aperture" in units of the projected half-light radius, ranging between $0.2R_{hl}$ and $5R_{hl}$. We select the stars contained within the aperture and apply our method for determining the number of populations. The results are shown with the red line in the left panel of Fig. 2.17, where we show the fraction of two-population galaxies identified correctly as a function of radius. Note that this requires all stars to be observed within this radius. The shaded regions represent the 1σ scatter from different lines of sight. It can be seen that the stars extending out to at least $2R_{hl}$ are required to correctly identify all galaxies. Within the half-light radius, ~80 per cent of systems are identified. This statistic is improved for dwarfs with significant spatial segregation between the two

---

*Note that Walker et al. (2009a) use spectroscopically determined magnesium and iron line indices as indicators of [Fe/H]. These authors note that the indices are better used as measures of *relative* metallicity.

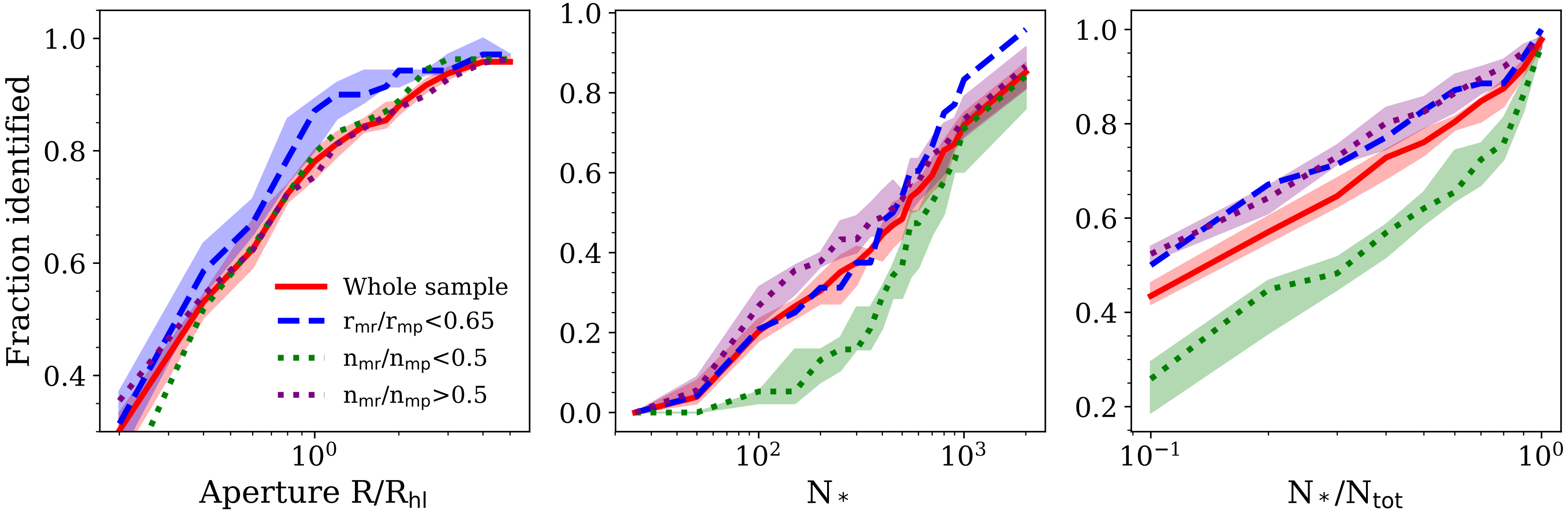

Figure 2.17: The fraction of two-population dwarfs detected when varying three key quantities. *Left:* the aperture within which the stellar sample is detected as a function of the projected half-light radius. *Middle:* the number of stars used within each galaxy. *Right:* fraction of the total number of stars. The colours show different subsamples of dwarfs, with the whole sample of two-population dwarfs in red; those that are well spatially-segregated in blue; dwarfs with a dominating metal-rich population in purple and dwarfs with a dominating metal-poor population in green. The shaded bands show the 16th and 84th percentiles from varying lines of sight. We only show the shaded bands for those subsamples of dwarfs that deviate significantly from the results for the whole sample.

populations (blue line), where the data within the half-light radius is sufficient to identify two peaks. Note that whilst the two peaks may be found, the spatial segregation may not be apparent if the metal-poor population is particularly extended. The galaxies with a dominant metal-rich (purple) and a dominant metal-poor (green) populations do not significantly differ from the trend for all galaxies.

In the middle panel of Fig. 2.17 we show the fraction of correctly identified galaxies as a function of the number of stellar particles within the sample. The shaded bands indicate the scatter due to particle sampling. Here we only include dwarfs with at least 2000 stellar particles. It can be seen that even with a sample of a 1000 stars only 70 per cent of the dwarfs show bimodality. For a typical sample of ~300 stars only 40 per cent show two metallicity peaks. The fraction is smaller for dwarfs with a dominant metal-poor population. This is characteristic of satellites that form their metal-rich population through the pericentric passage route. This is also evident in the rightmost panel, where we show the fraction of the total number of stars within the galaxy. A full sample is required to ensure 100 per cent detection of two peaks. From the leftmost panel, we can see that this requires data from within ~2-3R_{hl}.

From the sample of McConnachie (2012), there are collectively 25 Milky Way and Andromeda satellites that fall within the magnitude range explored in this work. If, similarly to our sample, 40 per cent of these have bimodality in their metallicity distribution (~ 10 galaxies), then, provided a sample of spectroscopically determined metallicities, and a typical sample size of ~300 stars, we expect that 2-5 of those will be found to exhibit bimodality.

With the above in mind, we examine the data provided by Kirby et al. (2013) for signs of bimodality in the metallicity distributions. This is described in Appendix C, where our method only identifies two populations in Sculptor, with a metallicity cut between the two consistent with Battaglia et al. (2008). The spatial extent of these data, however, does not allow inferences to be made about the spatial segregation of the two populations.

We conclude that whilst the sample sizes currently observed may be sufficient for our method to identify bimodality, further spectroscopic measurements are needed, in particular for the metal-poor population in the outer regions of dwarfs, although obtaining these may be extremely challenging due to increasing background contamination.

2.9 Conclusions

A number of dwarf galaxies of the Local Group contain two spatially and kinematically distinct stellar populations. The origin of this phenomenon is not fully understood although several scenarios have been proposed in the literature. In particular, mergers are thought to play an important role (Łokas et al., 2014; Starkenburg et al., 2015; Benítez-Llambay et al., 2016; Fouquet et al., 2017). This scenario has some backing from observations of substructure and rotation in dwarfs like Fornax and Andromeda II.

In this work, we have examined 142 field and 108 satellite dwarf galaxies from the APOSTLE suite of cosmological hydrodynamics simulations. We find that 43 per cent of field dwarfs and 53 per cent of satellite dwarfs show bimodality in their [Fe/H] distributions and among those ~30 per cent are well spatially segregated.

We first consider field dwarf galaxies. We find that their stellar accretion fraction is directly related to the degree of spatial segregation between the two metallicity populations. We find evidence that this is primarily due to the metal-poor stars migrating to larger orbital radii as a result of a merger. The metal-rich population is subsequently formed *in-situ*. Among the field dwarfs with two well-segregated metallicity populations, ~ 90 per cent form their metal-rich populations by this mechanism.

In addition to the merger scenario for the formation of two population dwarfs, we identified a formation mechanism that is specific to satellite galaxies. As the satellite falls into its host halo, ram pressure may compress the gas at the centre of the satellite whilst simultaneously stripping gas from the outer regions. As a result, a new population of stars forms at the centre of the satellite. Of the satellites with two well spatially segregated populations, ~ 60 per cent form their metal-rich population through this mechanism.

A related process which occurs in both satellites and field dwarfs is interaction with a gaseous cosmic filament. When a galaxy crosses a filament, ram pressure may trigger star formation activity, whilst simultaneously stripping the outer gas. Nonetheless, we find that this mechanism is responsible for the formation of metal-rich stars in only ∼10 per cent of galaxies with two well-segregated populations.

We also investigate the properties of the individual metallicity subpopulations, specifically rotation, sphericity and velocity anisotropy. In general, we find that both populations tend to have higher sphericities in satellites than in field dwarfs. This is consistent with previous work on the effects of tidal stripping (Barber et al., 2015). In field dwarfs the metal-poor population is typically rounder than the metal-rich population; stars in both populations tend to have radially-biased orbits, more so in the metal-poor population. In satellites this bias is smaller, due to the preferential stripping of stars in radial orbits.

The presence of two metallicity populations results in metallicity gradients similar to those in two-population Local Group dwarfs, particularly Sculptor and Fornax; these resemble galaxies in our sample that have undergone mergers. On the other hand, the ratio of the line-of-sight velocity dispersions of the two populations in Sculptor and Fornax appear inconsistent with the ratios in our sample. The origin of this discrepancy is unclear but it could be influenced by differences in the definitions of the two metallicity populations.

We investigated whether the spatial and kinematic information on the individual populations could help identify their formation mechanism, particularly in satellite dwarfs. We found that the available information is insufficient for this purpose. Nonetheless, measurements of stellar metallicities and constraints on dwarf orbits and star formation histories will provide important clues on their likely origin.

We have explored how many Local Group satellites, in the magnitude range similar to that explored in this work, are likely to be identified as having a bimodal metallicity distribution given observational limitations. Our results suggest that approximately 2-5 objects should be detectable, given spectroscopic samples of ∼300 stars. We use our method to identify two populations in Sculptor dwarf spheroidal, consistent with previous works. We point out that data with a large spatial extent, (> $2R_{hl}$), which contains over 1000 stars is required for ~70 per cent detection and is particularly important for identifying galaxies with dominant metal-poor populations, such as those that have formed their metal-rich population by passing through pericentre.

Chapter 3

Solving the core-cusp problem in dwarfs with two metallicity populations

3.1 Introduction

Dwarf spheroidal galaxies are promising objects to test ideas about the inner structure of dark matter haloes. Although they are faint, some are sufficiently close-by that their stellar populations can be resolved. Much effort has therefore been invested in trying to infer their halo profiles. A large body of work is concerned with field galaxies with measurable H I velocity fields; many such studies claim robust detections of central cores (e.g. Oh et al., 2011; Kuzio de Naray et al., 2006; Adams et al., 2014). However, a recent study (Oman et al., 2019), based on the same APOSTLE (A Project Of Simulating The Local Environment) simulations that we will analyse here, has revealed the presence of systematic effects in even the most detailed analyses of spatially resolved kinematics, casting doubt on claims that cores are present in those galaxies. Similar conclusions were reached by Pineda et al. (2017).

The kinematics of resolved stars in nearby galaxies offer an alternative to the kinematics of H I gas as a probe of the density structure of haloes. The detection of cores in several dwarf satellites of the Milky Way has been claimed on the basis of simple Jeans analyses (e.g. Gilmore et al., 2007), but the more general analysis by Strigari et al. (2010) has shown that current data are, in fact, unable to distinguish between cores and cusps in the Milky Way satellites. Some satellites of the Milky Way and Andromeda exhibit metallicity gradients: they have a centrally concentrated metal-rich population and a more extended, and kinematically hotter metal-poor population (Tolstoy et al., 2004; Battaglia et al., 2008, 2011). The possible origin of these systems has been disccussed in detail in the previous chapter, as well as the works of Benítez-Llambay et al. 2016 (mergers), Tolstoy et al. 2004; Battaglia et al. 2006 (reaccretion of gas), Kawata et al. 2006 (reionization and self-enrichment), Wright et al. 2019 (ram pressure) and El-Badry et al. 2016 (radial migration due to supenovae feedback).

The presence of two kinematically and spatially distinct metallicity components can be used to set constraints on the inner density profile of the common halo in which they move. Battaglia et al. (2008) identified a metal-rich ($[\mathrm{Fe/H}] > -1.5$) and a metal-poor ($[\mathrm{Fe/H}] < -1.7$) population in the Sculptor dwarf spheroidal and, using Jeans modelling, found that a wide range of profiles are consistent with the data, from a pseudo-isothermal sphere ($\rho \propto r^0$ at the centre) to an NFW profile. Amorisco and Evans (2012b) pointed out that some of those models are unphysical and, fitting the Sculptor data to a particular phase-space distribution function, found that while a profile with a core is preferred by their χ^2 fits, an NFW profile is also allowed by the data. Using more general phase-space distribution functions, Strigari et al. (2014) also showed that the two metallicity subpopulations in Sculptor are consistent with an NFW profile. A similar conclusion, using Schwarzschild modelling, was reached by Breddels et al. (2013) who found that a core profile is also allowed, while a cusp in Sculptor was found to be favoured by an analysis based on the fourth-order virial theorem by Richardson and Fairbairn (2014).

Walker and Peñarrubia (2011) took this idea further and developed a statistical methodology to distinguish the two metallicity subpopulations in Sculptor and Fornax. Making use of the interesting result of Wolf et al. (2010) and Walker et al. (2009b) that the mass of a spherical stellar system in equilibrium can be robustly estimated at the half-mass radius of the system, they developed the method discussed in this chapter and concluded that both Sculptor and Fornax have central cores, with Sculptor, in particular, ruling out an NFW profile at high statistical significance. Their method is based on estimating the total mass contained within the half-light radii of the metal-rich and metal-poor subpopulations, thus constraining the slope of the dark matter density profile. Wolf et al. (2010) and Walker et al. (2009b) have argued that the mass within a characteristic radius of a collisionless spherical system in dynamical equilibrium is well constrained by the velocity dispersion and average radial distribution of a population of star tracers, for a variety of stellar density and constant velocity anisotropy profiles.

Specifically, Wolf et al. (2010) showed that the mass is best constrained at radius, r_3, where the logarithmic slope of the stellar number density, $\mathrm{d}\log\nu/\mathrm{d}\log \mathrm{r} = -3$, which is close to the deprojected half-light radius ($\frac{4}{3}R_\mathrm{e}$, where R_e is the projected half-light radius) for a range of stellar distributions. Their estimator is:

$$M\left(<\frac{4}{3}R_e\right) = 4G^{-1}\langle\sigma_{\mathrm{LOS}}\rangle^2 R_e\,, \tag{3.1}$$

where $\langle\sigma_{\mathrm{LOS}}\rangle$ is the *luminosity-averaged* line-of-sight velocity dispersion. Similarly, Walker et al. (2009b) propose:

$$M\,(<R_e) = \frac{5}{2}G^{-1}\langle\sigma_{\mathrm{LOS}}\rangle^2 R_e\,. \tag{3.2}$$

Walker and Peñarrubia (2011) used a likelihood method to separate samples of stars in Sculptor and Fornax into two metallicity subcomponents and applied these mass estimators to each of them. For an object with mass density $\rho \propto r^{-\gamma}$ the enclosed mass is $M(r) \propto \frac{1}{3-\gamma}r^{3-\gamma}$. One can then define the asymptotic logarithmic mass slope as:

$$\Gamma = \lim_{r\to 0}\left[\frac{\mathrm{d}\log \mathrm{M}}{\mathrm{d}\log \mathrm{r}}\right] = 3-\gamma \tag{3.3}$$

For an NFW profile the asymptotic inner slope is $\gamma = 1$, so $\Gamma = 2$, while for a core with $\gamma = 0$, $\Gamma = 3$. In the case of a galaxy with two segregated subpopulations, the two half-light radii will be located away from the centre and thus $\Gamma = \Delta\log M/\Delta\log r$ is a measure of the (steeper) density slope further out (Walker and Peñarrubia, 2011). Assuming that the mass is given by the estimators above,

$$\Gamma \approx 1 + \frac{\log\left(\sigma_2^2/\sigma_1^2\right)}{\log\left(r_2/r_1\right)}\,, \tag{3.4}$$

where σ_i are the line-of-sight velocity dispersions and r_i are the half-light radii. Walker and Peñarrubia (2011) derived values of Γ for Sculptor and Fornax which exclude an NFW cusp at 99 and 96 per cent confidence levels, respectively, instead favouring a core. They argue that this conclusion is conservative because, if anything, the mass is likely to be overestimated for the central subpopulation.

In a recent paper, Campbell et al. (2017) tested the accuracy of the mass estimators by applying them to galaxies in the APOSTLE hydrodynamic cosmological simulations of Local Group analogues (for which the true mass is known; see Section 3.2). They report little bias in the median mass estimates but a scatter of 25 and 23 per cent for the Walker et al. (2009b) and Wolf et al. (2010) estimators respectively, which are much larger than the values inferred by these authors from simulations of spherical systems in dynamical equilibrium. Campbell et al. (2017) find that a major contribution to the scatter comes from deviations from spherical symmetry which are quite common in simulated galaxies. Subsequently, González-Samaniego et al. (2017) have generally confirmed the main conclusions of Campbell et al. (2017) regarding the scatter in the estimator from 12 dwarf galaxy analogues in the FIRE hydrodynamic simulations.

The effect of triaxality on Γ has been investigated by Laporte et al. (2013a), who tagged dark matter particles as stars in the (triaxial) dark matter haloes of the AQUARIUS simulations (Springel et al., 2008b). These authors find that an anti-correlation between the measured half-light radius and the projected velocity dispersion acts to keep the mass estimate approximately constant, causing little variation in the derived value of Γ. However, by construction, the dark matter and the stars in their analysis have strongly correlated shapes (Laporte et al., 2013b) which can introduce a systematic effect.

Kowalczyk et al. (2013) carried out idealized N-body simulations of the evolution of dwarf spheroidal galaxies in the gravitational potential of a Milky Way-like host. They introduced two spatially segregated disc subpopulations which evolve as the dwarf orbits in the halo of its host. They find that Γ may be over- or underestimated, depending on the line of sight. In particular, observations along the major axis of the dwarf tend to overestimate the mass and Γ. These simulations do not take into account dark matter halo triaxality, hydrodynamics, star formation or feedback processes.

Campbell et al. (2017) focused on the accuracy of the mass estimators applied to the stellar population of the dwarf galaxies in APOSTLE as a whole. Many of these galaxies, however, turn out to have two (or more) distinct metallicity subpopulations, analogous to those in Sculptor or Fornax. This offers the possibility of testing the validity of the conclusions of Walker and Peñarrubia (2011) using realistic dwarf galaxies formed in state-of-the-art cosmological simulations. This is the goal of this chapter. In Section 3.2 we outline the selection of our simulated galaxy sample and perform an analogous analysis to that of Walker and Peñarrubia (2011). In Section 3.3 we examine in detail a selection of case studies. We summarize our conclusions in Section 3.4.

3.2 Methods

3.2.1 Galaxy sample

In this work we use the APOSTLE simulations, the properties of which have been extensively discussed in Section 2.2.1. Haloes in the simulations are identified using the 'friends-of-friends' (FOF) algorithm with linking length of 0.2 times the mean particle separation (Davis et al., 1985). The SUBFIND algorithm is then used to identify gravitationally bound substructures within them (Springel et al., 2001). We define the host and subhalo centres as the centre of their potential (the position of the particle with the most negative potential energy).

Subhaloes bound to the main halo of a group are defined here as 'satellites'; other galaxies in the volume are labelled as 'field' galaxies. When computing the stellar mass of a subhalo, we include all particles located within 0.15 of the virial radius, R_{200}, for field galaxies and

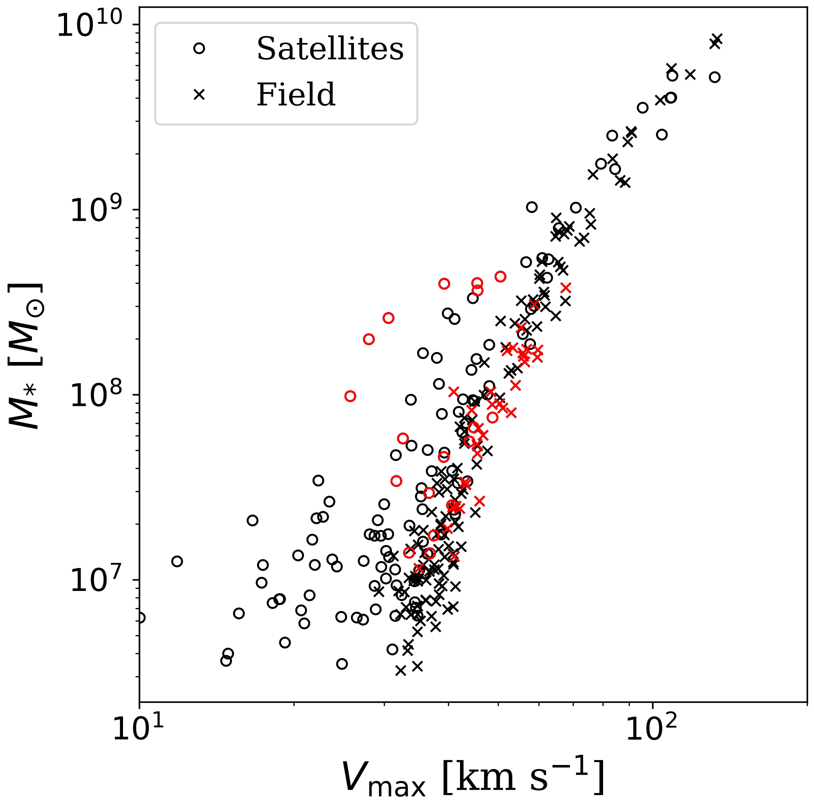

Figure 3.1: Stellar mass M_* as a function of maximum circular velocity $V_{\rm max}$ for satellite (circles) and field (crosses) galaxies in the five high-resolution volumes of APOSTLE. Galaxies matching the criteria described in Section 3.2.1 are shown in red. The sample is limited to galaxies with at least 1000 stellar particles to ensure adequate statistics.

particles located within the tidal radius*. We limit the sample of satellites and field galaxies to those with a minimum of 1000 stellar particles [corresponding to a stellar mass of the order of $(10^6 - 10^7)\ M_\odot$] to ensure reasonable statistics and good resolution within the half-mass† radius. The stellar mass as a function of the maximum circular velocity, $V_{\rm max}$, of galaxies in the five high resolution volumes is shown in Fig. 3.1.

In order to identify particles belonging to each stellar subpopulation, for every individual satellite and field galaxy we model the subcomponents using Gaussian Mixture Modelling (GMM) whereby the total metallicity distribution, $p(\log_{10} Z/Z_\odot)$, is fitted with a

---

[*] We define the tidal radius of a subhalo as a distance from subhalo centre where the mean enclosed density is equal to that of the host halo up to that distance for satellite galaxies. for satellite galaxies

[†] We use the term *half-mass radius* to refer to the radius enclosing half the stellar mass as measured directly from the simulations.

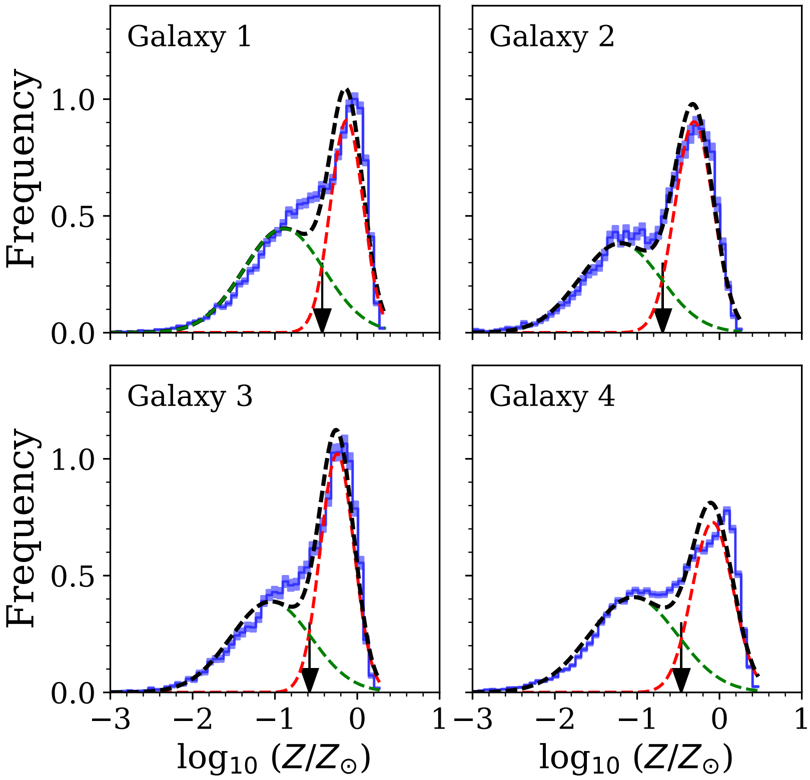

Figure 3.2: Metallicity histograms of the four galaxies that we use as case studies in this work. The blue curve represents the metallicity distribution and associated Poisson errors. The dashed black line shows the two-Gaussian fit. The dashed red and green lines show the individual Gaussians corresponding to the metal-rich and metal-poor subpopulations, respectively. The arrows show the metallicity at which the population is split. We have assumed a value of the solar metallicity of $Z_\odot = 0.0127$.

combination of two Gaussian probability density functions* (Hastie et al., 2001). Five parameters are fit altogether (w_1, μ_1, μ_2, σ_1, σ_2), with w_1 being the relative weight of one of the subpopulations, μ_i the mean metallicity and σ_i the metallicity dispersion. We then assign each particle to a subpopulation if its probability of being in that subpopulation is $p(i) > 0.5$. Effectively, the population is rigidly split at the value of metallicity where the two Gaussians cross. The subpopulation with a higher value of μ_i is denoted as metal-rich and that with the lower μ_i as metal-poor. A sharp cut in metallicity gives rise to some kinematic mixing of the two subpopulations. We have verified that mixing has only a minor effect on the main results of this work regarding the slope of the halo density profile (see

---

*As a measure of metallicity we use $\log_{10} Z/Z_\odot$, the logarithm of the abundance of elements other than hydrogen and helium. Stellar particles in APOSTLE are spawned probabilistically, with daughter particles inheriting smoothed metal abundances from their parent. For details see Okamoto et al. (2005, 2014).

Section E).

It is important to note, first, that the metallicity distributions of the two subpopulations will not necessarily be Gaussian, but will depend on the specifics of the history of star formation, accretion and mergers. We choose Gaussian probability densities for simplicity. As discussed in the previous chapter, cases may exist, where indeed more than two subpopulations are present. These objects would be of great interest for future work due to the possibility of constraining the inner density slope at two or more locations.

In principle, any probability distribution will be better fitted with Gaussian mixtures as the number of fitting parameters is increased. We therefore calculate the Akaike Information Criterion (AIC) corrected for finite sample (Akaike, 1998):

$$\mathrm{AIC} = 2k + \chi^2 + \frac{2k(k+1)}{n-k-1}\,, \tag{3.5}$$

where k is the number of fitted parameters, n is the number of data points and χ^2 is the chi-squared fit of our model to the data. We take the histogram errors to be Poisson-distributed. The first and third terms in Equation 3.5 represent the penalty on the number of free parameters in the model such that the difference between the AIC values for alternative models is indicative of the information gained by including extra parameters. We find the AIC for a model with a single Gaussian and a model with a mixture of two Gaussians for each galaxy in our sample. We then remove objects where the AIC for a single Gaussian is smaller than that for a mixture of two, as well as those where both models provide a poor fit. A total of 46 per cent of all galaxies satisfy these criteria. The metallicity histograms and subpopulation models of specific objects that we will discuss in particular detail later are shown in Fig. 3.2.

A simple split into two metallicity subcomponents does not guarantee that they will be spatially segregated. We remove from our sample the objects for which the separation between the two half-light radii is so small as to inflate Γ artificially, as $\Delta \log_{10} r$ approaches zero (see Fig. D1). We therefore discard all objects for which the logarithm of the ratio of 3D half-mass radii, $\log_{10}(r_2/r_1) < 0.06$. This condition removes a further 26 per cent of our original sample. For the remaining galaxies, we check that the metal-rich and metal-poor radii are well resolved as judged by the convergence radius defined by Power et al. (2003), at which the collisional relaxation time is approximately equal to the age of the Universe, ensuring that both radii are larger than this value. Overall, of all objects with over 1000 stellar particles in the five high-resolution volumes of APOSTLE, 18 per cent (50 objects) survive our selection criteria. The selected objects are shown in red in Fig. 3.1; they have stellar masses of the order of 10^7 - 10^8 $M_\odot$. We find that the fraction of stellar particles assigned to the metal-poor subpopulation ranges between 0.15 and 0.6, consistently with the results of Benítez-Llambay et al. (2016); the metal-rich stellar particles are typically the dominant subcomponent.

3.2.2 A test of the Walker-Peñarrubia prescription

We now carry out a straightforward test of the accuracy of the logarithmic mass slopes obtained following the Walker and Peñarrubia (2011) prescription. We generate 10 random lines of sight distributed uniformly on the surface of a sphere. For each line of sight, we obtain 1000 bootstrap stellar particle samples for each galaxy, with replacement and, for each sample, we calculate projected half-mass radii, R_e, directly as the projected radius within which half the total stellar mass is contained[*]. We then calculate the mass-averaged line-of-sight velocity dispersion as:

$$\sigma_\mathrm{LOS}^2 = \frac{\sum (v_i - \bar{v})^2 m_i}{\sum m_i}, \tag{3.6}$$

where m_i is the mass of each star particle, v_i is the velocity of the particle in projection and $\bar{v}$ is the mean velocity.

Inserting our measured values of R_e and $\langle \sigma_\mathrm{LOS} \rangle$ in the Walker et al. (2009b) estimator (Equation 3.2) we obtain the estimated mass within R_e of each subpopulation. For each galaxy, we repeat this calculation for the 1000 bootstrap resamplings and for 10 random directions. In Fig. 3.3 we plot Γ_true, the slope of the line joining the logarithm of the actual

---

[*] According to González-Samaniego et al. (2017) this method of estimating R_e results in the bias of ~ 0.9 in the estimated mass seen in the 12 FIRE simulations. However, using a much larger sample of galaxies in APOSTLE, Campbell et al. (2017) found that the mass estimate is, in fact, unbiased. We choose to calculate the projected half-mass radii as in Campbell et al. (2017).

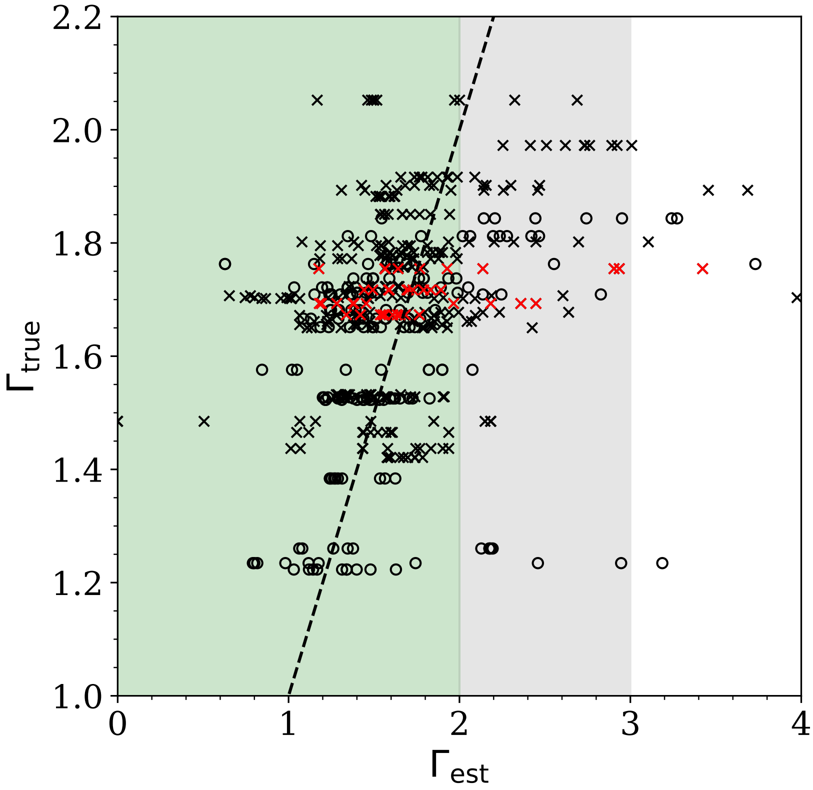

Figure 3.3: The slope of the logarithmic mass distribution, $\Gamma_{\rm est}$, obtained by applying the Walker et al. (2009b) estimator to simulated galaxies in our sample viewed from 10 random directions, plotted against the true slope at the projected 3D half-mass radius, $\Gamma_{\rm true}$. Field galaxies are shown as black crosses and satellites as black circles. Marked in red are the four particular cases that will be further discussed in detail in the next section. The green vertical band shows typical values of $\Gamma_{\rm est}$ for a cusp, (Γ = 2 corresponds to an NFW cusp); the grey band shows values of $\Gamma_{\rm est}$ typical for a core. The dashed line is the one-to-one locus. The slopes obtained from the estimator are slightly underestimated but exhibit significant scatter as the line of sight varies.

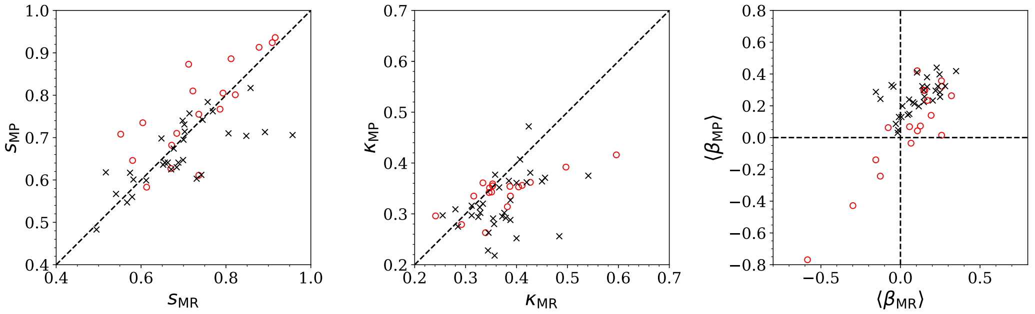

Figure 3.4: *Left:* the correlation of the sphericities of the metal-poor and the metal-rich subpopulations for satellites (red circles) and field galaxies (black crosses) in our sample. The dashed line indicates the one-to-one relation. *Middle:* $\kappa_{\rm rot}$ of the metal-poor and metal-rich subpopulations. *Right:* the correlation between the average velocity anisotropy of the metal-poor and metal-rich subpopulations. The dashed lines indicate isotropy, β=0.

mass within the true projected 3D half-mass radius of each subpopulation*, as a function of the median values of $\Gamma_{\rm est}$, the slope of the line joining the logarithm of the estimated mass within the measured $R_{\rm e}$ of each subpopulation.

It is clear that the estimated mass slopes tend to be underestimated on average, consistent with findings of Walker and Peñarrubia (2011), and thus the inferred slopes of the density profiles tend to be cuspier than the true values. (Recall that $\Gamma = 2$ corresponds to an NFW cusp, while $\Gamma = 3$ corresponds to a core.) The distribution is asymmetric and exhibits large scatter towards higher values of $\Gamma_{\rm est}$, with some objects reaching $\Gamma_{\rm est} \geq 3$. This bias reflects biases in the measurements of $R_{\rm e}$ and $\langle \sigma_{\rm LOS} \rangle$ as the galaxy is seen from different observer positions. We now investigate why the measured half-mass radii and velocity dispersions vary with the viewing direction.

3.2.3 Dynamical properties of the simulated galaxies

Campbell et al. (2017) identified asphericity, rotation and velocity anisotropy as the key properties that can introduce uncertainty in mass measurements based on stellar kinematics. We now quantify these properties for *each* metallicity subpopulation within each galaxy in our sample and examine the extent to which the properties of the two subpopulations are correlated with each other†.

3.2.3.1 Sphericity

Here we define the centre of each stellar subpopulation as its centre of mass. The shape of the system is characterized by the reduced inertia tensor (Bett et al., 2007):

$$I_{ij} = \frac{1}{M_{*,\rm sub}} \sum_n m_n \frac{r_{n,i} r_{n,j}}{r_n^2} , \tag{3.7}$$

where $M_{*,\rm sub}$ is the stellar mass of the subpopulation; m_n the mass of star particle n; $r_{n,i}$ and $r_{n,j}$ are the coordinates of particle n from the centre of the galaxy in directions i and

---

*We take the true projected 3D half-mass radius of an object to be 3/4 of the 3D half-mass radius measured from the simulation.

†As discussed in Section A, we have checked that the two subpopulations of the galaxies in our sample have a sufficiently large number of stellar particles for the properties of interest to be numerically converged.

j. The normalization r_n^2 ensures that only the angular distribution is taken into account, so that the shape is not unduly affected by distant particles. The eigenvectors of the inertia tensor correspond to the axes of the fitted ellipsoid and the eigenvalues, $a^2 \geq b^2 \geq c^2$ to squares of axis lengths. We define the sphericity $s = c/a$; $s = 1$ corresponds to a sphere.

The sphericities of the metal-rich and metal-poor subpopulations in our sample are plotted against each other in the left panel of Fig. 3.4. The two are positively correlated, albeit with significant scatter caused by one of the subpopulations in certain objects being appreciably more spherical than the other. These cases are of particular interest in this study. Also note that the satellites tend to be less aspherical than the field galaxies. This is likely due to the effects of tidal stripping as discussed in detail in the work of Barber et al. (2015).

3.2.3.2 Rotation

We quantify the degree to which each subpopulation is supported by rotation by computing $\kappa_{\rm rot}$, the fraction of kinetic energy invested in rotational motion (Sales et al., 2012):

$$\kappa_{\rm rot} = \frac{1}{K_{*,\rm sub}} \sum_n \frac{m_n}{2} \left(\frac{j_{z,n}}{R_{xy,n}} \right)^2 , \tag{3.8}$$

where $K_{*,\rm sub}$ is the stellar kinetic energy of the subpopulation, m_n the mass of star particle n, $j_{z,n}$ the component of the specific angular momentum of the particle in the direction of the total angular momentum and $R_{xy,n}$ the distance of the particle from the angular momentum axis. Objects with $\kappa_{\rm rot} > 0.5$ are considered to be primarily rotation-dominated, while objects with $\kappa_{\rm rot} < 0.5$ are considered to be primarily dispersion-dominated.

The values of $\kappa_{\rm rot}$ for subpopulations of galaxies in our sample are shown in the middle panel of Fig. 3.4. Our selected objects are generally dispersion-dominated and a strong bias exists towards higher $\kappa_{\rm rot}$ in the metal-rich subpopulation compared to the metal-poor. All simulated galaxies considered in this work have $\kappa_{\rm rot} < 0.5$ for the galaxy as a *whole*.

3.2.3.3 Velocity anisotropy

The velocity anisotropy is defined as $\beta(r)$=1-$\sigma_t^2/2\sigma_r^2$, where σ_r is the radial velocity dispersion and σ_t the tangential velocity dispersion including the contributions from azimuthal and polar directions. We construct velocity anisotropy profiles by calculating σ_r and σ_t for the 32 nearest neighbours of each star particle.

The right panel of Fig. 3.4 shows the average velocity anisotropy, $\langle\beta\rangle$, for each metallicity subpopulation (the average of local anisotropy of each particle). The majority of the galaxies in our sample tend to have radially biased stellar velocity distributions and the anisotropies are generally correlated in the two metallicity subpopulations. Yet, cases exist where $\langle\beta\rangle$ is radially biased for one subpopulation and tangentially biased or isotropic for the other. As we shall see, such discrepancies affect estimates of Γ.

3.3 The effects of projection: four case studies

In Fig. 3.3 we saw that a procedure analogous to that implemented by Walker and Peñarrubia (2011) in their analysis of the kinematics of Sculptor and Fornax dwarfs generally underestimates the logarithmic mass slopes Γ, albeit with a large scatter towards higher values, which would correspond to shallower inner density slopes. We now investigate the factors that affect the accuracy of the procedure. We first examine in detail four illustrative examples and in Section 3.3.2 we collect the results for our sample of 50 galaxies. We recall that the dark matter density profiles of all the galaxies in our sample are well described by an NFW profile.

The four examples are highlighted in red in Fig. 3.3. All four are isolated field galaxies, with no recent major mergers. Their two metallicity subpopulations are well segregated spatially. The line-of-sight velocity dispersion of the metal-poor subpopulation is higher than that of the metal-rich subpopulation (see Fig. 3.5 for the properties of the four examples). In two cases (Galaxies 1 and 2) the procedure on average recovers an accurate value of the slope, but in the other two (Galaxies 3 and 4) the procedure fails and, instead of a cusp, it often returns a profile with a core.

3.3.1 The effects of misalignment and anisotropy

We view each galaxy from 100 random directions generated uniformly on the surface of a sphere using the spherical spiral method outlined in González (2009). As in Section 3.2.2, for each line of sight we generate 1000 bootstrap resamplings (with replacement) of the stars in each galaxy and obtain median values of the quantities of interest. In Fig. 3.6, which is analogous to fig. 10 of Walker and Peñarrubia (2011), we plot the logarithm of the measured projected half-mass radii R_e of the bootstrap samples for each viewing angle, along with the corresponding logarithm of masses contained within these radii, inferred using the estimator of Equation 3.2. The measurements are coloured according to the angle between the line of sight and the major axis of the *metal-poor* subpopulation. (The major axes of the two subpopulations will not necessarily be aligned.) The true projected 3D half-mass radius and the enclosed mass of each subpopulation are marked by a cross. The sphericity and value of κ_rot for each metallicity subpopulation are given in the legend of each panel. For each viewing angle the inferred slope of the cumulative logarithmic mass profile can be obtained by joining points of the same colour in the metal-rich and metal-poor subpopulations. The dashed and dot-dashed lines show the minimum and maximum slopes inferred by this procedure.

The variation with viewing angle of relevant quantities for each galaxy is plotted in Fig. 3.7 and is discussed below. In this plot, α denotes the ratio, $M_\mathrm{est}/M_\mathrm{true}$, of the estimated to the true mass, where the true mass includes the dark matter, stellar and gas particles within the projected 3D half-mass radius; λ is the ratio, $\Gamma_\mathrm{est}/\Gamma_\mathrm{true}$, of the estimated to the true slope of the cumulative logarithmic mass profile, where Γ_est is the slope measured between the measured values of R_e and Γ_true is the slope between the projected true 3D half-mass radii of the two subpopulations.

Apart from the metal-rich subpopulation of Galaxy 4, which is close to spherical, all

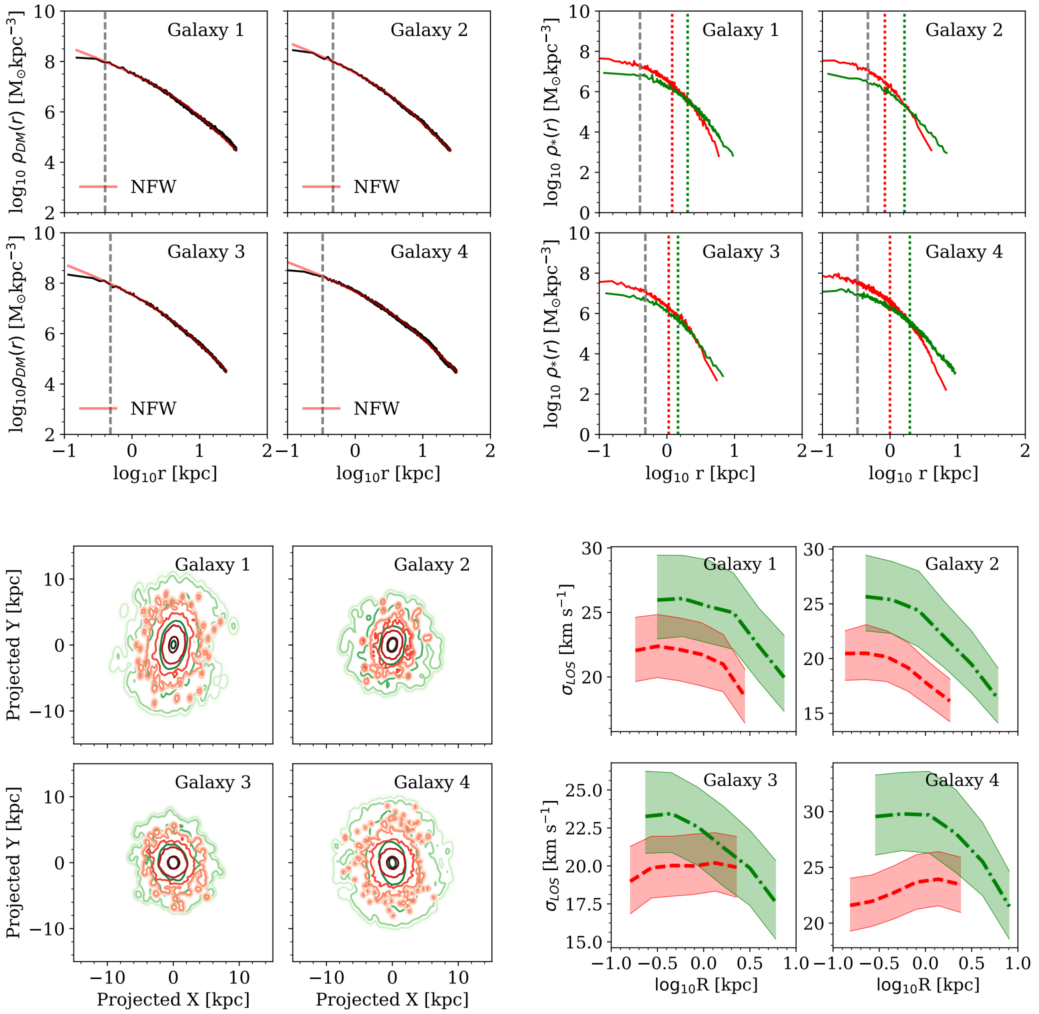

Figure 3.5: *Upper left:* dark matter profiles for the four illustrative examples discussed in this section. As for all galaxies in our sample, the inner density slope has a cusp; the best fitting NFW profile is shown in red. The grey dashed line marks the convergence radius defined by Power et al. (2003). *Upper right:* stellar density profiles for the metal-rich (red) and metal-poor subpopulations (green) for the four examples. The grey dashed line marks the convergence radius and the red and green dotted lines show the 3D half-mass radii of the metal-rich and metal-poor subpopulations respectively. The metal-poor component is more extended, with the metal-rich population concentrated near the centre. *Lower left:* probability density contours of the spatial distribution of stars in the four galaxies. The red and green contours represent the metal-rich and metal-poor subpopulations, respectively, with the highest contour enclosing $p(x, y) = 0.1$ and lower ones decreasing in probability density by factors of 10. The galaxies are viewed along the direction of the intermediate axis of the metal-poor subpopulation. *Lower right:* velocity dispersion profiles for the four examples, projected over 100 lines of sight, as a function of projected distance from the centre. The red dashed line and the green dash-dotted line show the medians of the metal-rich and the metal-poor subpopulations, respectively. The bands show the 1σ scatter. The metal-rich subpopulation is kinematically colder than the metal-poor subpopulation at small radii.

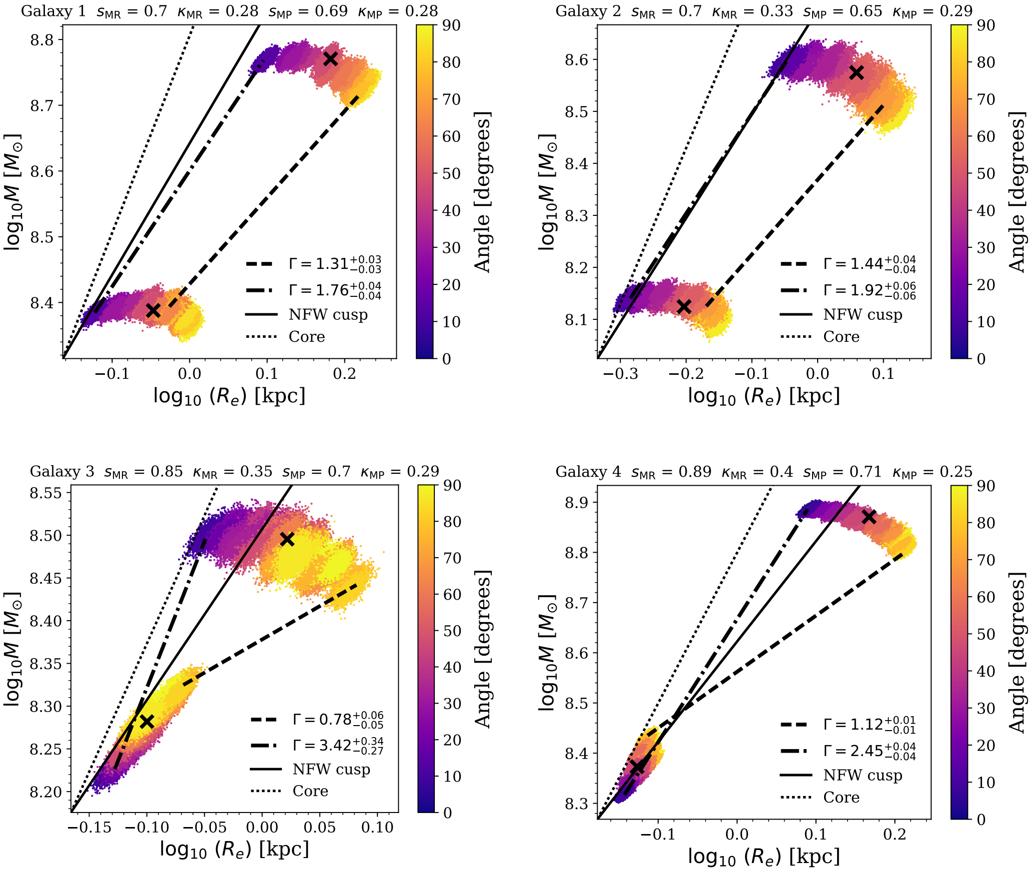

Figure 3.6: Logarithmic mass slopes for our four illustrative examples. The dots show measured projected half-mass radii and associated contained mass inferred from the Walker et al. (2009b) estimator of Equation 3.2 for each of the 1000 bootstrap resamplings of each galaxy; each galaxy is seen from 100 different directions. The points are coloured according to the viewing angle measured from the major axis of the metal-poor subpopulation. The black dashed and dash-dotted lines show the minimum and maximum slopes obtained from all 100 lines of sight, respectively. For reference, the black solid and dotted lines show the slopes of an NFW cusp and a core. The black crosses denote the true projected 3D half-mass radii and the masses within them, taken directly from the simulation. The labels above each panel give the sphericity and value of $\kappa_{\rm rot}$ for each subpopulation. A large scatter in projected half-mass radius can be seen in subpopulations that are strongly aspherical ($s < 1$).

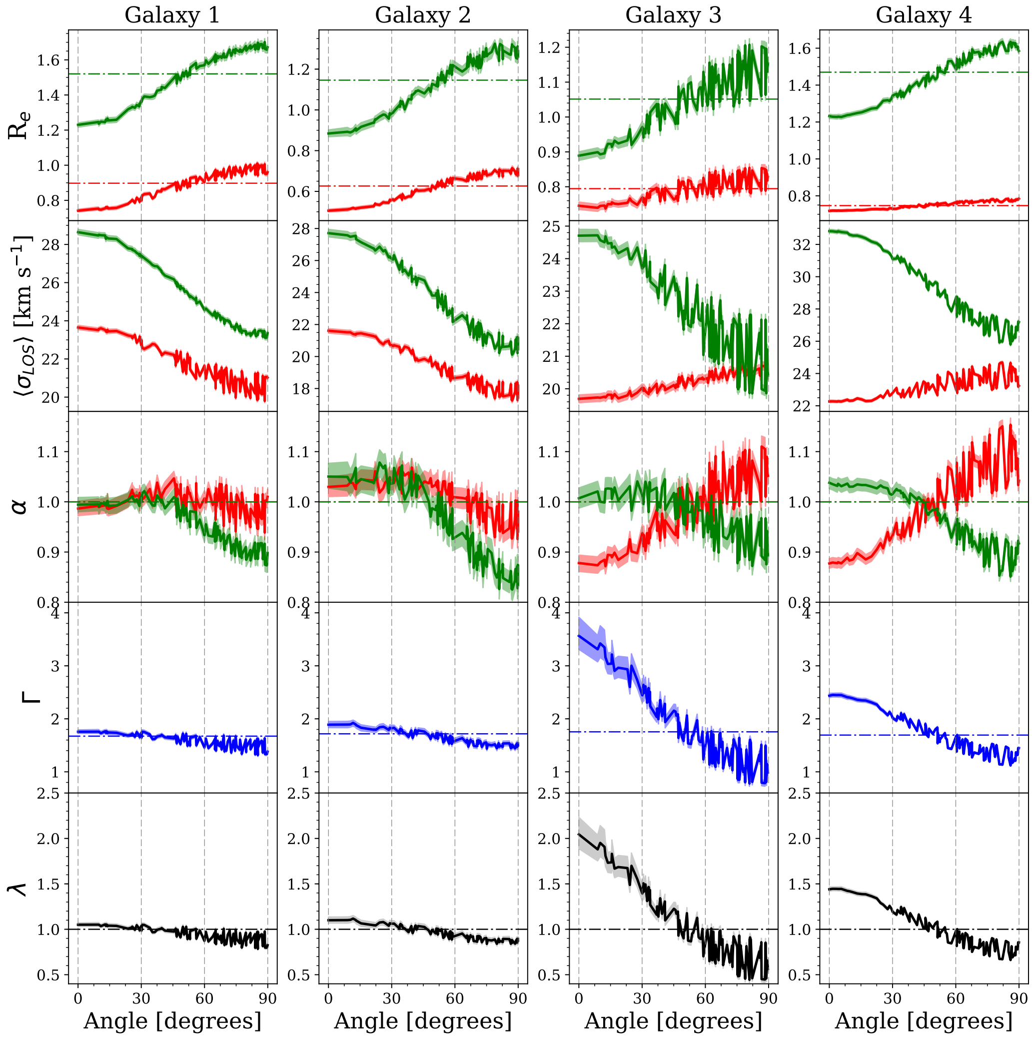

Figure 3.7: The variation with viewing angle of some of the key properties of our four illustrative example galaxies. *Angle* is the viewing angle measured from the major axis of the metal-poor subpopulation. Red and green colours represent the metal-rich and metal-poor subpopulations respectively. *First row*: the projected half-mass radius measured for each subpopulation. *Second row:* the estimated mass-weighted average line-of-sight velocity dispersion. For Galaxies 3 and 4 the velocity dispersion of the metal-rich subpopulation is anticorrelated with that of the metal-poor subpopulation. *Third row:* the accuracy of the mass estimator for each subpopulation, $\alpha = M_{\mathrm{est}}/M_{\mathrm{true}}$. *Fourth row:* the measured slope of the cumulative logarithmic mass distribution, Γ. *Fifth row:* the accuracy of the measured mass slope, $\lambda = \Gamma_{\mathrm{est}}/\Gamma_{\mathrm{true}}$.

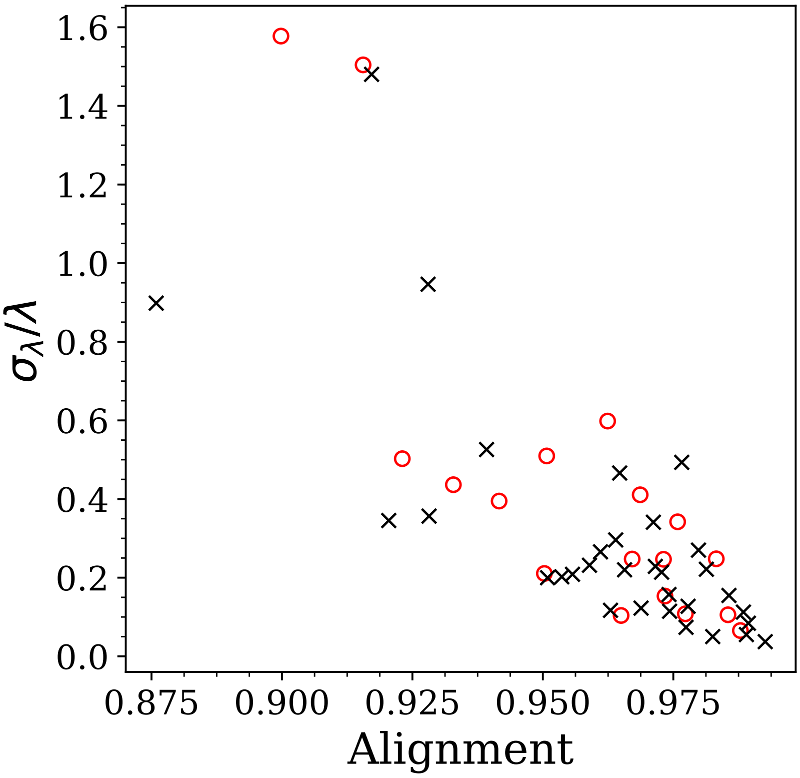

Figure 3.8: Relative upper error (the difference between the 84th and the 50th percentile divided by the median value) on the mass slope accuracy, λ, as a function of the alignment of the metal-rich and the metal-poor subpopulations, as defined in Section 3.3.1. Satellites and field galaxies are shown with red circles and black crosses respectively. Measurements in galaxies with more misaligned subpopulations are more likely to return larger values of Γ.

other subpopulations in the four examples of Fig. 3.6 are quite elongated. For the nearly spherical subpopulation, the estimated projected half-mass radius is, not surprisingly, almost independent of viewing angle. The values of the estimated mass show a mild systematic dependence on viewing angle which reflects the weak dependence of the velocity dispersion on the line of sight seen in Fig. 3.7.

The situation is quite different for the elongated subpopulations. Let us consider, for example, the metal-poor subpopulation of Galaxy 4. Its sphericity is $s_{\rm MP} = 0.71$, quite typical for our sample (see Fig. 3.4). Now the measured values of the projected half-mass radius vary greatly with viewing angle, from 1.2 kpc when the subpopulation is viewed along its major axis to 1.6 kpc when it is viewed along the perpendicular direction. Since

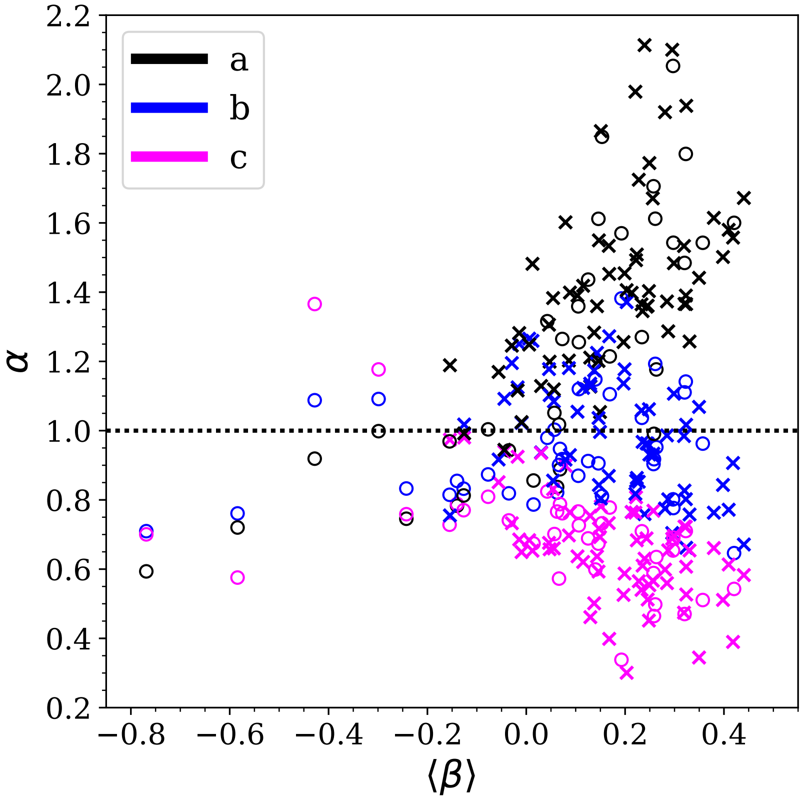

Figure 3.9: The accuracy of the mass estimator, $\alpha = M_{\rm est}/M_{\rm true}$, for the metal-rich and metal-poor subpopulations of all galaxies in our sample, as a function of the average velocity anisotropy, $\langle\beta\rangle$. The galaxies are viewed along their major (black), intermediate (blue) and minor (magenta) axes of *each* subpopulation. The black dotted line shows accurate mass estimates ($\alpha = 1$). Satellite galaxies are shown as circles and field galaxies as crosses. Along the major axis, the masses tend to be overestimated for subpopulations with radial anisotropy. For nearly isotropic subpopulations the accuracy is similar for all three directions.

the velocity anisotropy is radially biased (see Fig. 3.4), the measured velocity dispersion varies with viewing angle, from 33 km s^{-1} when viewed along the major axis to 27 km s^{-1} when viewed along the perpendicular direction. This decrease in velocity dispersion largely balances the increase in the projected half-mass radius with the result that the estimated mass of the metal-poor population varies little with viewing angle, by only ~ 0.1 dex. Thus, a very similar mass is associated with a relatively large range of projected half-mass radii. The biases in the measured mass are anticorrelated as the viewing angle varies, as shown in the third row of Fig. 3.7.

As Figs 3.6 and 3.7 show, the result is that the inferred slope of the cumulative logarithmic

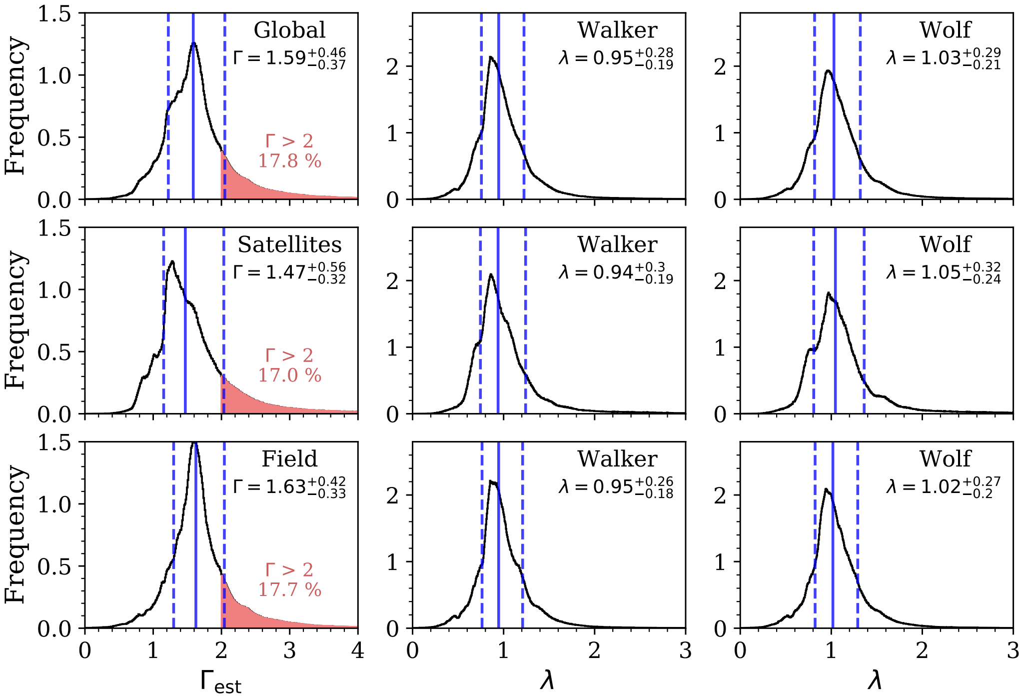

Figure 3.10: *Top panel:* overall distributions for the 50 objects in our sample of the measured slope, $\Gamma_{\rm est}$ (left), and slope accuracy, $\lambda = \Gamma_{\rm est}/\Gamma_{\rm true}$, for (middle) the Walker et al. (2009b) estimator and (right) the Wolf et al. (2010) estimator. Blue solid lines show the median values and the blue dashed lines show 16th and 84th percentiles. The slopes tend to be underestimated by 5 per cent on average using the Walker et al. (2009b) estimator and overestimated by 3 per cent on average using the Wolf et al. (2010) estimator; the distribution of λ is not symmetrical. $\Gamma \geq 2$ is measured in 17.8 per cent of cases and $\Gamma \geq 3$ in ~ 3.5 per cent of cases. *Middle panel:* same as above, but only for the 18 satellite galaxies in our sample. *Bottom panel:* as above, but showing the distributions of Γ and λ only for the 32 field galaxies in our sample. The estimators perform in a similar way for both satellites and field galaxies.

mass profile for Galaxy 4 can take on a wide range of values, from $\Gamma = 2.45$ when the galaxy is viewed along the major axis of the metal-poor population to $\Gamma = 1.12$ when it is viewed along the perpendicular direction. Thus, for viewing angles between about 0 and 50°, the mass distribution in this galaxy would, incorrectly, be measured to have a core.

Galaxies 1 and 2 are also quite elongated. However, in these two cases, both subpopulations are aspherical and their major axes are roughly aligned. Now the behaviour we have just seen for the metal-poor subpopulation of Galaxy 4 is reproduced *for both subpopulations*. The result is that both the projected half-mass radius and the mass contained within it for both subpopulations are incorrectly estimated by roughly the same factors and these biases vary similarly with viewing angle (third row of Fig. 3.7). Thus, although the masses and radii of both subpopulations are incorrectly estimated, the slopes come out roughly right: these two galaxies are correctly inferred to have cusps.

Galaxy 3 is an intermediate case. Its metal-poor subpopulation has similar sphericity to the metal-poor subpopulation of Galaxy 4 so the measured projected half-mass radius varies by a similar factor. While the inferred mass has greater scatter at a given viewing angle, the overall variation is still only slightly larger than 0.1 dex. The half-mass radius of the metal-rich subpopulation of Galaxy 3 shows some dependence on viewing angle (see Fig. 3.7). In this case, the systematic variation of the inferred mass is larger and, as seen in Fig. 3.7, it increases with viewing angle. This is enough to result in a wide range of estimated slopes. Similarly to Galaxy 4, this galaxy would be measured to have a core for viewing angles between about 20 and 50° and for even smaller viewing angles it would be measured to have a 'hole' in the central region ($\Gamma > 3$).

Although the systematic errors in the estimates of the slope of the cumulative logarithmic mass distribution using a procedure analogous to that of Walker and Peñarrubia (2011) result from a complex interplay between projection and kinematic effects, it is clear that a major factor behind them is the significant elongation of the stellar subpopulations, and particularly the misalignment between the major axes of the metal-rich and metal-poor subpopulations seen in a number of cases, including Galaxy 4. This lack of similarity arises naturally in our simulations and is linked to the different formation paths of the two subpopulations, as we have discussed in the previous chapter.

In order to quantify the effect of both the misalignment of the principal axes and the differences in sphericity of the two subpopulations on the scatter in the estimated logarithmic mass slopes, we define the following alignment statistic. We model the two subpopulations as concentric ellipsoids of unit volume, with axis ratios equal to those measured for each subpopulation and an offset angle equal the angle between the major axes of the two subpopulations. We then compute the fraction of volume within the intersection of the two ellipsoids. Subpopulations with similar axis ratios and spatial orientation would, therefore, have an alignment close to 1. In Fig. 3.8 we show the relative upper error (the difference between the 84th and 50th percentiles divided by the median value) on the slope accuracy, λ, as a function of the value of the alignment statistic. It is clear that measurements for galaxies with more misaligned subpopulations tend to return higher values of Γ, corresponding to shallower inner density slopes.

The non-trivial radial variation of the velocity anisotropy, β, which is generally different for the two metallicity subpopulations (see Fig. 3.4), also plays a role. This can be seen in Fig. 3.9, where we plot α, the error in the estimate of the mass for each of the two subpopulations in our sample, as a function of the average anisotropy parameter $\langle\beta\rangle$, when each subpopulation is viewed from directions aligned with the three principal axes. For directions along the minor and intermediate axes the values of α scatter about $\alpha = 1$, although there is a bias towards $\alpha < 1$, that is for an underestimate of the mass when the subpopulation is viewed along its minor axis. However, when the subpopulation is viewed along its major axis and the velocity anisotropy has a radial bias ($\beta > 0$) , its mass tends to be *overestimated* (in agreement with the conclusions of Kowalczyk et al. 2013) and the size of this bias increases systematically with increasing anisotropy. Along this particular viewing angle, the velocity dispersion is generally largest. When the velocity distribution is isotropic or tangentially biased, however, the mass is correctly estimated. (This is the reason why the estimate of the mass of the metal-rich subpopulation of Galaxy 3, which has an isotropic velocity distribution, is unbiased.)

3.3.2 Accuracy of the inferred mass slope for the sample as a whole

In this subsection, we present statistical results for our sample of 50 galaxies. This sample was selected according to the specific criteria described in Section 3.2.1, essentially requiring that there be two well-separated metallicity subpopulations, as judged by the statistic introduced in that section. These criteria need not match in detail those used for real objects. At present, there are only a handful of two-metallicity subpopulation galaxies known and those populations have been identified somewhat serendipitously. Nevertheless, our statistical results should be indicative of the frequency with which we might expect the slope of the dark matter density profile to be incorrectly estimated.

The top panel of Fig. 3.10 shows the distributions of $\Gamma_{\rm est}$ and $\lambda = \Gamma_{\rm est}/\Gamma_{\rm true}$ for the 1000 bootstrap resamplings of each galaxy in our sample, each viewed from 100 different random directions. (Recall that an NFW profile has $\Gamma = 2$ as $r \longrightarrow 0$ and a profile with a constant-density core has $\Gamma = 3$.) The distribution of $\Gamma_{\rm est}$ is asymmetric with mean value $\Gamma = 1.59^{+0.46}_{-0.37}$ and $\lambda = 0.95^{+0.28}_{-0.19}$ for the Walker et al. (2009b) estimator, implying that Γ is underestimated on average by ~ 5 per cent; the true value (corresponding to $\lambda = 1$) lies within 1σ of the mean. Slopes tend to be overestimated by ~ 3 per cent on average using the Wolf et al. (2010) estimator, with $\lambda = 1.03^{+0.29}_{-0.21}$.

Flatter slopes than NFW, $\Gamma > 2$ are measured in ~ 17.8 per cent of cases and $\Gamma > 3$ (corresponding to a ‘hole’ in the centre) in ~ 3.5 per cent of cases. In the middle and bottom panels we show equivalent distributions for satellite and field galaxies in our sample. Whilst the satellites generally tend to exhibit cuspier inner slopes ($\Gamma_{\rm est} = 1.47^{+0.56}_{-0.32}$ compared to $\Gamma_{\rm est} = 1.63^{+0.42}_{-0.33}$ for field dwarfs), the distribution of the accuracy of the inferred slopes, λ, is similar to that of the field galaxies. The greater scatter towards higher values of Γ in satellites can be explained by the fact that a greater fraction of satellites than field galaxies in our sample exhibit strong misalignment, as shown in Fig. 3.8. We have additionally verified that if we identify the true slope with the slope of the line joining the logarithm of true masses within R_e of each subpopulation, the bias and scatter in λ remain unaffected.

Walker and Peñarrubia (2011), who used the Walker et al. (2009b) estimator, found $\Gamma = 2.95^{+0.51}_{-0.39}$ for Sculptor and $\Gamma = 2.61^{+0.43}_{-0.37}$ for Fornax and concluded that these values exclude the NFW profile with significance greater than 99 and 96 per cent respectively. However, according to the distribution of $\Gamma_{\rm est}$ in Fig. 3.10 for the Walker et al. (2009b) and Wolf et al. (2010) estimators derived from our simulations, these values of Γ are only inconsistent with the NFW profile at 93.6 and 88.9 significance for Sculptor and Fornax respectively (where we have taken the 1σ lower limit of the original estimates).

3.4 Discussion and Conclusions

The question of whether or not the dark matter haloes of galaxies have central, constant-density cores is of great interest in cosmology. It is now well established that, in the absence of baryon effects, haloes of all masses develop NFW profiles (Navarro et al., 1996a, 1997) which have a central cusp. An incontrovertible measurement of a core would therefore have important implications: it would either signal the impact of exotic baryonic effects (Navarro et al., 1996a; Pontzen and Governato, 2012) or of exotic types of particles such as self-interacting dark matter (Spergel and Steinhardt, 2000). Unfortunately measuring dark matter profiles in the innermost regions of haloes, encompassing only at most a few per cent of the halo mass, is difficult.

In this work we have tested the Walker and Peñarrubia (2011) procedure for inferring the slope of the inner dark matter halo profile in galaxies with two metallicity subpopulations using galaxies from the APOSTLE cosmological simulations. These follow not only the evolution of dark matter, but also the evolution of gas, and incorporate subgrid prescriptions to model the processes thought to be at play in galaxy formation. The initial conditions correspond to a cold dark matter universe but are conditioned to form an analogue of the Local Group at the final time. Thus, this is the first test of the Walker and Peñarrubia (2011) procedure in fully realistic simulations which produce dwarf galaxies *ab initio*. These are not guaranteed to satisfy the key assumptions underlying the Wolf et al. (2010) and Walker et al. (2009b) mass estimators: sphericity and dynamical equilibrium, and indeed, many of our simulated galaxies violate them to varying degrees.

Gratifyingly, our simulations produce dwarf galaxies with two identifiable metallicity subpopulations reminiscent of Sculptor and Fornax. Out of 286 model galaxies resolved with more than 1000 stellar particles we identify 50 dwarfs with dual metallicity subpopulations, according to the criteria discussed in Section 3.2.1. Their kinematical properties are summarized in Fig. 3.4. The subpopulations tend to be significantly aspherical and often develop different asphericities: ~ 30 per cent of galaxies in our sample have metal-rich and metal-poor subpopulations differing in sphericity by over 10 per cent and, in many cases, the orientation of their major axes differs as well. The metal-rich subpopulations tend to show more rotation than the metal-poor ones and the velocity anisotropy of the subpopulations can also differ substantially. These differences occur both in satellites and in field dwarfs. The lack of similarity arises naturally in our simulations and is linked to the different formation paths of the two subpopulations (as discussed in the previous chapter).

Our main result is that the method introduced by Battaglia et al. (2008) and extended by Walker and Peñarrubia (2011), based on comparing the masses interior to the half-mass radii of the metal-rich and metal-poor subpopulations, can often lead to an incorrect inference of the slope of the inner profile of the galaxies' dark matter haloes. All the haloes in our simulations have cuspy NFW profiles, yet 17.8 per cent of the galaxies in our sample would be inferred to have flatter, core-like profiles. Multiple factors play a role in these failures but the main culprit is misalignment of the two elongated metallicity subpopulations (which generally have radially varying velocity anisotropy). This results in a wide range of inferred slopes for the mass distribution depending on the viewing angle. Four specific examples illustrating cases when the slope is correctly or incorrectly inferred have been shown.

The study of Walker and Peñarrubia (2011) is sometimes regarded as one of the more convincing arguments for the presence of cores in the dark matter haloes of dwarf galaxies (Amorisco and Evans, 2012b). However, their proposed method of measuring cumulative logarithmic mass profile slopes relies heavily on the assumption that the properties of the two metallicity subpopulations are correlated, such that any bias in the application of the mass estimator would cancel when obtaining the slope. This assumption fails in a number of our simulated galaxies where not only the elongation and orientation, but also the orbital anisotropy differs for the two subpopulations. Of course, it remains to be seen whether the properties of the two metallicity subpopulations in Sculptor and Fornax are correlated or not, but this is not currently feasible. The availability of proper motion data for individual stars within these galaxies would allow us to somewhat take away the dependence of the accuracy of the mass estimator on the angle of view, although, for an instrument like *Gaia*, the measurement uncertainties for a galaxy as distant as Sculptor is expected to be comparable to the velocities themselves (Gaia Collaboration et al., 2016; Massari et al., 2018). Given the sensitivity of the inferred slope to the viewing angle that we have demonstrated in this work, we concur with Kowalczyk et al. (2013) that a large statistical sample of *randomly oriented* galaxies is highly desirable. But for any particular observation, knowledge of the sphericity and velocity anisotropy of both subpopulations and their orientation with respect to one another and to the observer is required before any definitive conclusion can be reached regarding the slope of the galaxy's inner dark matter halo.

CHAPTER 4

Solving the core-cusp problem with higher-order Jeans analysis

4.1 Introduction

A number of cosmological and idealized simulations in ΛCDM predict formation of dark matter cores in dwarfs that have undergone extended periods of star formation. Outflows associated with supernova feedback have been shown to cause fluctuations in the gravitational potential, which can alter the inner structure of haloes. This may occur in a single violent burst (Navarro et al., 1996a), through repeated dark matter ‘heating’ over time (Read and Gilmore, 2005; Pontzen and Governato, 2012; Oñorbe et al., 2015; Read et al., 2016) or both (Benítez-Llambay et al., 2019). Cores in these models typically form on the scale of the half-light radius of dwarf galaxies.

The formation of cores in real Local Group dwarfs that have undergone extended periods of star formation is a testable hypothesis. This idea was explored in Read et al. (2019). These authors find that dwarf spheroidals which have continued to form stars until recent times, like Fornax and the Local Group dIrrs, have lower densities at 150 pc, ρ_{150}, than those predicted for isolated dwarfs using the halo mass-concentration relation in ΛCDM from Dutton and Macciò (2014). These lower densities could be explained by core formation through dark matter ‘heating’. Dwarfs that have ceased star formation a long time ago have higher values of ρ_{150}, consistent with a cusp.

The dark matter density distribution in dwarf galaxies can be constrained through Jeans analysis applied to line-of-sight stellar velocities and projected positions. This relies on the spherical Jeans equation:

$$\frac{1}{\nu}\frac{d}{dr}(\nu\sigma_r^2) + 2\frac{\beta\sigma_r^2}{r} = -\frac{GM(<r)}{r^2}, \tag{4.1}$$

where ν is the tracer number density distribution, σ_r is their radial velocity dispersion, β their velocity anisotropy, $M(<r)$ is the enclosed mass and G is Newton's gravitational constant. The velocity anisotropy, β, is defined as $\beta = 1 - \frac{\sigma_t^2}{2\sigma_r^2}$, where σ_t is the tangential velocity dispersion. The product $\nu(r)\sigma_r^2(r)$ is typically obtained through deprojection of $\Sigma(R)\sigma_P^2(R)$, where $\sigma_P(R)$ is the line-of-sight velocity dispersion and $\Sigma(R)$ is the projected tracer number density at a distance, R, both of which are observable quantities. If models are assumed for $\beta(r)$ and $M(<r)$, the equation can be solved for $\sigma(R)$ via sampling methods such as Markov chain Monte Carlo (MCMC). This analysis assumes a non-rotating spherical system in a steady pseudo-equilibrium state. These assumptions are known to be violated by Local Group dwarfs, which exhibit ellipticity (McConnachie, 2012), signs of rotation (Battaglia et al., 2008; del Pino et al., 2017a), and are susceptible to tidal effects from their hosts (Read et al., 2006; Peñarrubia et al., 2009; Ural et al., 2015).

Typically, only the line-of-sight motions of the stellar tracers are known. This means that β is poorly constrained, such that Jeans analysis suffers from the M–β degeneracy. This degeneracy results in a wide range of models that satisfy a set of observational constraints, such that cored and cuspy dark matter profiles both provide acceptable fits to line-of-sight data (Strigari et al., 2010).

The breaking of $M - \beta$ has been widely explored in the literature. Several works have focused on the use of multiple tracer populations in dwarf spheroidals and chemo-dynamical models (Walker and Peñarrubia, 2011; Amorisco and Evans, 2012b; Agnello and Evans, 2012; Zhu et al., 2016), as well as proper motions (Strigari et al., 2007, 2014). A number of works have used Schwarzschild orbit superposition methods (Schwarzschild, 1979; Jardel and Gebhardt, 2012; Breddels and Helmi, 2013; Kowalczyk et al., 2017, 2018, 2019), which are able to take into account the asphericity of stellar systems and have a benefit of making no assumptions about the velocity anisotropy. These methods, however, typically require significant computing time.

Other works, based on the Jeans equation, have focused on exploiting the higher-order velocity moments. Specifically, it has been shown that line-of-sight velocity distributions are non-Gaussian in the absence of isotropy (Merritt, 1987). This warrants the use of the 4th moment of the velocity distribution to place a constraint on the anisotropy parameter (Mamon et al., 2013). The use of the fourth velocity moments has been explored for the case of constant anisotropy by Łokas (2002); Łokas and Mamon (2003); Łokas et al. (2005); Łokas (2009) and was generalized for radially varying anisotropies by Richardson and Fairbairn (2013a). More recently, Diakogiannis et al. (2017) have presented a non-parametric method of reconstruction of the line-of-sight velocity dispersion profiles. An extension of the method employs a machine learning approach for data reconstruction that proves useful in the absence of large samples of kinematic data (Diakogiannis et al., 2019).

Another method for breaking this degeneracy is through the fourth order projected virial theorem, giving rise to two equalities (Merrifield and Kent, 1990):

$$\mathrm{VSP1} = \frac{2}{5}\int_0^\infty GM\nu(5-2\beta)\sigma_r^2 r\,dr = \int_0^\infty \Sigma\langle\sigma_P^4\rangle R\,dR \tag{4.2}$$

and

$$\mathrm{VSP2} = \frac{4}{35}\int_0^\infty GM\nu(7-6\beta)\sigma_r^2 r^3\,dr = \int_0^\infty \Sigma\langle\sigma_P^4\rangle R^3\,dR, \tag{4.3}$$

where VSP1 and VSP2 are referred to as the virial shape parameters (i.e. VSPs). Here $\langle\sigma_P^4\rangle$ is the fourth moment of the line-of-sight velocities. The right-hand sides of Equation 4.2 and Equation 4.3 contain quantities that can be directly inferred from data and the left-hand sides contain the same parameters as Equation 4.1. It is thus possible to place two additional constraints on the velocity anisotropy β (see e.g. Richardson and Fairbairn 2014, where VSPs were used to show that a dark matter cusp is favoured in the Sculptor dwarf galaxy). In practice, however, the finite quality of data may result in only a partial breaking of the $M-\beta$ degeneracy.

Read and Steger (2017) introduced the non-parametric Jeans method, GravSphere (used in Read et al. 2019), which employs the additional constraints from the VSPs in their MCMC analysis. GravSphere operates under the standard assumptions of the spherical Jeans equation (spherical symmetry, equilibrium and no rotation). The method had been shown to recover successfully the dark matter density distributions in mock observations of idealized spherical, triaxial and tidally stripped simulated dwarfs from the GaiaChallenge set*. The cases for which the method works less well, such as aspherical systems, are evident through poor quality fits to the line-of-sight velocity dispersion. The method has been shown to recover accurately the densities at 150 pc from the centre – a key region where core formation is expected to reduce dark matter densities, compared to ΛCDM predictions.

In this work, we test a new open-source Python implementation of the GravSphere method, pyGravSphere, on a sample of simulated dwarf galaxies from a cosmological hydrodynamics simulation of Local Group-like environments†. The aim of our work is to establish whether Jeans analysis, under the assumption of spherical symmetry, is a suitable method for constraining the mass profiles of dark matter haloes in a fully cosmological setting and how much information is typically gained through the inclusion of VSPs. We explore the biases associated with mass and dark matter density profile recovery for individual dwarfs as well as the sample as a whole. We examine in detail the cases where GravSphere fails and identify the reasons for this as well as potential warning signs.

In Section 4.2, we describe the setup of GravSphere. Our analysis of GravSphere's performance on each galaxy and the comparison to more conventional Jeans methods can be found in Section 4.3. We further discuss the various sources of bias in the performance of this method and suggest a χ^2 statistic to weed out particularly biased models. We summarise our findings and conclude in Section 4.4.

---

[*] `http://astrowiki.ph.surrey.ac.uk/dokuwiki/`

[†] We ran also these same tests in the original GravSphere code, yielding indistinguishable results from those presented here.

4.2 Simulations

4.2.1 Simulations in CDM and SIDM

In this work, we select analogues of classical dwarf spheroidals from the APOSTLE suite of cosmological simulations, as described in detail in Section 2.2.1. The original APOSTLE suite consists of five high-resolution cosmological volumes, with dark matter mass resolution of $\mathrm{m_{DM}} = 2.5 - 5 \times 10^4 \mathrm{M}_\odot$ and spatial resolution $\epsilon = 134$ pc. An extra cosmological volume was also run assuming a SIDM interaction cross-section of $\sigma/m = 10\ \mathrm{cm^2 g^{-1}}$ (Santos-Santos et al., 2020; Lovell et al., 2020). We note that this is an extreme value of the cross-section, which was chosen to explore the formation of the largest cores in SIDM. The SIDM implementation within EAGLE was introduced in Robertson et al. (2018), based on the SIDM simulation method described in Robertson et al. (2017).

In order to increase our sample of dwarfs with a dark matter core, we additionally used a SIDM version of the cosmological volume* presented in Benítez-Llambay et al. (2019), with an interaction cross-section of $\sigma/m = 10\ \mathrm{cm^2 g^{-1}}$ and galaxy formation prescriptions following Schaye et al. (2015) and Crain et al. (2015). This simulation was run with the same cosmological parameters as the APOSTLE simulations but does not feature a Local Group-like setting. The dark matter particle mass resolution is $\mathrm{m_{DM}} = 4 \times 10^5 \mathrm{M}_\odot$ and the softening is $\epsilon = 234$ pc.

APOSTLE resolves Sculptor-mass dwarf galaxies with $\sim 10^2$-10^3 stellar particles and Fornax-mass dwarf galaxies with $\sim 10^3$-10^4 particles. The SIDM run of the volume presented in Benítez-Llambay et al. (2019) has an initial gas particle mass $\mathrm{m_{gas}} = 6.6 \times 10^4 \mathrm{M}_\odot$. Fornax-mass dwarfs are resolved with $\sim 10^2 - 10^3$ stellar particles, sufficient for the purposes of this work.

---

*The SIDM version of this volume has not yet been published. The simulation data were obtained through private communications.

4.2.2 Numerical considerations

In order to establish whether GravSphere reproduces the mass profiles of the simulated dwarfs, we must first define what the 'true' mass profile is within the simulations.

The mass profiles of dark matter haloes identified in pure N-body simulations are affected by collisional relaxation. The enclosed mass profiles of haloes are suppressed (relative to a higher resolution simulation) below a radius where the 2-body relaxation time, $\mathrm{t_{relax}}$, is comparable to the age of the Universe, t_0 (see e.g. Power et al. 2003; Ludlow et al. 2019a). For the typical number of dark matter particles in systems that are considered in this work, the Power et al. (2003) radius, where $\mathrm{t_{relax}} \sim 0.6t_0$, corresponds to ~60 per cent of the half-light radius (about 0.7 kpc for high-resolution APOSTLE CDM and SIDM dwarfs and $\sim$ 2 kpc for the lower-resolution SIDM volume from Benítez-Llambay et al. 2019). Moreover, the APOSTLE simulations model dark matter and stars using particles of unequal mass, making them subject to energy equipartition, which artificially inflates galaxy sizes (Ludlow et al., 2019b, 2020). These effects are most problematic for systems with stellar half-mass radii smaller than $\sim$ 0.055 of the mean interparticle separation (dark matter, stars and gas), corresponding to $\sim$ 0.5 kpc for the APOSTLE simulations and $\sim$ 1.2 kpc for the SIDM volume of Benítez-Llambay et al. (2019). We note, however, that the relaxation times at these radii are still considerably longer than the dynamical times of the stars. Therefore, our simulated dwarfs may be considered to be in a steady state locally. The ability of GravSphere to recover masses in the innermost regions is of interest in this work; therefore we will present results below the convergence radius derived by Power et al. (2003) and Ludlow et al. (2019a), although we will interpret these with caution*.

The use of the gravitational softening in N-body simulations sets a limit on the central density, such that the innermost regions of simulated haloes exhibit a small artificial core on the scale of the gravitational softening. In comparing GravSphere to N-body simulations, we thus restrict ourselves to radii greater than 2.8ϵ, where ϵ is the Plummer-equivalent gravitational softening. For the APOSTLE high-resolution simulations $\epsilon = 134$ pc and

---

*The Power et al. (2003) criterion was derived for dark matter-only simulations and it is unclear how applicable this criterion is in the presence of a baryonic component.

ϵ = 234 pc for the SIDM version of the volume introduced in Benítez-Llambay et al. (2019)[*]. At the radius of 2.8ϵ the forces become exactly Newtonian.

4.2.3 Sample of dwarfs

For our sample of galaxies, we have selected simulated dwarfs which have comparable properties to classical Milky Way satellites and at least 400 bound stellar particles. As the GRAVSPHERE method relies on the standard assumptions of the spherical Jeans equation (namely, spherical symmetry, lack of rotation and equilibrium), we further restrict our sample of galaxies to those with no bound gas and those that do not exhibit significant signs of rotation. We do, however, include aspherical dwarfs in our sample. These conditions are satisfied by classical Milky Way dwarfs, for which there are no HI detections, only weak rotation is observed and asphericity is often present (Battaglia et al., 2008; McConnachie, 2012). We quantify rotation by the fraction of stellar particles which are rotating in the same direction as the total stellar angular momentum vector, $f_{\rm corot}$. We select galaxies with $f_{\rm corot} < 0.6$. We restrict our sample to satellites only, defined as the objects within 300 kpc of the Milky Way and Andromeda analogues. Note that, in order to obtain a statistically significant sample of dwarfs in both CDM and SIDM dark matter models, we did not include restrictions on the orbits or star formation histories in the selection of our sample of simulated dwarfs.

Our selection criteria have significantly cut down the available sample of high-resolution SIDM dwarfs (which have large dark matter cores), prompting inclusion of simulated dwarfs from the lower-resolution SIDM version of the volume presented in Benítez-Llambay et al. (2019). The relative lack of suitable dwarfs in SIDM is intriguing, however, the peculiarities of galaxy formation and evolution in alternative dark matter models are beyond the focus of this work (see Lovell et al. 2020 for details of star formation in the APOSTLE SIDM volume).

---

[*] Although 2.8ϵ for this volume is near 0.5 kpc, the core sizes are typically much larger than that, such that we are still able to probe the interesting regions in these dwarfs.

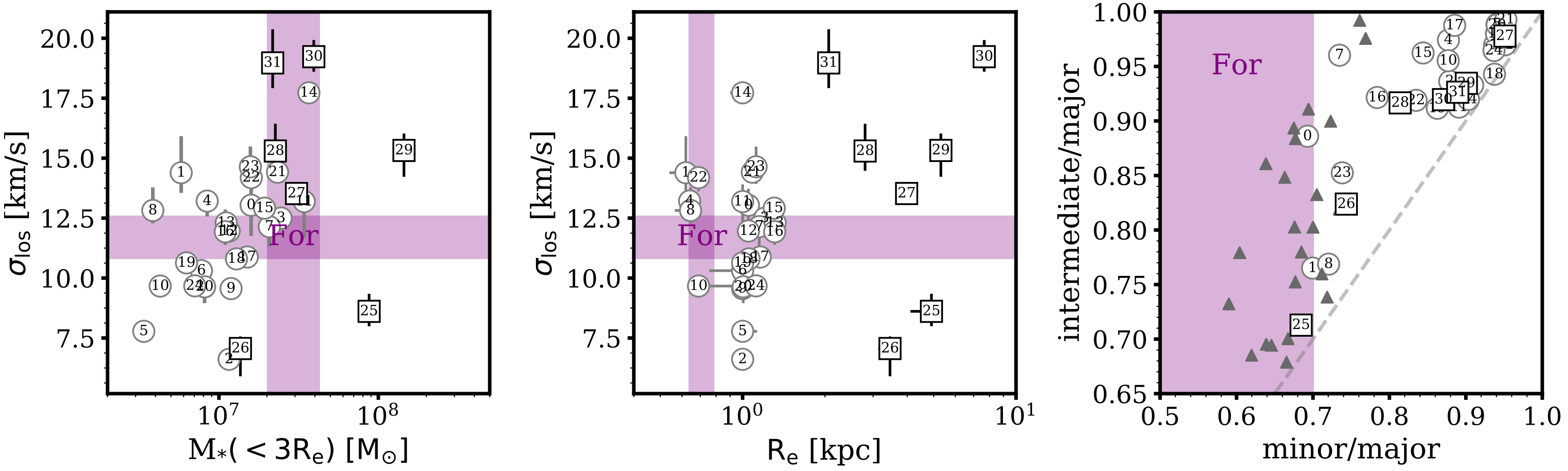

Figure 4.1: The sample of classical dwarf analogues. CDM dwarfs are shown with grey circles and SIDM dwarfs are shown with black squares. *Left:* line-of-sight velocity dispersion as a function of stellar mass within three times the projected half-light radius. The purple bands show the measurements for Fornax from McConnachie (2012) and de Boer et al. (2012). *Middle:* line-of-sight velocity dispersion as a function of the projected half-light radius. *Right:* ratio of intermediate to major axes as a function of the ratio of minor to major axes for our sample of dwarfs. The limits on the sphericity of Fornax dwarf galaxy (minor-to-major axis ratio $\simeq 0.7$), which has a 2D ellipticity $e \simeq 0.3$, are shown with a purple shaded band. The grey triangles show a sample of 24 isolated APOSTLE dwarfs with axis ratios comparable to the upper limit set on Fornax. The dashed one-to-one line highlights prolate galaxy shapes.

The resulting sample consists of dwarfs with properties that are generally similar to Fornax. This includes 25 CDM dwarfs and 7 SIDM dwarfs (2 high-resolution and 5 lower-resolution). Structural and kinematic properties of the sample are plotted in Fig. 4.1. For each dwarf in Fig. 4.1, we show the distribution of projected half-light radii, R_e, from various line-of-sight projections, line-of-sight velocity dispersion, $\sigma_{\rm los}$, and stellar mass within $3R_e$, $M_*(< 3R_e)$. These properties are computed using 192 isotropically distributed lines of sight generated with the HEALPIX algorithm (Górski et al., 2005). HEALPIX provides a convenient way of generating an isotropically distributed set of lines of sight with a more uniform distribution than one generated randomly. To calculate R_e, to each projection we fit a 3-component 2D Plummer profile (more details may be found in Section 4.2.4.1) and compute the radius which contains half the projected stellar mass. The means and standard deviations of these values are shown with circles and their error bars, with errors primarily reflecting the asphericity of each system. Similarly, we compute the mass-weighted mean velocity dispersion along each projection, taking into account the error from sample size (standard error on the mean). The stellar masses within $3R_e$ are computed by summing the masses of stellar particles identified as bound by the SUBFIND algorithm (Springel et al., 2001; Dolag et al., 2009) and removing the contaminant stars that belong to the host galaxy*. The contaminant stars are also removed in the calculation of other galaxy properties and the Jeans analysis. Purple bands in Fig. 4.1 show corresponding properties of the Fornax dwarf galaxy. The velocity dispersion and the half-light radius of Fornax were taken from McConnachie (2012). Stellar masses for Fornax span the range of values from literature (McConnachie, 2012; de Boer et al., 2012).

The rightmost panel of Fig. 4.1 shows intermediate-to-major axis ratios as a function of minor-to-major axis ratios, computed for the stellar component. The axes have been derived from the eigenvalues of the reduced inertia tensor, computed for the stellar particles (see e.g. Bett et al. 2007). The purple dashed line is the upper limit set on the minor-to-major axis ratio of Fornax, determined by the measured projected ellipticity, $e = 1 - b/a \simeq 0.3$

---

*Due to the specifics of particle assignment to haloes in SUBFIND, some low-velocity host halo stars may end up attributed to a subhalo. We remove these stars by ensuring they were not 'bound' to any given subhalo in the previous simulation snapshot (Springel et al., 2001).

(Battaglia et al., 2006). Our sample, which has an average axis ratio of $c/a \sim 0.9$, is considerably more spherical than Fornax ($c/a \simeq 0.7$). This is a consequence of our selection criteria, specifically the lack of rotation and the lack of gas for the selected sample of dwarfs. These are more likely to be features of dwarf galaxies that have undergone tidal effects, which tends to reduce asphericity (Barber et al., 2015).

In order to further investigate the effects of asphericity, we included a sample of 24 isolated CDM dwarfs with $c/a \sim 0.7$ (grey triangles in Fig. 4.1). The sample has been chosen to contain galaxies where gas does not dominate by mass within the 3D half-mass radius of the stars. This is the reason for the lack of isolated dwarfs available for the SIDM sample. In fact, we did find 4 isolated SIDM dwarfs that match these criteria, but they turned out to be very oblate. We excluded these dwarfs from our analysis. Since the GravSphere method explicitly accounts for the mass contributed by stars, but not by gas, when comparing GravSphere's performance for these dwarfs with the 'true' values, we compare to the combined mass in gas and dark matter.

In order to generate the photometric and kinematic data required by GravSphere, we obtained the stellar positions and velocities for particles in each subhalo, which were classified as bound by subfind (Dolag et al., 2009). We removed all contaminant stars belonging to the host halo. Each stellar system was centred at the central peak of the density field, computed using the 'shrinking spheres' algorithm (Power et al., 2003). The positions and velocities were then projected along three different lines of sight – major, minor or intermediate axes of the subhalos. The stellar particles within $2R_{\mathrm{2D}}$, where R_{2D} is the projected radius that contains half the stellar particle mass, were randomly sampled, providing 400 - 2500 particles for the kinematic sample of each dwarf. The photometric sample included 400 - 2500 particles and was chosen to be the same or bigger in size than the kinematic sample. The velocities within the kinematic sample were perturbed with Gaussian noise with a standard deviation of 2 km s^{-1}, representing typical measurement errors. The mass within $3R_{\mathrm{2D}}$ has additionally been provided, $M(< 3R_{2D})$, such that GravSphere may include the stellar mass contribution to the gravitational potential in the Jeans modelling.

4.2.4 The pyGravSphere code

In this work, we present a Python implementation of the GravSphere method. pyGravSphere is open source software*. As in the work of Read and Steger (2017), pyGravSphere is based on the affine-invariant ensemble sampler emcee (Foreman-Mackey et al., 2013). emcee differs from the classic Metropolis-Hasting algorithm in that each individual Markov chain, or 'walker', communicates with the other 'walkers' at each step, thus allowing the chains to efficiently sample the posterior distribution. emcee has parallel functionality, which we exploit in this work. In the following, we outline the assumptions and parameters that enter into our emcee setup.

4.2.4.1 emcee parameters

As in Read and Steger (2017), to parametrize the dark matter distribution, pyGravSphere employs a broken power-law model with 5 spatial bins defined as logarithmically spaced fractions of the half-light radius†, R_e, with bins r_j = [0.25, 0.5 ,1, 2, 4] R_e. Within each bin, the density follows a power law defined by slopes γ_j. The overall distribution is described by

$$\rho_{\rm dm}(r) = \begin{cases} \rho_0 \left(\dfrac{r}{r_0}\right)^{-\gamma_0}, & r < r_0 \\ \rho_0 \left(\dfrac{r}{r_{j+1}}\right)^{-\gamma_{j+1}} \displaystyle\prod_{n=0}^{n<j+1} \left(\dfrac{r_{n+1}}{r_n}\right)^{-\gamma_{n+1}}, & r_j < r < r_{j+1} \end{cases} \tag{4.4}$$

where ρ_0 is the density at r_0. Beyond the outermost bin, the power law is extrapolated. Note that this radial extent typically covers the positions of available kinematic tracers.

For the light profile, pyGravSphere uses a sum of three Plummer (1911) components

---

*`https://github.com/AnnaGenina/pyGravSphere`

†In this work, we use multiple definitions of the half-mass radius, which we list here for the purposes of clarification. R_{2D} is the projected radius which contains half of a dwarf's stellar mass and it is computed by direct summation. R_e is the projected radius containing half the stellar mass, derived from a 3-component Plummer profile fit to the *sample* of stellar particle data. We frequently refer to R_e as the half-light radius.

($N_P = 3$):

$$\nu(r) = \sum_{j}^{N_P} \frac{3M_j}{4\pi a_j^3}\left(1 + \frac{r^2}{a_j^2}\right)^{-5/2}, \tag{4.5}$$

where M_j and a_j are the relative weight and spatial extent of each component, respectively. This distribution is straightforward to project, yielding:

$$\Sigma(R) = \sum_{j}^{N_P} \frac{M_j}{\pi a_j^2}\left(1 + \frac{R^2}{a_j^2}\right)^{-2}. \tag{4.6}$$

The velocity anisotropy is parametrized following Baes and van Hese (2007):

$$\beta(r) = \beta_0 + (\beta_\infty - \beta_0)\frac{1}{1 + \left(\frac{r_t}{r}\right)^{\eta}}, \tag{4.7}$$

where β_0 is the central value of the anisotropy, β_∞ is the value at infinity, r_t is the radius of transition and η is its steepness.

4.2.4.2 PYGRAVSPHERE data input

The photometric sample of stars is split into bins of $\sqrt{N_{\rm phot}}$ particles per bin, where $N_{\rm phot}$ is the size of the photometric sample. This choice allows for efficient spatial coverage and low Poisson error. We weight each particle by the relative number of stars it represents (i.e. we define the weight of each particle as $w_{\rm p} = m_{\rm p}N_{\rm tot}/M(< 3R_{\rm 2D})$, where $N_{\rm tot}$ is the total number of particles in the sample). For each photometric bin, we calculate the Poisson errors and use the LMFIT algorithm (Newville et al., 2014) to obtain the best 3-component Plummer fit (Equation 4.6). This profile is then input into EMCEE.

The kinematic data are also split into bins of $\sqrt{\rm N_{kin}}$ particles per bin, where $N_{\rm kin}$ is the size of the kinematic sample. The error in each bin is computed by adding the Poisson and sampling errors in quadrature, where we again weight each particle by w_p. This procedure is described in detail in Read and Steger (2017). The effect of the number of particles per bin was explored in Read and Steger (2017), who found little impact on their results. We

Table 4.1: Default GravSphere priors

Property	Parameter	Prior
Dark Matter	$\log_{10}\rho_0/\mathrm{M_\odot kpc^{-3}}$	[5, 10]
	$\gamma_{0,1,2,3,4}$	[0, 3], $\Delta\gamma_{\max} = 1$
Anisotropy	$\tilde{\beta}_0$	[-1, 1]
	$\tilde{\beta}_\infty$	[-1, 1]
	$\log_{10} r_0/\mathrm{kpc}$	$\log_{10}[R_e/2, 2R_e]$
	η	[1, 3]
Tracers	$\log_{10} M_j/\mathrm{M_\odot}$	$\log_{10}[M_{\mathrm{bf,j}}/2\ ,\ 3/2M_{\mathrm{bf,j}}\ ]$
	a_j/kpc	$[a_{\mathrm{bf,j}}/2\ ,\ 3/2a_{\mathrm{bf,j}}]$
Baryons	$\log_{10} M_*/\mathrm{M_\odot}$	$\log_{10}[0.75M(<3R_{\mathrm{2D}}),$ $1.25M(<3R_{\mathrm{2D}})]$

confirm this to be the case, provided the signal-to-noise is not low due to 'overbinning' in the inner, dense, regions.

We use the same kinematic bins to compute the mean and errors of the two VSPs. Because VSP2 is sensitive to the behaviour of the velocity dispersion profile in the outer regions (due to the R^3 term), we fit a power law to the computed v_P^4 profile outside of the projected half-light radius and extrapolate it following Read et al. (2018).

4.2.4.3 EMCEE set-up and priors

The priors on each of the parameters in the default pyGravSphere set-up are shown in Table 4.1. Parameters $\log_{10} M_j$ and a_j of the best 3-component Plummer fit are allowed to vary within 50 per cent of their linear best-fit values, as determined by LMFIT, while the stellar masses $\log_{10} M_*$ were varied within 25 per cent of the $M(<3R_{2D})$ value.

In order to ensure that the walkers sample the whole hypervolume of parameter space defined by the parameter constraints, the starting positions of walkers are ideally generated to follow a uniform distribution. This is difficult to achieve when the values of the dark matter slope, γ_j, in each radial bin, r_j, are constrained to monotonically increase. We find that typically ~ 5 per cent of the initially generated walker positions fall within these defined bounds. If the chains are allowed to run for long enough, the walkers that are 'stuck' in forbidden regions of the parameter space may eventually make their way to the allowed regions. This process is, however, dependent on the efficiency of the active walkers in probing the posterior distribution. In cases where the posterior is multimodal, for example, some regions of the parameter space will not be probed due to the nature of the ensemble sampler, where the walkers communicate with each other, unlike in the classical Metropolis-Hastings algorithm.

We thus use the following procedure to generate the initial walker positions. For each walker, we generate the free parameters following a uniform distribution. We then throw away the walkers that do not satisfy our γ_j constraints. For the discarded walker positions we generate new ones, accepting those that satisfy the constraints and rejecting the others. This procedure is repeated recursively until each walker has a randomly generated initial position that satisfies the constraints. The effective priors and the advantages of the method over the one implemented in the original works using GravSphere (e.g. Read and Steger 2017; Read et al. 2018) are discussed in Appendix F.

We use 1000 walkers to probe the posterior distribution. Each walker is run for 10^4 steps as a conservative 'burn-in' measure, and then for a further 10^4 steps. The results presented in Appendix F suggest that our walkers are converged after $\sim 6 \times 10^3$ steps, so the above choices are rather extreme.

Since the anisotropy parameter, β, can take on values between 1 and $-\infty$, one would benefit from transforming this into a finite range. As in Read and Steger (2017), we use the symmetrized anisotropy parameter,

$$\tilde{\beta} = \frac{\beta}{2-\beta}, \quad \text{with} \quad -1 < \tilde{\beta} < 1. \tag{4.8}$$

This allows the MCMC to probe the entire range of the allowed anisotropy values. In practice, we apply the constraints $\tilde{\beta}_0 > -0.95$ and $\tilde{\beta}_\infty > -0.95$, as for more negative values the calculation becomes numerically unstable.

pyGravSphere solves the Jeans equation for the projected velocity dispersion profile, $\sigma_P(R)$. It additionally fits the projected number density distribution, $\Sigma(R)$, and the two VSPs. We define the 'log-likelihood function' as the chi-squared sum of these four components:

$$\ln \mathcal{L} = -\frac{1}{2}\left(\chi^2_{\sigma_{LOS}} + \chi^2_{\Sigma} + \chi^2_{VSP1} + \chi^2_{VSP2}\right). \tag{4.9}$$

We note that Equation 4.9 involves quantities that are, to some extent, correlated. We must, therefore, consider whether the form of the likelihood function in Equation 4.9 is justified. It has been pointed out in Łokas and Mamon (2003) and Łokas (2009) that the correlation between the second and the fourth velocity moments is typically weak. Aside from the fourth velocity moment, the virial shape parameters are also related to the projected surface density, $\Sigma(R)$. Given that the photometric samples for classical dwarfs are typically large, $\Sigma(R)$ is measured to a sufficiently high accuracy, such that its uncertainties are negligible compared to those of the fourth velocity moment. Moreover, Read and Steger (2017) find that the estimates of the second velocity moment and the virial shape parameters are typically normally distributed. This, together with the weak correlation between the second and fourth velocity moments, suggests that Equation 4.9 is a good approximation to the true likelihood function.

4.3 Results

In this section, we present the performance of the GravSphere method, under a default setup, on each of the dwarfs in our sample. We further quantify its global performance, for the entire sample, and compare to standard Jeans analysis approaches. We identify the causes of bias and scatter in the recovered enclosed mass profiles.

4.3.1 Individual dwarfs

Fig. 4.2 shows the recovery by GravSphere of the cumulative mass profile, density profile and the velocity anisotropy profile for each dwarf in our sample. In this figure, we only display results for projections along the vector to the centre of the host galaxy. The 'true'

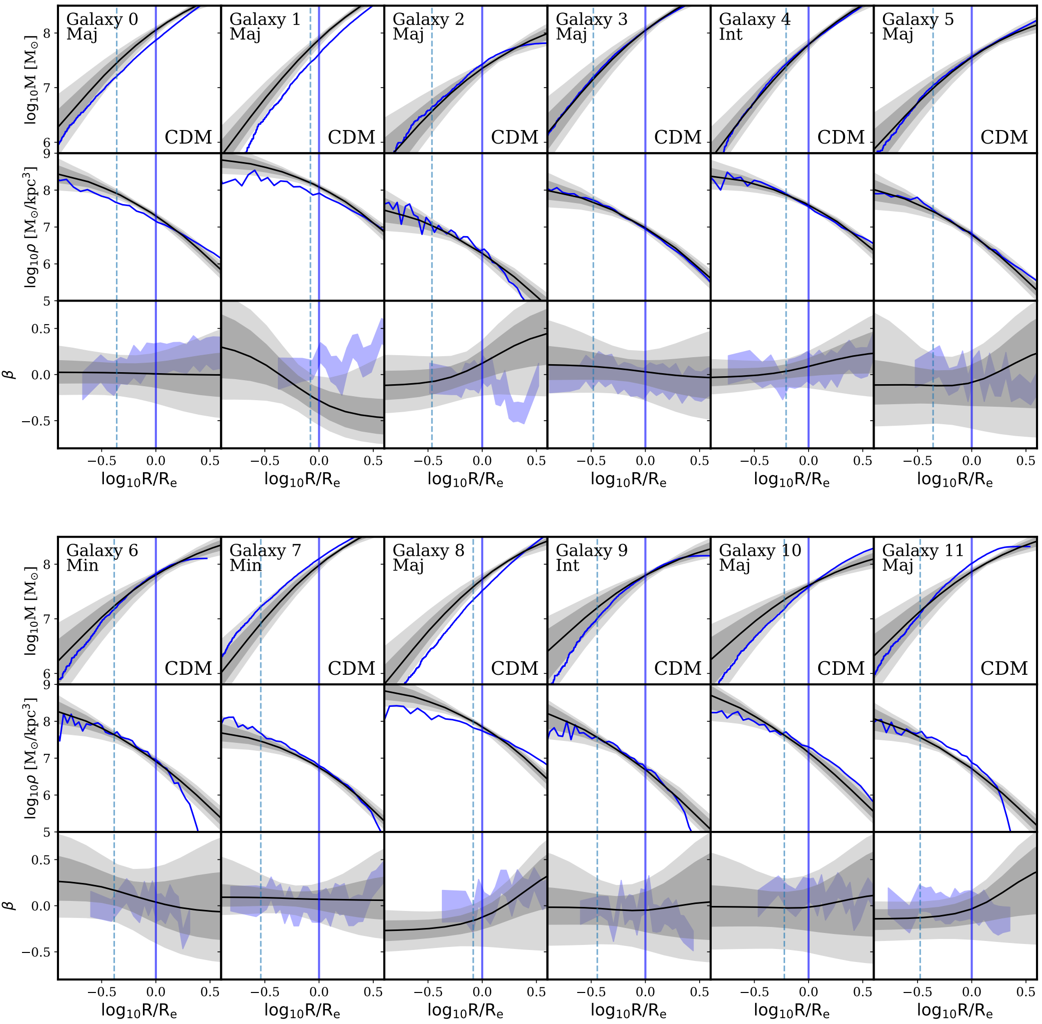

Figure 4.2: Enclosed dynamical mass profiles (top), density profiles (middle) and symmetrized anisotropy profiles recovered for a sample of 32 simulated dwarf galaxies using the GravSphere method. Only one projection (from the centre of the host galaxy) is shown for each dwarf. The profiles are shown as a function of 3D radius, normalized by the projected half-light radius, R_e. The black lines and the dark and light grey shaded bands display the median, 68 and 95 per cent confidence limits, respectively. The 'true' mass and density profiles, measured directly from the simulation, are shown in blue. The solid vertical blue line shows the location of the projected half-light radius and the dashed blue line shows 2.8ϵ (≈380 pc for CDM dwarfs and SIDM dwarfs (25,26) and ≈655 kpc for SIDM dwarfs 27-31), which is close to the convergence radius for these systems. The 'true' velocity anisotropy, as measured directly from the stellar particles, is shown with a shaded blue band. Each galaxy is labelled by its number, the principal axis along the which the dwarf is projected (which is the principal axes most closely aligned to the vector to the host galaxy) and whether the dwarf is from CDM or SIDM cosmology.

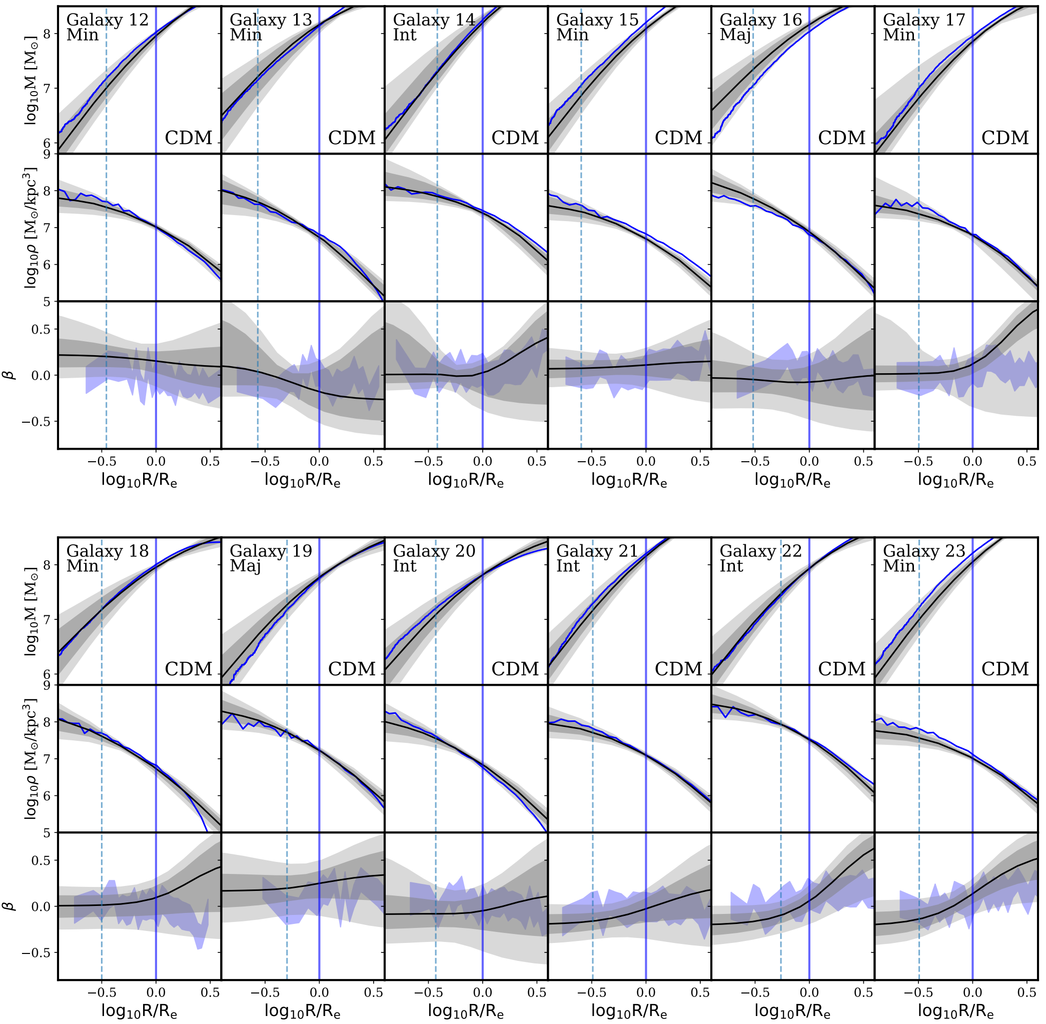

Figure 4.2: continued.

mass, density and anisotropy profiles are displayed in blue and the GravSphere results in grey shaded bands. To generate the GravSphere profiles we took 10^5 random samples from the output MCMC chains and for each radial position computed the median and the 68th and 95th percentile confidence levels. The choice of 10^5 samples is sufficient to produce representative posteriors but is otherwise arbitrary.

Mass profiles of simulated dwarfs were computed by summing dark matter particle masses one-by-one radially from the centre of the dwarf, where we defined the centre as the centre of mass of the stellar component. Densities were computed form 31 logarithmically-spaced bins in radius, from $\log_{10} r/\mathrm{kpc} = -2$ up to the furthest bound dark matter particle. In order to compute the stellar velocity anisotropy in the simulated dwarfs, we bin the stars

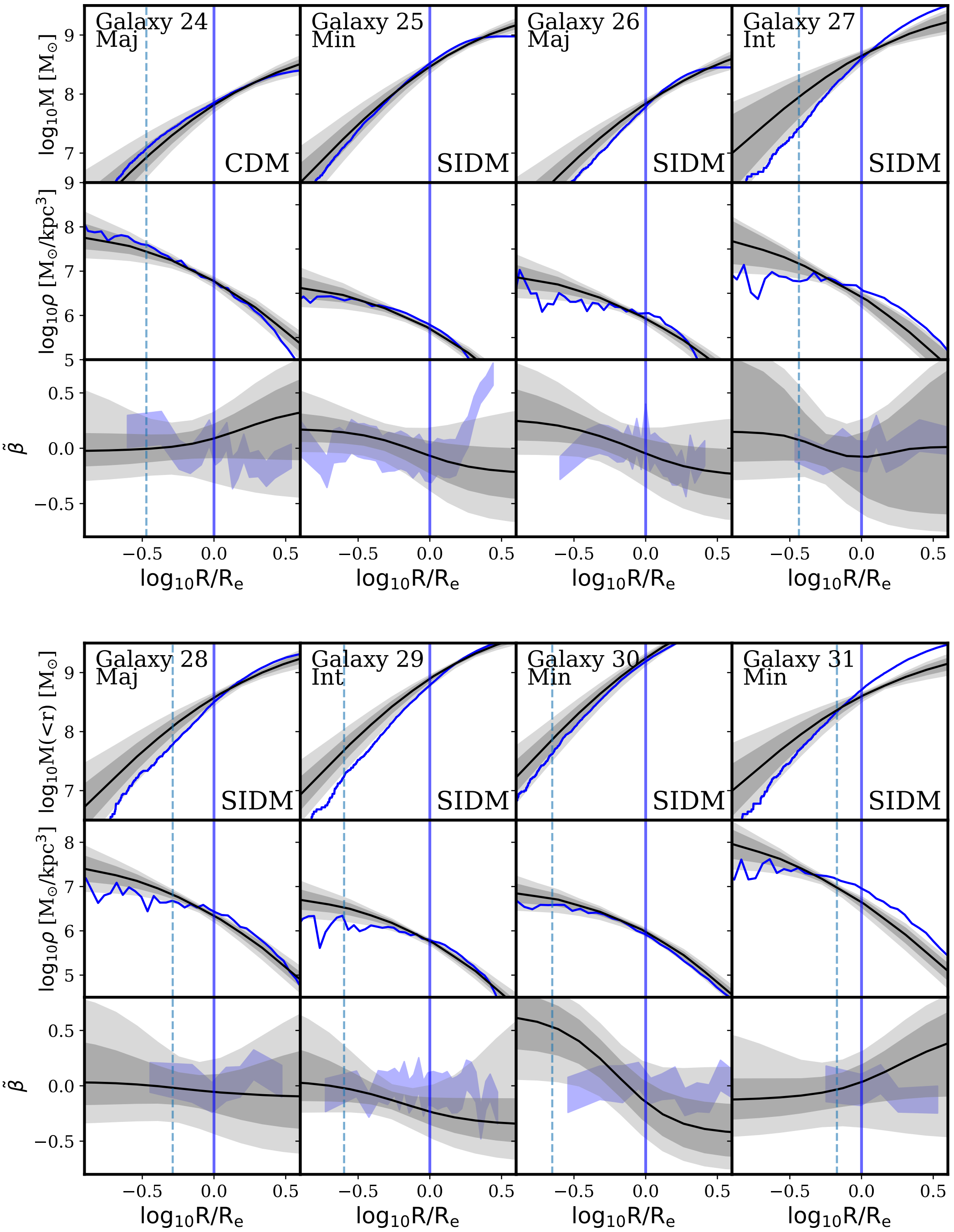

Figure 4.2: Galaxies 25 - 31 are SIDM dwarfs. Note that for a number of these dwarfs the spatial resolution, 2.8ϵ (vertical dashed line), is below $0.125R_e$ and below the limits of the figure.

into 50 logarithmically spaced bins, starting from the position of the star that is closest to the centre of mass and ending at the outermost star. We then reduce the number of bins and widen the bin edges such that each bin has at least 50 stars within. We construct 1σ error bars by taking 1000 random samples of 25 stars with replacement and computing the standard deviation of the velocity anisotropy in each bin.

In this analysis, we focus on the key region within the half-light radius of each galaxy (solid vertical blue line) and above 2.8ϵ. GravSphere appears to be unbiased on average. For the CDM sample, the dwarf mass, density and anisotropy profiles are typically contained within the 68 per cent confidence limits, although the uncertainties can be large. Notable exceptions in the CDM sample are Galaxies 1 and 8. These are known aspherical objects (see Fig. 4.1). Similar systematics can be seen for the remainder of the aspherical sample of dwarfs. It is clear that in SIDM dwarfs the enclosed mass is *always* overestimated, although even in these galaxies the true profiles are contained within the 95 per cent confidence regions. We will return to this issue in Section 4.3.5.

We also note that the symmetrized anisotropy profiles in our simulations are generally consistent with being constant and isotropic ($\tilde{\beta} = 0$). Deviations from this are seen in galaxies that are aspherical, and, as we will see in Section 4.3.7.3, in those which are affected by tides.

4.3.2 Comparison to standard estimators

We now compare the performance of GravSphere in recovering enclosed masses to three mass estimators from the literature. The mass estimators take the form:

$$M(< \mu R_e) = \frac{\lambda R_e \langle \sigma_P^2 \rangle}{G}, \tag{4.10}$$

where μ and λ are constants.

The estimator provided by Wolf et al. (2010) gives the mass enclosed within the deprojected half-light radius R_3, with $R_3 \approx 4/3R_e$; the Walker et al. (2009b) estimator at the projected half-light radius, R_e. Another estimator has been derived by Campbell et al. (2017) for the mass within $1.44\mathrm{R}_{\mathrm{2D}}$, where R_{2D} is the projected radius containing half the stellar mass. The latter has been calibrated on dwarfs from the APOSTLE suite of simulations that we use here. We omit the estimator derived by Errani et al. (2018), which we find produces similar results to those of Campbell et al. (2017).

As input for the estimators, we use the half-light radius, R_e, obtained from the best-fit 3-component Plummer profile, as this is expected to provide more accurate results than the circular radius containing half the stellar mass, R_{2D} (González-Samaniego et al., 2017). The latter definition was used in the calibration of the Campbell et al. (2017) estimator, however, we refrain from using this definition as the spatial extent of the sample of stellar particles in each dwarf is already cut off at $2R_{2D}$. For Wolf et al. (2010) and Walker et al. (2009b) estimators we calculate the mean velocity dispersion and the associated errors using the technique of Walker et al. (2006), where we incorporate weighting by the number of stars per stellar particle, w_p, in the likelihood function. For the Campbell et al. (2017) estimator we compute the mass-weighted mean velocity dispersion below $1.04R_e$, as prescribed.

In Fig. 4.3, we show the median bias in mass profiles returned by GravSphere (mass recovered by GravSphere divided by the true mass) for our sample of dwarfs, and the 68 and 95 per cent confidence levels, as a function of normalised radius, R/R_e. We use the following procedure to compute the global radial bias and the associated confidence levels. For each galaxy and for each distance, R, we obtain a cumulative mass distribution from 10^5 random samples of the MCMC posteriors. We then use this cumulative distribution for Monte Carlo sampling of accuracies, combining the samples from all galaxies at each distance. This allows us to take into account the asymmetry in the GravSphere confidence limits, as seen in Fig. 4.2.

The lower axis limit on R/R_e in Fig. 4.3 has been chosen to be the average value of $2.8\epsilon/R_e$ for our sample and the upper axis limit was chosen so as to contain the smallest dark matter halo in the sample. The bias and associated errors for each galaxy are only included in the making of this figure for distances $R > 2.8\epsilon$.

In purple, we show the CDM sample and in black the SIDM sample. The symbols with error bars show the performance of dynamical mass estimators from Walker et al. 2009b, Wolf et al. 2010 and Campbell et al. 2017 (circles for CDM and squares for SIDM). The Wolf et al. (2010) and Walker et al. (2009b) estimators are accurate to better than 10 per cent, however, we observe bias in the Campbell et al. (2017) estimator. This is likely due to the aforementioned difference in the definition of the half-light radius. In all cases, the true mass is contained within the uncertainty of the estimators.

From Fig. 4.3 it is clear that, for CDM dwarfs, GravSphere performs just as well as the Wolf et al. (2010) and Walker et al. (2009b) estimators, and with similar scatter. The inferred masses are, on average, very accurate across the entire radial range, with the scatter becoming more significant in the innermost regions as well as the outer regions. For the large values of R/R_e this is caused by the lack of kinematic tracers. Moreover, our priors permit only a narrow range of slopes ($0 < \gamma_j < 3$), whilst our sample is expected to have undergone tidal effects, resulting in an outer slope $\gamma \approx 4$ (Peñarrubia et al., 2009). Nevertheless, the estimate is accurate, on average, out to $3R_e$, with a root mean square (RMS) fractional error* of only 5 per cent. It is clear that the masses for SIDM dwarfs are significantly overestimated in the inner regions (on average, up to 80 per cent), with very large scatter. The mass is accurate near the half-light radius and beyond that it is underestimated by $\sim$ 20 per cent.

4.3.3 The core-cusp problem

What do these results mean in the context of the core-cusp problem? We now consider two ways to infer cores or cusps in dark matter haloes: via their characteristic inner density (as in Read et al. 2019) and via an accurate inference of profile shape.

---

*We define RMS $= \sqrt{\frac{1}{N}\sum_{i=1}^{i=N}(M_{\rm calc}/M_{\rm true}-1)^2}$, where $M_{\rm calc}$ is the mass obtained through GravSphere, or another method, N is the number of radial intervals at which $M_{\rm calc}$ is computed and $M_{\rm true}$ is the true enclosed mass at these intervals, found directly from the simulation. We use a maximum of 30 intervals to construct Fig. 4.3.

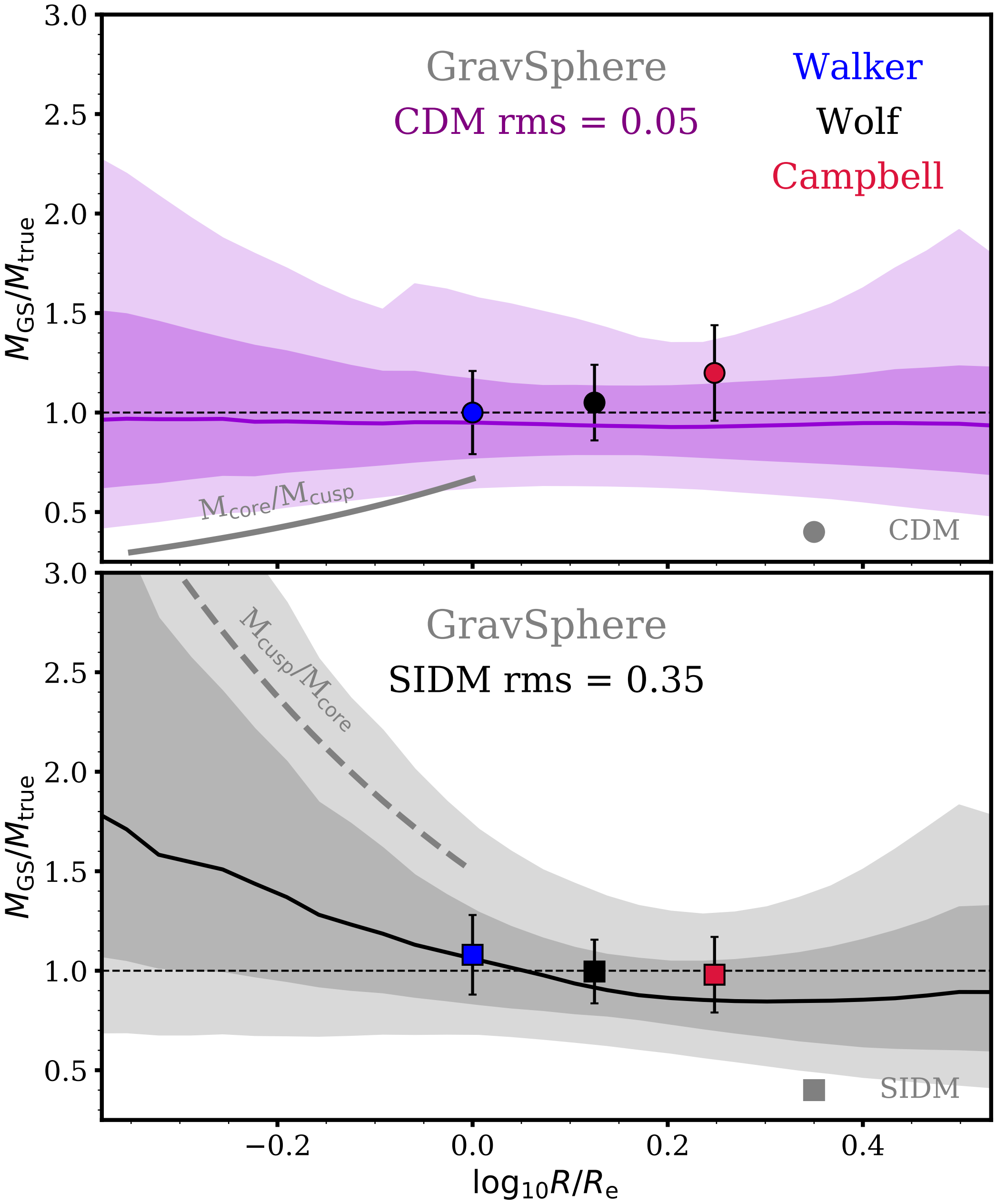

Figure 4.3: Ratio of the recovered to true enclosed mass as a function of radial distance in units of the half-light radius, R_e. The purple line and purple shaded bands show the median, 68 and 95 per cent confidence limits for the CDM galaxy sample. The black line and the corresponding shaded bands show the sample of SIDM dwarfs. The symbols and their error bars show the accuracy of standard estimators from Walker et al. (2009b),Wolf et al. (2010) and Campbell et al. (2017), identified by their colours. Circles are for the CDM dwarfs and squares for SIDM. The 'rms' values show the root-mean-square offset of the median value from 1 along the entire radial range displayed. The grey dashed line shows the radially-dependent bias in the mass profiles that is required to infer an NFW cusp, when in reality there is a core. The solid grey line shows the bias required to infer a dark matter core, when in reality there is a cusp.

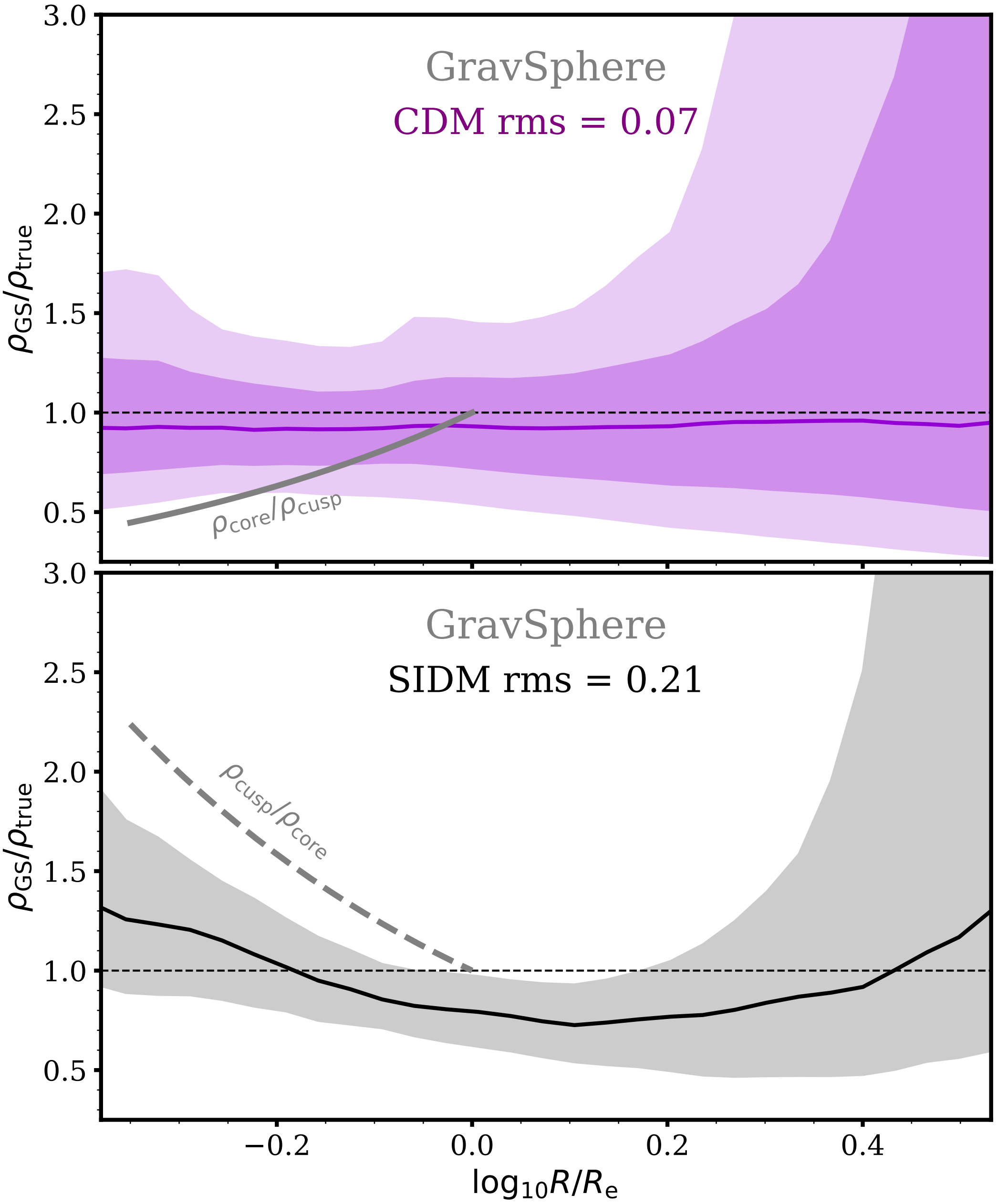

Figure 4.4: Ratio of the recovered to true density as a function of radial distance in units of the half-light radius. The grey dashed line shows the bias in the recovered density profiles required to infer an NFW cusp when in reality there is a core. The solid grey line shows the corresponding bias for an incorrect inference of a core when the true profiles are cuspy.

4.3.3.1 Cores vs. cusps via characteristic densities

In Fig. 4.4 we show the recovery by GravSphere of the dark matter density profiles of our sample of dwarfs. For CDM dwarfs, the density profiles are accurate across the entire radial range (RMS = 0.07) and the scatter is only ~30 per cent in the inner regions. In fig. 5 of Read et al. (2019) it can be seen that, for a dwarf of Fornax-like pre-infall halo mass, the core and cusp-like densities, ρ_{150}, differ by a factor of at least 3.5. The spatial resolution of our simulations does not allow us to probe radii below 380 pc; however, if GravSphere provides a similar level of bias and scatter for ρ_{150} (corresponding to $\log_{10} R/R_e \approx -0.7$ for a Fornax-size dwarf), it is certainly possible to differentiate between the core and cusp-like densities, provided there is complete core formation below the half-light radius and no reduction of central dark matter density due to tides (Read et al., 2016). For SIDM dwarfs, the density is overestimated in the inner regions by up to 50 per cent and underestimated above the half-light radius by $\sim$ 30 per cent, reflecting the pattern with enclosed mass. This suggests that in the case of SIDM dwarfs with cores, GravSphere is biased towards cusps in its standard configuration.

4.3.3.2 Cores vs. cusps via profile shape

Let us now approximate the density profiles in the inner regions by a single power law

$$\rho(r) = \rho(R_e)\left(\frac{r}{R_e}\right)^{-\gamma}, \tag{4.11}$$

where $\rho(R_e)$ is the density at R_e and γ is the slope of the power law, with $\gamma = 0$ corresponding to a core and $\gamma = 1$ to a cusp. If we assume that a core forms below the radius R_e, where otherwise the density within R_e follows $\rho \propto r^{-1}$, then the density ratio is

$$\frac{\rho_{\rm cusp}}{\rho_{\rm core}} = \left(\frac{r}{R_e}\right)^{-1}, \tag{4.12}$$

and the mass ratio is

$$\frac{M_{\rm cusp}}{M_{\rm core}} = \frac{3}{2}\left(\frac{r}{R_e}\right)^{-1}. \tag{4.13}$$

We display these relations, and their inverse, with dashed (an incorrectly inferred cusp) and solid (an incorrectly inferred core) grey lines in Figs. 4.3 and 4.4. The relations are displayed out to the radius $R = R_e$ for the case where a core forms below the half-light radius*. Beyond this radius, the relations are expected to converge to 1. The relations should be taken more as visual guides for the radial dependence of the bias that we expect in order to incorrectly infer a core or a cusp. Note that for a core that forms at some fraction of the half-light radius, we would only need to scale the relation in Equation 4.12 by a corresponding factor (or shift the relation up and down in log-space). Unfortunately, cores on the scale of $0.5R_e$ are too small to be probed by our simulations for the dwarf galaxy masses we consider here.

For the case of CDM dwarfs, it is clear that within the 68 per cent confidence regions the mass and density profiles returned by GravSphere are fully consistent with cusps. Cores lie outside the 95 per cent confidence regions. For SIDM dwarfs there is a clear bias towards more cuspy profiles. Fully cored profiles below the half-light radius are contained within the 68 per cent regions, but so are cusps that are only slightly shallower than $\rho \propto r^{-1}$.

4.3.4 Comparison to other methods and parametrizations

We now compare the performance of GravSphere to that of more conventional Jeans approaches. We will focus on the enclosed mass profiles, rather than densities. Masses are more robust than their differentials, they are simply measured in simulations and are a fundamental property in Jeans analysis.

4.3.4.1 Comparison to Zhao (1996) profile

We compare the performance of GravSphere to the method outlined by Bonnivard et al. (2015), who used the profile proposed by Zhao (1996) to parametrize the dark matter

---

*We have verified that the relations in Equations 4.12 and 4.13 are good approximations for a dwarf with a Fornax-like pre-infall halo mass (Read et al., 2019) with full core formation below the half-light radius and an NFW profile otherwise (Read et al., 2016).

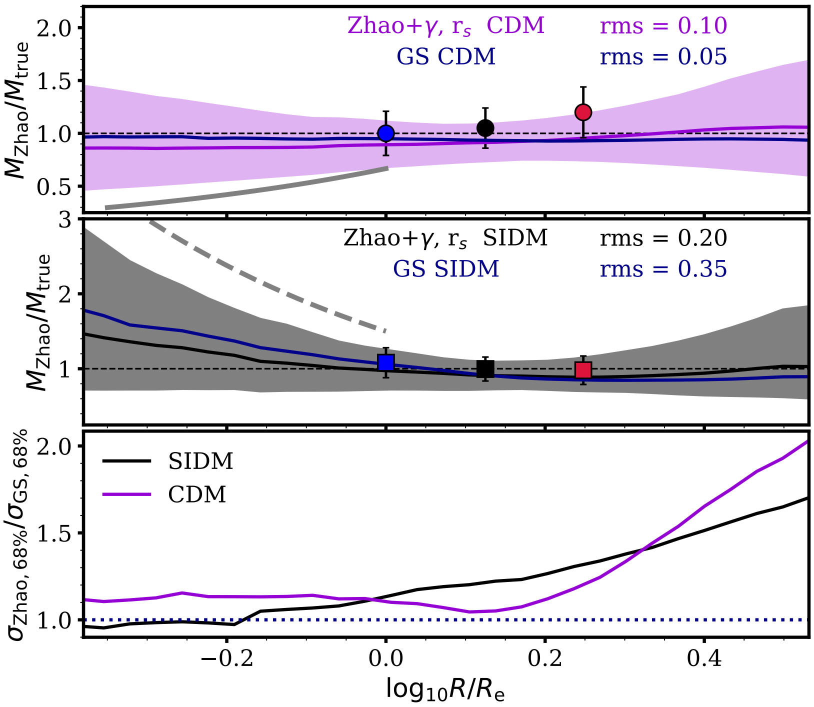

Figure 4.5: Bias in enclosed mass profiles found assuming a Zhao (1996) profile and using priors as outlined in Table 4.2, together with post-processing cuts ($\gamma < 1$ and $r_s > R_e$). The median for the original GravSphere run is shown in blue. The medians for the CDM and SIDM samples are shown with purple (top subplot) and black (middle subplot) lines, respectively. The shaded bands of the same colour show the 68 per cent confidence limits on the bias, $M/M_{\rm true}$, for CDM (top) and SIDM (middle) samples. The bottom subplot shows the magnitude ratio of the 68 per cent confidence intervals between the Zhao (1996) and default GravSphere results. The colour symbols are the Walker et al. 2009b (blue), Wolf et al. 2010 (black) and Campbell et al. 2017 (red) estimators. The grey dashed line corresponds to the bias required for an incorrect inference of an NFW cusp when in reality there is a core, and the solid grey line is the bias required for an inference of a core when in reality there is an NFW cusp.

distribution:

$$\rho_{\rm dm} = \frac{\rho_0}{\left(\frac{r}{r_s}\right)^{-\gamma}\left(1+\left(\frac{r}{r_s}\right)^{\alpha}\right)^{\frac{\beta-\gamma}{\alpha}}} \tag{4.14}$$

where r_s and ρ_0 are the scale radius and scale density, γ is the inner slope, β the outer slope and α governs the steepness of transition between γ and β.

The priors for this run, which we refer to as Zhao + γ, r_s, are given in Table 4.2. The method requires two post-processing cuts: one on $\gamma \leq 1$, which was shown to reduce the

Table 4.2: Zhao (1996)+γ, r_s MCMC priors and the cuts applied in post-processing

Parameter	Prior	Constraint
$\log_{10}\rho_s/\mathrm{M_\odot kpc^{-3}}$	[5, 13]	
$\log_{10} r_s/\mathrm{kpc}$	[-3, 1]	$\log_{10} r_s \geq \log_{10} R_e$
α	[0.5, 3]	
β	[3, 7]	
γ	[0, 1.5]	$\gamma \leq 1$

overall scatter, and another on $r_s \geq R_e$, which weeds out unphysical models from the fit. The results are shown in Fig. 4.5.

It can be seen that this method underestimates the enclosed mass by ~10 per cent in the inner regions for CDM dwarfs and is unbiased in the outskirts. In SIDM dwarfs, however, the bias in the centre is less severe than with GravSphere. In the inner regions, for CDM and SIDM dwarfs, the scatter has not changed significantly, but outside the half-light radius and in the outer parts the width of the scatter increases by over 50 per cent. This is likely due to the priors (Table 4.2) allowing a much wider range of outer slopes β than permitted by the default GravSphere priors (Table 4.1). The exclusion of virial shape parameters likely also plays a role. We explore this below.

4.3.4.2 GravSphere, excluding the VSPs

What is gained by including the virial shape parameters? We repeat our GravSphere run, this time excluding the two VSPs from Equation 4.9. The results are shown in Fig 4.6. It can be seen that the accuracy in the inner regions has suffered from excluding the VSPs in CDM dwarfs. In SIDM, however, the bias is slightly reduced. As we shall see below, this reduction is consistent with excluding only the second virial shape parameter. The bottom panel shows the ratio of the upper and lower errors (84^{th} and 16^{th} percentiles) compared to the default GravSphere run (including the VSPs). It is evident that the scatter has increased beyond the half-light radius. This suggests that GravSphere runs that exclude the VSPs result in a wider range of allowed models. Evidently, the inclusion of VSPs plays a key role in minimizing the scatter in allowed anisotropy models, particularly in the outer regions. These results mimic those produced with the priors in Table 4.2, although the

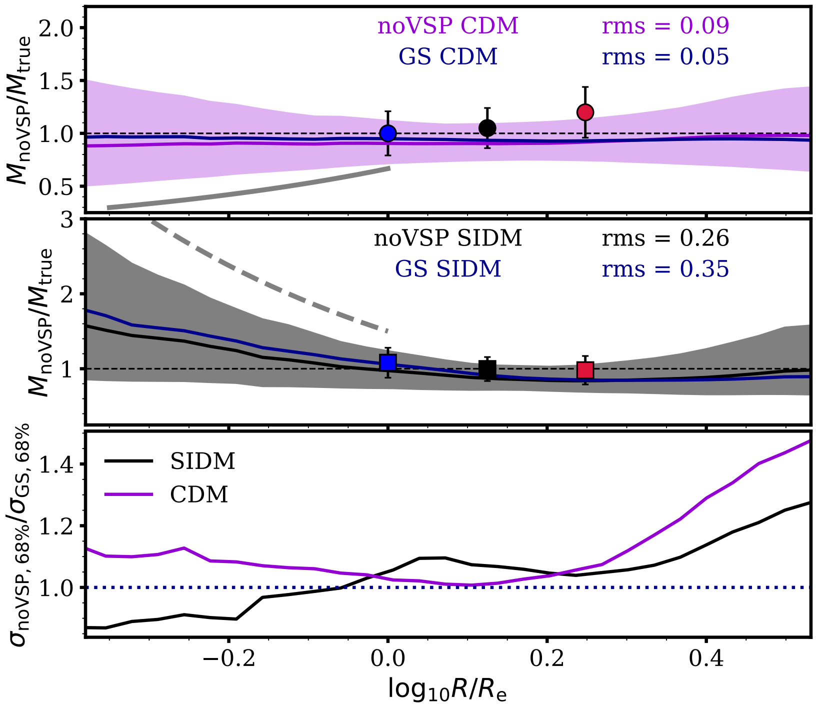

Figure 4.6: As Fig. 4.5, but for bias found with GravSphere assumptions, excluding the VSPs (noVSP).

increase in the scatter in the outer regions is smaller. This suggests that another significant source of this scatter is, in fact, the wider range of allowed slopes β.

4.3.4.3 Constant anisotropy and no VSPs

We now explore the performance of GravSphere under the assumption of constant anisotropy and no VSPs. From Fig. 4.2, it is clear that the vast majority of our simulated dwarfs have nearly constant stellar velocity anisotropy profiles. It is therefore possible that forcing the anisotropy profile to be constant with distance may encourage the MCMC algorithm to select better models. The comparison with GravSphere is shown in Fig. 4.7. Similar accuracy to GravSphere is achieved (RMS = 0.06) across the entire radial range. The errors for CDM dwarfs are similar to GravSphere in the innermost regions, but outside R_e the errors are larger. This could be partly due to lack of flexibility as compared to the Baes and van Hese (2007) profile, but this is also overall consistent with the noVSP run, suggesting a lack of constraint in the outer profile due to the exclusion of VSPs.

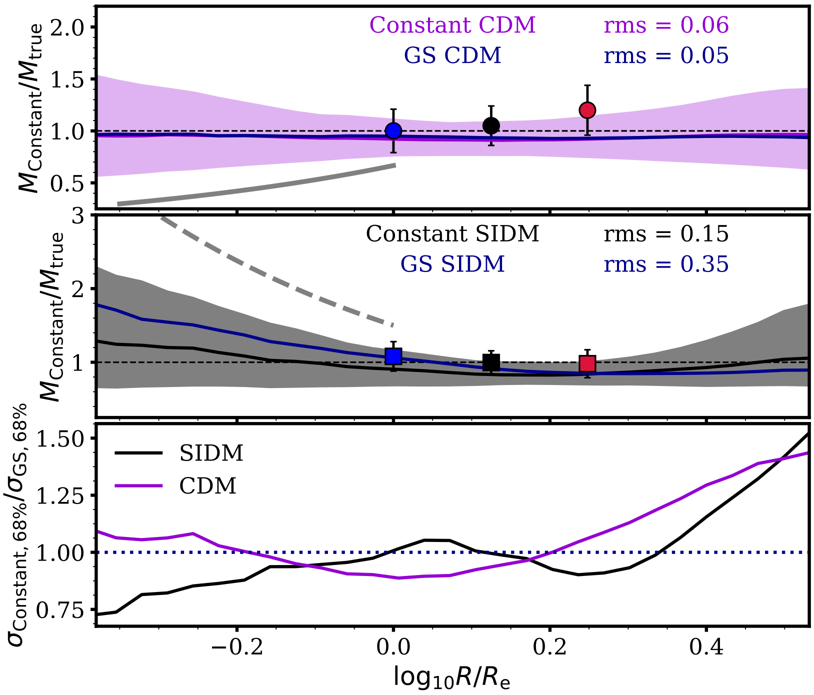

Figure 4.7: As Fig. 4.5, but for bias found assuming constant anisotropy and no VSPs.

For SIDM dwarfs the bias has reduced remarkably (now below 20 per cent in the inner regions). The scatter has also reduced by ~ 25 per cent compared to GravSphere. This would suggest that anisotropy profiles are not very well recovered with GravSphere and are a significant source of bias for SIDM dwarfs. In Fig. 4.2 we can see that the true anisotropy profiles are generally enclosed within the confidence limits. These limits are, however, quite large and so the $M-\beta$ degeneracy is not fully broken. The breaking of the degeneracy is forced when imposing a constant form for the anisotropy, resulting in the reduction in bias. Note also that the bias associated with a CDM cusp (dashed grey line in Fig. 4.7) is now far above the 68 per cent limits, compared to the case of GravSphere.

We note that, based on the sample of dwarfs presented in this chapter, our simulations suggest that dwarfs may have anisotropy profiles that are well described by a constant value of β. For this sample, the assumption of constant velocity anisotropy is sufficient to accurately recover mass profiles in the innermost regions of dwarfs and this does not require the use of the VSPs.

4.3.4.4 Removing VSP2

In their recent work, Kaplinghat et al. (2019) have opted to exclude the second virial shape parameter, which is extremely sensitive to the behaviour of the fourth velocity moment in the outer regions of the dwarfs (due to the R^3 weighting), where the velocity distribution is typically poorly constrained. In GravSphere, the uncertainty in the $\langle v_P^4 \rangle$ profile is encapsulated within the errors, though these errors are indeed very large. In this subsection, we investigate the effects of excluding the second virial shape parameter from our analysis.

The results can be seen in Fig. 4.8. We can see that, for CDM dwarfs, the mass profiles are now underestimated in the inner regions by nearly 10 per cent, while the scatter is reduced. For SIDM dwarfs, the accuracy has marginally improved and the scatter has also reduced. We conclude that the inclusion of VSP2 in Jeans analysis tends to slightly increase the scatter (due to its large errors), but the accuracy of the mass profiles is improved at the expense of this scatter.

4.3.5 Bias towards cusps in SIDM haloes

We now return to the issue of the overestimation of the enclosed mass profiles in SIDM dwarfs. We consider the effects of possible offsets between the centre of mass of the stars and the dark matter as well as the effect of our priors on the recovered mass profiles.

4.3.5.1 Galaxy – halo offsets in SIDM

For a profile with a core, it is particularly difficult to establish the location of the density centre. If this centre is offset from the true dynamical centre this may introduce a bias in the recovered mass profile. Although it is unlikely that this bias would always cause an overestimation of the true mass, we have investigated the differences between the centre of mass of the stars and the dark matter for each dwarf in our sample. We found that offsets are present, with a typical magnitude of 80 ± 35 pc for the CDM sample. For SIDM

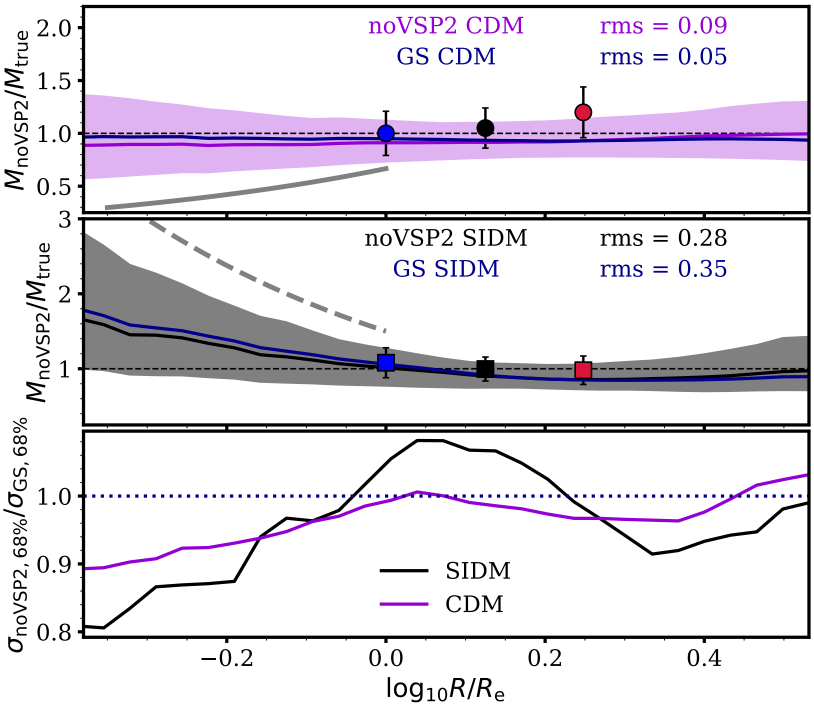

Figure 4.8: As Fig. 4.5, but for bias found with the exclusion of the second virial shape parameter.

halos the offsets are particularly extreme, up to 1 kpc in size. We repeated our analysis, comparing the mass profiles recovered by GravSphere to those computed directly from the simulation, now centering the 'true' profiles at the centre-of-mass of the dark matter. We found no discernible differences from the results presented in Fig. 4.3. Centering on the centre of potential instead also did not change our results. We conclude that galaxy–halo offsets have no significant effect on the results presented in this work. This is because these offsets are rather small compared to the half-light radii of SIDM dwarfs.

4.3.5.2 Using priors that favour a core

The systematic overestimation of enclosed mass at small radii has been encountered previously in the work of Read et al. (2018). The priors in Table 4.1 may bias the results towards more cusp-like values when the data are not sufficiently constraining, as a core (with $\gamma = 0$) lies on the boundary of the allowed range of slopes (see Appendix F). In Read et al. (2018), a different set of priors was introduced, which extends the parameter space of

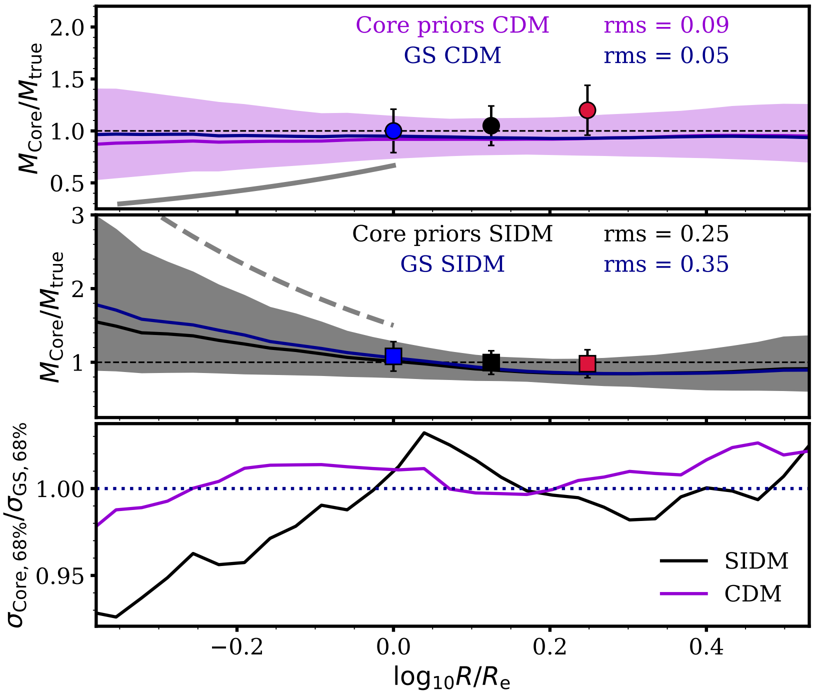

Figure 4.9: Bias found using wider priors on the slopes γ_j that allow a 'hole' in the central regions. All values of $\gamma_j < 0$ output by the MCMC are then equated to 0. The coloured symbols and grey lines are as in Fig. 4.5.

the dark matter density slopes γ_j such that EMCEE walkers are more likely to probe regions of space that are compatible with a core. This is achieved by allowing the slopes to range between $-2 < \gamma_j < 3$. Note that $\gamma_j < 0$ corresponds to a 'hole' in the central regions of the dwarf. While not implausible in principle, in this work we assume that, in these extreme cases, the dark matter distribution has a core. When computing the confidence limits of the enclosed mass and density distributions in each dwarf, we thus fix the γ_j position of any walkers venturing into the space where $\gamma_j < 0$ to $\gamma_j = 0$.

The results of this may be seen in Fig. 4.9. For SIDM dwarfs, we can see that the bias along the entire radial range has been reduced to ~ 25 per cent and the scatter is reduced by ~ 10 per cent in the inner regions. We also display the results for individual SIDM dwarfs in Appendix G, where a reduction in bias compared to Fig. 4.2 is evident. For CDM dwarfs, the new priors slightly bias the recovered mass profiles towards cores, although the true profiles still lie within the 68 per cent confidence levels. This is consistent with the findings of Read et al. (2018).

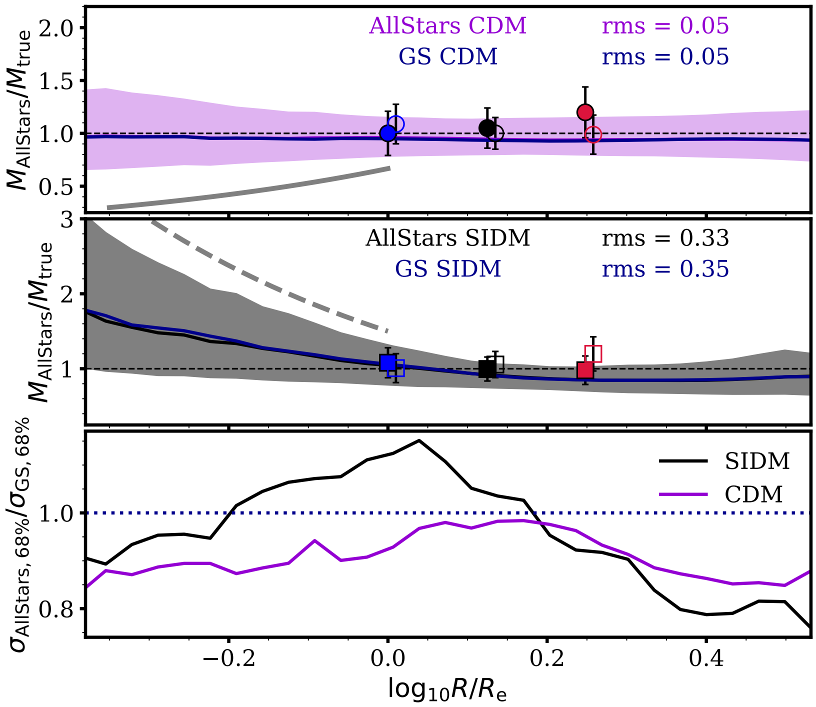

Figure 4.10: Bias found under standard GravSphere assumptions, but using all available stars in each dwarf. The symbols are as in Fig. 4.5. The additional empty symbols representing the accuracy of mass estimators were evaluated using all available stars within $2R_e$.

We conclude that the lack of exploration of the models with $\gamma_j = 0$ by GravSphere is clearly an issue, however, the data still lack sufficient constraining power to prefer cores over cusps in SIDM.

4.3.6 Using all available stars

In this section, we briefly explore how much information is gained by including all stars within $2R_e$ of each dwarf (ranging from 10^3 to 10^4 stars for CDM), as opposed to a Fornax-like sample of 500 − 2500 stars. We note, however, that for the majority of SIDM dwarfs the available samples are less than 1000 stellar particles.

The results of this can be seen in Fig. 4.10, where it is clear that the accuracy in the inner regions has slightly improved and the size of the errors is reduced by ∼ 10 per cent at smaller radii and closer to ∼ 20 per cent at large radii. Larger samples of data from future spectroscopic surveys will undoubtedly reduce the uncertainties associated with recovered dark matter mass profiles; however, this improvement is expected to be rather small when using line-of-sight data only. Moreover, GravSphere is able to achieve the same level of bias with present data samples. Further reduction in uncertainty is more likely to come from exploiting kinematically distinct stellar populations or proper motion data (Read and Steger, 2017).

4.3.7 Sources of bias and scatter in GravSphere

We now explore the possible origin of scatter in Fig. 4.3. Projection effects, asphericity and tides are of particular interest.

4.3.7.1 Line-of-sight effects

How does asphericity affect the accuracy of the enclosed mass profiles recovered by GravSphere? In the top panel of Fig. 4.11 we split our sample of dwarfs in bins of minor-to-major axis ratio $s = c/a$. It can be seen that, on average, dwarfs of all asphericities in CDM have mass profiles recovered to better than 10 per cent; however it is also clear that the scatter is much larger for more aspherical objects ($s < 0.9$). Our sample has been chosen to contain galaxies projected along their three principal axes. We can therefore split our sample into 3 categories: dwarfs seen along the minor, major and intermediate axes, and examine the accuracy of GravSphere in recovering mass profiles in each case. For this, we select dwarfs with $s < 0.8$ in CDM (6 galaxies) and $s < 0.85$ in SIDM (3 galaxies) [*].

The results are shown in the bottom panel of Fig. 4.11. For CDM dwarfs, there is a clear distinction between mass profiles obtained when viewing along the minor (blue), intermediate (red) and major (black) axis. Along the intermediate axis, the mass profiles are generally unbiased, but they are underestimated along the minor axis and overestimated along the major axis. On average, this over- and under-estimation is of magnitude ∼

---

[*] We have considered projection effects for the more spherical dwarfs in the sample and found that they are irrelevant in those cases.

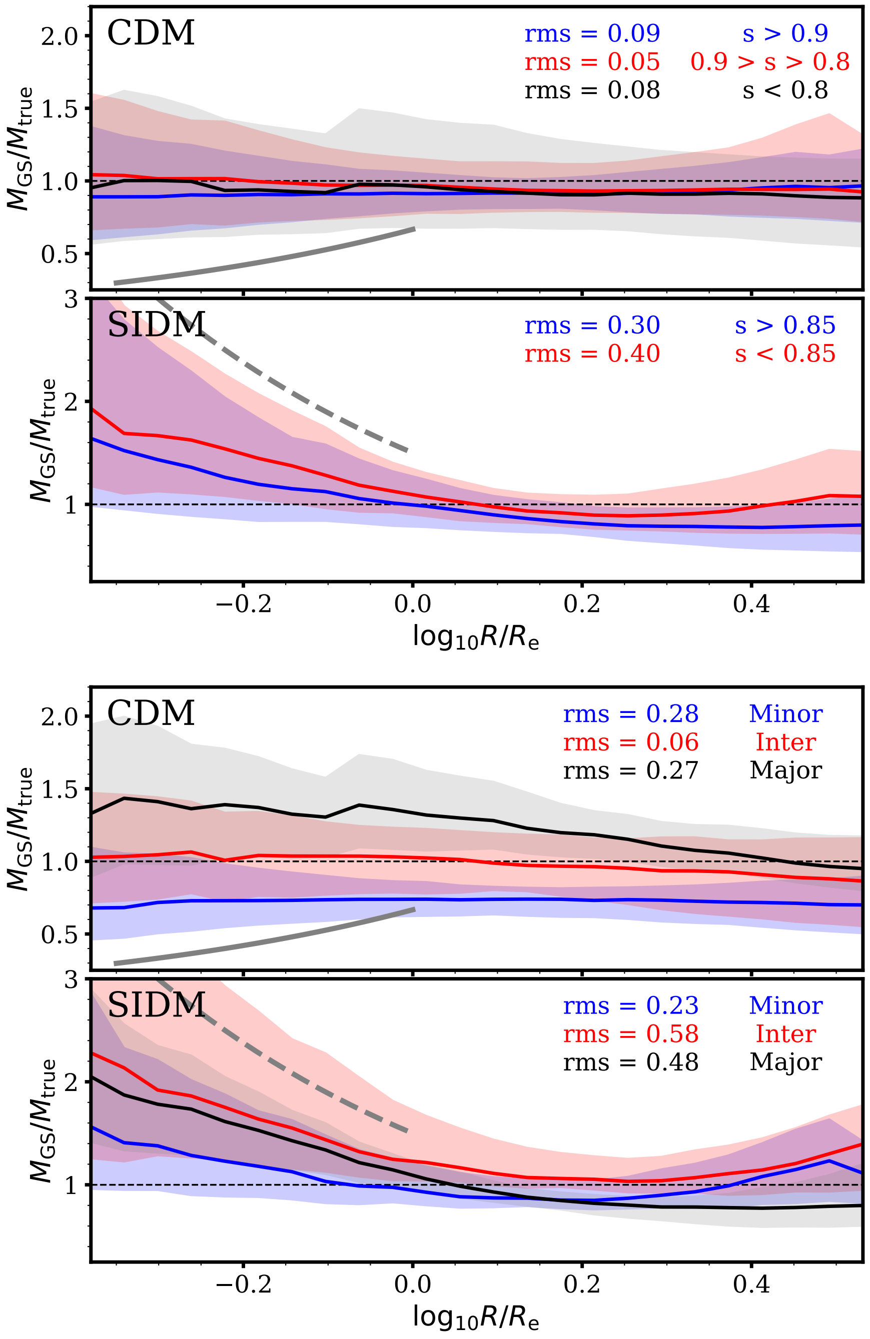

Figure 4.11: *Top:* bias in mass profiles returned by GravSphere for dwarfs, grouped by their minor-to-major axis ratio c/a. The top panel shows the CDM sample and the bottom panel shows the SIDM sample. *Bottom:* line-of-sight effects on the accuracy of the mass profile recovery by GravSphere. The sample of galaxies is split into those viewed along the minor (blue line and bands), intermediate (red) and major (black) axis. Only dwarfs with $s < 0.8$ for CDM and $s < 0.85$ for SIDM are shown. The dotted black line in each plot represents unbiased results. The solid grey line corresponds to the bias expected in order to incorrectly infer a core within the half-light radius of a cuspy dark matter halo. The dashed grey line corresponds to the bias expected to incorrectly infer an NFW cusp, when in reality there is a core.

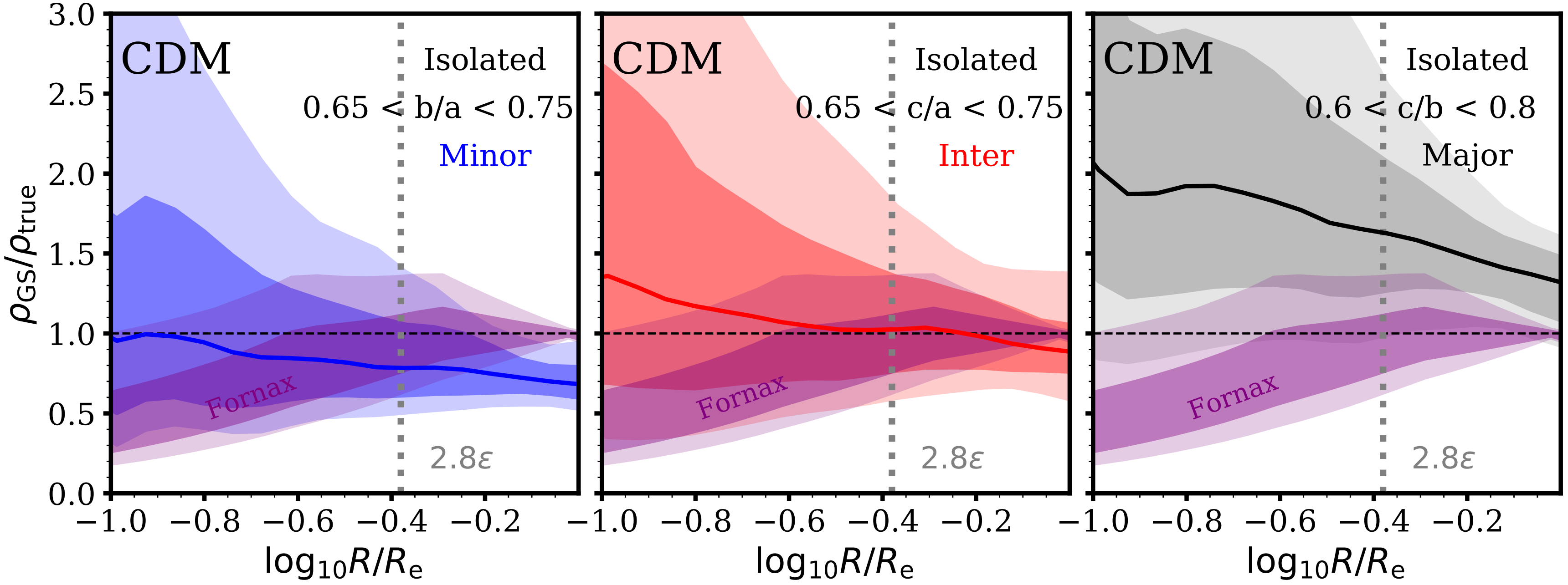

Figure 4.12: The bias in density profiles inferred by GravSphere for 24 isolated CDM dwarfs that match the criteria of having an on-the-sky ellipticity $e \sim 0.3$ when viewed along their minor (left, blue), intermediate (middle, red) and major (right, black) axes. The dark and light bands show the 68 and 95 per cent confidence levels, respectively. The dotted grey line shows the average value of $2.8\epsilon/R_e$. The purple line and bands show the inferred density profile for Fornax from Read et al. (2019), divided by a cuspy profile, $\rho \propto r^{-1}$, which is normalized to the recovered density of Fornax at R_e.

30 per cent. For prolate systems, this is consistent with the variation of line-of-sight velocity dispersion when viewing along the 3 principal axes.

The picture is somewhat different for SIDM dwarfs, where the mass profiles are overestimated more significantly when viewed along the intermediate axes. We note that this sample contains only 3 dwarfs and their 3 projections. We found that two of these have dark substructure present within their halos, resulting in inflated velocity dispersion along the intermediate axis of these dwarfs.

We have also considered the effects of dark matter halo asphericity. We found that the shapes of dark matter haloes are typically consistent with the stellar component, apart from a number of dwarfs with aspherical stellar distributions, for which the dark matter component was generally *less aspherical* than the stars. We conclude that the systematics are driven by the asphericity of the stellar component.

4.3.7.2 The core-cusp problem in Fornax

Results presented in Read et al. (2019) suggest that Fornax may have an inner core, based on the low inferred dark matter density and the inner slope, $\gamma_0 = 0.3^{+0.28}_{-0.21}$, below $0.25R_e$ (and see also Goerdt et al. 2006, Cole et al. 2012 and Pascale et al. 2019). Earlier, we have established that, for aspherical stellar distributions, line-of-sight effects may bias the recovered mass and density profiles. What do these results mean for the Fornax dwarf galaxy?

Fornax has a measured on-the-sky ellipticity $e \simeq 0.3$, matched by only a few satellites in our sample. We therefore focus instead on a sample of 24 isolated, dispersion-supported dwarfs from the APOSTLE simulations in CDM. For consistency with Fornax, these dwarfs were chosen to have an ellipticity $e \sim 0.3$ when viewed along at least one of their principal axes. Otherwise, we marginalize over various shapes of the stellar and dark matter components. The axis ratios for these galaxies can be seen on the right panel of Fig. 4.1 (grey triangles).

Fig. 4.12 shows the bias in density profiles recovered with GravSphere for dwarfs viewed along the minor, intermediate and major axes (and $e \sim 0.3$ in each case). The results are shown for radii between $0.1R_e$ and R_e, a key region where core formation would be apparent. Note that we have now gone below 2.8ϵ (grey dotted line), close to the softening length of our simulations. We must be wary of the discreteness noise contribution to the scatter at these radii. The purple bands show the 68 and 95 per cent confidence levels of the Fornax density profile recovered with GravSphere (Read et al., 2019), divided by the profile in Equation 4.11, with ρ_0 equal to the density recovered by GravSphere for Fornax at R_e.

It is important to point out that, due to the mass resolution in APOSTLE, the innermost regions of our simulated dwarfs are insufficiently sampled as compared to the real Fornax data, which results in systematically larger errors in the recovered density profiles. Indeed, the typical span of the 68 per cent confidence intervals below $0.25R_e$ in Fig. 4.2 is 0.5-0.6 in $\log_{10}\rho$, while for Fornax it is below 0.4, with the size of the errors being approximately the same for simulations and Fornax above 2.8ϵ. In order to compensate partially for this, in Fig. 4.12 we scale the errors for each dwarf by the ratio between the fractional errors (the span of the 68 per cent confidence intervals divided by the median) in a given APOSTLE dwarf and Fornax. This scaling, however, is not able to alleviate the large growth in uncertainty below $R = 2.8\epsilon$ for the mock data. Tackling this will require higher resolution simulations that are beyond the scope of this work.

A particularly striking result in Fig. 4.12 is that, above $0.1R_e$, the inferred density distribution in Fornax appears to be consistent within its 95 per cent confidence intervals with a cuspy dark matter halo viewed along any of the three principal axes. However, Read et al. (2019) disfavour this interpretation – at least in the context of a ΛCDM cosmology. This is because it requires an uncomfortably low pre-infall halo mass* for Fornax ($M_{200} \simeq 5 \times 10^9\,\mathrm{M}_\odot$) as compared to expectations from abundance matching ($M_{200} \simeq 2 \times 10^{10}\,\mathrm{M}_\odot$; Read and Erkal 2019). It also requires a smaller halo concentration than is characteristic of such a halo mass in ΛCDM (Dutton and Macciò, 2014). It remains to be seen whether a cuspy Fornax in a low pre-infall mass and concentration halo can self-consistently explain the relatively low density of Fornax in the context of ΛCDM

---

*M_{200} is the enclosed mass at r_{200}, the radius which encloses 200 times the critical density of the Universe.

cosmology. We will revisit this in the next chapter, but note it here as a potential caveat to the conclusion of Read et al. (2019) that favours a core in Fornax in a more massive pre-infall halo.

Finally, Fig. 4.12 shows that the bias in GravSphere tends to remain fairly constant below the half-light radius. This is an encouraging result, since, in the context of the core-cusp problem, we must be particularly wary of any radially-dependent systematics. If higher-resolution simulations find similarly little radial dependence in the systematic errors down to $0.25R_e$ and below, then this would suggest that the dominant source of uncertainty, at present, in estimating the inner dark matter density profile of the Fornax dwarf lies in the random sampling error (i.e. the number of stars with kinematic data), rather than the systematic error due to asphericity and the projection of Fornax on the sky.

4.3.7.3 The effect of tides

Dwarfs in our sample were selected to be satellites and these are susceptible to tidal stripping by their host galaxy. In this section, we explore whether the mass profiles recovered by GravSphere could be affected by tides.

In the top panel of Fig. 4.13 we plot the pericentre of the satellite orbits as a function of the dark matter mass lost since infall. We find the pericentres by interpolating the position of each dwarf with respect to its host with a cubic spline. This method may underestimate the pericentres (see Richings et al. 2020); however, for all of our dwarfs, we see little difference between pericentres found through the linear and cubic splines. Moreover, the majority of the dwarfs have infall times of ~8 Gyr, such that typically 2-3 orbital periods are available for pericentre calculation, with snapshots having shorter temporal spacings at early times. We define the infall time as the snapshot at which the subhalo has its maximum dark matter mass. As expected, dwarfs with smaller pericentres tend to lose larger fractions of their mass.

In the bottom panel of Fig. 4.13 we show anisotropy gradients as a function of lost dark matter mass. We measure the anisotropy gradients between two points: the mean stellar

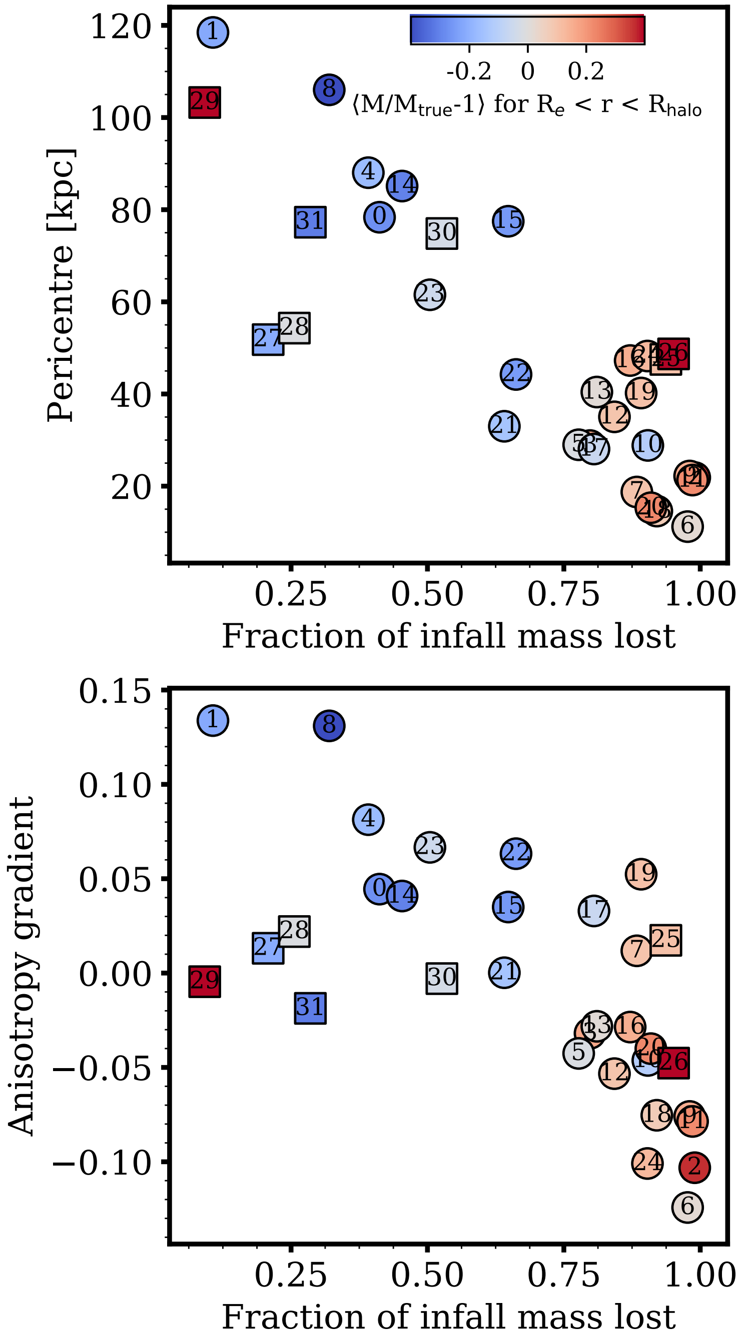

Figure 4.13: *Top:* the pericentre of the dwarf galaxy orbit as a function of the fraction of dark matter mass that has been lost since infall. The points are coloured by the mean bias of the recovered mass profile above the half-light radius and below the spatial extent of the dark matter halo. This is averaged for the three principal axes. Red indicates overestimation and blue indicates underestimation. Circles represent CDM dwarfs and squares the SIDM dwarfs. *Bottom:* the radial change in anisotropy, quantified by an anisotropy gradient measured below and above the half-light radius, as a function of the fraction of dark matter mass lost through stripping.

particle radii below and above the projected half-light radius. A clear trend is evident, whereby tides cause more tangential anisotropy in the outer parts of galaxies. This is due to the preferential stripping of the stars moving on radial orbits (Henon, 1970; Keenan and Innanen, 1975; Kravtsov et al., 2004; Read et al., 2006; D'Onghia et al., 2010b). We note the apparent simplicity of the two relations in Fig. 4.13, excluding perhaps the SIDM dwarfs whose orbits are more isotropic and the anisotropy is approximately constant.

We colour the points in Fig. 4.13 by the mean bias, $\langle M/M_{\rm true} - 1\rangle$, measured for all radii outside R_e and below the spatial extent of the halo. This is averaged for the three lines of sight along the principal axes of the dwarfs. We note that the bias is dominated by the line of sight closest to that which points from the centre of the host galaxy to the dwarf. This is indeed where we expect to see the largest effects on mass modelling due to the ongoing process of tidal stripping (Klimentowski et al., 2007).

It can be seen in Fig. 4.13 that for dwarfs that have undergone stronger tidal effects the mass profile is overestimated. This is unsurprising given that tides will result in the steepening of the outer slope (Peñarrubia et al., 2009), beyond the $0 < \gamma_j < 3$ permitted by our priors. Note for example, the increased accuracy in the outer mass profile when using the Zhao (1996) dark matter parmetrization (Fig. 4.5), where such steep slopes are allowed. An exception from this trend is SIDM Galaxy 29, where the mass profile is overestimated in the outer parts, yet tidal effects seem to be less significant. Nonetheless, the steepening of the density profile of this dwarf beyond $\gamma = 3$ is evident in Fig. 4.2.

We note the average underestimation of the outer mass profiles in dwarfs with weaker tidal effects. It is unclear how significant this result is, given that a number of these dwarfs (Galaxies 0,1,8,23) are amongst the more aspherical objects in our sample and thus are subject to other sources of bias.

Most importantly, we point out that we found no significant trend for the accuracy of the enclosed mass profile below R_e in our sample of dwarfs with tidal effects. This suggests that Jeans analysis is a valid method of mass modelling for dwarfs susceptible to tidal interactions, provided the impact of stars that are in the process of being tidally stripped is minimized. Here we achieve this by limiting our sample of stellar particles to those within $2R_{2D}$, as well as only using the stellar particles considered as 'bound' by the subhalo finder by definition. The study of the performance of GravSphere on a realistically contaminated sample of stars is certainly warranted and has been addressed, with a smaller sample of galaxies, by Read and Steger (2017).

4.3.8 Identifying failing models

Is it possible to identify the cases where GravSphere produces a biased result? In Read and Steger (2017), it was shown that for triaxial haloes it is possible to tell that the model has been unsuccessful through the value of the χ^2. Is this true for our sample of dwarfs?

In Fig. 4.14 we display the mean number of standard deviations to the true mass profile from the profile recovered by GravSphere, computed within the half-light radius of each dwarf, as a function of the total normalized χ^2 value (i.e. we divide the χ^2 for the surface density profile and the line-of-sight velocity dispersion profile by the total number of photometric and kinematic bins, respectively). The points are coloured by the number of standard deviations from the 'truth', with red indicating an overestimate and blue indicating an underestimate. The grey shaded regions, highlighting the 1σ and 2σ intervals form the true mass profile, are labelled by the fraction of our galaxies falling within there regions. We thus confirm that in just under 60 per cent of the dwarfs in our sample, GravSphere returns the true mass profile within 1σ and in just under 90 per cent within 2σ, with the worst results encountered for SIDM dwarfs and the most aspherical objects in our sample.

Strictly speaking, we would expect to classify models with $\chi^2 > 4$ as poor fits. Indeed, we see that for the values of $\chi^2 \gtrsim 3.5$ (black dashed line) a stronger bias is observed. In general, there is a significant scatter in the quality of results for dwarfs with $\chi^2 \gtrsim 3.5$. Among these galaxies, we see the particularly aspherical dwarfs and some SIDM galaxies (which are biased towards cusps), but not all. Evidently, this cut in χ^2 may be used for the selection of models that are more likely to be unbiased, such that the scatter in the accuracy of mass profiles returned by GravSphere is minimized.

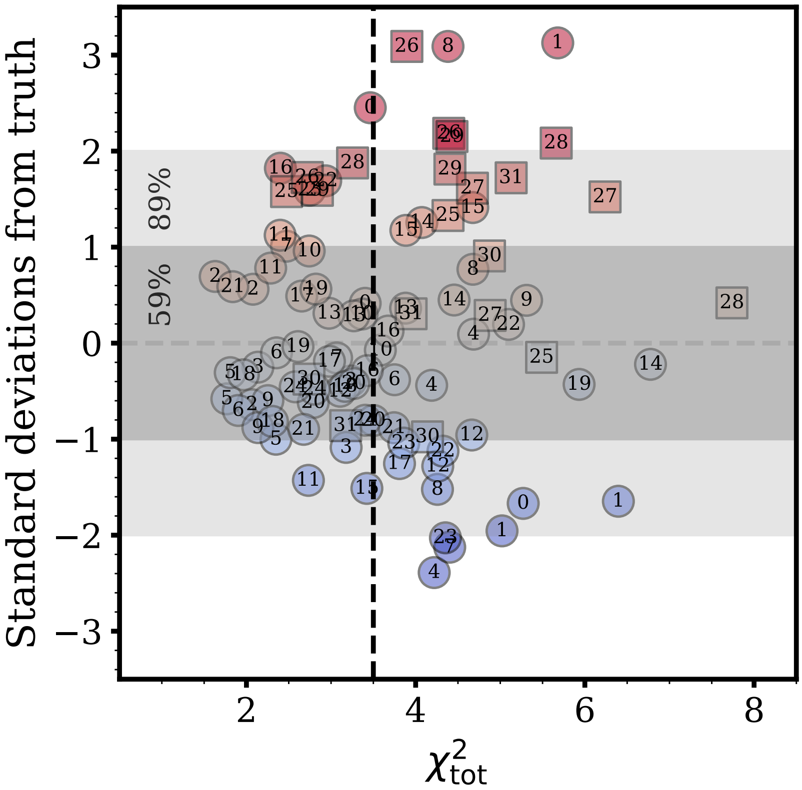

Figure 4.14: Number of standard deviations between the GravSphere result and the true mass profile, computed below the half-light radius and above 2.8ϵ, as a function of the total, reduced χ^2. CDM dwarfs are shown with circles and SIDM dwarfs with squares. Red highlights an overestimation of true mass and blue an underestimation (y-axis values). The grey dashed line indicates unbiased results. The black dashed line shows our suggestion for a 'cut' in χ^2 to separate 'successful' and likely biased models. The shaded regions display the 1σ and 2σ regions and are labelled by the percentage of our sample, where the true mass profile is contained within these regions.

4.4 Conclusions

Dwarf spheroidals are some of the best objects in which to study dark matter due to their proximity and high mass-to-light ratios. With the increasing availability of high-quality spectroscopic, photometric and proper motion data, studies of mass modelling methods and their limitations using realistic N-body simulations are certainly becoming more important in our efforts to narrow down the identity of dark matter and its behaviour on small scales. Here we presented such a study for GravSphere, a higher-order non-parametric Jeans analysis method (Read and Steger, 2017).

First, we selected a sample of 32 dwarf galaxies from a suite of cosmological hydrodynamic simulations in ΛCDM and SIDM cosmologies. These simulated galaxies were chosen to resemble classical Local Group dwarfs like Fornax. We then applied GravSphere, with its standard set of priors, to each of these dwarfs. We present the following findings:

- Within the key region inside the projected half-light radius, where dark matter cores form in some simulations (Navarro et al., 1996a; Tollet et al., 2016; Fitts et al., 2017; Oñorbe et al., 2015; Read et al., 2016; Pontzen and Governato, 2012; Benítez-Llambay et al., 2019), the enclosed mass distributions are recovered within the 68 per cent confidence limits for ~60 per cent of the dwarfs in our sample and within the 95 per cent confidence limits for ~ 90 per cent of the dwarfs.
- For our sample of CDM dwarfs, GravSphere returns unbiased mass profiles (RMS = 0.05) along the radial range of (0.4-3)R_e, but with ~ 50 per cent scatter in the innermost regions and ~ 25 per cent scatter at the projected and deprojected half-light radii; this is comparable to standard mass estimators (see Fig. 4.3). In comparison to other Jeans methods, GravSphere achieves a more consistent performance across the radial range considered and, typically, has smaller scatter in the recovered mass profiles (see Figs. 4.5,4.6,4.7,4.8).
- The density profiles for our CDM sample recovered by GravSphere are also accurate to better than 10 per cent (RMS = 0.07) and exhibit a scatter of 30 per cent (see Fig. 4.4). Within the 68 per cent confidence levels, this is sufficient to reject cores that form on the scale of the half-light radius (when, in reality, there is a cusp). Due to the spatial and mass resolution of our simulations, we were only able to test GravSphere in regions outside 380 pc; however, if the uncertainty in the density profile does not increase for regions near 100 pc, it should be possible to separate core and cusp-like densities for Fornax-like dwarfs that have undergone complete core formation on the scale of the half-light radius, as described in Read et al. (2016), provided the central density has not been reduced by tides and the pre-infall halo mass is well constrained.

- For the sample of SIDM dwarfs with interaction cross-section of $\langle \sigma/m \rangle = 10\,\mathrm{cm}^2\mathrm{g}^{-1}$, which have cores on the scale of the half-light radius, we find that GravSphere is biased towards cuspy models. The density is overestimated by $\sim$ 20 per cent in the central regions. We show that this bias is relieved when imposing the correct form of anisotropy ($\beta = \beta_0$), suggesting that the data are not sufficiently constraining to break the $M - \beta$ degeneracy for these dwarfs (see Fig. 4.7). Moreover, our priors do not allow a full exploration of parameter space when there is a core in the central density distribution. Widening the priors to allow 'holes' in central regions leads GravSphere to a reduction in the bias for the SIDM sample (see Fig. 4.9), although at the expense of slightly biasing the CDM sample towards cores, with a 10 per cent underestimation in the inner regions.

- We explored the benefits gained by having larger stellar samples for our dwarfs (see Fig. 4.10). We found that using all available stellar particles within $2\mathrm{R}_e$ mildly improves the accuracy of the mass profiles and reduces the scatter by $\sim$ 15 per cent for the CDM sample and $\sim$ 5 per cent for the SIDM sample (where we are limited in the number of available stellar particles due to mass resolution).

- Our simulations suggest that Fornax-like dwarfs may have anisotropy profiles consistent with a constant value, $\beta = \beta_0$. In fact, for dwarfs in CDM, assuming a constant β and no VSPs results in a similar bias and scatter in the inner regions as GravSphere (with an increase in the size of the errors in the outer parts). For SIDM dwarfs, the assumption of constant β significantly reduces the bias and scatter at small radii compared to GravSphere, without the need to change the priors on the dark matter density slopes to allow for more models with cores (see Fig. 4.7).

We have explored the reasons for the scatter in GravSphere's performance. We found the following:

- The scatter in the accuracy of the recovered mass profiles is largest for objects that are particularly aspherical (see top panel of Fig. 4.11). In our CDM sample of dwarfs with the minor-to-major axis ratio, $c/a \sim 0.7$, galaxies viewed along their intermediate axis typically have their masses recovered accurately (RMS = 0.05) compared to objects viewed along the minor axis (where the mass is underestimated by $\sim$ 30 per cent) or the major axis (where the mass is typically overestimated by $\sim$30 per cent). If Fornax has a sphericity of $c/a \simeq 0.7$ and is viewed along the intermediate axis, GravSphere is expected to accurately recover the mass (and the density) profile out to the half-light radius.

- We have explored the effect of tides on the performance of GravSphere. We found no significant effect on the recovery of the mass profiles below the half-light radius. However, we did find that the mass profiles of systems which are more significantly affected by tides are typically overestimated in the outer regions (see Fig. 4.13), primarily due to the imposed priors on the outer density slope. This suggests that Jeans analysis is still valid for systems affected by tidal interactions, provided the impact of stars in the outer regions, which could be in the process of becoming unbound, is minimized.
- We have investigated whether models which are biased (for example, due to the underlying asphericity of the system) manifest themselves through poorer fits to the data. We found that these models typically have a higher total value of the χ^2 (see Fig. 4.14). We suggest a $\chi^2_{\rm tot} = 3.5$ cut to weed out biased models and reduce the uncertainty in the recovered profiles.

In conclusion, GravSphere is certainly a promising method for modelling dark matter distributions in dwarf galaxies. It remains to be seen whether it can maintain its lack of bias in the innermost regions of dwarfs (below $R_e/2$), which would be possible with higher-resolution simulations. In this work, we focused on studying the effects of the violation of the assumptions of the spherical Jeans equation on GravSphere's performance. This study could, in the future, be extended with an inclusion of the effects of stellar binaries and contamination from the Galactic halo to provide a more realistic description of the expected systematics. This, together with modelling of multiple tracer populations and proper motions, has been explored on more idealized systems in Read and Steger (2017). We aim to extend this study with N-body and hydrodynamics simulations of realistic dwarf spheroidals in future work.

Chapter 5

Is the low dark matter density in Fornax a signature of a dark matter core?

5.1 Introduction

One particularly problematic galaxy, in terms of the core-cusp problem, is the Fornax dwarf spheroidal. Fornax is one of the brightest nearby dwarfs, allowing a collection of large quantities of spectroscopic and photometric data (Battaglia et al., 2006; Walker et al., 2009a; Letarte et al., 2010; del Pino et al., 2015; Kirby et al., 2010; Kirby et al., 2013). These data can be used to place a constraint on the gravitational potential of the dark matter. A number of studies using stellar kinematics have favoured cores in Fornax (Łokas, 2002; Walker and Peñarrubia, 2011; Amorisco et al., 2013; Pascale et al., 2018; Jardel and Gebhardt, 2012), however a cusp cannot be ruled out (Strigari et al., 2006; Richardson and Fairbairn, 2013b; Genina et al., 2018; Strigari et al., 2018). Some of the strongest evidence for a core in Fornax comes from the survival and present-day positions of its globular clusters (Goerdt et al., 2006; Cole et al., 2012; Orkney et al., 2019; Boldrini et al., 2018; Leung et al., 2020), while the works of Boldrini et al. (2019) and Meadows et al. (2020) show a cusp cannot be ruled out based on globular cluster survival arguments.

The possibility of a dark matter core in Fornax has encouraged solutions using alternative dark matter models (Spergel and Steinhardt, 2000; Hui et al., 2017; Lancaster et al., 2020; Elbert et al., 2015; Correa, 2020); however, a simpler explanation for a core in Fornax within the ΛCDM framework is that feedback from supernovae may be able to produce a core (Navarro et al., 1996a; Read and Gilmore, 2005; Pontzen and Governato, 2012; Read et al., 2016; Amorisco et al., 2014b). Core formation due to supernovae feedback has been predicted in some cosmological N-body simulations (Tollet et al., 2016; Fitts et al., 2017; Oñorbe et al., 2015), but not others (Fattahi et al., 2016b; Bose et al., 2019). An important distinction is the choice of 'subgrid' parameters, such as the density threshold for star formation (Benítez-Llambay et al., 2019), where simulations which employ higher thresholds allow the gas to dominate the gravitational potential and hence to drive core formation through outflows.

In a recent publication, using a higher-order Jeans analysis method GravSphere (the validity of which has been extensively tested in Read and Steger 2017 and in Chapter 4 of this thesis) on the stellar kinematic data in Fornax, Read et al. (2019) have shown that Fornax appears to have a particularly low dark matter density for its pre-infall halo mass. This low density was shown to be more compatible with a dark matter core. In fact, Read et al. (2019) have found that dwarfs which have undergone long periods of star formation, suggesting susceptibility to the effects of supernovae feedback, have 'core-like' inner densities. An important caveat to this method of solving the core-cusp problem in dwarf galaxies is that some dwarfs could have undergone tidal stripping and tidal shocks, which tend to lower the dark matter density (Read et al., 2006; Peñarrubia et al., 2009). Read et al. (2019) argue that the recent star formation in Fornax (de Boer et al., 2012) and its typically large pericentre inferred from proper motions (Walker et al., 2008; Gaia Collaboration et al., 2018; Fritz et al., 2018) suggest that Fornax is unlikely to have been subjected to significant tidal effects. Indeed, the observations of the stellar density profile of Fornax and N-body models of its orbit have so far disfavoured such interpretations (Walker et al., 2006; Battaglia et al., 2015; Wang et al., 2019b). On the other hand, comparisons with cosmological simulations favour a tidally stripped Fornax (Fattahi et al., 2016b), where the tails are faint and, likely, metal-poor (Wang et al., 2017). Simulations in CDM and binding energy arguments also favour an infall time for Fornax of $\sim$ 8 Gyr ago (Rocha et al., 2012; Wang et al., 2016; Fillingham et al., 2019), which suggests that Fornax has spent a long time under the influence of tides.

It is clear that the structural and kinematic properties of Fornax are becoming increasingly difficult to explain in a ΛCDM framework, unless tides have had strong influences on this galaxy. In this work, we test whether the inferred inner dark matter density in Fornax can be reproduced in cosmological N-body hydrodynamics simulations in ΛCDM, where dwarf galaxies do not form cores. In Section 5.2, we briefly describe our suite of simulations and we identify appropriate analogues of Fornax, given its dynamical mass, luminosity, star-formation history and the most recent orbital constraints from *Gaia*. In Section 5.3 we analyse the formation paths of the Fornax analogues and compare their inner densities to that inferred for Fornax. In Section 5.4 we conclude.

5.2 Methods

As in the previous chapters, we use the APOSTLE suite simulations of Local Group-like environments (Fattahi et al., 2016a; Sawala et al., 2016). In order to identify bound substructures, we employ the HBT+ algorithm of Han et al. (2018). HBT+ makes it particularly straightforward to track haloes across time by assigning each halo a unique 'TrackID'.

Our aim is to investigate mass loss in simulated dwarfs similar to Fornax. The dwarfs analogues are required to match Fornax in the following criteria: *i)* an orbit that is compatible with the *Gaia* data; *ii)* halo mass and luminosity; *iii)* star formation history. In the following, we outline the methods behind our sample selection.

5.2.1 Proper motions and orbit integration

As a first step, we select satellite dwarfs from our simulations. We define these as the galaxies that are presently within 300 kpc of either the Milky Way or Andromeda analogues

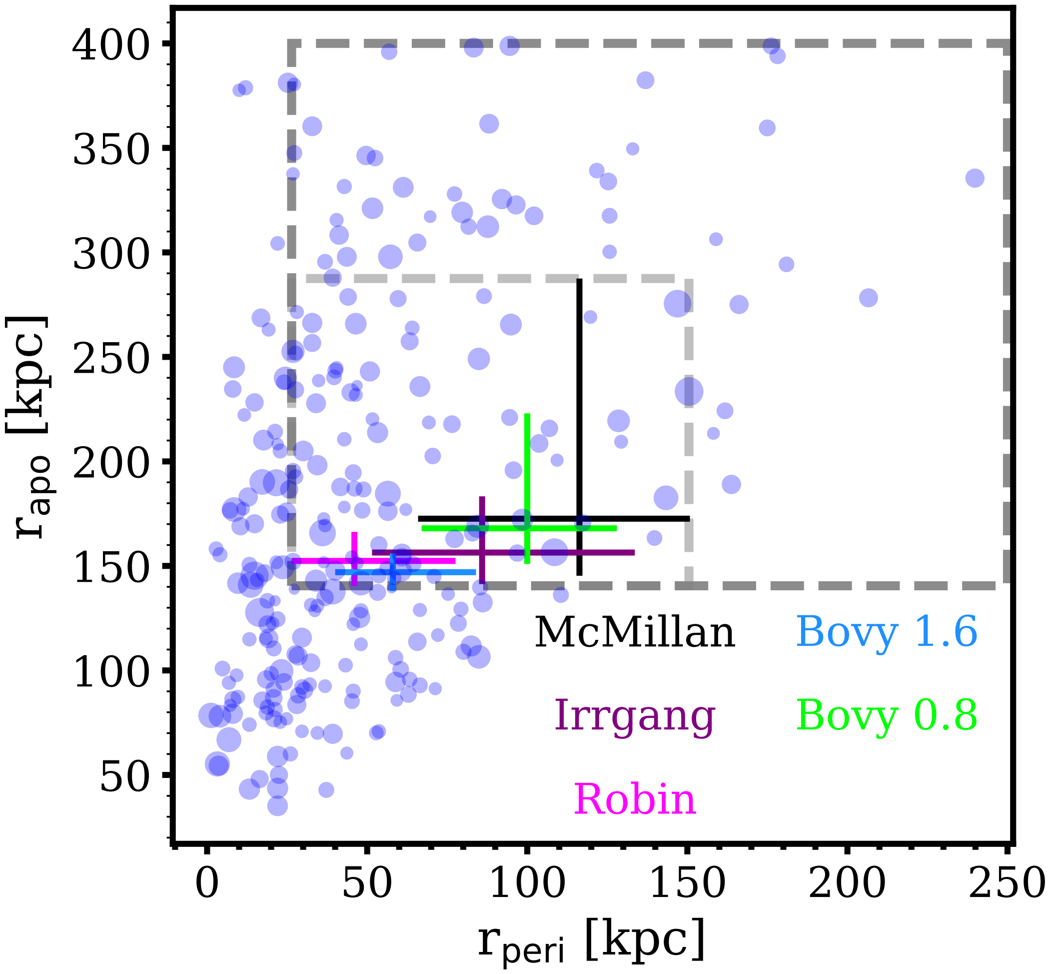

Figure 5.1: The inferred apocentres and pericentres in all dwarfs within APOSTLE volumes, which are currently located within 300 kpc of the Milky Way analogues. The area of each point is proportional to the logarithm of the stellar mass of the corresponding dwarf. The labelled error bars mark constraints from various potentials described in Gaia Collaboration et al. (2018) and Fritz et al. (2018). The light grey box shows the selection of our sample of Fornax-like orbits and the dark grey box shows a wider selection of dwarfs that have even larger apocentres than those predicted for Fornax.

in APOSTLE. Next, we approximate the potential of each host galaxy as spherically symmetric. The potential of known spherically-symmetric mass distribution is given by (Mo et al., 2010):

$$\Phi(r) = -G \int_r^\infty dr' \frac{M(< r')}{r'^2}. \tag{5.1}$$

We compute the potential out to the radius of 400 kpc, where we fix $\Phi(400\ \mathrm{kpc}) = 0$.

For each dwarf, we compute the total energy, E, and the angular momentum, L. Then, for the orbital extremes, where the velocity $\dot{r} = 0$, we have that

$$\dot{r}^2 = 2[E - \Phi(r)] - \frac{L^2}{r^2} = 0. \tag{5.2}$$

The solutions of the above equation correspond to the apocenter, r_{apo}, and the pericenter, r_{peri}, of the orbit (Binney and Tremaine, 1987). We verify that the approximation of the potential as spherically symmetric is a valid one in Appendix H.

In Fig. 5.1 we show the distribution of orbital pericentres and apocentres for all satellite dwarfs with $M_* > 10^5\ \mathrm{M}_\odot$. The error bars of various colours represent constraints for Fornax using the three Milky Way models from Gaia Collaboration et al. (2018) and two Milky Way models from Fritz et al. (2018). The first three are the potentials from McMillan (2016), Irrgang et al. (2012) and Robin et al. (2003, 2012). The three potentials vary most significantly within $\sim$ 2 kpc and outside $\sim$ 40 kpc. *Bovy 1.6* and *Bovy 0.8* are two realizations of the potential from Bovy (2015) with M_{200} of $1.6 \times 10^{12} M_\odot$ and $0.8 \times 10^{12} M_\odot$, respectively. In our sample, we include all orbits contained within the error bars of these models. This is shown with a light grey box in Fig. 5.1. Additionally, we include dwarfs with larger peri- and apo-centres, as we wish to investigate mass loss in these seemingly ‘benign’ orbits. This additional selection is highlighted with a dark grey box in Fig. 5.1.

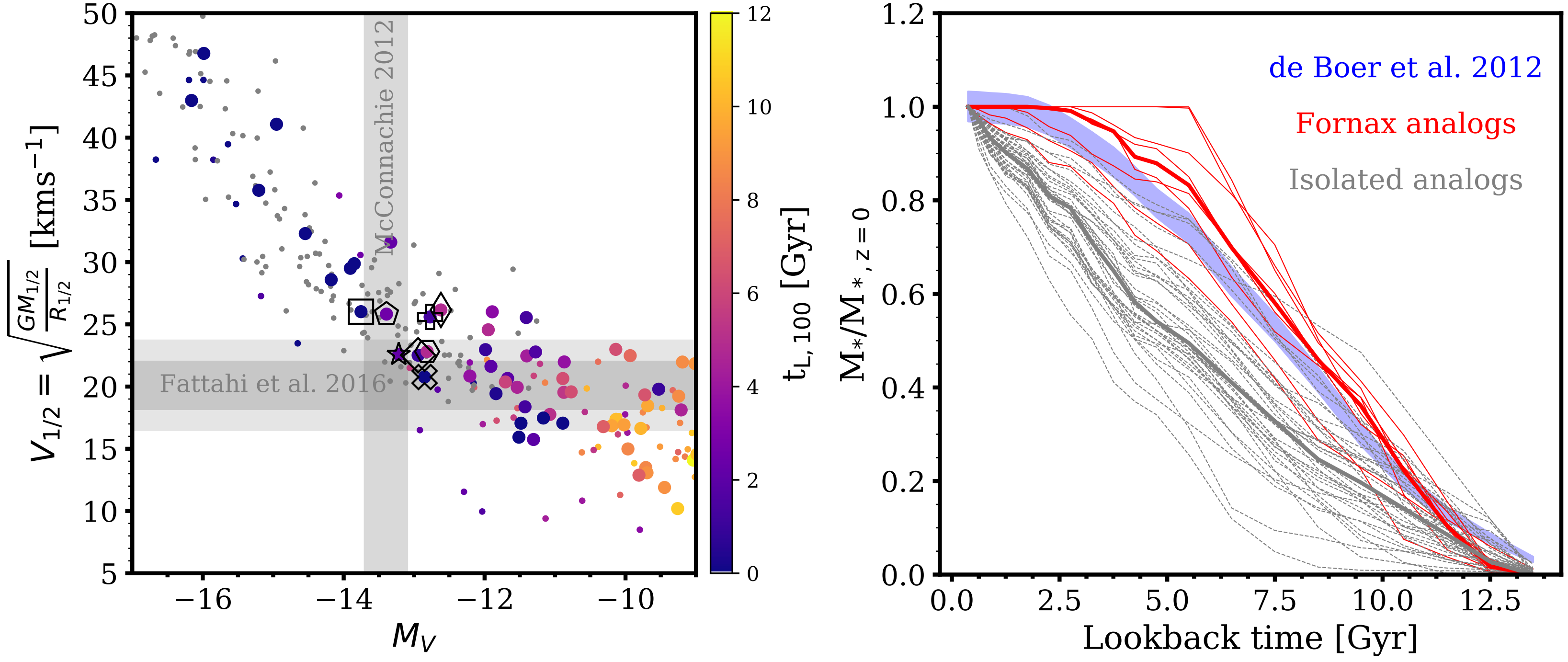

Figure 5.2: *Left:* the circular velocity at the 3D half-light radius, $V_{1/2}$, as a function of the absolute visible magnitude, M_V. The thick circles are dwarfs with orbits comparable to Fornax and thin dots are other satellite dwarfs. Grey dots are isolated dwarf galaxies. The sample of satellites is coloured by the lookback time when they form their last star, $t_{L,100}$. Symbols of various shapes mark our 8 best Fornax analogues. *Right:* the normalized star formation history of Fornax (blue band) from de Boer et al. (2012). The thin red lines show histories for our Fornax analogues and the thick red line is their median. The thin grey lines are histories of isolated dwarf galaxies and the thick grey line is their median.

5.2.2 $V_{1/2}$ - M_V relation

Now that the satellite galaxies with orbits similar to Fornax have been identified, we intend to select those objects which resemble Fornax in their present-day stellar and halo mass. Since neither of these two properties can be measured directly, we use the circular velocity at the half-light radius, $V_{1/2}$, and the absolute magnitude in visible light, M_V, as indicative quantities. $V_{1/2}$ is computed as $\sqrt{\frac{GM(<R_{1/2})}{R_{1/2}}}$, where $R_{1/2}$ is the half-light radius and G the gravitational constant. $M(< R_{1/2})$ is obtained by applying the mass estimator from Wolf et al. (2010) to obtain $M(< R_{1/2} \approx 4/3R_e) = 4G^{-1}\langle\sigma_{\rm los}\rangle^2 R_e$, where R_e is the projected half-light radius and $\langle\sigma_{\rm los}\rangle$ is the mean line-of-sight velocity dispersion. The accuracy of this mass estimator in APOSTLE dwarfs was investigated in Campbell et al. (2017). We obtain the visible magnitudes for the dwarfs following the method described in Section 2.2.3. For comparison with Fornax, we use the corresponding quantities from Fattahi et al. (2016b) and McConnachie (2012).

The values of $V_{1/2}$ and M_V for our sample of dwarfs are shown in the left panel of Fig. 5.2, where large coloured circles represent the galaxies contained within the dark grey box in Fig. 5.1, small circles are other satellite galaxies and grey dots are isolated dwarf galaxies. The satellite dwarfs are coloured by $t_{\rm L,100}$, the lookback time at which the last stellar particle was formed. It can be seen that above the M_V of Fornax, the majority of satellites are still star-forming today.

It is clear from the left panel of Fig. 5.2 that Fornax is, indeed, somewhat of an outlier in the APOSTLE $V_{1/2}$ - M_V relation. Nevertheless, we select a sample of 8 galaxies for further inspection. These are marked with different shapes in Fig. 5.2, which we will continue using in the remainder of this chapter. It can be seen that the ‘star’ dwarf is our best Fornax analogue. There is a larger number of isolated dwarfs that match these constraints for Fornax, however, as we shall see below, their star formation histories are incompatible with this dwarf.

5.2.3 Star formation histories

We would now like to ensure that our simulated analogues are indeed similar to Fornax in terms of their star formation history (SFH). We first obtain the SFH of Fornax from the work of de Boer et al. (2012). We bin the formation times of the stellar particles in APOSTLE into the same set of bins. The right panel of Fig. 5.2 shows the cumulative SFHs of these galaxies with lookback time, normalized by the present-day stellar mass. The solid red line is the median of the 8 simulated dwarf analogues. The blue shaded band is the result of de Boer et al. (2012).

Our simulated dwarfs, on average, exhibit a similar shape of the SFH to Fornax. There are two dwarfs that have stopped star formation $\sim$ 6 Gyr ago. This is clearly at odds with Fornax, which, at most, quenches $\sim$ 2 Gyr ago. In the next section, we will investigate whether quenching time is indicative of a dwarf's tidal history.

The thin grey lines on the right of Fig. 5.2 show the SFHs of isolated dwarfs and the thick grey line is their median. It is clear that these galaxies are still star-forming today and many have accelerated in star formation over the past 5 Gyr. This is incompatible with Fornax, which begins slowing down in star formation around that time. The SFH of Fornax is certainly more compatible with that of a dwarf currently within the virial radius of the Milky Way.

Now that our sample of dwarf galaxies has been selected we will proceed with our analysis and results.

5.3 Results

5.3.1 Does orbital pericentre reflect tidal history?

It has been argued in Read et al. (2019) that Fornax is unlikely to have undergone significant tidal stripping, given its relatively large pericentre and nearly circular orbit. These values, of course, depend on the potential chosen to model the Milky Way. Given the various

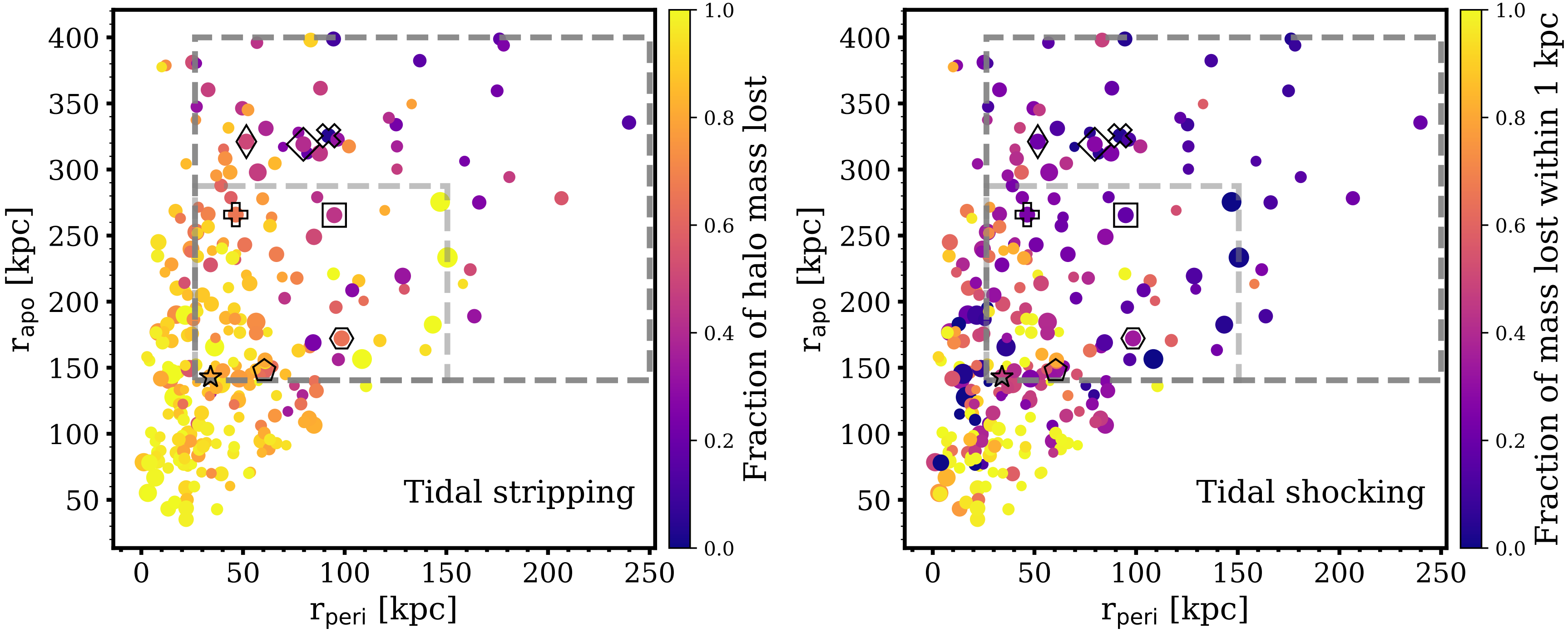

Figure 5.3: *Left:* the inferred apo- and peri-centres of simulated dwarfs, coloured by the fraction of mass lost from their dark matter haloes from the time these dwarfs had their maximum dark matter halo mass, indicative of tidal stripping. The area of the circles represents the logarithm of the stellar mass. The grey dashed boxes are as in Fig. 5.1. The symbols with various shapes mark our 8 best Fornax analogues. *Right:* as the figure on the left, but coloured by the mass lost in each dwarf within their central 1 kpc, indicative of tidal shocks.

pericentre values in different potentials from Gaia Collaboration et al. (2018) and Fritz et al. (2018), we examine whether this statement is accurate in our simulations. We note that the stellar mass of the Milky Way and Andromeda analogues in APOSTLE is *smaller* than what is inferred for the Milky Way, while the virial masses of the haloes, M_{200}, are in the range of literature values (Wang et al., 2020). Moreover, the stellar disk is less pronounced in APOSTLE (Sawala et al., 2017). This implies that, for a given orbit, the tidal effects are expected to be *less severe* in these simulated potentials than in the Milky Way.

We track each of the APOSTLE satellites back to the time when their dark matter halo mass reached its peak. In Fig. 5.3 we show the fraction of dark matter mass that has been lost since that time (left), indicative of tidal stripping, and the dark matter mass lost within 1 kpc from the centre of each dwarf, indicative of tidal shocks. It can be seen that the vast majority of dwarfs with pericentres below 50 kpc lose more than 80 per cent of their halo mass. Even dwarfs with pericentres of 150 kpc lose significant fractions of their mass. Dwarfs with large pericentres (> 150 kpc) and less eccentric orbits, on the other hand, lose very little.

Mass loss in the innermost 1 kpc appears to require more extreme conditions. Dwarfs with pericentres <50 kpc and apocentres <100 kpc tend to lose more than 80 per cent of the halo mass within 1 kpc. At larger peri- and apo-centres, dwarfs typically lose no more than 50 per cent. There are, however, some clear exceptions to the trend, where, curiously, a number of dwarfs with pericentres as large as 100 kpc can lose large fractions of their innermost dark matter mass.

The symbols, as in Fig. 5.2, show our Fornax analogues. We can see that all of these have pericentres below 100 kpc. Let us look at, for example, the ‘hexagon’ Fornax. This object is on a fairly non-eccentric orbit, with a pericentre of $\sim$ 100 kpc, and matches the constraints for Fornax rather well. Nevertheless, it loses $\sim$ 70 per cent of its halo mass and $\sim$ 40 per cent of the mass within 1 kpc. Clearly, even for non-eccentric obits with large pericentres, dwarfs can lose large fractions of dark matter and this occurrence is not infrequent. Within the light grey box, on the right panel of Fig. 5.3, 43 per cent of dwarfs lose more than 50 per cent of their dark matter mass within 1 kpc. We will return to the implications of this for the dark matter density of Fornax in Section 5.3.5.

5.3.2 Does recent quenching indicate recent infall?

We now consider whether the quenching time is a good indicator of the infall time of a dwarf galaxy and, consequently, whether it is an indicator of how much a given dwarf has been affected by tides.

On the left of Fig. 5.4, we show the quenching time of each dwarf, $t_{\mathrm{L},100}$, as a function of its infall time, $t_{\mathrm{L,infall}}$. We define the infall time as the time when the dwarf first crosses the virial radius of a Milky Way analogue. It can be seen that there is almost a one-to-one relation between the infall and the quenching time (i.e. many dwarfs quench immediately after infall). However, it can also be seen that a number of dwarf galaxies quench prior to infall and a number of them quench after infall. The area of the points in Fig. 5.4 is proportional to the logarithm of their present-day stellar mass. It is, thus, clear that there exists a population of low-mass dwarfs that quench prior to infall (because of reionization and feedback from star formation). In fact, it can be seen that the smallest dwarfs have very early quenching times ($\sim$ 12 Gyr) and as the mass increases, for a given $t_{\mathrm{L,infall}}$, the quenching is postponed. On the other hand, there exists a population of dwarfs that are generally more massive (closer to Fornax mass), where quenching occurs after infall (because of ram pressure stripping and tidal stripping of gas inside the host halo). Moreover, as discussed in Chapter 2, a number of dwarfs with large gas supplies are able to form more stars near the pericentre of their orbit. If gas remains after the first pericentre, another star formation burst may occur at the next pericentre. As such, it is clear that, for higher mass objects, the quenching time is not a good indicator of the infall time. Moreover, from the colour of the points (representing the fraction of mass lost within 1 kpc), it can be seen that a number of dwarfs which quench after infall also lose large fractions of their dark matter mass.

On the right of Fig. 5.4, we show the time at which the dwarf had its maximum dark matter

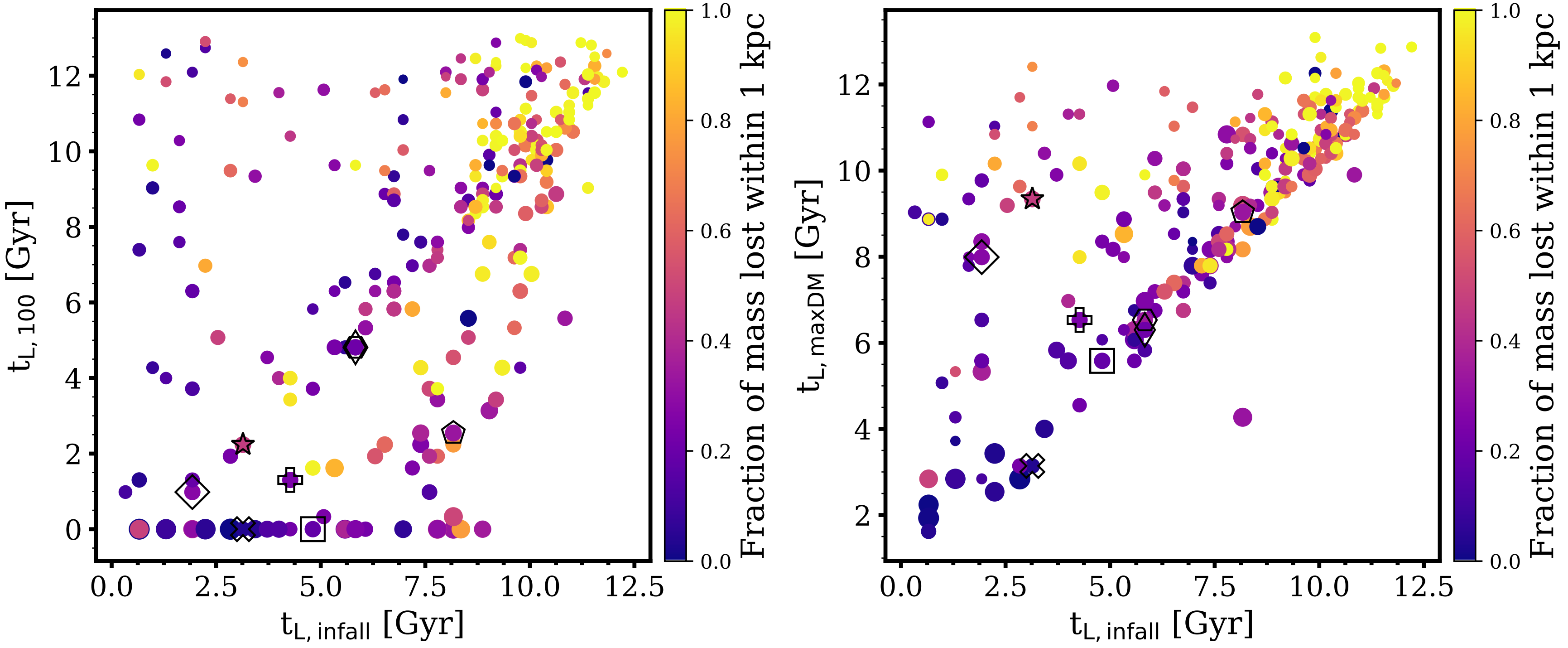

Figure 5.4: *Left:* the lookback time when each dwarf forms its last stellar particle, $t_{\mathrm{L},100}$, as a function of the lookback time when it first crosses the virial radius of the host halo, $t_{\mathrm{L,infall}}$. The points are coloured by the fraction of mass lost within 1 kpc. The area of the circles represents the logarithm of the stellar mass. *Right:* the lookback time when each dwarf had its maximum dark matter halo mass as a function of the infall time, $t_{\mathrm{L,infall}}$. The points are coloured by the mass lost within 1 kpc. In both plots, the various symbols mark the 8 best Fornax analogues.

mass, $t_{\mathrm{L,maxDM}}$ as a function of infall time, $t_{\mathrm{L,infall}}$. In principle, these quantities should correspond to the same value. Indeed, we see that for a large number of dwarfs the relation is nearly one-to-one. However, there also exists a population of dwarfs which start losing their mass long before infall. Among these objects are some of our best Fornax analogues, including the 'star' Fornax, which is a match in both $V_{1/2}$ and M_V. We find that among the population of dwarfs, with orbits compatible with Fornax (light grey box in Fig. 5.3), nearly 36 per cent have started losing mass more than 2 Gyr prior to infall. From the colours of these dwarfs, indicating mass loss within 1 kpc, it is clear that these objects can consequently lose up to $\sim 90-99$ per cent of their maximum halo mass, despite very recent infall times in some cases. We conclude that the infall time is not always an adequate indicator of a dwarf's tidal history.

5.3.3 The diverse formation histories of Fornax analogues

We now explore the various mechanisms that lead to the formation of our Fornax analogues. These are shown in Fig. 5.5, where the first four plots show the closest matches to Fornax in terms of $V_{1/2}$ and M_V and the last four plots show slightly more massive haloes with M_V compatible with Fornax. In the top subplots, the thick black line shows the distance to the host galaxy. The coloured lines show the orbits of dwarfs that at some point in time were the nearest more massive galaxy to our analogues. In the bottom subplots, we show the evolution of the dark matter, gas and stellar content. Note that for a number of dwarfs there is a steep rise in mass at early times ($\sim$ 11 Gyr). This is likely because HBT+ incorrectly identifies the main progenitor.

The majority of dwarfs follow a very similar formation history, where their dark matter haloes are built up early on and the dark matter is consequently lost after infall. Sudden drops in the dark matter content can be seen when the dwarfs approach their pericentres. Note, in particular, the 'hexagon' Fornax analogue. The pericentre here is 98 kpc; however, as the dwarf falls in $\sim$ 6 Gyr ago we observe a drop in the dark matter mass by a factor of 2. Around the same time, we can see that this dwarf is approached by a series of more massive haloes that come as close as 50 kpc. This accounts for the enhanced stripping in this dwarf.

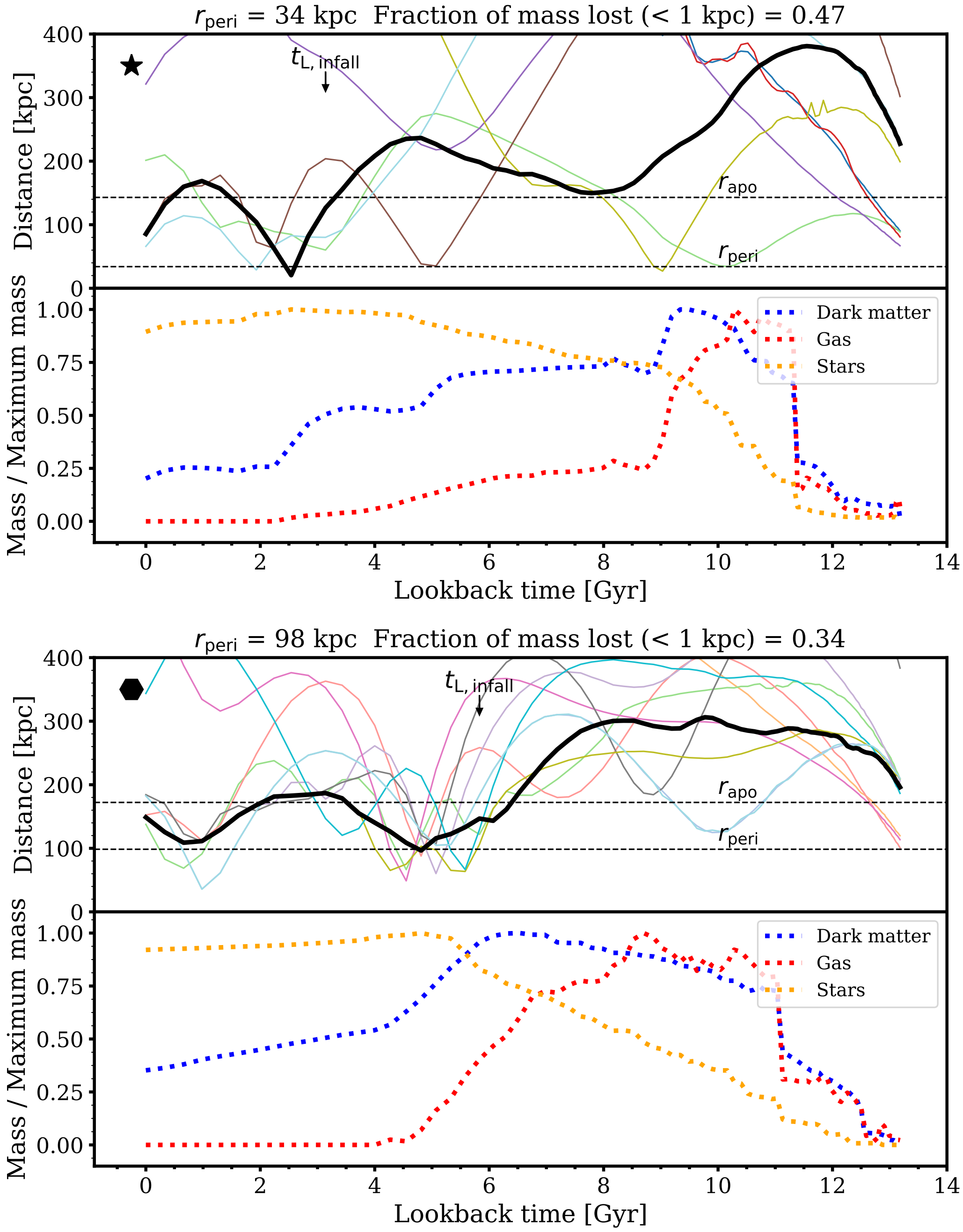

Figure 5.5: The individual formation and evolution histories of the 8 Fornax analogues. Each analogue is marked by a corresponding symbol that we use throughout this work. The top subplots show the distance to the host galaxy (thick solid line) as a function of lookback time. The inferred peri- and apo-centres are shown with thin dashed lines. Lines of different colours show distances to dwarf galaxies which at any one point were the nearest more massive galaxy than a given Fornax analogue. The black arrow marks the infall time of each dwarf. The title of the plot shows the inferred value of the orbital pericentre and the fraction of mass lost within 1 kpc. The bottom subplots show the bound dark matter (blue), gas (red) and stellar (yellow) masses, normalized by their historical maximum.

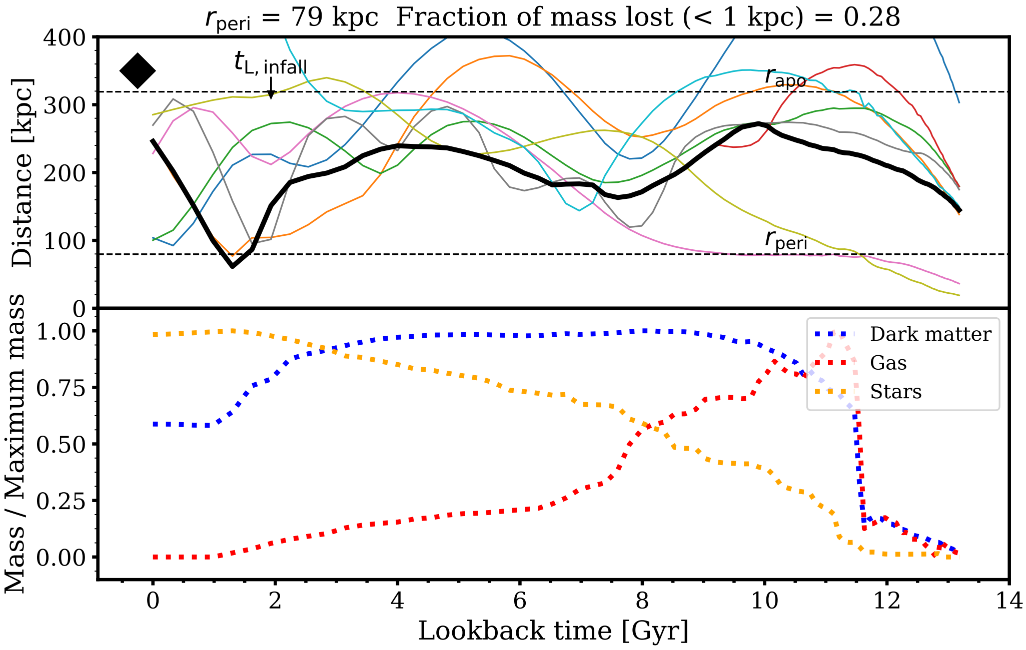

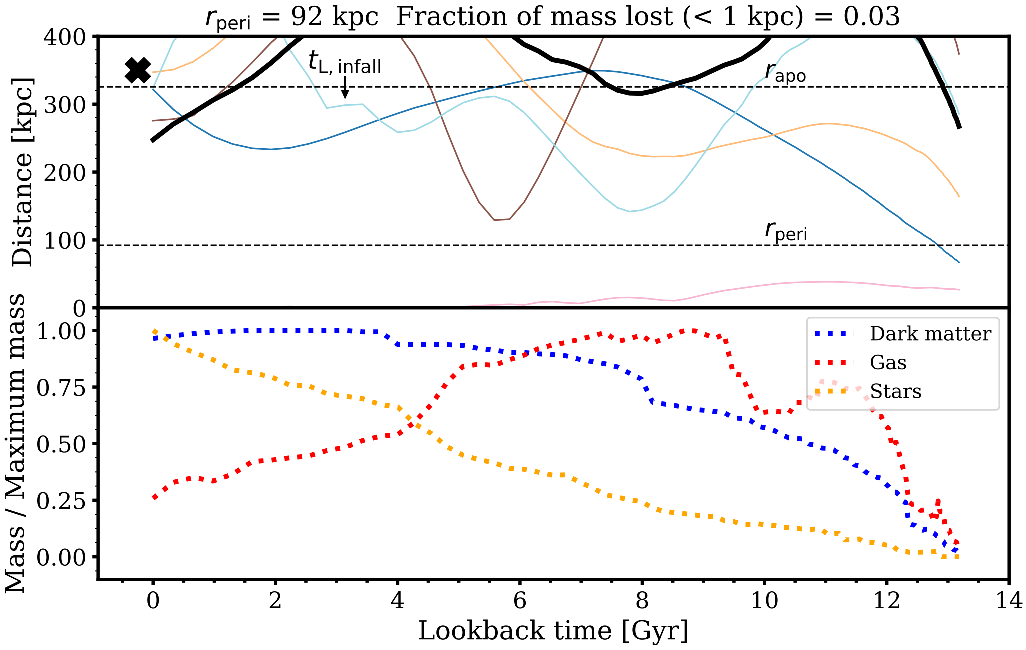

Figure 5.5: continued.

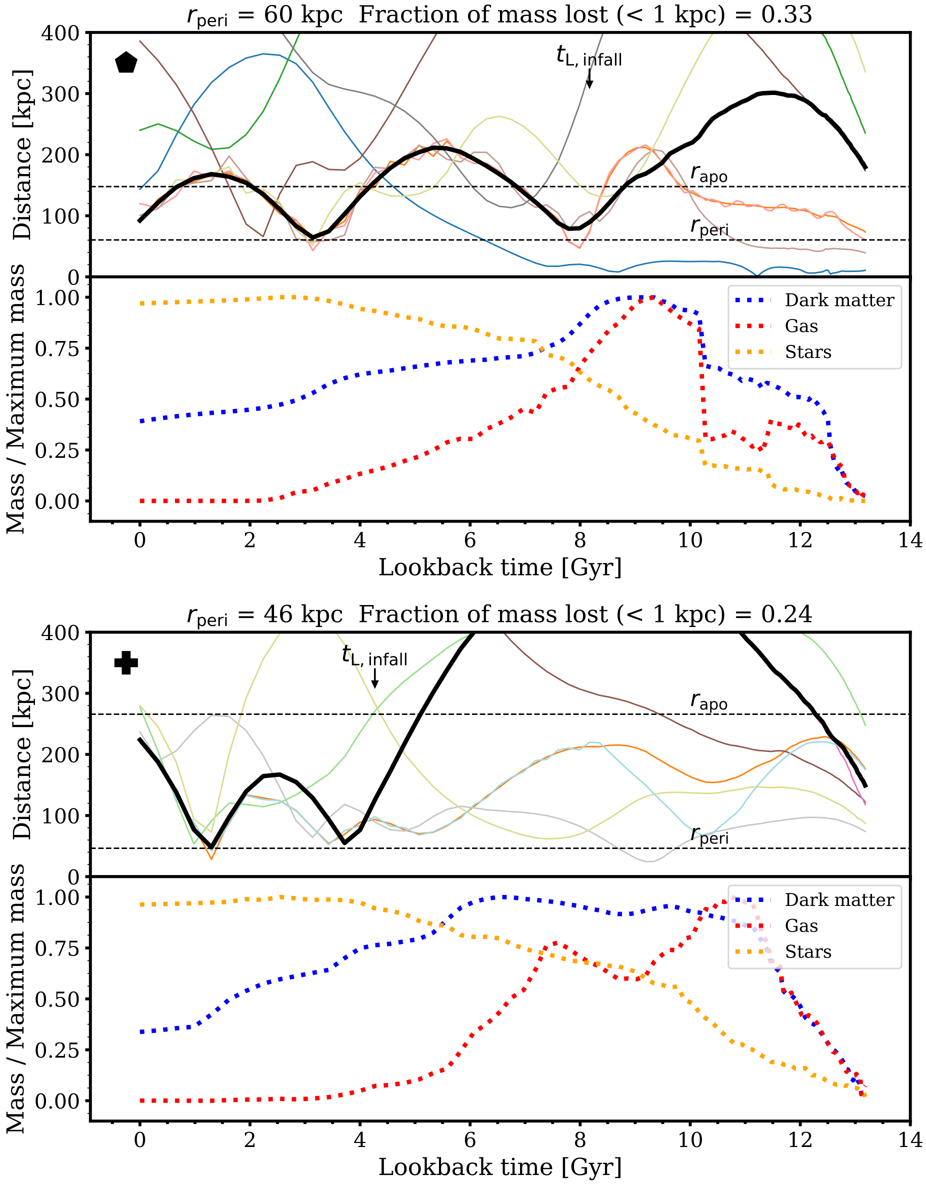

Figure 5.5: continued.

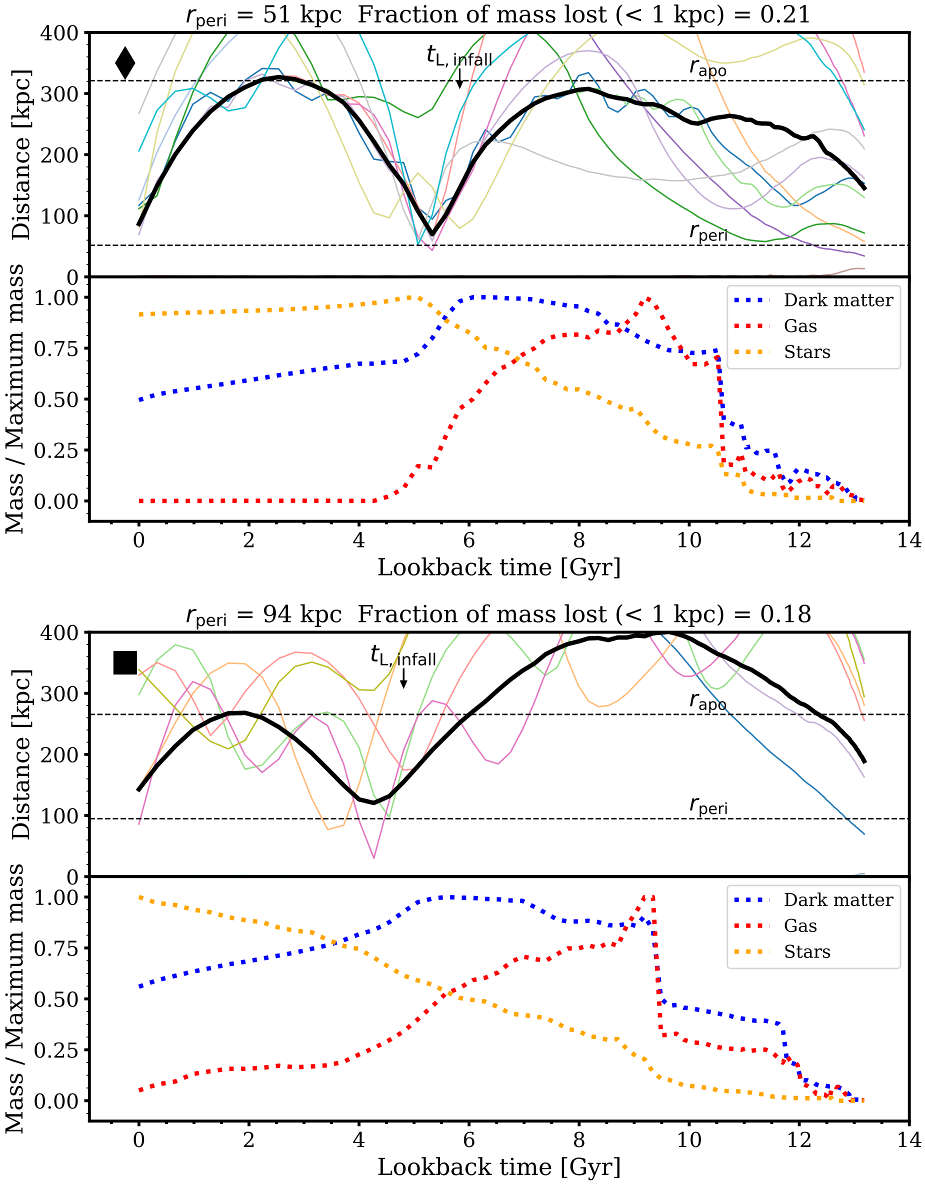

Figure 5.5: continued.

We see a similar, less severe, occurrence in the 'thin diamond' Fornax, where the galaxy loses ~40 per cent of its initial mass. Also note that at the first pericentre, $\sim$ 5 Gyr ago in these galaxies, there is a burst in star formation. This is consistent with one of the scenarios for the formation of two distinct metallicity populations described in Chapter 2. Neither of these galaxies is star-forming today, however, we also note that APOSTLE does not resolve the cold gas phase, which is more difficult to strip (Hausammann et al., 2019).

A very peculiar example is the 'star' Fornax, which is also our best analogue in terms of M_V and $V_{1/2}$. Although this dwarf fell in only $\sim$ 4 Gyr ago, it has been losing mass for nearly 9 Gyr. By redshift z=0, the dwarf has lost 80 per cent of the maximum mass it once had and 47 per cent of the mass within 1 kpc. This is because, on two separate occasions, the dwarf interacts with more massive dwarf fly-bys that each strip ~25 per cent of its initial mass. In this case, while the pericentre is indeed small (34 kpc), it is still not a good indicator of just how much mass the dwarf has really lost. We observe a similar, but less significant, occurrence in the 'plus' Fornax. Just before the first pericentre, this dwarf loses $\sim$ 20 per cent of its maximum mass as it interacts with a larger halo (orange and blue merged lines).

A complete outlier in terms of the formation history is the 'cross' Fornax. This dwarf only falls in $\sim$ 1 Gyr ago and has lost less than 10 per cent of its mass. Instead, this dwarf had undergone two minor mergers in the last 8 Gyr. This dwarf is slightly fainter than Fornax but has the same $\mathrm{V}_{1/2}$. Evidently, it started off as a very low mass halo that had built up to have a similar $V_{1/2}$ to Fornax. Tidal effects are clearly not important for this galaxy.

Finally, we see evidence of group infall in the 'pentagon' Fornax (blue line). While it does not seem to play a role in the tidal stripping of this dwarf, which can be seen to start occurring following infall, we note it here as a plausible mechanism of 'pre-processing' a satellite galaxy, prior to it crossing the virial radius of the host.

So far we have seen that, while the processes that lead to the formation of Fornax analogues are quite similar (mass loss at the pericentre), $\frac{2}{8}$ of our best Fornaxes have lost some dark matter mass prior to infall and $\frac{1}{8}$ came from a low mass halo that assembled through late minor mergers and never experienced significant mass loss.

5.3.4 The density profiles of tidally stripped Fornax analogues

Now that we have established that the majority of our Fornax analogues are able to lose dark matter mass within the inner 1 kpc due to tidal effects, we wish to compare their dark matter profiles to the one inferred for Fornax from its stellar kinematics in Read et al. (2019).

In the left panel of Fig. 5.6 we show the enclosed density profiles of our analogue Fornaxes at the time they had their maximum dark matter mass (blue) and today (black). It is clear that the inner density has reduced in these dwarfs. A number of present-day enclosed central densities appear compatible, within the 68-95$^{\text{th}}$ per cent confidence levels, with the result of Read et al. 2019 (green shaded bands); however, there is an important caveat. Approximately on the scale of $2.8\epsilon \approx 380$ pc, the dark matter profiles exhibit a softened central density and the profiles can only be "trusted" above this radius (i.e. the profiles will converge at these radii to a higher resolution simulation).

A more robust prediction for the convergence radius comes from the work of Power et al. (2003), who show that the profiles are converged at the radius where the collisional relaxation timescale is $t_{\text{relax}} \approx 0.6 t_0$, where t_0 is the age of the Universe. This corresponds to approximately 0.6 kpc for our dwarfs (black vertical lines in the left of Fig. 5.6). Fattahi et al. (2016b) have carried out a convergence study on the various resolution levels in APOSTLE. They propose a simple relation to 'correct' the enclosed mass profiles such that they converge to a higher-resolution volume. The correction is:

$$\ln\left(1 - \overline{\rho}/\overline{\rho}_{\text{conv}}\right) = -0.04(\ln\kappa)^2 - 0.5(\ln\kappa) - 1.05, \tag{5.3}$$

where $\overline{\rho}$ is the enclosed density, $\overline{\rho}_{\text{conv}}$ is the converged enclosed density and $\kappa = 0.6$.

This formula was designed to correct lower-resolution APOSTLE volumes to the highest-resolution one (which we use here). In this work, we apply this formula to the dwarfs in

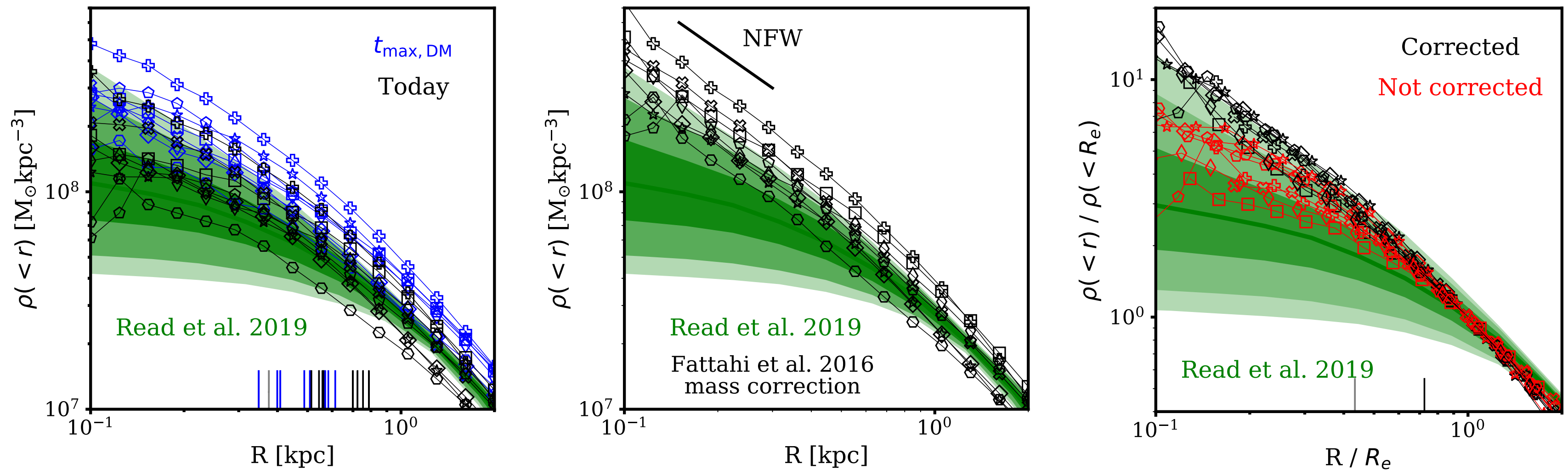

Figure 5.6: *Left:* the enclosed dark matter density profiles of our Fornax analogues, marked with their respective symbols, at the time they had their maximum dark matter mass (blue) and today (black). The green shaded bands are the 1,2 and 3σ intervals for Fornax from Read et al. (2019). The grey vertical line marks $2.8\epsilon = 380$ pc. The black and blue vertical lines mark the locations of the Power et al. (2003) radius for each dwarf today and at the time of maximum halo mass, respectively. *Middle:* the enclosed density profiles for our Fornax analogues today, obtained through applying the mass correction from Fattahi et al. (2016b). The thick black line shows a slope expected from an NFW profile. *Right:* the enclosed density profiles, normalized by their value at the half-light radius, R_e, shown for each factor of R_e. Black shows the analogue dwarfs, where the mass correction from Fattahi et al. (2016b) has been applied and red shows the profiles with no mass correction. The grey vertical line marks the mean location of 2.8ϵ and the black vertical line marks the mean location of the Power et al. (2003) radius.

the highest-resolution volume to extrapolate the density profile in the innermost regions such that we can make a more straightforward comparison with Fornax. The results of this can be seen in the middle panel of Fig. 5.6, where the profiles have now acquired their expected NFW form (as illustrated in that figure). We will continue to use this correction in the remainder of this chapter. While we do not claim that this recovers the enclosed density of equivalent dwarfs from a much higher resolution simulation, it is known that subhaloes maintain their NFW shape in higher-resolution dark-matter-only N-body simulations (Springel et al., 2008b; Navarro et al., 2009; Errani and Peñarrubia, 2020). As our analysis is sensitive to the densities in the inner regions, we shall use the correction as an *approximation* of the true enclosed density, motivated by the fact that the correction recovers the expected NFW form.

From the middle panel of Fig. 5.6, it is clear that only a few density profiles remain compatible with the result of Read et al. (2019). A problematic aspect of the comparison is that the profiles have a slight scatter in their normalization. In order to more effectively compare the *shapes* of the profiles, we normalize them by the enclosed density at the half-light radius, $R_e \approx (3/4)R_{1/2}$. The result of this can be seen in the right panel of Fig. 5.6. The red lines show normalized profiles obtained directly from the simulations and black lines show the profiles 'corrected' with Equation 5.3. It can be seen that the profiles with a softened central density, similar to a core of $\sim$ 400 pc, are consistent with the result of Read et al. (2019) within 1-2σ, while the "corrected" NFW-like profiles are only consistent within 3σ.

It is clear from Fig. 5.6 that central dark matter densities, which are compatible with Fornax, can be obtained through the effects of tidal stripping; however, the density profile *shapes* of stripped NFW haloes are less compatible with Fornax than haloes which have shallow cusps or small cores in the central regions.

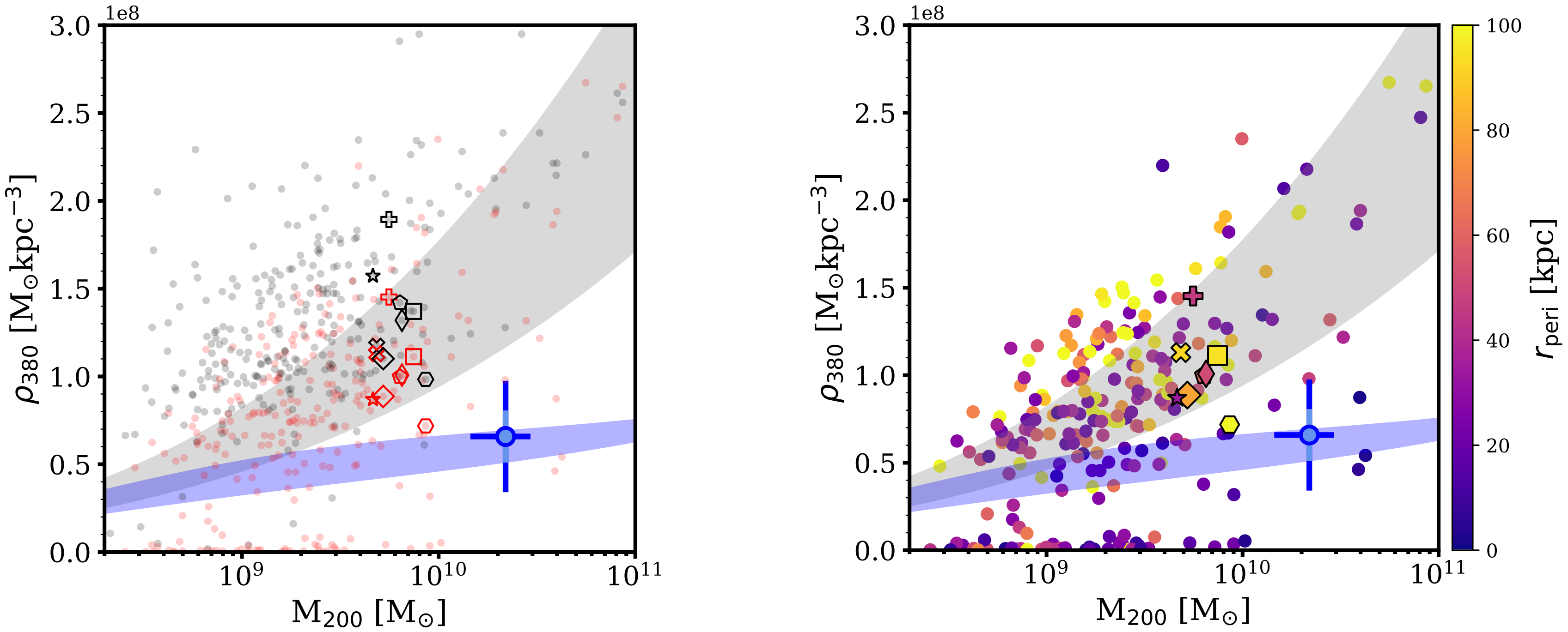

Figure 5.7: *Left:* the enclosed density below 380 pc, ρ_{380}, as a function of all-time maximum virial mass, M_{200} of each satellite dwarf. The black dots show the densities at the time of maximum M_{200} and red shows the densities at present day. The blue error bar displays the result for Fornax from Read et al. (2019). The grey shaded band is derived from the mass-concentration relation of Dutton and Macciò (2014) and the blue shaded band comes from the same relation applied to CDM haloes which form a core below the half-light radius (see the "core-NFW" profile from Read et al. 2016). The various symbols mark our 8 Fornax analogues. *Right:* The values of the present-day ρ_{380} and all-time maximum M_{200}, coloured by the inferred orbital pericentres of each dwarf. Different symbols highlight our Fornax analogues.

5.3.5 The tidally induced reduction in the central densities of Fornax analogues

We now explore how dwarfs in our sample compare to Fornax in the context of the inner density - virial mass (ρ - M_{200}) relation (see the middle panel of fig. 5 in Read et al. 2019). Unlike the work of Read et al. (2019), which uses the density at 150 pc, we will use the *enclosed* density at 380 pc (approximately 2.8ϵ). Firstly, this is the radius above which we expect to see some convergence in the density profiles (grey vertical line in the right panel of Fig. 5.6, where the radius corresponds to $\approx 0.4R_e$). Secondly, in terms of differentiating between cores and cusps, the enclosed density is a more robust quantity since it takes into account the increasing density towards the centre in a cuspy halo and stays constant for a halo with a core.

In the left panel of Fig. 5.7 we show the enclosed density at 380 pc, ρ_{380}, as a function of M_{200} at the time each dwarf had a maximum halo mass. The red dots correspond to densities measured today and the black dots correspond to densities measured at the time the halo had its maximum mass. The black and red markers of different shapes represent our Fornax analogues. The grey shaded band is taken from the mass-concentration relation of Dutton and Macciò (2014) and the blue band is the densities expected for dwarfs, with the same masses and concentrations, which have undergone complete core formation below the half-light radius (the corresponding "core-NFW" profile is described in Read et al. 2016). The blue point with error bars is the Fornax measurement from Read et al. (2019). In this figure, we notice two interesting features. Firstly, the pre-infall M_{200} for our analogue sample of Fornaxes is systematically lower than that inferred in Read and Erkal (2019). We predict a Fornax $M_{200} \approx 4 - 9 \times 10^9 M_{\odot}$. Secondly, there is a large number of dwarfs, including our dwarf analogues, where ρ_{380} is consistent with that of Fornax due to tidal effects.

An important aspect of the argument presented in Read et al. (2019) is that the classical dwarfs in their fig. 5, including Fornax, are unlikely to have undergone significant tidal stripping and shocking based on their orbits inferred from *Gaia*. Thus, the low density in Fornax and some dwarf irregulars, which lie on the blue shaded band, are interpreted as being due to core formation rather than tides. In the right panel of Fig. 5.7, we show the present-day densities of dwarfs as a function of M_{200}, coloured by their inferred pericentres. We emphasize that these pericentres are derived under the conditions of complete knowledge of the spherically symmetric host halo potential. Indeed, the majority of dwarfs with particularly low central densities have low pericentres, yet there are a number of outliers. Most notably, our 'hexagon' Fornax, with a pericentre of 98 kpc has a compatible density to Fornax. We do, however, note that, unlike Fornax, this galaxy quenches ~ 4 Gyr ago. The 'thick diamond' Fornax is another example with a pericentre of 79 kpc and a central density compatible with Fornax. This galaxy only quenches 1 Gyr ago. Its halo mass, however, makes its central density fully consistent with an NFW halo. In haloes below $10^{10} M_{\odot}$ we see a number of examples with pericentres > 70 kpc that have lost almost an order of magnitude in ρ_{380}. We note again that a number of Milky Way potentials in the literature predict pericentres for Fornax as low as 20-30 kpc.

We have so far shown that in some ΛCDM simulations, where baryonic feedback *does not* cause core formation, 'core-like' densities may be encountered in Fornax-like haloes with eventful tidal histories, which are not always reflected by their inferred orbital pericentre. We summarize this result in Fig. 5.8, where we show all subhaloes in our simulations that match the Fornax constraint on $V_{1/2}$ from Fattahi et al. (2016b). For these subhaloes, we show the pericentre, as derived from their present-day motions, and the enclosed density at 380 pc. The blue line and shaded bands show the Fornax result from Read et al. (2019). It can be seen that, while the density typically increases with an increasing orbital pericentre, values of density compatible with Fornax can be found within 1σ at all pericentres.

In view of these results we see three main sources of tension with the conclusions of Read et al. (2019): *i)* the value of the pre-infall M_{200} of Fornax *ii)* the assumed pericentre of Fornax *iii)* possible numerical effects. We discuss these below.

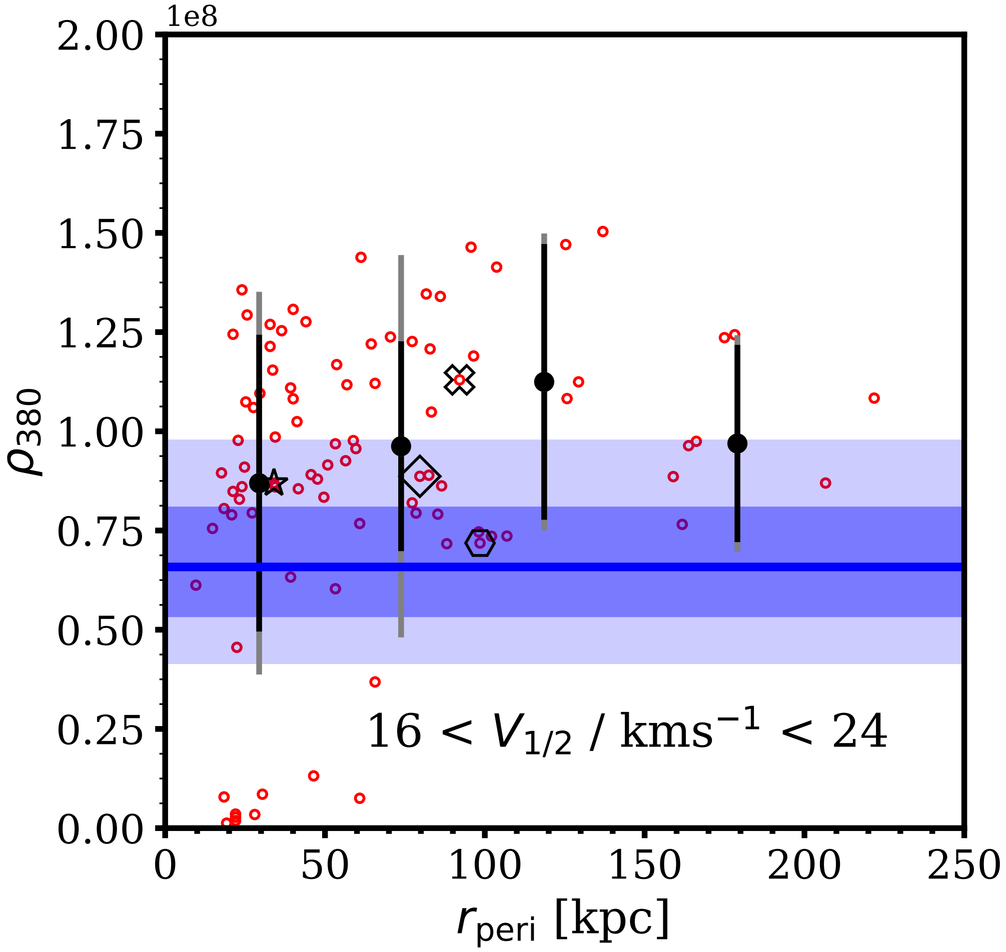

Figure 5.8: Red circles show the present-day value of the enclosed density at 380 pc, ρ_{380}, as a function of the inferred pericentre for all dwarfs with $16 < V_{1/2} < 24$ kms^{-1}, matching Fornax. Various symbols are our Fornax analogues. The error bars show the 1 and 2σ intervals for each bin in pericentre. The blue shaded regions mark the 1 and 2σ intervals in the enclosed density of Fornax below 380 pc from Read et al. (2019). The thick blue line is the median for Fornax.

5.3.5.1 What is the halo mass of Fornax?

The kinematic analysis of Fornax points to a value of the dynamical mass $M_{\rm dyn} = 2.4^{+0.8}_{-0.5} \times 10^9 M_\odot$ (Read and Erkal, 2019). This is significantly offset to the left and downwards of the stellar-halo mass relation of Read et al. (2017), indicating the effects of tides. In order to compensate for the tidal effects and quenching, as dwarfs fall into their host haloes, Read and Erkal (2019) reformulate the stellar-to-halo mass relation to a relation between the mean star formation rate, $\langle$SFR$\rangle$, and halo mass instead . The SFR is averaged over times when the galaxy is forming stars. The inferred M_{200} for any given galaxy is then dependent on when the quenching is defined. The relation is most useful when the star formation rate reflects the halo mass of the galaxy (i.e. its ability to accrete and maintain gas and to form stars). Now, if we imagine a situation where star formation is enhanced for reasons other than halo build-up, for example, due to passage through pericentre (as in our Chapter 2), then the $\langle$SFR$\rangle$ could be biased if SFR(t) is not truncated appropriately. The recent work on the star formation history in Fornax, using the *HST* data, by Rusakov et al. (2020) supports a scenario where Fornax has had a recent (~5 Gyr ago) burst in star formation, which could coincide with its pericentric passage (Patel et al., 2020). In fig.A1 of Read and Erkal (2019) it is shown that if SFR(t) is truncated at around 5 Gyr ago, their $\langle$SFR$\rangle$-based abundance matching method could give an M_{200} for Fornax of $\sim 7 \times 10^9 M_\odot$, compatible with our Fornax analogues.

Another important aspect of the $\langle$SFR$\rangle$ - M_{200} relation is the estimate of the total stellar mass. Such a quantity is impossible to measure directly and many photometry-based efforts are susceptible to various selection and modelling biases. A lower stellar mass of Fornax ($< 4.3 \times 10^7 M_\odot$) would be able to fix the discrepancy between the values of M_{200} predicted in our simulations and the $\langle$SFR$\rangle$ abundance-matching arguments. At the same time, note that if we were abundance matching by stellar mass alone, the M_{200} of Fornax would be consistent with our APOSTLE analogues.

Finally, it is possible that the stellar-halo mass relation in APOSTLE is not representative of the Local Group satellites. Note, however, that the work of Fattahi et al. (2018) finds a general agreement.

5.3.5.2 How well is the pericentre of Fornax known?

The inferred pericentre depends strongly on the model of the Milky Way potential. This is evident in Fig. 5.1, where 5 different potentials give pericentres between ~25 kpc and ~150 kpc. These pericentres are derived from sophisticated models that take into account the various Milky Way components (Gaia Collaboration et al., 2018; Bajkova and Bobylev, 2020). A pericentre for Fornax that is less than 50 kpc will naturally explain its low density and these pericentres are, at the moment, not ruled out. Future improvements will come from accurate mass models of the Milky Way (see Wang et al. 2020 for an extensive review), which include adiabatic contraction (Callingham et al., 2020; Cautun et al., 2020) as well as dynamical models that take into account the potentials of the Large and Small Magellanic Clouds (Patel et al., 2020) and the Milky Way halo growth (Correa et al., 2015a,b,c).

5.3.5.3 Tidal stripping in cosmological simulations

It has been recently shown in the works of van den Bosch et al. (2018) and van den Bosch and Ogiya (2018) (see also Errani and Peñarrubia 2020) that subhaloes in simulations can be subject to artificial disruption (that is disruption due to numerical effects, rather than physical processes). This can be caused by a gravitational softening that is too large as well as discreteness effects, resulting in a runaway instability. If our simulated subhaloes get tidally stripped too quickly, this would be a potential limitation to our results. In Appendix I, we show that, particularly for our Fornax analogues, we expect that the change in the radius of the maximum circular velocity, $R_{\rm max}$, is consistent with the “tidal tracks” of Peñarrubia et al. (2008) and Green and van den Bosch (2019) and the reduction in $V_{\rm max}$ could be overestimated by $\sim$ 10 per cent. This does not change the fact that our analogues are similar to Fornax in terms of their present-day $V_{1/2}$ (given this quantity evolves similarly to $V_{\rm max}$). Nevertheless, we believe that a comprehensive convergence study of the tidal disruption of haloes in a cosmological setting, with the inclusion of baryonic effects, is certainly warranted.

5.4 Summary and Conclusions

Fornax is one of the largest and brightest satellite dwarfs in the Milky Way, making it a prime target for spectroscopic and photometric surveys that, over the years, have provided an abundance of data. In particular, the measurements of the motions of individual stars in Fornax have been used to place constraints on its underlying gravitational potential. In particular, Read et al. (2019) have found that Fornax must have a low inner dark matter density, which could be a sign of a dark matter core in its central regions. Core formation is at odds with the predictions of dark-matter-only CDM simulations.

A number of works have used cosmological hydrodynamics simulations to show that baryonic feedback could be responsible for cusp-to-core transformations within the CDM model (Oñorbe et al., 2015; Tollet et al., 2016; Fitts et al., 2017); however, not all simulations predict this behaviour (Bose et al., 2019) and it is well-known that 'subgrid' prescriptions are responsible for this discrepancy (Benítez-Llambay et al., 2019).

In this work, we test an alternative scenario, where the low inferred density in Fornax could instead be due to tidal effects. This scenario has been disfavoured by Read et al. (2019), who argue that the proper motions, star formation history and the inferred pre-infall halo-mass of Fornax disagree with this interpretation. We test their arguments on a large sample of dwarfs from a suite of cosmological N-body hydrodynamics simulations in Local Group-like environments. We find the following:

- We confirm that the star formation history of Fornax is indeed consistent with that of a dwarf galaxy that is a satellite of the Milky Way (see right of Fig. 5.2).

- Close matches to Fornax in *both* the visible magnitude, M_V, and the circular velocity at the half-light radius, $V_{1/2}$, are quite rare in our simulations (see left of Fig. 5.2), however, we find 8 Fornax analogues (4 of which are particularly close matches). These analogues also have inferred orbital apo- and peri-centres compatible with Fornax (Gaia Collaboration et al., 2018; Fritz et al., 2018).

- Through examining mass loss from dwarf galaxies with orbital properties compatible with Fornax, we show that, even at large inferred present-day pericentres, dwarfs can exhibit significant mass loss. We find that, for galaxies on Fornax-like orbits (independent of mass), 43 per cent lose more than 50 per cent of their mass within 1 kpc (see Fig.5.3).

- We explore the relevance of the star-formation history in the determination of the extent of tidal effects a given dwarf has experienced. We show that, in many cases, the quenching time is directly related to the infall time; however, there exist a population of Galaxies with a similar stellar mass to Fornax, or higher, which quench long after infall. This is because they are able to preserve their gas supplies after infall and, in extreme cases, after multiple orbital pericentres (see the left panel of Fig. 5.4).

- We find that for ~ 36 per cent of dwarfs, with orbits similar to Fornax, the mass loss had begun more than 2 Gyr prior to infall. As such, the infall time is not always a reliable estimate of the time at which the dwarf had its maximum mass (see right of Fig. 5.4). Through examining individual Fornax analogues, we found that, in some cases, dwarfs can lose mass prior to infall due to interactions with more massive dwarf galaxies, perhaps due to infall as part of a group or a fly-by. This is the case for our best Fornax analogue (the ‘star’ Fornax in Fig. 5.5).

- Through comparing the density profiles of our Fornax analogues to that derived by Read et al. 2019, we show that the profiles of stripped dwarfs are only consistent with Fornax at a 3σ level. A much better fit to the result of Read et al. (2019) is a stripped dwarf with a very shallow cusp or a small core (see Fig. 5.6).

- We repeat the analysis of Read et al. (2019), which uses the inner densities and pre-infall halo masses of dwarfs to infer cores and cusps in their central regions. We show that for dwarfs with the same $V_{1/2}$ as Fornax, for pericentres between 20 and 250 kpc, the densities are comparable to Fornax within 1σ (see Figs. 5.7 and 5.8). It is clear that there exist Fornax-like dwarfs that have been tidally stripped more significantly than their pericentres would suggest, however, we note that a small ($<$ 50 kpc) pericentre for Fornax is not presently ruled out.

- We disagree with the result of Read and Erkal (2019) on the pre-infall halo mass for Fornax. Our simulations suggest that a galaxy with the present-day properties of Fornax should have a pre-infall halo mass of $4 - 9 \times 10^9 M_\odot$, while Read and Erkal (2019) infer $2 \times 10^{10} M_\odot$. This discrepancy comes down to the definition of the star formation rate of Fornax and its stellar mass. For example, the $\langle \mathrm{SFR} \rangle$ value for Fornax in Read and Erkal (2019) could be biased due to Fornax undergoing star formation after infall, when the halo no longer grows. Alternatively, it may be that APOSTLE provides an inadequate representation of the stellar-to-halo or $\langle \mathrm{SFR} \rangle$-to-halo mass relation on Fornax scales.

In conclusion, even with the quality of data available today, it is still difficult to separate the scenario where Fornax has a dark matter core from the one where it has been significantly affected by tides. Our results suggest that the most stringent test of this will come from an accurate inference of the dark matter profile *shape*, rather than the characteristic inner density, as proposed by Read et al. (2019). At present, an NFW profile in Fornax cannot be ruled out, although the data does seem to favour a shallow cusp. More precise determinations of the dark matter distributions should become possible with long-baseline proper motion measurements with *Gaia* and *HST*, accounting for asymmetry (Hayashi et al., 2020) and rotation (Zhu et al., 2016) in Fornax and the inclusion of independent constraints from its multiple stellar populations (Walker and Peñarrubia, 2011).

Chapter 6

Summary and Future Work

6.1 Overview

It is clear that baryonic processes play a key role in the assembly and structure of dark matter haloes. In the Milky Way, these processes would affect the spatial distribution of the satellites, their mass function and internal structure. It is thus becoming increasingly important to accurately model these processes in N-body hydrodynamics simulations. A particularly difficult aspect of this is choosing a reliable implementation of the 'subgrid' parameters in simulations, which is presently a necessity in cosmologically relevant volumes.

Some 'zoom-in' simulations, like *Elvis* and *Latte* (based on the GIZMO code), and *NIHAO* (based on the GASOLINE code), predict that large dwarf galaxies, like Fornax, should be able to form cores (Wetzel et al., 2016; Tollet et al., 2016; Garrison-Kimmel et al., 2019). This is a consequence of their 'subgrid' prescriptions for star formation. These models have been successful in reproducing the properties of the Milky Way and the Local Group, however, so have APOSTLE simulations (run using the EAGLE code), in which cores do not form (Fattahi et al., 2016b; Bose et al., 2019). While cores formation via feedback from supernovae is certainly a plausible physical process, it is not clear whether it should necessarily occur in galaxies. With APOSTLE, there is a unique opportunity to test whether observable properties of dwarfs, that are often attributed to core formation, could instead be a feature of galactic evolution in cuspy CDM haloes.

The evidence for cores in dwarf spheroidals comes from their dynamical mass modelling. With APOSTLE simulations, which resolve the visible components of dwarf galaxies with a number of particles comparable to spectroscopic data sets, it is possible to test such modelling methods in a realistic cosmological setting, where the density profiles are known to be cuspy, and to evaluate their efficacy in resolving the core-cusp problem. This has been the focus of this thesis, which I summarise in the following.

6.2 Solving the core-cusp problem using distinct stellar populations in dwarf spheroidals (Chapters 2 & 3)

The spatially and chemo-dynamically distinct stellar populations in dwarf galaxies have sparked particular interest as probes of cores and cusps in dark matter haloes. Constraints from two distinct populations are, in principle, capable of breaking the mass-anisotropy degeneracy along the line of sight. The work of Walker and Peñarrubia (2011) has been considered as, perhaps, the strongest evidence for cores in the Sculptor and Fornax dwarfs. Using dynamical mass estimators on the two populations to derive a mass slope, they showed that an NFW cusp is ruled out in Fornax and Sculptor at 96 and 99 per cent confidence levels, respectively. In this thesis, I applied their method to simulated dwarfs with two metallicity populations in APOSTLE simulations and found that ~17 per cent of the time values of the slope that are more shallow than an NFW are obtained and ~4 per cent of the time a 'hole' may be inferred in the central regions. This significantly weakens the result of Walker and Peñarrubia (2011). We show that their method is successful when the properties of the two stellar populations are correlated and, if not, the method is biased due to variation in sphericity and misalignment of the two populations.

The existence of two metallicity populations in dwarf galaxies and the differences in their properties poses an interesting problem for our understanding of galaxy formation and evolution. With N-body hydrodynamics simulations it is possible to track simulated dwarfs back in time and to identify the mechanisms behind their formation. We thus infer three different mechanisms through which a dwarf may acquire spatially distinct metallicity populations: mergers, passage through pericentre and star formation encouraged through ram pressure in the cosmic web. The merger scenario, in particular, would help explain both the formation of a metal-rich population in Fornax and the various substructures that have been observed in this dwarf (Coleman et al., 2003; de Boer et al., 2013). We show that 80 per cent of satellites with a present-day stellar mass of Fornax form their metal-rich population by passing through the pericentre of their host. This is the case provided a sufficient supply of gas is available at the time when the galaxy reaches its pericentre. Otherwise, in line with the predictions for isolated dwarfs, it is likely that Fornax formed a metal-rich population through a merger. It has been pointed out that Fornax may actually have three metallicity populations (Amorisco and Evans, 2012b; Amorisco et al., 2013), and, as such, both of these events could, in principle, have occurred.

6.3 Solving the core-cusp problem using higher-order Jeans analysis (Chapter 4)

An alternative method of breaking the mass-anisotropy degeneracy, to place a stronger constraint on the dark matter density distribution, comes from the use of higher-order velocity moments. Merrifield and Kent (1990) propose two "virial shape parameters", which use the fourth moment of the line-of-sight velocity. These can be used as two constraints in addition to the Jeans equation. Following a prescription of Read and Steger (2017), I have developed the pyGravSphere code, which uses Markov Chain Monte Carlo to solve for the dark matter density profile and stellar velocity anisotropy, while incorporating the virial shape parameters. In Chapter 4, I have tested the method on a sample of Fornax-like dwarfs from the APOSTLE simulations in CDM and SIDM models, allowing me to investigate cusps and cores in density distributions. In CDM, the density profiles were recovered with a bias of no more than 10 per cent and a scatter of 30 per cent in the inner regions. For SIDM dwarfs, the density profiles were recovered within 2σ, but were shown to be biased towards cuspy profiles. This was primarily due to a lack of constraints from the data and not due to the priors of the model. The uncertainties on the results of pyGravSphere were smaller than those for comparable Jeans methods. I also found that cosmological simulations favour constant and, mostly, isotropic velocity distributions. Setting this as a prior in the Jeans analysis removes the need for virial shape parameters and provides more accurate results in the case of SIDM.

In the case of the Fornax dwarf spheroidal, which has an on-the-sky ellipticity of $e \approx 0.3$, pyGravSphere was shown to be biased when the dwarf is viewed along its minor and major axis. Within the 1σ errors, the density profile of Fornax from Read et al. (2019) (which uses the GravSphere method) appears to be consistent with that of a cuspy dwarf, with an ellipticity of 0.3, viewed along the minor or intermediate axis. This is primarily due to the size of the error bars on the dark matter profile of Fornax as well as discreteness noise in the central regions of our simulated dwarfs. Indeed, if the *shape* of the dark matter profile of Fornax from Read et al. (2019) was to be taken at face value, it is likely that future data sets will enable a clear distinction between a cusp and a core in this dwarf.

6.4 Solving the core-cusp problem via inference of central density (Chapter 5)

It is well established that Fornax has a relatively low density of dark matter in its central regions. This has been hypothesized to be due to the presence of a constant-density dark matter 'core' in this dwarf (Read et al., 2019). Within the context of ΛCDM, the low density in Fornax can also be explained by the effects of Galactic tides. This scenario has so far been disfavoured due to the orbital parameters of Fornax and its star formation history. In Chapter 5, I revisited these arguments. I have shown that the star formation history of Fornax is not a good tracer of infall time, as sufficiently large haloes are able to form stars after infall. Moreover, it appears that small pericentres for Fornax (<50 kpc) are presently not ruled out in the literature; however, even for large orbital pericentres, I have found cases where the dark matter halo is stripped prior to infall due to interactions with more massive dwarfs during group infall or a fly-by. Finally, I have shown that while tidal effects can produce a low dark matter density in Fornax, 'cuspy' profiles are only consistent with the data within 3σ. Instead, dark matter profiles with very shallow cusps or small cores provide a significantly better fit to Fornax.

6.5 Future work

In the following, I will build on the findings of this thesis to suggest a number of projects that could be undertaken to further our understanding of the core-cusp problem in dwarf spheroidals.

6.5.1 The Jeans equation

One of the primary findings of this thesis is that the spherical Jeans analysis works well for spherical systems, even in cases that have been strongly tidally influenced. Local Group dwarfs, however, are known to be quite elliptical (McConnachie, 2012). This calls for modelling of galaxy shapes and inclinations in, at least, axisymmetric Jeans models (Hayashi et al., 2018; Hayashi et al., 2020). For triaxial systems, the solutions to the Jeans equations become highly non-trivial (van De Ven et al., 2003) and one may, therefore, choose to abandon the Jeans approach altogether in favour of Schwarzschild orbital superposition models or made-to-measure approaches, where no assumptions need to be made on the underlying velocity anisotropy of the tracers (Schwarzschild, 1979; Dehnen, 2009; Rodionov et al., 2009; van den Bosch et al., 2008; Vasiliev, 2013) and asphericity and rotation of stellar populations are easily modelled. These techniques are typically very computationally expensive, though the availability of the required computing power has certainly increased in recent years. These models could then also be extended to include multiple tracer populations in dwarf spheroidals and proper motion data.

6.5.2 How much data do we need?

A common theme has developed over the past decade, where larger and larger spectroscopic data sets are being used in the Jeans modelling only to show that the data is just as compatible with a core as it is with a cusp (Strigari et al., 2010). In recent years, proper motion data from *Gaia* and *HST* have become available and these still appear to be unable to lift the degeneracy (Massari et al., 2018; Strigari et al., 2018). While in the case of the line-of-sight velocities the weakness of the constraints likely has to do with the lack of stellar samples in the centre, for proper motions it is also the size of the error bars on individual stars (since the baselines of the *HST* and *Gaia* are not sufficiently long). As such, there is certainly a need for a systematic study to determine *i)* how many stars are needed, and at which radii, for a better than 3σ detection of a cusp or a core of a given size and *ii)* how big should the measurement errors be. This approach would appropriately inform observational studies on the scientific goals and the timescales needed to achieve them.

6.5.3 Simulation comparison

6.5.3.1 To observations

As bigger, higher resolution, cosmological simulations become available, which include a wealth of galaxy formation physics, it is becoming extremely important to ensure that that the predictions of the simulations are compared to observations in a fair manner. Simulations give us a benefit of knowing precisely the quantities which observations can only infer (stellar mass, halo mass, galaxy sizes etc.). It is paramount that, in the calibration of simulation parameters and in comparisons with data, the same modelling techniques are used as in observations, accounting for measurement uncertainties and any observational biases. It is then possible to test the robustness of various galaxy scaling relations, for example, the stellar mass - halo mass relation and its behaviour in the low-mass end, with direct consequences for the core-cusp problem and the “too-big-to-fail” problem.

6.5.3.2 To other simulations

A sufficiently large number of N-body and galaxy formation codes have been developed at this stage to enable detailed comparisons of cosmological volumes, in the spirit of the work by Frenk et al. (1999). There is an abundance of Milky Way and Local Group-like volumes, run with different galaxy formation codes, each appearing to solve the small scale problems of ΛCDM. These simulations do, however, vary in the halo and stellar masses of the main haloes, sizes of stellar disks and subhalo luminosity functions. The running of a single cosmological volume with different codes, but at the same spatial and mass resolution, would undoubtedly ease the comparison of galaxy formation models on the small scales and disentangle the 'subgrid' and numerical effects on the properties and abundance of the simulated substructure.

6.5.4 Separating baryon-induced core formation from core-forming alternative dark matter

An important aspect of the core-cusp problem, which we have not significantly touched upon in this thesis, is the possibility of alternative dark matter as a solution. There are two important aspects to this in the context of state-of-the-art simulations: the details of galaxy formation and the effects of the environment.

6.5.4.1 Galaxy formation

Alternative dark matter solutions were brought up for the core-cusp problem at the time when baryonic effects on galaxies were not fully understood. By now, a number of sophisticated galaxy formation models have been developed for cosmological simulations and, as such, any solution that involves an alternative model for dark matter requires that populations of galaxies produced in these models match observational constraints at least as well as in CDM. Moreover, models of galaxy formation, such as EAGLE, are calibrated to match observed galaxy populations *assuming* CDM. It is then not clear whether the same model can be reapplied in alternative dark matter, or a new re-calibration is required to gauge a model's success. One can, perhaps, learn from both approaches. Ideally, of course, one would not need to calibrate a galaxy formation model, though this is difficult to achieve when physical processes must be modelled on a 'subgrid'.

6.5.4.2 Environment

A particularly interesting aspect of satellite galaxy evolution in alternative dark matter models is the details of their tidal stripping and stellar stream formation. Streams are potentially a very effective probe of dark matter models. Firstly, detection of 'gaps' in stellar streams, due to small dark matter haloes, could place an important constraint on the identity of dark matter (Erkal and Belokurov, 2015). For instance, detection of small perturbations could rule out warm dark matter models, where small haloes are not able to form. Secondly, it is becoming clear that the details of tidal stripping are highly sensitive to the dark matter distribution in dwarfs (Errani et al., 2015) and the nature of dark matter (Dooley et al., 2016). With *Gaia*, more and more stellar substructures are found in the Galactic halo. Their properties, as well as those of surviving satellite galaxies, can be compared to the predicted ones from cosmological simulations in alternative dark matter models, placing important constraints on the nature of dark matter.

6.6 Concluding remarks

N-body cosmological simulations have become increasingly sophisticated over the last decade, allowing us to study the formation of large- and small-scale structure, as well as the physics of galaxy formation and evolution, in extraordinary detail. As the observational data improves in quality and quantity in the coming years, particularly with instruments like *Gaia* and *JWST*, simulations will undoubtedly prove to be invaluable tools in informing the analyses and interpretations of this data. As a proof of concept, this thesis focused on the solutions to the core-cusp problem in Local Group dwarf spheroidals and it serves as a prime example of what cosmological simulations have to offer in the development of dynamical analysis methods and in the understanding of their shortcomings within a realistic cosmological setting. As highlighted above, there are many more avenues to explore in this area and I hope that this thesis serves as a motivation for more detailed investigations in the future.

Appendix

A Numerical convergence of galaxy properties

In this Section, we test the convergence of the rotation parameter κ_{rot} and the sphericity parameter s. We carry out the following test for convergence. We take a sample of 37 dwarfs with $10^5 - 10^6$ stellar particles from the five high-resolution APOSTLE volumes and we calculate the 'true' values of κ_{rot} and s, where we include all particles belonging to the galaxy. We then take progressively smaller particle samples and recalculate these properties. The result of this test may be seen in Fig. A1, where we show the accuracy of the estimates as a function of the number of particles with which they were calculated. It can be seen that the scatter in the estimate accuracy increases significantly for smaller particle subsamples. The median estimates of κ_{rot} are generally accurate, even for < 100 stellar particles, while the sphericity, s, can be substantially underestimated. We conclude that we would require over 100 particles in a given stellar population for convergence.

B The gas content of simulated dwarfs

The mechanisms of formation of the two metallicity populations that we identify in this work are largely dependent on the availability of star-forming gas within the dwarfs. It is therefore important to establish whether the HI content of dwarf galaxies within the APOSTLE suite resembles that of the real Local Group dwarfs.

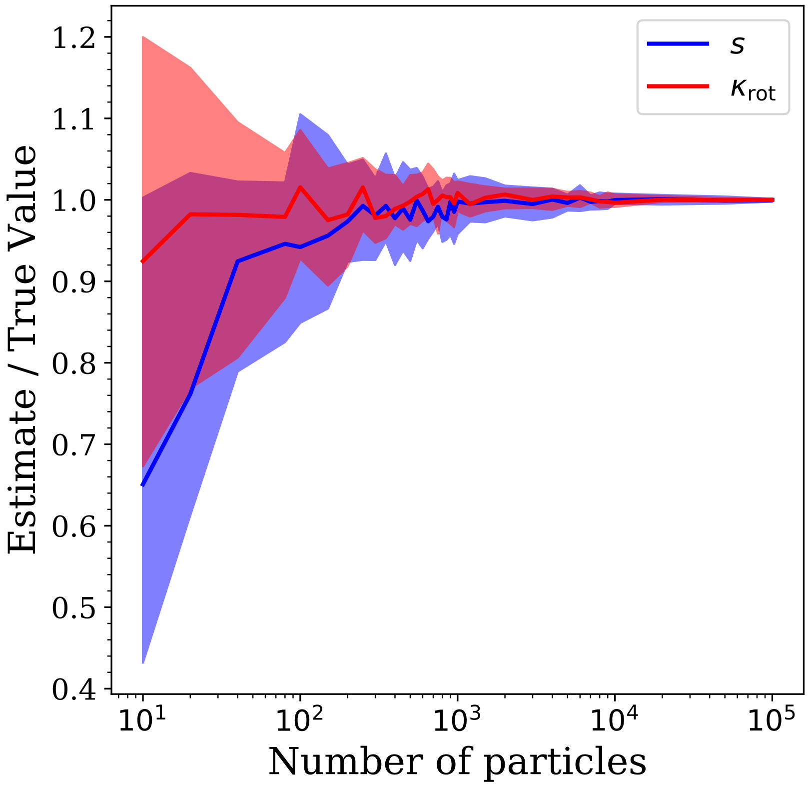

Figure A1: The accuracy of the estimates of sphericity s (blue) and $\kappa_{\rm rot}$ (red) as a function of the number of stellar particles with which they were calculated, shown for a sample of 37 dwarfs containing 10^5 to 10^6 stellar particles. The 'true' values are those calculated using all particles belonging to each galaxy. The blue and red bands represent 1σ scatter for s and $\kappa_{\rm rot}$, respectively. Above a 1000 particles, the values are well converged and at ~400 particles (the minimum number of particles belonging to a subpopulation in our sample of 50 galaxies) the estimates are, on average, accurate and the scatter is less than 10 per cent.

The determination of HI content would ideally involve the inclusion of radiative transfer schemes and the cold dense ISM within the simulation code. Unfortunately, these schemes are computationally expensive and are not included within the APOSTLE suite. We thus obtain the HI content of the APOSTLE dwarfs using the fitting function of Rahmati et al. (2013) that relates the total photoionization rate to the hydrogen number density at $z = 0$ and is calibrated on radiative transfer simulations. The atomic hydrogen fraction is then found using a scaling relation between a fraction of molecular hydrogen and gas pressure. The results of applying this prescription can be seen in Fig. B1. The observations (McConnachie, 2012; Spekkens et al., 2014) are shown with solid symbols and the simulated dwarfs with open symbols. The arrows denote upper limits. It may be

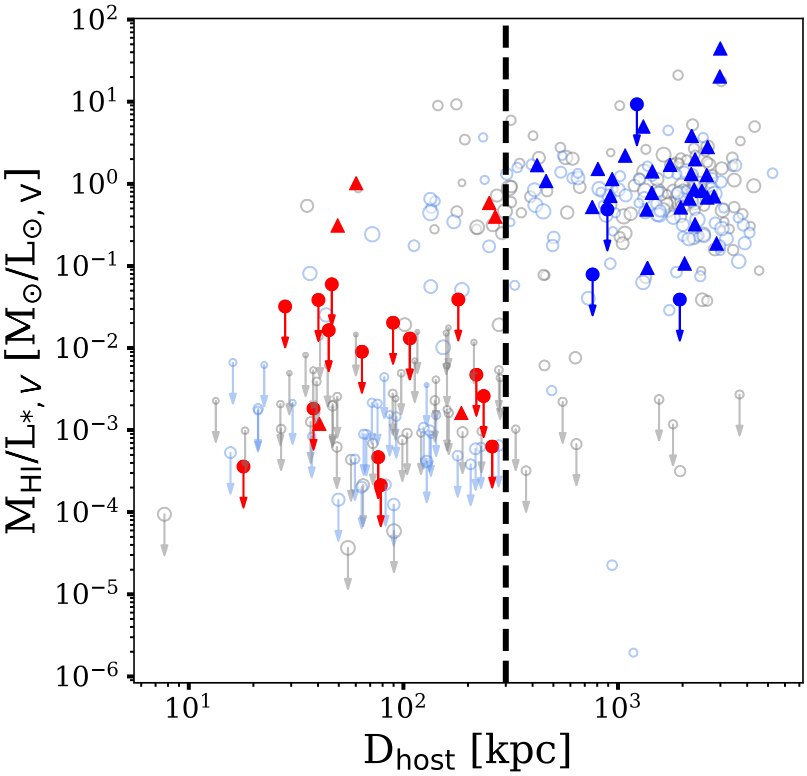

Figure B1: The ratio of mass in HI to the stellar V-band luminosity as a function of the dwarf's distance from the nearest host galaxy at $z = 0$. The grey empty circles are single population galaxies and the blue are two-population dwarfs. The size of the circles is reflective of the logarithm of their stellar mass. The empty circles with arrows represent galaxies with no resolved HI content. Their value is set by the SPH particle mass. The filled red and blue symbols show the measurements for satellites and Local Volume dwarfs, respectively, taken from McConnachie (2012) and Spekkens et al. (2014). Filled symbols with arrows show upper limits. The black dashed line at 300 kpc represents a typical value of the Milky Way's virial radius.

seen that the fraction of HI in the APOSTLE dwarfs broadly agrees with the observed values at z = 0. The satellites (galaxies within 300 kpc of the host) contain little or no gas, whilst the field dwarfs are clustered at $M_{HI}/L_{*,V}$ ~1 $M_\odot/L_{\odot,V}$, compatible with observations.

C Two populations in Sculptor

A number of studies have collected spectroscopically determined stellar metal abundances for Milky Way dwarfs (Tolstoy et al., 2004; Helmi et al., 2006; Battaglia et al., 2007; Walker et al., 2009a; Kirby et al., 2013). In particular, many measurements are available

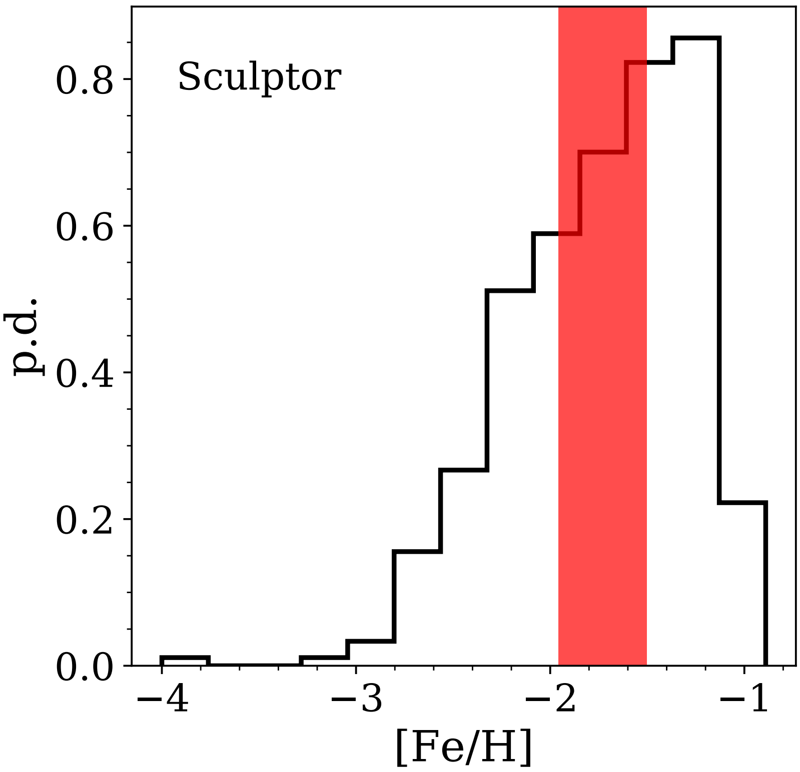

Figure C1: The metallicity distribution of Sculptor members from Kirby et al. (2013). The red band shows the range of cuts, separating the two populations, found with our method.

for Sculptor and Fornax. Kirby et al. (2013) have published measurements from medium resolution spectroscopy for 376 Sculptor high-probability members and 676 Fornax members, although for Sculptor the measurements extend to ~350 pc (approximately the half-light radius of this dwarf McConnachie (2012)). Walker et al. (2009a) published a larger sample for both dwarfs (1088 stars for Fornax and 1152 for Sculptor with membership probabilities greater than 0.99), with Sculptor members extending to ~2 kpc. According to Fig. 2.17, the analysis of the metallicity distributions should include stars up to $2R_{\mathrm{hl}}$ to cover the extent of both populations. Thus, the sample of Walker et al. (2009a) would be preferred. However, through identifying overlapping stars in the high-resolution spectroscopy data published in Battaglia et al. (2007), we find that the magnesium and iron indices relate to [Fe/H] with very large scatter. We, therefore, choose to apply our method to the Kirby et al. (2013) data, where we only select dwarfs for which at least 200 measurements are available.

We sample the errors of each metallicity measurement 1000 times and apply our technique to each sample. We find that none of the dwarfs other than Sculptor display signs of two metallicity populations. For Sculptor, in ~40 per cent of samples, two populations can be found. This is shown in Fig. C1. Interestingly, the typical cut between the two populations at [Fe/H]~1.7 (red band) is consistent with that found by Tolstoy et al. (2004) for a more extended sample of stars. Based on the shape of the metallicity distribution alone, with a larger metal-rich population, we lean towards a merger scenario for Sculptor, with consequent gas stripping from the Milky Way halo, preventing the formation of more metal-rich stars.

D Definition of Γ

By definition, the value of Γ becomes undefined as the radii of the two metallicity subpopulations coincide, $\Delta \log_{10} r_2/r_1 \rightarrow 0$. In selecting our sample, it is therefore important to include only galaxies in which the two subpopulations are well separated. We applied the GMM technique to all galaxies in the five high-resolution APOSTLE simulations and, for each, we measured the 3D half-mass radius of the metal-rich and the metal-poor subpopulations and obtained the slope $\Gamma_{\rm true}$. Fig. D1 shows $\Gamma_{\rm true}$ as a function of the ratio of the 3D half-mass radii of the two metallicity subpopulations. Below $\log_{10}(r_2/r_1) \sim 0.06$, where r_2 is the larger radius of the two, very low values of $\Gamma_{\rm true}$ are obtained. We require $\log_{10}(r_2/r_1) > 0.06$ for our sample, as shown by the dashed yellow line in Fig. D1.

E Subpopulation mixing

As described in Section 3.2.1, we define each subpopulation by placing a rigid cut at the intersection of two fitted Gaussians. This treatment ignores mixing between the two subpopulations, which can affect the measurement of the velocity dispersion thus introducing a correlation in the kinematics of the metal-rich and the metal-poor subpopulations. Battaglia et al. (2008), for instance, allow a metallicity gap of $-1.7 <$ [Fe/H] < -1.5.

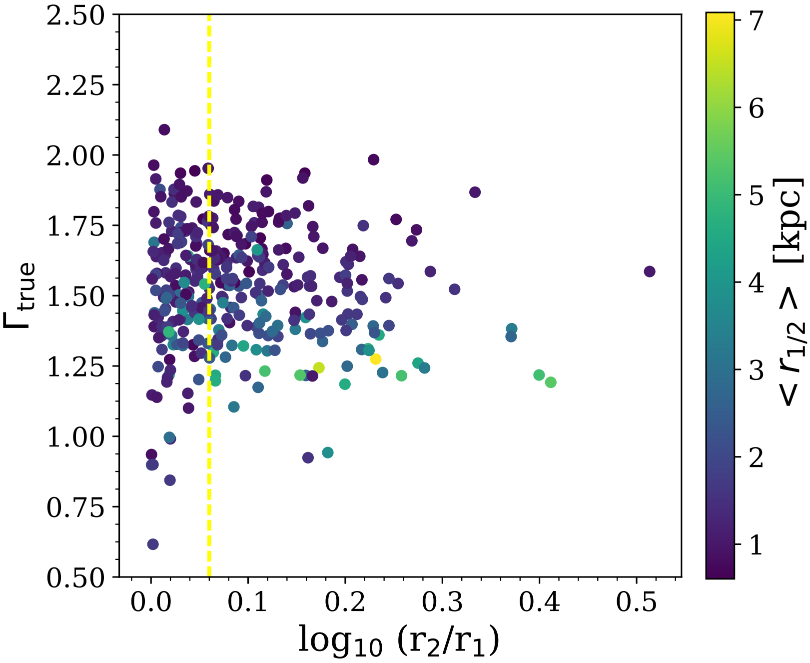

Figure D1: True slope of the cumulative mass function as a function of the ratio of the half-mass radius of the metal-poor and the metal-rich subpopulations. The points are coloured by the mean of the metal-poor and the metal-rich half-mass radii. $\Gamma_{\rm true}$ reaches low values below $\log_{10}(r_2/r_1) \sim 0.06$ as a near-zero value of $\Delta \log_{10}$ M becomes comparable to near zero values of $\Delta \log_{10}$ r. At much larger separations the slope is measured further away from the centre and is correspondingly steeper.

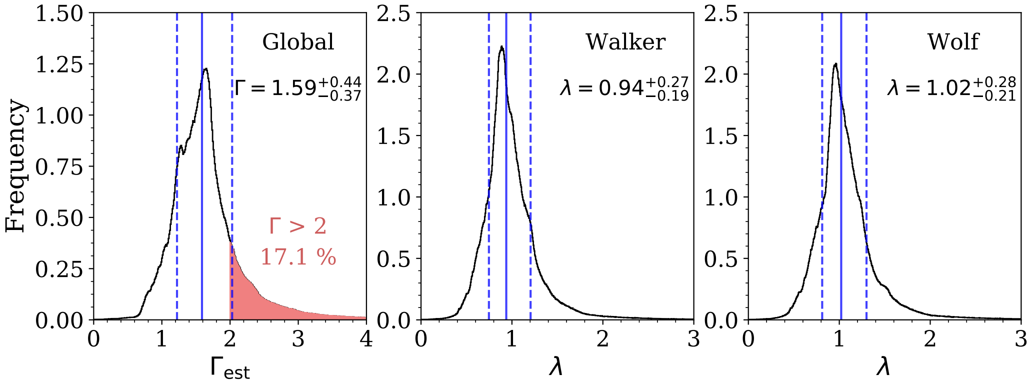

Figure E1: Overall distributions of estimated $\Gamma_{\rm est}$ (left) and λ for Walker et al. (2009b) (middle) and Wolf et al. (2010) (right) estimators for galaxies in our sample when a metallicity gap is introduced between the two subpopulations, taking out a quarter of each subpopulation on either side of the metallicity cut. The distributions are consistent with our previous results (top panel of Fig. 3.10), suggesting that kinematic mixing between the subpopulations does not play a major role in the inferred distribution of slopes Γ.

We, therefore, repeated our analysis, this time taking out one quarter of each subpopulation on both sides of the metallicity cut. The result may be seen in Fig. E1. We obtain $\Gamma = 1.59^{+0.44}_{-0.37}$ and $\lambda = 0.94^{+0.27}_{-0.19}$ for the Walker et al. (2009b) estimator and $\lambda = 1.02^{+0.28}_{-0.21}$ for the Wolf et al. (2010) estimator when including the metallicity gap. This result is clearly consistent with our previous results for the Walker et al. (2009b) and Wolf et al. (2010) estimators when a metallicity gap was not included (Section 3.3.2).

F Convergence criteria and generating initial positions

In this Section, we describe the effect of our choice of the initial positions of EMCEE walkers on the convergence of GravSphere's results.

F1 Effective priors

As mentioned in the main text, we generate the initial positions through the selection of walkers that satisfy the condition of radial increase in power-law slopes, γ_j, and the constraint on smoothness, $\Delta\gamma = 1$.

The top panel of Fig. F1 shows the effective priors on each slope. It is clear that these priors are not uniform as the selection of the slopes is not independent; however, the width of these distributions allows for a variety of density profiles. The inset shows the priors for the density at 150 pc, ρ_{150}. Despite the non-uniform nature of the γ_0 prior, when combined with a uniform prior on the scale density, ρ_0, the resulting ρ_{150} prior is effectively uniform and is not biased towards more core or cusp-like values (Read et al., 2019).

The middle panel of Fig. F1 suggests that the posteriors on γ are not completely determined by the priors. The prior and posterior distributions are offset, as seen from their median values, and their shapes are noticeably different. The γ_4 posterior is clearly pushing against the prior boundary, suggesting that a wider prior on this parameter is desirable.

In the bottom panel, we see similar posterior distributions for SIDM dwarfs. It is clear that the regions with $\gamma_0 = 0$ are not prioritized by the EMCEE walkers, resulting in an inference

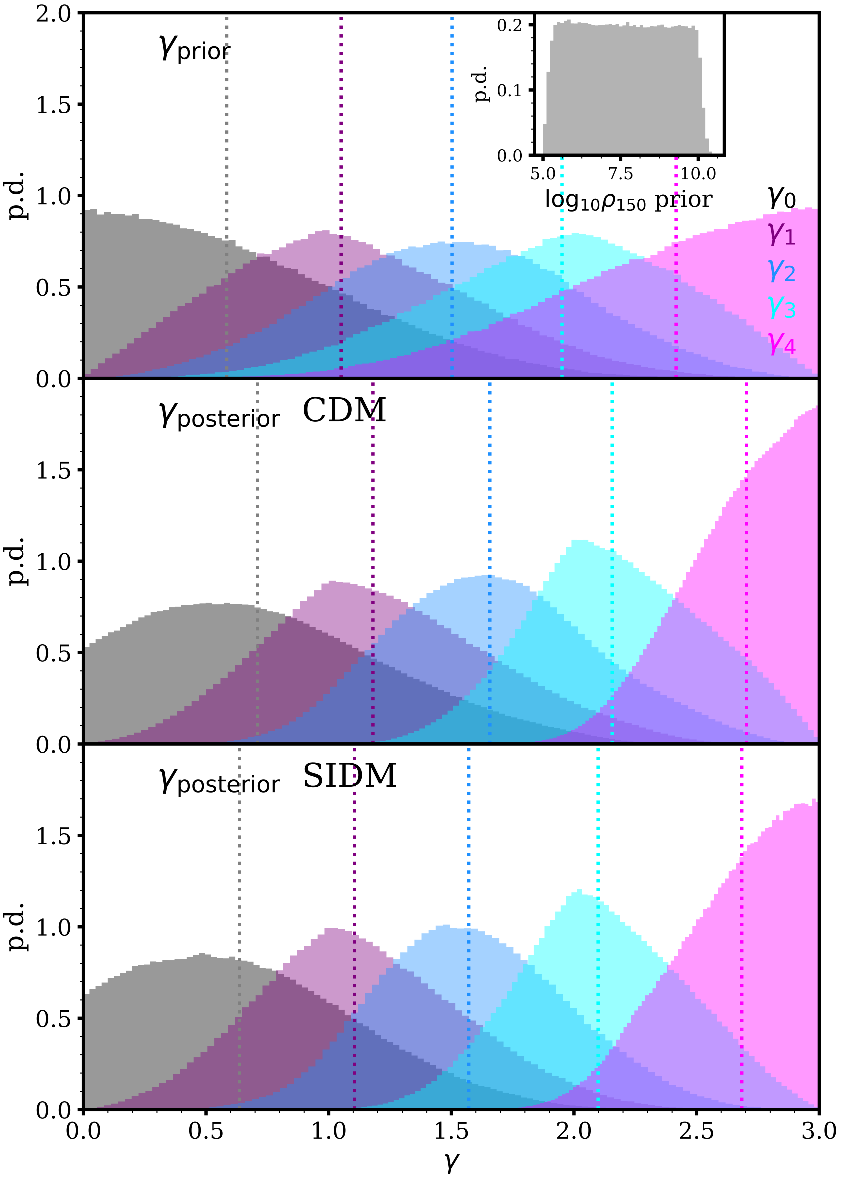

Figure F1: *Top:* effective priors on the logarithmic slopes γ_j. Each slope is identified by its colour. The inset shows priors on the density at 150 pc, assuming a 1 kpc half-light radius. *Middle:* posterior distributions, collected from all CDM dwarfs within our sample, weighted equally. The dotted lines are the medians of the distributions. *Bottom:* posterior distributions, collected from all SIDM dwarfs within our sample, weighted equally. The dotted lines are the medians of the distributions.

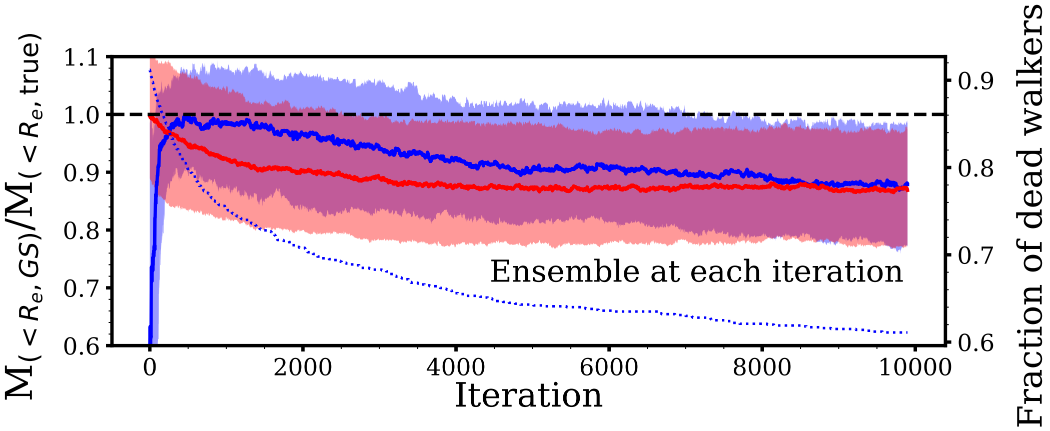

Figure F2: The convergence of mass within the half-light radius, expressed as an accuracy compared to the true value, for two different prior selection methods. Priors that are generated completely uniformly are shown in solid blue, and those selected in a uniform, yet conditional, fashion (such that all priors satisfy the monotonic increase in the values of γ_j) are shown in red. The shaded bands represent 68 per cent confidence limits. The blue dotted line shows the fraction of 'dead walkers' (those stuck in the infinitely negative log-likelihood space) when using fully uniform priors.

of more cuspy dark matter density profiles. It can be seen, however, that lower values of γ_j are preferred, compared to the CDM sample.

F2 Walker convergence compared to previous implementations

Previous implementations of GravSphere have used initial positions of the walkers for the broken power-law slopes γ_j that are completely uniform. This results in a large number of emcee walkers starting off in regions of infinitely negative log-likelihood. This is because these walkers do not satisfy the constraints for monotonically increasing values of γ_j. We will refer to these as 'dead walkers'. Eventually, some of these climb out and explore the posterior distribution, but not all, and this can take many iterations. In Read and Steger (2017), the chains were run for 5000 iterations, with the last 2500 used for analysis. In Fig. F2 we compare this method to one employed in this work.

We pick Galaxy 4 as our representative example and we select the mass within the half-light radius, $M(<R_e)$, as a quantity for which we wish to establish convergence. Fig. F2 shows the median value of the bias, $M(<R_e)/M_{\mathrm{true}}$, and the 68 per cent confidence levels for *each* walker iteration using the original GravSphere's method for generating initial positions

(blue) and the initial positions generated using the method described in this work (red). The blue dotted line shows the fraction of dead walkers remaining after each iteration when using the original GravSphere method (right vertical axis).

It can be seen that our new method reaches convergence after $\sim 5 \times 10^3$ iterations, whereas the original method requires ~500 iterations to get out of the low log-likelihood regions and, in fact, does not reach the converged distribution until after $\sim 9 \times 10^3$ MCMC iterations. The chains start off with over 90 per cent dead walkers. This percentage drops to ~ 60 per cent near 10^4 iterations and can be seen to decrease slowly. We conclude that our new method of initial position selection allows for faster chain convergence and efficient walker exploitation.

G Extended priors that favour cores

In Fig. G1 we display the mass, density and anisotropy profile recovery with GravSphere for our sample of SIDM dwarfs when the priors on the power-law density slopes γ_j are allowed to vary between $\gamma_j = [-2, 3]$, allowing 'holes' in the density distribution. In the post-processing, we fix all $\gamma_j < 0$ to $\gamma_j = 0$. This effectively increases the sampling by emcee walkers of the parameter space regions where the dark matter distribution is cored.

H Spherical approximation to the potential

In this Section, we show that the spherical approximation to the potential is a valid one by ensuring that the positions of the stellar particles, bound to the host halo, with the radial velocity $v_r = 0$ kms^{-1} correspond to the apo- and peri-centres obtained via Equation 5.2. In practice, we select particles with $v_r = 0 \pm 1$kms^{-1}. The results are shown in Fig. H1. It is clear that the apocentres of the stars at 50 kpc are known, under the spherical approximation, to better than 5 per cent, and at 25 kpc they are known to better than 10 per cent. We thus conclude that the spherical approximation is valid for our purposes.

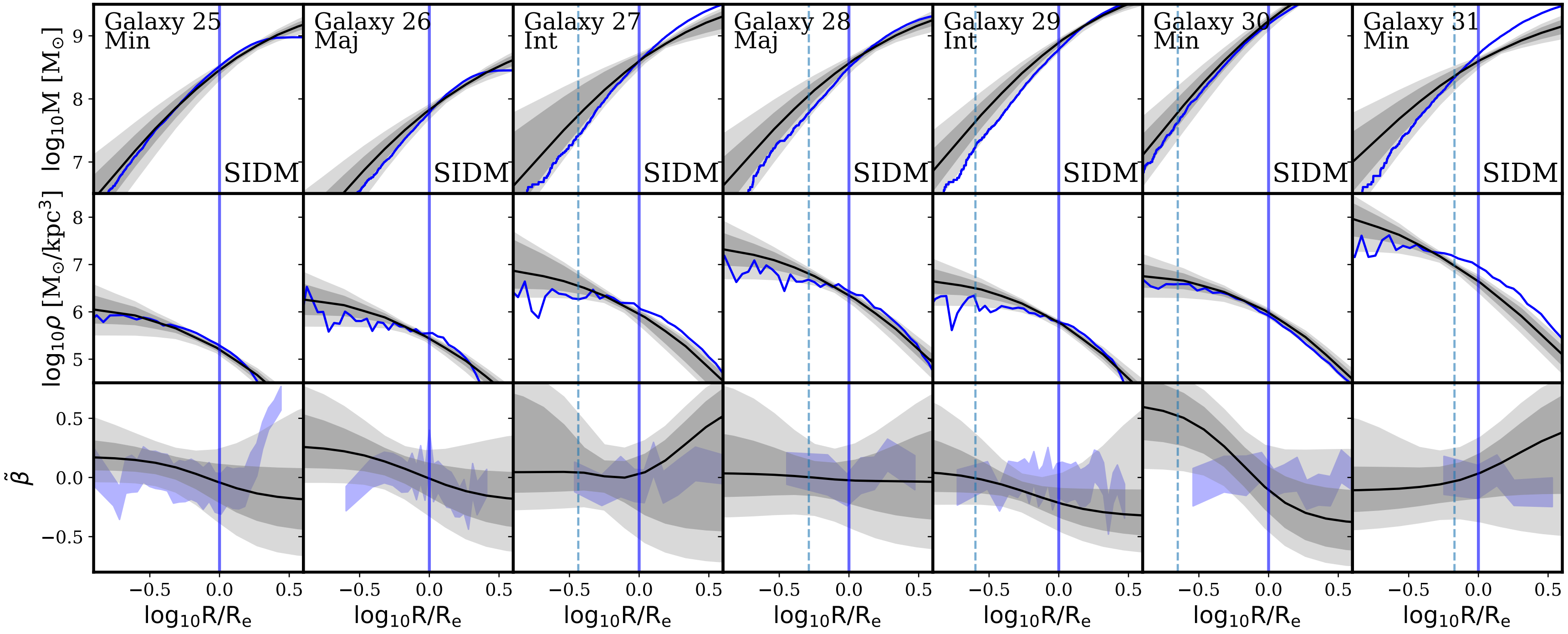

Figure G1: As Fig. 4.2, but now using an extended set of priors on the density slopes γ_j, allowing ‘holes’ in central regions of dwarfs. Note that for a number of these dwarfs the spatial resolution, 2.8ϵ (vertical dashed line), is below $0.125R_e$ and below the limits of the figure.

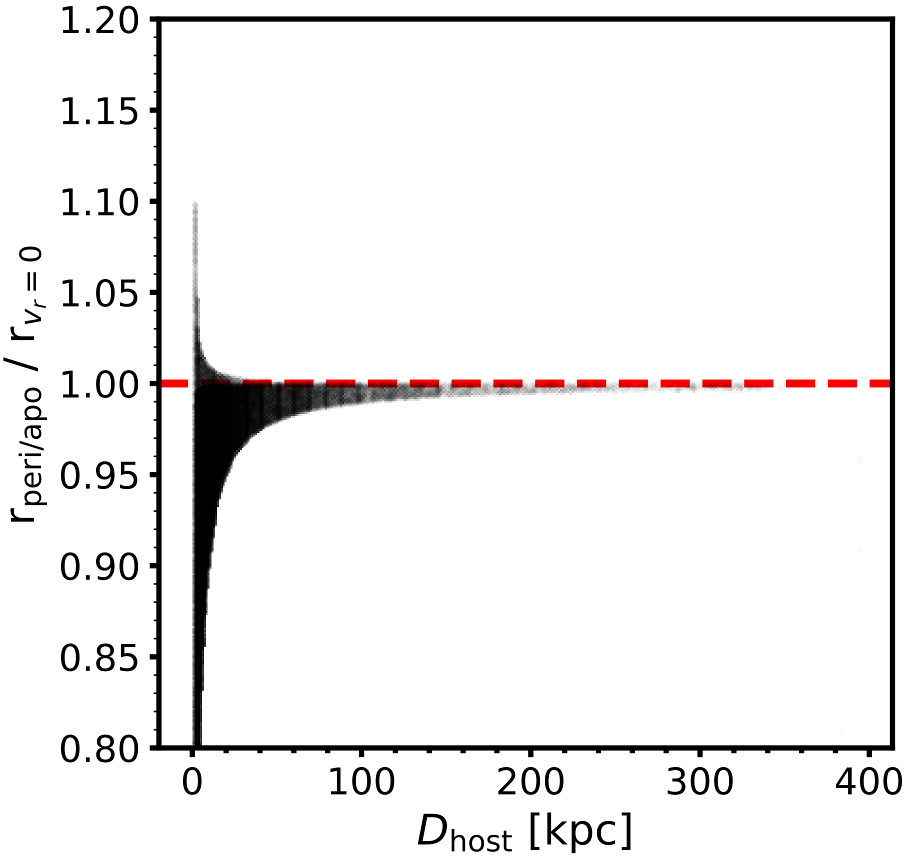

Figure H1: For each stellar particle in a Milky Way analog halo, with a radial velocity $v_r = 0 \pm 1$ kms^{-1}, we show the values of the orbital apocentre or pericentre (whichever is closest to the position of the particle), divided by the distance of the particle from the centre of the host galaxy. We show these values as a function of distance to the host galaxy, $D_{\rm host}$. The red dashed line highlights where the pericentre/apocentre and the distance of the particle from the centre are the same.

I The ‘tidal tracks’ of cosmological subhaloes

In this Section, we briefly consider how much our results could be affected by numerical artifacts. In particular, we wish to know, whether subhaloes in our simulations are stripped too fast, compared to the predictions of higher-resolution idealized models in the works of Peñarrubia et al. (2008); van den Bosch and Ogiya (2018); Green and van den Bosch (2019). We note, however, that it is not clear whether the results in those papers should directly translate to cosmological hydrodynamics simulations.

Motivated by the analysis of Green and van den Bosch (2019), in Fig. I1, we show the convergence between the fractional changes in the maximum circular velocity, $V_{\max}$, its radius $R_{\max}$ and the 'tidal tracks' of Peñarrubia et al. (2008) as a function of the fraction of bound mass left in the halo, $f_{\rm bound}$. Indeed, for the haloes that get stripped more (smaller $f_{\rm bound}$) the reduction in $V_{\max}$ is more significant in our cosmological simulations. Where haloes lose $\sim$2 orders of magnitude in halo mass, the loss in $V_{\max}$ is enhanced by $\sim$20 per cent. For our Fornax analogs, however, which lose no more than 80 per cent of their mass ($f_{\rm bound} \approx 0.2$), we expect that $V_{\max}$ would be underestimated by $\sim$ 10 per cent. If we consider the left panel of Fig. 5.2, our Fornax analogs are still consistent with the $V_{1/2}$ (assuming it changes similarly to $V_{\max}$).

An interesting feature of Fig. I1 is that the reduction in $R_{\max}$ is clearly dependent on halo concentration, c_{200}. This is consistent with the results of Green and van den Bosch (2019). However, Green and van den Bosch (2019) also predict that we should observe this dependence with the reduction in $V_{\max}$, which we do not see here. This could, in principle, be related to the presence of baryons in these haloes. Nevertheless, further investigations of the convergence of tidal stripping in cosmological simulations are beyond the scope of this work.

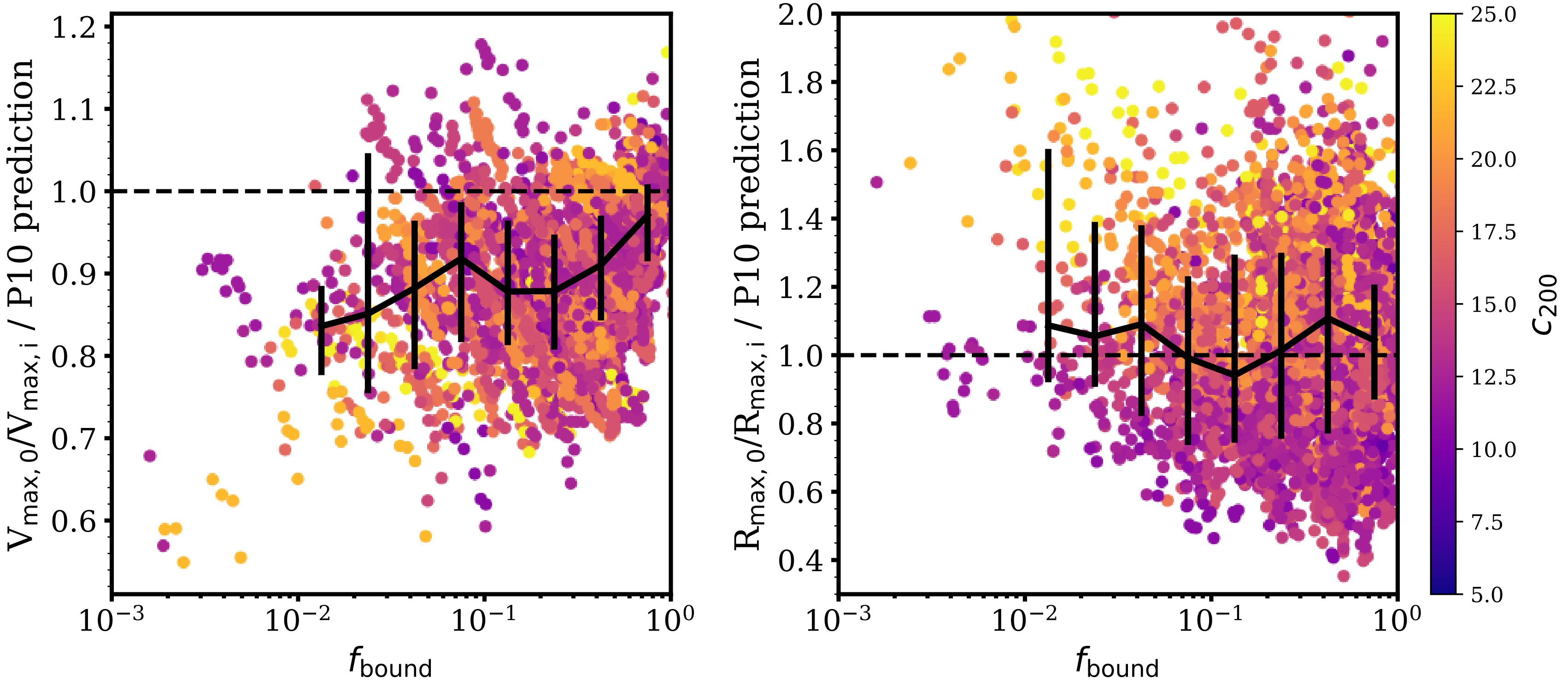

Figure I1: *Left:* The fractional change in the maximum circular velocity, V_{max}, in our satellite dwarfs, divided by the fractional change predicted in Peñarrubia et al. (2008), as a function of the fraction of bound mass remaining in the satellite since it had its maximum mass, f_{bound}. For each satellite we use multiple snapshots after infall, but we exclude those where the satellites come within 50 kpc of the host halo. The points are coloured by the halo concentration, at the time of its maximum halo mass, c_{200}. The error bars are the median and 1σ intervals in bins of bound mass. *Right:* As before, but the fractional change in the radius of the maximum circular velocity, R_{max}, compared to the predictions from Peñarrubia et al. (2008).

Bibliography

Adams, J. J. et al. (2014). Dwarf Galaxy Dark Matter Density Profiles Inferred from Stellar and Gas Kinematics. *ApJ*, 789(1):63.

Adelman-McCarthy, J. K. et al. (2007). The Fifth Data Release of the Sloan Digital Sky Survey. *ApJS*, 172(2):634–644.

Agnello, A. and Evans, N. W. (2012). A Virial Core in the Sculptor Dwarf Spheroidal Galaxy. *ApJL*, 754:L39.

Akaike, H. (1998). *Information Theory and an Extension of the Maximum Likelihood Principle*, pages 199–213. Springer New York, New York, NY.

Amorisco, N. C., Agnello, A., and Evans, N. W. (2013). The core size of the Fornax dwarf spheroidal. *MNRAS*, 429:L89–L93.

Amorisco, N. C. and Evans, N. W. (2012a). A Troublesome Past: Chemodynamics of the Fornax Dwarf Spheroidal. *ApJL*, 756:L2.

Amorisco, N. C. and Evans, N. W. (2012b). Dark matter cores and cusps: the case of multiple stellar populations in dwarf spheroidals. *MNRAS*, 419(1):184–196.

Amorisco, N. C., Evans, N. W., and van de Ven, G. (2014a). The remnant of a merger between two dwarf galaxies in Andromeda II. *Nature*, 507:335–337.

Amorisco, N. C., Zavala, J., and de Boer, T. J. L. (2014b). Dark Matter Cores in the Fornax and Sculptor Dwarf Galaxies: Joining Halo Assembly and Detailed Star Formation Histories. *ApJL*, 782(2):L39.

Anderhalden, D., Schneider, A., Macciò, A. V., Diemand, J., and Bertone, G. (2013). Hints on the nature of dark matter from the properties of Milky Way satellites. *JCAP*, 2013(3):014.

Arraki, K. S., Klypin, A., More, S., and Trujillo-Gomez, S. (2014). Effects of baryon removal on the structure of dwarf spheroidal galaxies. *MNRAS*, 438(2):1466–1482.

Athanassoula, E., Bosma, A., and Papaioannou, S. (1987). Halo parameters of spiral galaxies. *A&A*, 179:23–40.

Avila-Reese, V., Colín, P., Valenzuela, O., D'Onghia, E., and Firmani, C. (2001). Formation and Structure of Halos in a Warm Dark Matter Cosmology. *ApJ*, 559(2):516–530.

Baes, M. and van Hese, E. (2007). Dynamical models with a general anisotropy profile. *A&A*, 471:419–432.

Bajkova, A. T. and Bobylev, V. V. (2020). Orbits of 47 Dwarf Satellite Galaxies of the Milky Way in Three Models of the Gravitational Potential with Different Masses. *arXiv e-prints*, page arXiv:2007.02350.

Barber, C., Starkenburg, E., Navarro, J. F., and McConnachie, A. W. (2015). Galactic tides and the shape and orientation of dwarf galaxy satellites. *MNRAS*, 447:1112–1125.

Battaglia, G. et al. (2006). The DART imaging and CaT survey of the Fornax dwarf spheroidal galaxy. *A&A*, 459(2):423–440.

Battaglia, G., Helmi, A., Tolstoy, E., Irwin, M., Hill, V., and Jablonka, P. (2008). The Kinematic Status and Mass Content of the Sculptor Dwarf Spheroidal Galaxy. *ApJL*, 681:L13.

Battaglia, G., Irwin, M., Tolstoy, E., de Boer, T., and Mateo, M. (2012). The Extensive Age Gradient of the Carina Dwarf Galaxy. *ApJL*, 761:L31.

Battaglia, G., Irwin, M., Tolstoy, E., Hill, V., Helmi, A., Letarte, B., and Jablonka, P. (2007). Analysis and calibration of Ca II triplet spectroscopy of red giant branch stars from VLT/FLAMES observations. *MNRAS*, 383(1):183–199.

Battaglia, G., Sollima, A., and Nipoti, C. (2015). The effect of tides on the Fornax dwarf spheroidal galaxy. *MNRAS*, 454(3):2401–2415.

Battaglia, G., Tolstoy, E., Helmi, A., Irwin, M., Parisi, P., Hill, V., and Jablonka, P. (2011). Study of the Sextans dwarf spheroidal galaxy from the DART Ca II triplet survey. *MNRAS*, 411:1013–1034.

Bechtol, K. et al. (2015). Eight New Milky Way Companions Discovered in First-year Dark Energy Survey Data. *ApJ*, 807(1):50.

Beǹitez-Llambay, A. and Frenk, C. (2020). The detailed structure and the onset of galaxy formation in low-mass gaseous dark matter haloes. *arXiv e-prints*, page arXiv:2004.06124.

Benítez-Llambay, A., Frenk, C. S., Ludlow, A. D., and Navarro, J. F. (2019). Baryon-induced dark matter cores in the EAGLE simulations. *MNRAS*, 488(2):2387–2404.

Benítez-Llambay, A., Navarro, J. F., Abadi, M. G., Gottlöber, S., Yepes, G., Hoffman, Y., and Steinmetz, M. (2013). Dwarf Galaxies and the Cosmic Web. *ApJL*, 763:L41.

Benítez-Llambay, A., Navarro, J. F., Abadi, M. G., Gottlöber, S., Yepes, G., Hoffman, Y., and Steinmetz, M. (2015). The imprint of reionization on the star formation histories of dwarf galaxies. *MNRAS*, 450:4207–4220.

Benítez-Llambay, A., Navarro, J. F., Abadi, M. G., Gottlöber, S., Yepes, G., Hoffman, Y., and Steinmetz, M. (2016). Mergers and the outside-in formation of dwarf spheroidals. *MNRAS*, 456:1185–1194.

Benson, A. J., Frenk, C. S., Lacey, C. G., Baugh, C. M., and Cole, S. (2002). The effects of photoionization on galaxy formation - II. Satellite galaxies in the Local Group. *MNRAS*, 333(1):177–190.

Bertschinger, E. (2001). Multiscale Gaussian Random Fields and Their Application to Cosmological Simulations. *ApJS*, 137(1):1–20.

Bett, P., Eke, V., Frenk, C. S., Jenkins, A., Helly, J., and Navarro, J. (2007). The spin and shape of dark matter haloes in the Millennium simulation of a Λ cold dark matter universe. *MNRAS*, 376:215–232.

Binney, J. and Tremaine, S. (1987). *Galactic dynamics*.

Bocquet, S., Saro, A., Dolag, K., and Mohr, J. J. (2015). Halo mass function: Baryon impact, fitting formulae and implications for cluster cosmology. *MNRAS*, 456:2361.

Bode, P., Ostriker, J. P., and Turok, N. (2001). Halo Formation in Warm Dark Matter Models. *ApJ*, 556(1):93–107.

Boldrini, P., Mohayaee, R., and Silk, J. (2018). Does Fornax have a cored halo? Implications for the nature of dark matter. *arXiv e-prints*, page arXiv:1806.09591.

Boldrini, P., Mohayaee, R., and Silk, J. (2019). Fornax globular cluster distributions: implications for the cusp-core problem. *MNRAS*, 485(2):2546–2557.

Bonnivard, V., Combet, C., Maurin, D., and Walker, M. G. (2015). Spherical Jeans analysis for dark matter indirect detection in dwarf spheroidal galaxies - impact of physical parameters and triaxiality. *MNRAS*, 446(3):3002–3021.

Borrow, J., Anglés-Alcázar, D., and Davé, R. (2020). Cosmological baryon transfer in the SIMBA simulations. *MNRAS*, 491(4):6102–6119.

Bose, S. et al. (2019). No cores in dark matter-dominated dwarf galaxies with bursty star formation histories. *MNRAS*, 486:4790–4804.

Bosma, A. (1978). *The distribution and kinematics of neutral hydrogen in spiral galaxies of various morphological types*. PhD thesis, -.

Bovy, J. (2015). galpy: A python Library for Galactic Dynamics. *ApJS*, 216(2):29.

Boylan-Kolchin, M., Bullock, J. S., and Kaplinghat, M. (2011). Too big to fail? The puzzling darkness of massive Milky Way subhaloes. *MNRAS*, 415(1):L40–L44.

Boylan-Kolchin, M., Bullock, J. S., and Kaplinghat, M. (2012). The Milky Way's bright satellites as an apparent failure of ΛCDM. *MNRAS*, 422(2):1203–1218.

Breddels, M. A. and Helmi, A. (2013). Model comparison of the dark matter profiles of fornax, sculptor, carina and sextans. *A&A*, 558:A35.

Breddels, M. A., Helmi, A., van den Bosch, R. C. E., van de Ven, G., and Battaglia, G. (2013). Orbit-based dynamical models of the Sculptor dSph galaxy. *MNRAS*, 433:3173–3189.

Brooks, A. M. and Zolotov, A. (2014). Why Baryons Matter: The Kinematics of Dwarf Spheroidal Satellites. *ApJ*, 786(2):87.

Bruzual, G. and Charlot, S. (2003). Stellar population synthesis at the resolution of 2003. *MNRAS*, 344:1000–1028.

Bullock, J. S. and Boylan-Kolchin, M. (2017). Small-Scale Challenges to the ΛCDM Paradigm. *ARAA*, 55(1):343–387.

Callingham, T. M., Cautun, M., Deason, A. J., Frenk, C. S., Grand, R. J. J., Marinacci, F., and Pakmor, R. (2020). The orbital phase space of contracted dark matter haloes. *MNRAS*, 495(1):12–28.

Campbell, D. J. R. et al. (2017). Knowing the unknowns: uncertainties in simple estimators of galactic dynamical masses. *MNRAS*, 469:2335–2360.

Cautun, M., Benítez-Llambay, A., Deason, A. J., Frenk, C. S., Fattahi, A., Gómez, F. A., Grand, R. J. J., Oman, K. A., Navarro, J. F., and Simpson, C. M. (2020). The Milky Way total mass profile as inferred from Gaia DR2. *MNRAS*, 494(3):4291–4313.

Cautun, M., Bose, S., Frenk, C. S., Guo, Q., Han, J., Hellwing, W. A., Sawala, T., and Wang, W. (2015). Planes of satellite galaxies: when exceptions are the rule. *MNRAS*, 452(4):3838–3852.

Chabrier, G. (2003). Galactic Stellar and Substellar Initial Mass Function. *PASP*, 115:763–795.

Cicuéndez, L. and Battaglia, G. (2018). Appearances can be deceiving: clear signs of accretion in the seemingly ordinary Sextans dSph. *MNRAS*, 480:251–260.

Cole, D. R., Dehnen, W., Read, J. I., and Wilkinson, M. I. (2012). The mass distribution of the Fornax dSph: constraints from its globular cluster distribution. *MNRAS*, 426(1):601–613.

Cole, D. R., Dehnen, W., and Wilkinson, M. I. (2011). Weakening dark matter cusps by clumpy baryonic infall. *MNRAS*, 416:1118–1134.

Cole, S. et al. (2005). The 2dF Galaxy Redshift Survey: power-spectrum analysis of the final data set and cosmological implications. *MNRAS*, 362(2):505–534.

Cole, S., Lacey, C. G., Baugh, C. M., and Frenk, C. S. (2000). Hierarchical galaxy formation. *MNRAS*, 319(1):168–204.

Coleman, M., Costa, G. S. D., Bland-Hawthorn, J., Martinez-Delgado, D., Freeman, K. C., and Malin, D. (2003). Shell structure in the fornax dwarf spheroidal galaxy. *The Astronomical Journal*, 127:832–839.

Colless, M. et al. (2001). The 2df galaxy redshift survey: Spectra and redshifts. *MNRAS*, 328(4):1039–1063.

Contenta, F. et al. (2018). Probing dark matter with star clusters: a dark matter core in the ultra-faint dwarf Eridanus II. *MNRAS*, 476(3):3124–3136.

Correa, C. A. (2020). Constraining Velocity-dependent Self-Interacting Dark Matter with the Milky Way's dwarf spheroidal galaxies. *arXiv e-prints*, page arXiv:2007.02958.

Correa, C. A., Wyithe, J. S. B., Schaye, J., and Duffy, A. R. (2015a). The accretion history of dark matter haloes - I. The physical origin of the universal function. *MNRAS*, 450(2):1514–1520.

Correa, C. A., Wyithe, J. S. B., Schaye, J., and Duffy, A. R. (2015b). The accretion history of dark matter haloes - II. The connections with the mass power spectrum and the density profile. *MNRAS*, 450(2):1521–1537.

Correa, C. A., Wyithe, J. S. B., Schaye, J., and Duffy, A. R. (2015c). The accretion history of dark matter haloes - III. A physical model for the concentration-mass relation. *MNRAS*, 452(2):1217–1232.

Crain, R. A. et al. (2015). The EAGLE simulations of galaxy formation: calibration of subgrid physics and model variations. *MNRAS*, 450:1937–1961.

Croton, D. J. et al. (2006). The many lives of active galactic nuclei: cooling flows, black holes and the luminosities and colours of galaxies. *MNRAS*, 365(1):11–28.

Dalla Vecchia, C. and Schaye, J. (2012). Simulating galactic outflows with thermal supernova feedback. *MNRAS*, 426:140–158.

Davis, M., Efstathiou, G., Frenk, C. S., and White, S. D. M. (1985). The evolution of large-scale structure in a universe dominated by cold dark matter. *ApJ*, 292:371–394.

Davis, M., Huchra, J., Latham, D. W., and Tonry, J. (1982). A survey of galaxy redshifts. II. The large scale space distribution. *ApJ*, 253:423–445.

Davé, R., Anglés-Alcázar, D., Narayanan, D., Li, Q., Rafieferantsoa, M. H., and Appleby, S. (2019). simba: Cosmological simulations with black hole growth and feedback. *MNRAS*, 486(2):2827–2849.

Davé, R., Rafieferantsoa, M. H., Thompson, R. J., and Hopkins, P. F. (2016). Mufasa: Galaxy star formation, gas, and metal properties across cosmic time. *MNRAS*, 467:115.

de Boer, T. J. L. et al. (2012). The star formation and chemical evolution history of the Fornax dwarf spheroidal galaxy. *A&A*, 544:A73.

de Boer, T. J. L., Tolstoy, E., Saha, A., and Olszewski, E. W. (2013). A new study of stellar substructures in the Fornax dwarf spheroidal galaxy . *A & A*, 551:A103.

Deason, A., Wetzel, A., and Garrison-Kimmel, S. (2014). Satellite dwarf galaxies in a hierarchical universe: The prevalence of dwarf-dwarf major mergers. *ApJ*, 794:115.

de Blok, W. J. G. (2010). The Core-Cusp Problem. *Advances in Astronomy*, 2010:789293.

Dehnen, W. (2009). Tailoring triaxial N-body models via a novel made-to-measure method. *MNRAS*, 395(2):1079–1086.

del Pino, A., Aparicio, A., and Hidalgo, S. L. (2015). Merger traces in the spatial distribution of stellar populations in the fornax dsph galaxy. *MNRAS*, 454:3996–4012.

del Pino, A., Aparicio, A., Hidalgo, S. L., and Łokas, E. L. (2017a). Rotating stellar populations in the Fornax dSph galaxy. *MNRAS*, 465:3708–3723.

del Pino, A., Łokas, E. L., Hidalgo, S. L., and Fouquet, S. (2017b). The structure of Andromeda II dwarf spheroidal galaxy. *MNRAS*, 469:4999–5015.

del Popolo, A. and Kroupa, P. (2009). Density profiles of dark matter haloes on galactic and cluster scales. *A&A*, 502:733–747.

Diakogiannis, F. I., Lewis, G. F., Ibata, R. A., Guglielmo, M., Kafle, P. R., Wilkinson, M. I., and Power, C. (2017). A novel JEAnS analysis of the Fornax dwarf using evolutionary algorithms: mass follows light with signs of an off-centre merger. *MNRAS*, 470(2):2034–2053.

Diakogiannis, F. I., Lewis, G. F., Ibata, R. A., Guglielmo, M., Wilkinson, M. I., and Power, C. (2019). Reliable mass calculation in spherical gravitating systems. *MNRAS*, 482(3):3356–3372.

Diemand, J., Kuhlen, M., Madau, P., Zemp, M., Moore, B., Potter, D., and Stadel, J. (2008). Clumps and streams in the local dark matter distribution. *Nature*, 454(7205):735–738.

Digby, R. et al. (2019). The star formation histories of dwarf galaxies in local group cosmological simulations. *MNRAS*.

Doane, D. P. (1976). Aesthetic frequency classifications. *The American Statistician*, 30(4):181–183.

Dolag, K., Borgani, S., Murante, G., and Springel, V. (2009). Substructures in hydrodynamical cluster simulations. *MNRAS*, 399(2):497–514.

Dolphin, A. E., Weisz, D. R., Skillman, E. D., and Holtzman, J. A. (2005). Star Formation Histories of Local Group Dwarf Galaxies. *preprint (astro-ph/0506430)*.

Dong, S.-F., Lin, D. N. C., and Murray, S. D. (2003). Star formation and feedback in dwarf galaxies. *ApJ*, 596:930.

D'Onghia, E., Springel, V., Hernquist, L., and Keres, D. (2010a). Substructure Depletion in the Milky Way Halo by the Disk. *ApJ*, 709(2):1138–1147.

D'Onghia, E., Vogelsberger, M., Faucher-Giguere, C.-A., and Hernquist, L. (2010b). Quasi-resonant Theory of Tidal Interactions. *ApJ*, 725(1):353–368.

Dooley, G. A., Peter, A. H. G., Vogelsberger, M., Zavala, J., and Frebel, A. (2016). Enhanced tidal stripping of satellites in the galactic halo from dark matter self-interactions. *MNRAS*, 461(1):710–727.

Drlica-Wagner, A. et al. (2015). Eight Ultra-faint Galaxy Candidates Discovered in Year Two of the Dark Energy Survey. *ApJ*, 813(2):109.

Dubinski, J. and Carlberg, R. G. (1991). The structure of cold dark matter halos. *ApJ*, 378:496–503.

Dubois, Y. et al. (2014). Dancing in the dark: galactic properties trace spin swings along the cosmic web . *MNRAS*, 444:1453–1468.

Dutton, A. A. and Macciò, A. V. (2014). Cold dark matter haloes in the Planck era: evolution of structural parameters for Einasto and NFW profiles. *MNRAS*, 441(4):3359–3374.

Dutton, A. A., Macciò, A. V., Frings, J., Wang, L., Stinson, G. S., Penzo, C., and Kang, X. (2016). NIHAO V: too big does not fail - reconciling the conflict between ΛCDM predictions and the circular velocities of nearby field galaxies. *MNRAS*, 457(1):L74–L78.

Efstathiou, G. (1992). Suppressing the formation of dwarf galaxies via photoionization. *MNRAS*, 256(2):43P–47P.

Efstathiou, G., Sutherland, W. J., and Maddox, S. J. (1990). The cosmological constant and cold dark matter. *Nature*, 348(6303):705–707.

Einasto, J., Kaasik, A., and Saar, E. (1974a). Dynamic evidence on massive coronas of galaxies. *Nature*, 250(5464):309–310.

Einasto, J., Saar, E., Kaasik, A., and Chernin, A. D. (1974b). Missing mass around galaxies - Morphological evidence. *Nature*, 252:111–113.

Eisenstein, D. J. et al. (2005). Detection of the Baryon Acoustic Peak in the Large-Scale Correlation Function of SDSS Luminous Red Galaxies. *ApJ*, 633(2):560–574.

El-Badry, K., Wetzel, A., Geha, M., Hopkins, P. F., Kereš, D., Chan, T. K., and Faucher-Giguère, C.-A. (2016). Breathing FIRE: How Stellar Feedback Drives Radial Migration, Rapid Size Fluctuations, and Population Gradients in Low-mass Galaxies. *ApJ*, 820:131.

El-Zant, A., Shlosman, I., and Hoffman, Y. (2001). Dark Halos: The Flattening of the Density Cusp by Dynamical Friction. *ApJ*, 560:636–643.

Elbert, O. D., Bullock, J. S., Garrison-Kimmel, S., Rocha, M., Oñorbe, J., and Peter, A. H. G. (2015). Core formation in dwarf haloes with self-interacting dark matter: no fine-tuning necessary. *MNRAS*, 453(1):29–37.

Erkal, D. and Belokurov, V. (2015). Properties of dark subhaloes from gaps in tidal streams. *MNRAS*, 454(4):3542–3558.

Errani, R. and Peñarrubia, J. (2020). Can tides disrupt cold dark matter subhaloes? *MNRAS*, 491(4):4591–4601.

Errani, R., Peñarrubia, J., and Walker, M. G. (2018). Systematics in virial mass estimators for pressure-supported systems. *MNRAS*, 481(4):5073–5090.

Errani, R., Penarrubia, J., and Tormen, G. (2015). Constraining the distribution of dark matter in dwarf spheroidal galaxies with stellar tidal streams. *MNRAS*, 449:L46–L50.

Faber, S. M. and Gallagher, J. S. (1979). Masses and mass-to-light ratios of galaxies. *ARAA*, 17:135–187.

Fattahi, A. et al. (2016a). The APOSTLE project: Local Group kinematic mass constraints and simulation candidate selection. *MNRAS*, 457:844–856.

Fattahi, A., Navarro, J. F., and Frenk, C. S. (2020). The missing dwarf galaxies of the Local Group. *MNRAS*, 493(2):2596–2605.

Fattahi, A., Navarro, J. F., Frenk, C. S., Oman, K. A., Sawala, T., and Schaller, M. (2018). Tidal stripping and the structure of dwarf galaxies in the Local Group. *MNRAS*, 476(3):3816–3836.

Fattahi, A., Navarro, J. F., Sawala, T., Frenk, C. S., Sales, L. V., Oman, K., Schaller, M., and Wang, J. (2016b). The cold dark matter content of Galactic dwarf spheroidals: no cores, no failures, no problem. *arXiv e-prints*, page arXiv:1607.06479.

Feng, Y., Di-Matteo, T., Croft, R. A., Bird, S., Battaglia, N., and Wilkins, S. (2015). The bluetides simulation: First galaxies and reionization. *MNRAS*, 455:2778–2791.

Ferrero, I., Abadi, M. G., Navarro, J. F., Sales, L. V., and Gurovich, S. (2012). The dark matter haloes of dwarf galaxies: a challenge for the Λ cold dark matter paradigm? *MNRAS*, 425(4):2817–2823.

Fillingham, S. P., Cooper, M. C., Kelley, T., Rodriguez Wimberly, M. K., Boylan-Kolchin, M., Bullock, J. S., Garrison-Kimmel, S., Pawlowski, M. S., and Wheeler, C. (2019). Characterizing the Infall Times and Quenching Timescales of Milky Way Satellites with *Gaia* Proper Motions. *arXiv e-prints*, page arXiv:1906.04180.

Fitts, A. et al. (2017). Fire in the field: simulating the threshold of galaxy formation. *MNRAS*, 471(3):3547–3562.

Flores, R. A. and Primack, J. R. (1994). Observational and theoretical constraints on singular dark matter halos. *ApJL*, 427:L1–L4.

Foreman-Mackey, D., Hogg, D. W., Lang, D., and Goodman, J. (2013). emcee: The MCMC Hammer. *PASP*, 125(925):306.

Fouquet, S., Łokas, E. L., del Pino, A., and Ebrová, I. (2017). Formation of Andromeda II via a gas-rich major merger and an interaction with M31. *MNRAS*, 464:2717–2729.

Frenk, C. S. et al. (1999). The Santa Barbara Cluster Comparison Project: A Comparison of Cosmological Hydrodynamics Solutions. *ApJ*, 525(2):554–582.

Frenk, C. S., White, S. D. M., and Davis, M. (1983). Nonlinear evolution of large-scale structure in the universe. *ApJ*, 271:417–430.

Frenk, C. S., White, S. D. M., Davis, M., and Efstathiou, G. (1988). The Formation of Dark Halos in a Universe Dominated by Cold Dark Matter. *ApJ*, 327:507.

Frenk, C. S., White, S. D. M., Efstathiou, G., and Davis, M. (1985). Cold dark matter, the structure of galactic haloes and the origin of the Hubble sequence. *Nature*, 317(6038):595–597.

Fritz, T. K., Battaglia, G., Pawlowski, M. S., Kallivayalil, N., van der Marel, R., Sohn, S. T., Brook, C., and Besla, G. (2018). Gaia DR2 proper motions of dwarf galaxies within 420 kpc. Orbits, Milky Way mass, tidal influences, planar alignments, and group infall. *A&A*, 619:A103.

Gaia Collaboration et al. (2016). Gaia Data Release 1. Summary of the astrometric, photometric, and survey properties. *A&A*, 595:A2.

Gaia Collaboration et al. (2018). Gaia Data Release 2. Kinematics of globular clusters and dwarf galaxies around the Milky Way. *A&A*, 616:A12.

Gallart, C. et al. (2015). The ACS LCID project: On the origin of dwarf galaxy types: a manifestation of the halo assembly bias? *ApJ*, 811:L18.

Gao, L., White, S. D. M., Jenkins, A., Frenk, C. S., and Springel, V. (2005). Early structure in ΛCDM. *MNRAS*, 363(2):379–392.

Garrison-Kimmel, S. et al. (2017). Not so lumpy after all: modelling the depletion of dark matter subhaloes by Milky Way-like galaxies. *MNRAS*, 471(2):1709–1727.

Garrison-Kimmel, S. et al. (2019). The Local Group on FIRE: dwarf galaxy populations across a suite of hydrodynamic simulations. *MNRAS*, 487(1):1380–1399.

Gaskins, J. M. (2016). A review of indirect searches for particle dark matter. *Contemporary Physics*, 57(4):496–525.

Genina, A. et al. (2018). The core-cusp problem: a matter of perspective. *MNRAS*, 474:1398–1411.

Gilmore, G., Wilkinson, M. I., Wyse, R. F. G., Kleyna, J. T., Koch, A., Evans, N. W., and Grebel, E. K. (2007). The Observed Properties of Dark Matter on Small Spatial Scales. *ApJ*, 663:948–959.

Goerdt, T., Moore, B., Read, J. I., Stadel, J., and Zemp, M. (2006). Does the Fornax dwarf spheroidal have a central cusp or core? *MNRAS*, 368(3):1073–1077.

González, Á. (2009). Measurement of areas on a sphere using fibonacci and latitude–longitude lattices. *Mathematical Geosciences*, 42(1):49.

González-Samaniego, A., Bullock, J. S., Boylan-Kolchin, M., Fitts, A., Elbert, O. D., Hopkins, P. F., Kereš, D., and Faucher-Giguère, C.-A. (2017). Dwarf galaxy mass estimators versus cosmological simulations. *MNRAS*, 472(4):4786–4796.

Górski, K. M., Hivon, E., Banday, A. J., Wandelt, B. D., Hansen, F. K., Reinecke, M., and Bartelmann, M. (2005). HEALPix: A Framework for High-Resolution Discretization and Fast Analysis of Data Distributed on the Sphere. *ApJ*, 622:759–771.

Gottlöber, S., Hoffman, Y., and Yepes, G. (2010). Constrained local universe simulations (clues). In Wagner, S., Steinmetz, M., Bode, A., and Müller, M. M., editors, *High Performance Computing in Science and Engineering, Garching/Munich 2009*, pages 309–322, Berlin, Heidelberg. Springer Berlin Heidelberg.

Green, S. B. and van den Bosch, F. C. (2019). The tidal evolution of dark matter substructure - I. subhalo density profiles. *MNRAS*, 490(2):2091–2101.

Haardt, F. and Madau, P. (2001). Modelling the UV/X-ray cosmic background with CUBA. In Neumann, D. M. and Tran, J. T. V., editors, *Clusters of Galaxies and the High Redshift Universe Observed in X-rays*.

Hahn, O. and Abel, T. (2011). Multi-scale initial conditions for cosmological simulations. *MNRAS*, 415(3):2101–2121.

Han, J., Cole, S., Frenk, C. S., Benitez-Llambay, A., and Helly, J. (2018). HBT+: an improved code for finding subhaloes and building merger trees in cosmological simulations. *MNRAS*, 474:604–617.

Han, J., Jing, Y. P., Wang, H., and Wang, W. (2012). Resolving subhaloes' lives with the hierarchical bound-tracing algorithm. *MNRAS*, 427(3):2437–2449.

Hanany, S. et al. (2000). MAXIMA-1: A Measurement of the Cosmic Microwave Background Anisotropy on Angular Scales of 10'-5°. *ApJL*, 545(1):L5–L9.

Hargis, J. R., Willman, B., and Peter, A. H. G. (2014). Too Many, Too Few, or Just Right? The Predicted Number and Distribution of Milky Way Dwarf Galaxies. *ApJL*, 795(1):L13.

Hastie, T., Tibshirani, R., and Friedman, J. (2001). *The Elements of Statistical Learning*. Springer Series in Statistics. Springer New York Inc., New York, NY, USA.

Hausammann, L., Revaz, Y., and Jablonka, P. (2019). Satellite dwarf galaxies: stripped but not quenched. *A&A*, 624:A11.

Hayashi, K., Chiba, M., and Ishiyama, T. (2020). Diversity of dark matter density profiles in the Galactic dwarf spheroidal satellites. *arXiv e-prints*, page arXiv:2007.13780.

Hayashi, K., Fabrizio, M., Łokas, E. L., Bono, G., Monelli, M., Dall'Ora, M., and Stetson, P. B. (2018). Dark halo structure in the carina dwarf spheroidal galaxy: joint analysis of multiple stellar components. *MNRAS*, 481:250.

Helmi, A. et al. (2006). A New View of the Dwarf Spheroidal Satellites of the Milky Way from VLT FLAMES: Where Are the Very Metal-poor Stars? *ApJ*, 651(2):L121–L124.

Henon, M. (1970). Numerical exploration of the restricted problem. VI. Hill's case: Non-periodic orbits. *A&A*, 9:24–36.

Ho, N. et al. (2012). Stellar Kinematics of the Andromeda II Dwarf Spheroidal Galaxy. *ApJ*, 758:124.

Hoffman, Y. and Ribak, E. (1991). Constrained Realizations of Gaussian Fields: A Simple Algorithm. *ApJL*, 380:L5.

Hopkins, P. F., Narayanan, D., and Murray, N. (2013). The meaning and consequences of star formation criteria in galaxy models with resolved stellar feedback. *MNRAS*, 432(4):2647–2653.

Hui, L., Ostriker, J. P., Tremaine, S., and Witten, E. (2017). Ultralight scalars as cosmological dark matter. *Ph.Rv.D*, 95(4):043541.

Ibata, R. A. et al. (2013). A vast, thin plane of corotating dwarf galaxies orbiting the Andromeda galaxy. *Nature*, 493(7430):62–65.

Irrgang, A., Wilcox, B., Tucker, E., and Schiefelbein, L. (2012). Milky way mass models for orbit calculations. *A&A*, 549:A137.

Jardel, J. R. and Gebhardt, K. (2012). The dark matter density profile of the fornax dwarf. *ApJ*, 746(1):89.

Jasche, J. and Wandelt, B. D. (2013). Methods for Bayesian Power Spectrum Inference with Galaxy Surveys. *ApJ*, 779(1):15.

Jenkins, A. (2013). A new way of setting the phases for cosmological multiscale Gaussian initial conditions. *MNRAS*, 434:2094–2120.

Jenkins, A. et al. (1998). Evolution of Structure in Cold Dark Matter Universes. *ApJ*, 499(1):20–40.

Kahn, F. D. and Woltjer, L. (1959). Intergalactic Matter and the Galaxy. *ApJ*, 130:705.

Kalnajs, A. (1983). Mass distribution and dark halos: Discussion. In Athanassoula, E., editor, *Internal Kinematics and Dynamics of Galaxies*, volume 100 of *IAU Symposium*, pages 87–88.

Kaplinghat, M., Tulin, S., and Yu, H.-B. (2016). Dark Matter Halos as Particle Colliders: Unified Solution to Small-Scale Structure Puzzles from Dwarfs to Clusters. *PRL*, 116(4):041302.

Kaplinghat, M., Valli, M., and Yu, H.-B. (2019). Too big to fail in light of Gaia. *MNRAS*, 490(1):231–242.

Katz, N. and White, S. D. M. (1993). Hierarchical Galaxy Formation: Overmerging and the Formation of an X-Ray Cluster. *ApJ*, 412:455.

Kauffmann, G., White, S. D. M., and Guiderdoni, B. (1993). The formation and evolution of galaxies within merging dark matter haloes. *MNRAS*, 264:201–218.

Kawata, D., Arimoto, N., Cen, R., and Gibson, B. K. (2006). Origin of Two Distinct Populations in Dwarf Spheroidal Galaxies. *ApJ*, 641:785–794.

Keenan, D. W. and Innanen, K. A. (1975). Numerical investigation of galactic tidal effects on spherical stellar systems. *AJ*, 80:290–302.

Kent, S. M. (1986). Dark matter in spiral galaxies. I. Galaxies with optical rotation curves. *AJ*, 91:1301–1327.

Kent, S. M. (1987). Dark Matter in Spiral Galaxies. II. Galaxies with H I Rotation Curves. *AJ*, 93:816.

Kent, S. M. (1988). Dark Matter in Spiral Galaxies. III. The SA Galaxies. *AJ*, 96:514.

Khandai, N., Matteo, T. D., Croft, R., Wilkins, S. M., Feng, Y., Tucker, E., DeGraf, C., and Liu, M.-S. (2014). The massiveblack-ii simulation: The evolution of halos and galaxies to z 0. *MNRAS*, 450:1349–1374.

Kim, S. Y., Peter, A. H. G., and Hargis, J. R. (2018). Missing satellites problem: Completeness corrections to the number of satellite galaxies in the milky way are consistent with cold dark matter predictions. *Phys. Rev. Lett.*, 121:211302.

Kirby, E. N., Bullock, J. S., Boylan-Kolchin, M., Kaplinghat, M., and Cohen, J. G. (2014). The dynamics of isolated Local Group galaxies. *MNRAS*, 439(1):1015–1027.

Kirby, E. N., Cohen, J. G., Guhathakurta, P., Cheng, L., Bullock, J. S., and Gallazzi, A. (2013). The Universal Stellar Mass-Stellar Metallicity Relation for Dwarf Galaxies. *ApJ*, 779(2):102.

Kirby, E. N., Guhathakurta, P., Bolte, M., Sneden, C., and Geha, M. C. (2009). Multi-element Abundance Measurements from Medium-resolution Spectra. I. The Sculptor Dwarf Spheroidal Galaxy. *ApJ*, 705(1):328–346.

Kirby, E. N., Lanfranchi, G. A., Simon, J. D., Cohen, J. G., and Guhathakurta, P. (2010). Multi-Element Abundance Measurements from Medium-Resolution Spectra. III. Metallicity Distributions of Milky Way Dwarf Satellite Galaxies . *ApJ*, 727:78.

Klimentowski, J., Łokas, E. L., Kazantzidis, S., Prada, F., Mayer, L., and Mamon, G. A. (2007). Mass modelling of dwarf spheroidal galaxies: the effect of unbound stars from tidal tails and the Milky Way. *MNRAS*, 378(1):353–368.

Klypin, A., Hoffman, Y., Kravtsov, A. V., and Gottlöber, S. (2003). Constrained Simulations of the Real Universe: The Local Supercluster. *ApJ*, 596(1):19–33.

Klypin, A., Kravtsov, A. V., Valenzuela, O., and Prada, F. (1999). Where Are the Missing Galactic Satellites? *ApJ*, 522(1):82–92.

Komatsu, E. et al. (2011). Seven-year Wilkinson Microwave Anisotropy Probe (WMAP) Observations: Cosmological Interpretation. *ApJs*, 192:18.

Koposov, S. and Belokurov, V. (2008). Observational Constraints on the “Missing Satellite” Problem from SDSS. *Astrophysics and Space Science Proceedings*, 5:195.

Koposov, S. E., Belokurov, V., Torrealba, G., and Evans, N. W. (2015). Beasts of the Southern Wild: Discovery of Nine Ultra Faint Satellites in the Vicinity of the Magellanic Clouds. *ApJ*, 805(2):130.

Kowalczyk, K., del Pino, A., Łokas, E. L., and Valluri, M. (2019). Schwarzschild dynamical model of the Fornax dwarf spheroidal galaxy. *MNRAS*, 482(4):5241–5249.

Kowalczyk, K., Łokas, E. L., Kazantzidis, S., and Mayer, L. (2013). Can we measure the slopes of density profiles in dwarf spheroidal galaxies? *MNRAS*, 431:2796–2807.

Kowalczyk, K., Łokas, E. L., and Valluri, M. (2017). Recovering the mass profile and orbit anisotropy of mock dwarf galaxies with Schwarzschild modelling. *MNRAS*, 470(4):3959–3969.

Kowalczyk, K., Łokas, E. L., and Valluri, M. (2018). The effect of non-sphericity on mass and anisotropy measurements in dSph galaxies with Schwarzschild method. *MNRAS*, 476(3):2918–2930.

Kravtsov, A. V., Gnedin, O. Y., and Klypin, A. A. (2004). The Tumultuous Lives of Galactic Dwarfs and the Missing Satellites Problem. *ApJ*, 609(2):482–497.

Kroupa, P., Theis, C., and Boily, C. M. (2005). The great disk of Milky-Way satellites and cosmological sub-structures. *A&A*, 431:517–521.

Kunkel, W. E. and Demers, S. (1976). The Magellanic Plane. In *The Galaxy and the Local Group*, volume 182, page 241.

Kuzio de Naray, R., McGaugh, S. S., de Blok, W. J. G., and Bosma, A. (2006). High-Resolution Optical Velocity Fields of 11 Low Surface Brightness Galaxies. *ApJs*, 165:461–479.

Lancaster, L., Giovanetti, C., Mocz, P., Kahn, Y., Lisanti, M., and Spergel, D. N. (2020). Dynamical friction in a Fuzzy Dark Matter universe. *JCAP*, 2020(1):001.

Laporte, C. F. P., Walker, M. G., and Peñarrubia, J. (2013a). Measuring the slopes of mass profiles for dwarf spheroidals in triaxial cold dark matter potentials. *MNRAS*, 433:L54–L58.

Laporte, C. F. P., White, S. D. M., Naab, T., and Gao, L. (2013b). The growth in size and mass of cluster galaxies since z = 2. *MNRAS*, 435:901–909.

Letarte, B. et al. (2010). A high-resolution VLT/FLAMES study of individual stars in the centre of the Fornax dwarf spheroidal galaxy. *A&A*, 523:A17.

Leung, G. Y. C., Leaman, R., van de Ven, G., and Battaglia, G. (2020). A dwarf-dwarf merger and dark matter core as a solution to the globular cluster problems in the Fornax dSph. *MNRAS*, 493(1):320–336.

Libeskind, N. I., Hoffman, Y., Tully, R. B., Courtois, H. M., Pomarède, D., Gottlöber, S., and Steinmetz, M. (2015). Planes of satellite galaxies and the cosmic web. *MNRAS*, 452(1):1052–1059.

Libeskind, N. I., Knebe, A., Hoffman, Y., and Gottlöber, S. (2014). The universal nature of subhalo accretion. *MNRAS*, 443(2):1274–1280.

Łokas, E. L. (2002). Dark matter distribution in dwarf spheroidal galaxies. *MNRAS*, 333(3):697–708.

Łokas, E. L. (2009). The mass and velocity anisotropy of the Carina, Fornax, Sculptor and Sextans dwarf spheroidal galaxies. *MNRAS*, 394(1):L102–L106.

Łokas, E. L., Ebrová, I., Pino, A. d., and Semczuk, M. (2014). Andromeda II as a merger remnant. *MNRAS: Letters*, 445(1):L6–L10.

Łokas, E. L. and Mamon, G. A. (2003). Dark matter distribution in the Coma cluster from galaxy kinematics: breaking the mass-anisotropy degeneracy. *MNRAS*, 343(2):401–412.

Łokas, E. L., Mamon, G. A., and Prada, F. (2005). Dark matter distribution in the Draco dwarf from velocity moments. *MNRAS*, 363(3):918–928.

Lovell, M. R. et al. (2012). The haloes of bright satellite galaxies in a warm dark matter universe. *MNRAS*, 420(3):2318–2324.

Lovell, M. R., Gonzalez-Perez, V., Bose, S., Boyarsky, A., Cole, S., Frenk, C. S., and Ruchayskiy, O. (2016). Addressing the too big to fail problem with baryon physics and sterile neutrino dark matter. *MNRAS*, 468:2836.

Lovell, M. R., Hellwing, W., Ludlow, A., Zavala, J., Robertson, A., Fattahi, A., Frenk, C. S., and Hardwick, J. (2020). Local Group star formation in warm and self-interacting dark matter cosmologies. *arXiv e-prints*, page arXiv:2002.11129.

Ludlow, A. D., Schaye, J., and Bower, R. (2019a). Numerical convergence of simulations of galaxy formation: the abundance and internal structure of cold dark matter haloes. *MNRAS*, 488(3):3663–3684.

Ludlow, A. D., Schaye, J., Schaller, M., and Bower, R. (2020). Numerical convergence of hydrodynamical simulations of galaxy formation: the abundance and internal structure of galaxies and their cold dark matter haloes. *MNRAS*, 493(2):2926–2951.

Ludlow, A. D., Schaye, J., Schaller, M., and Richings, J. (2019b). Energy equipartition between stellar and dark matter particles in cosmological simulations results in spurious growth of galaxy sizes. *MNRAS*, 488(1):L123–L128.

Lynden-Bell, D. (1976). Dwarf galaxies and globular clusters in high velocity hydrogen streams. *MNRAS*, 174:695–710.

Lyubimov, V., Novikov, E., Nozik, V., Tretyakov, E., and Kosik, V. (1980). An estimate of anti-electron-neutrino mass from the beta spectrum of tritium in the valine molecule. *Yad. Fiz.*, 32:301–302.

Macciò, A. V., Udrescu, S. M., Dutton, A. A., Obreja, A., Wang, L., Stinson, G. R., and Kang, X. (2016). NIHAO X: reconciling the local galaxy velocity function with cold dark matter via mock H I observations. *MNRAS*, 463(1):L69–L73.

Madau, P., Shen, S., and Governato, F. (2014). Dark Matter Heating and Early Core Formation in Dwarf Galaxies. *ApJL*, 789(1):L17.

Maddox, S. J., Efstathiou, G., Sutherland, W. J., and Loveday, J. (1990). Galaxy correlations on large scales. *MNRAS*, 242:43.

Mamon, G. A., Biviano, A., and Boué, G. (2013). MAMPOSSt: Modelling Anisotropy and Mass Profiles of Observed Spherical Systems - I. Gaussian 3D velocities. *MNRAS*, 429(4):3079–3098.

Mashchenko, S., Wadsley, J., and Couchman, H. M. P. (2008). Stellar Feedback in Dwarf Galaxy Formation. *Science*, 319:174.

Massari, D., Breddels, M. A., Helmi, A., Posti, L., Brown, A. G. A., and Tolstoy, E. (2018). Three-dimensional motions in the Sculptor dwarf galaxy as a glimpse of a new era. *Nature Astronomy*, 2:156–161.

Mateo, M. L. (1998). Dwarf Galaxies of the Local Group. *ARAA*, 36:435–506.

McCarthy, I. G., Schaye, J., Bird, S., and Brun, A. M. C. L. (2016). The BAHAMAS project: Calibrated hydrodynamical simulations for large-scale structure cosmology . *MNRAS*, 465:2936.

McConnachie, A. W. (2012). The observed properties of dwarf galaxies in and around the local group. *AJ*, 144:4.

McMillan, P. J. (2016). The mass distribution and gravitational potential of the milky way. *MNRAS*, 465:76.

Meadows, N., Navarro, J. F., Santos-Santos, I., Benítez-Llambay, A., and Frenk, C. (2020). Cusp or core? Revisiting the globular cluster timing problem in Fornax. *MNRAS*, 491(3):3336–3342.

Melchiorri, A., Ade, P. A. R., de Bernardis, P., Bock, J. J., Borrill, J., Boscaleri, A., Crill, B. P., De Troia, G., Farese, P., Ferreira, P. G., and et al. (2000). A measurement of ω from the north american test flight of boomerang. *ApJ*, 536(2):L63–L66.

Merrifield, M. R. and Kent, S. M. (1990). Fourth moments and the dynamics of spherical systems. *AJ*, 99:1548–1557.

Merritt, D. (1987). The Distribution of Dark Matter in the Coma Cluster. *ApJ*, 313:121.

Metz, M. and Kroupa, P. (2007). Dwarf spheroidal satellites: are they of tidal origin? *MNRAS*, 376(1):387–392.

Metz, M., Kroupa, P., and Jerjen, H. (2007). The spatial distribution of the Milky Way and Andromeda satellite galaxies. *MNRAS*, 374(3):1125–1145.

Metz, M., Kroupa, P., and Libeskind, N. I. (2008). The Orbital Poles of Milky Way Satellite Galaxies: A Rotationally Supported Disk of Satellites. *ApJ*, 680(1):287–294.

Mo, H., van den Bosch, F. C., and White, S. (2010). *Galaxy Formation and Evolution*.

Moore, B. (1994). Evidence against dissipationless dark matter from observations of galaxy haloes. *Nature*, 370:629.

Moore, B., Ghigna, S., Governato, F., Lake, G., Quinn, T., Stadel, J., and Tozzi, P. (1999). Dark Matter Substructure within Galactic Halos. *ApJL*, 524(1):L19–L22.

Navarro, J. F., Eke, V. R., and Frenk, C. S. (1996a). The cores of dwarf galaxy haloes. *MNRAS*, 283:L72–L78.

Navarro, J. F. et al. (2009). The diversity and similarity of simulated cold dark matter haloes. *Monthly Notices of the Royal Astronomical Society*, 402(1):21–34.

Navarro, J. F., Frenk, C. S., and White, S. D. M. (1995). The assembly of galaxies in a hierarchically clustering universe. *Monthly Notices of the Royal Astronomical Society*, 275(1):56–66.

Navarro, J. F., Frenk, C. S., and White, S. D. M. (1996b). The Structure of Cold Dark Matter Halos. *ApJ*, 462:563.

Navarro, J. F., Frenk, C. S., and White, S. D. M. (1997). A Universal Density Profile from Hierarchical Clustering. *ApJ*, 490:493–508.

Newton, O., Cautun, M., Jenkins, A., Frenk, C. S., and Helly, J. C. (2018). The total satellite population of the Milky Way. *MNRAS*, 479(3):2853–2870.

Newton, O., Cautun, M., Jenkins, A., Frenk, C. S., and Helly, J. C. (2019). The Milky Way's total satellite population and constraining the mass of the warm dark matter particle. In McQuinn, K. B. W. and Stierwalt, S., editors, *Dwarf Galaxies: From the Deep Universe to the Present*, volume 344 of *IAU Symposium*, pages 109–113.

Newville, M., Stensitzki, T., Allen, D. B., and Ingargiola, A. (2014).

Oñorbe, J., Boylan-Kolchin, M., Bullock, J. S., Hopkins, P. F., Kereš, D., Faucher-Giguère, C.-A., Quataert, E., and Murray, N. (2015). Forged in FIRE: cusps, cores and baryons in low-mass dwarf galaxies. *MNRAS*, 454(2):2092–2106.

Oh, S. H., Brook, C., Governato, F., Brinks, E., Mayer, L., de Blok, W. J. G., Brooks, A., and Walter, F. (2011). The Central Slope of Dark Matter Cores in Dwarf Galaxies: Simulations versus THINGS. *AJ*, 142:24.

Oh, S.-H., de Blok, W. J. G., Walter, F., Brinks, E., and Kennicutt, Robert C., J. (2008). High-Resolution Dark Matter Density Profiles of THINGS Dwarf Galaxies: Correcting for Noncircular Motions. *AJ*, 136(6):2761–2781.

Oh, S. H. et al. (2015). High-resolution Mass Models of Dwarf Galaxies from LITTLE THINGS. *AJ*, 149:180.

Okamoto, T., Eke, V. R., Frenk, C. S., and Jenkins, A. (2005). Effects of feedback on the morphology of galaxy discs. *MNRAS*, 363:1299–1314.

Okamoto, T., Shimizu, I., and Yoshida, N. (2014). Reproducing cosmic evolution of galaxy population from z = 4 to 0. *PASJ*, 66:70.

Oman, K. A., Marasco, A., Navarro, J. F., Frenk, C. S., Schaye, J., and Benítez-Llambay, A. (2019). Non-circular motions and the diversity of dwarf galaxy rotation curves. *MNRAS*, 482(1):821–847.

Oman, K. A., Navarro, J. F., Sales, L. V., Fattahi, A., Frenk, C. S., Sawala, T., Schaller, M., and White, S. D. M. (2016). Missing dark matter in dwarf galaxies? *MNRAS*, 460(4):3610–3623.

Orkney, M. D. A., Read, J. I., Petts, J. A., and Gieles, M. (2019). Globular clusters as probes of dark matter cusp-core transformations. *MNRAS*, 488(3):2977–2988.

Ostriker, J. P. and Peebles, P. J. E. (1973). A Numerical Study of the Stability of Flattened Galaxies: or, can Cold Galaxies Survive? *ApJ*, 186:467–480.

Ostriker, J. P., Peebles, P. J. E., and Yahil, A. (1974). The Size and Mass of Galaxies, and the Mass of the Universe. *ApJL*, 193:L1.

Pascale, R., Binney, J., Nipoti, C., and Posti, L. (2019). Action-based models for dwarf spheroidal galaxies and globular clusters. *MNRAS*, 488(2):2423–2439.

Pascale, R., Posti, L., Nipoti, C., and Binney, J. (2018). Action-based dynamical models of dwarf spheroidal galaxies: application to Fornax. *MNRAS*, 480(1):927–946.

Patel, E., Kallivayalil, N., Garavito-Camargo, N., Besla, G., Weisz, D. R., van der Marel, R. P., Boylan-Kolchin, M., Pawlowski, M. S., and Gómez, F. A. (2020). The Orbital Histories of Magellanic Satellites Using Gaia DR2 Proper Motions. *ApJ*, 893(2):121.

Pawlowski, M. S. (2016). The alignment of SDSS satellites with the VPOS: effects of the survey footprint shape. *MNRAS*, 456(1):448–458.

Pawlowski, M. S. and Kroupa, P. (2013). The rotationally stabilized VPOS and predicted proper motions of the Milky Way satellite galaxies. *MNRAS*, 435(3):2116–2131.

Pawlowski, M. S. and Kroupa, P. (2020). The Milky Way's disc of classical satellite galaxies in light of Gaia DR2. *MNRAS*, 491(2):3042–3059.

Pawlowski, M. S. and McGaugh, S. S. (2014). Co-orbiting Planes of Sub-halos are Similarly Unlikely around Paired and Isolated Hosts. *ApJL*, 789(1):L24.

Pawlowski, M. S., Pflamm-Altenburg, J., and Kroupa, P. (2012). The VPOS: a vast polar structure of satellite galaxies, globular clusters and streams around the Milky Way. *MNRAS*, 423(2):1109–1126.

Peñarrubia, J., Benson, A. J., Walker, M. G., Gilmore, G., McConnachie, A. W., and Mayer, L. (2010). The impact of dark matter cusps and cores on the satellite galaxy population around spiral galaxies. *MNRAS*, 406(2):1290–1305.

Peñarrubia, J., Navarro, J. F., and McConnachie, A. W. (2008). The Tidal Evolution of Local Group Dwarf Spheroidals. *ApJ*, 673(1):226–240.

Peñarrubia, J., Navarro, J. F., McConnachie, A. W., and Martin, N. F. (2009). The Signature of Galactic Tides in Local Group Dwarf Spheroidals. *ApJ*, 698(1):222–232.

Perlmutter, S. et al. (1999). Measurements of Ω and Λ from 42 High-Redshift Supernovae. *ApJ*, 517(2):565–586.

Pineda, J. C. B., Hayward, C. C., Springel, V., and Mendes de Oliveira, C. (2017). Rotation curve fitting and its fatal attraction to cores in realistically simulated galaxy observations. *MNRAS*, 466:63–87.

Planck Collaboration (2018). Planck 2018 results. VI. Cosmological parameters. *arXiv e-prints*, page arXiv:1807.06209.

Plummer, H. C. (1911). On the problem of distribution in globular star clusters. *MNRAS*, 71:460–470.

Pontzen, A. and Governato, F. (2012). How supernova feedback turns dark matter cusps into cores. *MNRAS*, 421:3464–3471.

Power, C., Navarro, J. F., Jenkins, A., Frenk, C. S., White, S. D. M., Springel, V., Stadel, J., and Quinn, T. (2003). The inner structure of ΛCDM haloes - I. A numerical convergence study. *MNRAS*, 338:14–34.

Pryor, C. and Kormendy, J. (1990). The dark matter halos of Draco and Ursa Minor. *AJ*, 100:127–140.

Rahmati, A., Pawlik, A. H., Raičević, M., and Schaye, J. (2013). On the evolution of the H I column density distribution in cosmological simulations. *MNRAS*, 430(3):2427–2445.

Read, J. I., Agertz, O., and Collins, M. L. M. (2016). Dark matter cores all the way down. *MNRAS*, 459(3):2573–2590.

Read, J. I. and Erkal, D. (2019). Abundance matching with the mean star formation rate: there is no missing satellites problem in the Milky Way above $M_{200} \sim 10^9$ $M_\odot$. *MNRAS*, 487(4):5799–5812.

Read, J. I. and Gilmore, G. (2005). Mass loss from dwarf spheroidal galaxies: the origins of shallow dark matter cores and exponential surface brightness profiles. *MNRAS*, 356:107–124.

Read, J. I., Iorio, G., Agertz, O., and Fraternali, F. (2017). The stellar mass-halo mass relation of isolated field dwarfs: a critical test of ΛCDM at the edge of galaxy formation. *MNRAS*, 467(2):2019–2038.

Read, J. I. and Steger, P. (2017). How to break the density-anisotropy degeneracy in spherical stellar systems. *MNRAS*, 471:4541–4558.

Read, J. I., Walker, M. G., and Steger, P. (2018). The case for a cold dark matter cusp in Draco. *MNRAS*, 481(1):860–877.

Read, J. I., Walker, M. G., and Steger, P. (2019). Dark matter heats up in dwarf galaxies. *MNRAS*, 484(1):1401–1420.

Read, J. I., Wilkinson, M. I., Evans, N. W., Gilmore, G., and Kleyna, J. T. (2006). The importance of tides for the Local Group dwarf spheroidals. *MNRAS*, 367(1):387–399.

Revaz, Y. and Jablonka, P. (2012). The dynamical and chemical evolution of dwarf spheroidal galaxies with GEAR. *A&A*, 538:A82.

Revaz, Y. and Jablonka, P. (2018). Pushing back the limits: detailed properties of dwarf galaxies in a ΛCDM universe. *A&A*, 616:A96.

Richardson, T. and Fairbairn, M. (2013a). Analytical solutions to the mass-anisotropy degeneracy with higher order Jeans analysis: a general method. *MNRAS*, 432(4):3361–3380.

Richardson, T. and Fairbairn, M. (2013b). Cores in Classical Dwarf Spheroidal Galaxies? A Dispersion-Kurtosis Jeans Analysis Without Restricted Anisotropy. *arXiv e-prints*, page arXiv:1305.0670.

Richardson, T. and Fairbairn, M. (2014). On the dark matter profile in Sculptor: breaking the β degeneracy with Virial shape parameters. *MNRAS*, 441(2):1584–1600.

Richings, J. et al. (2020). Subhalo destruction in the APOSTLE and AURIGA simulations. *MNRAS*, 492(4):5780–5793.

Riess, A. G. et al. (1998). Observational Evidence from Supernovae for an Accelerating Universe and a Cosmological Constant. *AJ*, 116(3):1009–1038.

Roberts, M. S. and Whitehurst, R. N. (1975). The rotation curve and geometry of M31 at large galactocentric distances. *ApJ*, 201:327–346.

Robertson, A. et al. (2018). The diverse density profiles of galaxy clusters with self-interacting dark matter plus baryons. *MNRAS*, 476(1):L20–L24.

Robertson, A., Harvey, D., Massey, R., Eke, V., McCarthy, I. G., Jauzac, M., Li, B., and Schaye, J. (2019). Observable tests of self-interacting dark matter in galaxy clusters: cosmological simulations with SIDM and baryons. *MNRAS*, 488(3):3646–3662.

Robertson, A., Massey, R., and Eke, V. (2017). What does the Bullet Cluster tell us about self-interacting dark matter? *MNRAS*, 465(1):569–587.

Robin, A. C., Marshall, D. J., Schultheis, M., and Reylé, C. (2012). Stellar populations in the Milky Way bulge region: towards solving the Galactic bulge and bar shapes using 2MASS data. *A&A*, 538:A106.

Robin, A. C., Reylé, C., Derrière, S., and Picaud, S. (2003). A synthetic view on structure and evolution of the Milky Way. *A&A*, 409:523–540.

Rocha, M., Peter, A. H. G., and Bullock, J. (2012). Infall times for Milky Way satellites from their present-day kinematics. *MNRAS*, 425(1):231–244.

Rocha, M., Peter, A. H. G., Bullock, J. S., Kaplinghat, M., Garrison-Kimmel, S., Oñorbe, J., and Moustakas, L. A. (2013). Cosmological simulations with self-interacting dark matter - I. Constant-density cores and substructure. *MNRAS*, 430(1):81–104.

Rodionov, S. A., Athanassoula, E., and Sotnikova, N. Y. (2009). An iterative method for constructing equilibrium phase models of stellar systems. *MNRAS*, 392(2):904–916.

Rubin, V. C., Ford, W. K., J., and Thonnard, N. (1980). Rotational properties of 21 SC galaxies with a large range of luminosities and radii, from NGC 4605 (R=4kpc) to UGC 2885 (R=122kpc). *ApJ*, 238:471–487.

Rubin, V. C., Ford, W. K., J., Thonnard, N., Roberts, M. S., and Graham, J. A. (1976a). Motion of the Galaxy and the Local Group determined from the velocity anisotropy of distant Sc I galaxies. I. The data. *AJ*, 81:687–718.

Rubin, V. C. and Ford, W. Kent, J. (1970). Rotation of the Andromeda Nebula from a Spectroscopic Survey of Emission Regions. *ApJ*, 159:379.

Rubin, V. C., Thonnard, N., Ford, W. K., J., and Roberts, M. S. (1976b). Motion of the Galaxy and the Local Group determined from the velocity anisotropy of distant Sc I galaxies. II. The analysis for the motion. *AJ*, 81:719–737.

Rusakov, V., Monelli, M., Gallart, C., Fritz, T. K., Ruiz-Lara, T., Bernard, E. J., and Cassisi, S. (2020). The bursty star formation history of the Fornax dwarf spheroidal galaxy revealed with the HST. *arXiv e-prints*, page arXiv:2002.09714.

Sales, L. V., Helmi, A., and Battaglia, G. (2010). The Effect of Tidal Stripping on Composite Stellar Populations in Dwarf Spheroidal Galaxies. *Adv. Astron.*, 2010:194345.

Sales, L. V., Navarro, J. F., Theuns, T., Schaye, J., White, S. D. M., Frenk, C. S., Crain, R. A., and Dalla Vecchia, C. (2012). The origin of discs and spheroids in simulated galaxies. *MNRAS*, 423:1544–1555.

Sánchez-Salcedo, F. J., Reyes-Iturbide, J., and Hernandez, X. (2006). An extensive study of dynamical friction in dwarf galaxies: the role of stars, dark matter, halo profiles and MOND. *MNRAS*, 370:1829–1840.

Santos-Santos, I. M. E. et al. (2020). Baryonic clues to the puzzling diversity of dwarf galaxy rotation curves. *MNRAS*, 495(1):58–77.

Sawala, T. et al. (2016). The APOSTLE simulations: solutions to the Local Group's cosmic puzzles. *MNRAS*, 457:1931–1943.

Sawala, T., Pihajoki, P., Johansson, P. H., Frenk, C. S., Navarro, J. F., Oman, K. A., and White, S. D. M. (2017). Shaken and stirred: the Milky Way's dark substructures. *MNRAS*, 467(4):4383–4400.

Schaye, J. (2004). Star Formation Thresholds and Galaxy Edges: Why and Where. *ApJ*, 609(2):667–682.

Schaye, J. and Dalla Vecchia, C. (2008). On the relation between the Schmidt and Kennicutt-Schmidt star formation laws and its implications for numerical simulations. *MNRAS*, 383:1210–1222.

Schaye, J. et al. (2015). The EAGLE project: simulating the evolution and assembly of galaxies and their environments. *MNRAS*, 446:521–554.

Schneider, A., Smith, R. E., Macciò, A. V., and Moore, B. (2012). Non-linear evolution of cosmological structures in warm dark matter models. *MNRAS*, 424(1):684–698.

Schwarzschild, M. (1979). A numerical model for a triaxial stellar system in dynamical equilibrium. *ApJ*, 232:236–247.

Shao, S., Cautun, M., and Frenk, C. S. (2019). Evolution of galactic planes of satellites in the EAGLE simulation. *MNRAS*, 488(1):1166–1179.

Shao, S., Gao, L., Theuns, T., and Frenk, C. S. (2013). The phase-space density of fermionic dark matter haloes. *MNRAS*, 430(3):2346–2357.

Simpson, C. M., Grand, R. J. J., Gómez, F. A., Marinacci, F., Pakmor, R., Springel, V., Campbell, D. J. R., and Frenk, C. S. (2018). Quenching and ram pressure stripping of simulated milky way satellite galaxies. *MNRAS*, page 748.

Smith, S. (1936). The Mass of the Virgo Cluster. *ApJ*, 83:23.

Spekkens, K., Urbancic, N., Mason, B. S., Willman, B., and Aguirre, J. E. (2014). The Dearth of Neutral Hydrogen in Galactic Dwarf Spheroidal Galaxies. *ApJ*, 795(1):L5.

Spergel, D. N. et al. (2003). First-Year Wilkinson Microwave Anisotropy Probe (WMAP) Observations: Determination of Cosmological Parameters. *ApJS*, 148(1):175–194.

Spergel, D. N. and Steinhardt, P. J. (2000). Observational Evidence for Self-Interacting Cold Dark Matter. *Physical Review Letters*, 84:3760–3763.

Springel, V. (2005). The cosmological simulation code GADGET-2. *MNRAS*, 364:1105–1134.

Springel, V. et al. (2005). Simulations of the formation, evolution and clustering of galaxies and quasars. *Nature*, 435(7042):629–636.

Springel, V. et al. (2008a). Prospects for detecting supersymmetric dark matter in the Galactic halo. *Nature*, 456(7218):73–76.

Springel, V. et al. (2008b). The Aquarius Project: the subhaloes of galactic haloes. *MNRAS*, 391:1685–1711.

Springel, V. et al. (2018). First results from the IllustrisTNG simulations: matter and galaxy clustering . *MNRAS*, 475:676.

Springel, V., Frenk, C. S., and White, S. D. M. (2006). The large-scale structure of the Universe. *Nature*, 440(7088):1137–1144.

Springel, V., White, S. D. M., Tormen, G., and Kauffmann, G. (2001). Populating a cluster of galaxies - I. Results at z=0. *MNRAS*, 328:726–750.

Starkenburg, E., Oman, K. A., Navarro, J. F., Crain, R. A., Fattahi, A., Frenk, C. S., Sawala, T., and Schaye, J. (2017). The oldest and most metal-poor stars in the APOSTLE Local Group simulations. *MNRAS*, 465:2212–2224.

Starkenburg, T. K., Helmi, A., and Sales, L. V. (2015). Dark influences ii: gas and star formation in minor mergers of dwarf galaxies with dark satellites. *A&A*, 587:A24.

Strigari, L. E. (2018). Dark matter in dwarf spheroidal galaxies and indirect detection: a review. *Reports on Progress in Physics*, 81(5):056901.

Strigari, L. E., Bullock, J. S., and Kaplinghat, M. (2007). Determining the Nature of Dark Matter with Astrometry. *ApJL*, 657(1):L1–L4.

Strigari, L. E., Bullock, J. S., Kaplinghat, M., Kravtsov, A. V., Gnedin, O. Y., Abazajian, K., and Klypin, A. A. (2006). A Large Dark Matter Core in the Fornax Dwarf Spheroidal Galaxy? *ApJ*, 652(1):306–312.

Strigari, L. E., Frenk, C. S., and White, S. D. M. (2010). Kinematics of Milky Way satellites in a Lambda cold dark matter universe. *MNRAS*, 408:2364–2372.

Strigari, L. E., Frenk, C. S., and White, S. D. M. (2014). Dynamical models for the Sculptor dwarf spheroidal in a Lambda CDM universe. *ArXiv e-prints*.

Strigari, L. E., Frenk, C. S., and White, S. D. M. (2018). Dynamical constraints on the dark matter distribution of the sculptor dwarf spheroidal from stellar proper motions. *ApJ*, 860(1):56.

Thielemann, F.-K. et al. (2003). Supernova Nucleosynthesis and Galactic Evolution. In Hillebrandt, W. and Leibundgut, B., editors, *From Twilight to Highlight: The Physics of Supernovae*, page 331.

Thoul, A. A. and Weinberg, D. H. (1996). Hydrodynamic Simulations of Galaxy Formation. II. Photoionization and the Formation of Low-Mass Galaxies. *ApJ*, 465:608.

Tollerud, E. J., Bullock, J. S., Strigari, L. E., and Willman, B. (2008). Hundreds of Milky Way Satellites? Luminosity Bias in the Satellite Luminosity Function. *ApJ*, 688(1):277–289.

Tollet, E. et al. (2016). NIHAO - IV: core creation and destruction in dark matter density profiles across cosmic time. *MNRAS*, 456:3542–3552.

Tolstoy, E. et al. (2004). Two Distinct Ancient Components in the Sculptor Dwarf Spheroidal Galaxy: First Results from the Dwarf Abundances and Radial Velocities Team. *ApJL*, 617:L119–L122.

Tolstoy, E., Hill, V., and Tosi, M. (2009). Star-Formation Histories, Abundances, and Kinematics of Dwarf Galaxies in the Local Group. *ARA&A*, 47:371–425.

Tormen, G., Bouchet, F. R., and White, S. D. M. (1997). The structure and dynamical evolution of dark matter haloes. *MNRAS*, 286(4):865–884.

Tremmel, M., Karcher, M., Governato, F., Volonteri, M., Quinn, T., Pontzen, A., Anderson, L., and Bellovary, J. (2016). The Romulus Cosmological Simulations: A Physical Approach to the Formation, Dynamics and Accretion Models of SMBHs . *MNRAS*, 470:1121.

Ural, U., Wilkinson, M. I., Read, J. I., and Walker, M. G. (2015). A low pre-infall mass for the Carina dwarf galaxy from disequilibrium modelling. *Nature Communications*, 6:7599.

van de Hulst, H. C., Raimond, E., and van Woerden, H. (1957). Rotation and density distribution of the Andromeda nebula derived from observations of the 21-cm line. *BAIN*, 14:1.

van De Ven, G., Hunter, C., Verolme, E. K., and de Zeeuw, P. T. (2003). General solution of the Jeans equations for triaxial galaxies with separable potentials. *MNRAS*, 342(4):1056–1082.

van den Bosch, F. C. and Ogiya, G. (2018). Dark matter substructure in numerical simulations: a tale of discreteness noise, runaway instabilities, and artificial disruption. *MNRAS*, 475(3):4066–4087.

van den Bosch, F. C., Ogiya, G., Hahn, O., and Burkert, A. (2018). Disruption of dark matter substructure: fact or fiction? *MNRAS*, 474(3):3043–3066.

van den Bosch, R. C. E., van de Ven, G., Verolme, E. K., Cappellari, M., and de Zeeuw, P. T. (2008). Triaxial orbit based galaxy models with an application to the (apparent) decoupled core galaxy NGC 4365. *MNRAS*, 385(2):647–666.

Vasiliev, E. (2013). A new code for orbit analysis and Schwarzschild modelling of triaxial stellar systems. *MNRAS*, 434(4):3174–3195.

Vogelsberger, M. et al. (2014a). Introducing the Illustris Project: simulating the coevolution of dark and visible matter in the Universe. *MNRAS*, 444(2):1518–1547.

Vogelsberger, M., Genel, S., Springel, V., Torrey, P., Sijacki, D., Xu, D., Snyder, G., Bird, S., Nelson, D., and Hernquist, L. (2014b). Properties of galaxies reproduced by a hydrodynamic simulation. *Nature*, 509(7499):177–182.

Vogelsberger, M., Marinacci, F., Torrey, P., and Puchwein, E. (2020). Cosmological simulations of galaxy formation. *Nature Reviews Physics*, 2(1):42–66.

Vogelsberger, M., Zavala, J., and Loeb, A. (2012). Subhaloes in self-interacting galactic dark matter haloes. *MNRAS*, 423(4):3740–3752.

Walker, M. G., Mateo, M., and Olszewski, E. W. (2008). Systemic Proper Motions of Milky Way Satellites from Stellar Redshifts: The Carina, Fornax, Sculptor, and Sextans Dwarf Spheroidals. *ApJL*, 688(2):L75.

Walker, M. G., Mateo, M., and Olszewski, E. W. (2009a). Stellar Velocities in the Carina, Fornax, Sculptor, and Sextans dSph Galaxies: Data From the Magellan/MMFS Survey. *AJ*, 137(2):3100–3108.

Walker, M. G., Mateo, M., Olszewski, E. W., Bernstein, R., Wang, X., and Woodroofe, M. (2006). Internal Kinematics of the Fornax Dwarf Spheroidal Galaxy. *AJ*, 131(4):2114–2139.

Walker, M. G., Mateo, M., Olszewski, E. W., Peñarrubia, J., Wyn Evans, N., and Gilmore, G. (2009b). A Universal Mass Profile for Dwarf Spheroidal Galaxies? *ApJ*, 704:1274–1287.

Walker, M. G. and Peñarrubia, J. (2011). A Method for Measuring (Slopes of) the Mass Profiles of Dwarf Spheroidal Galaxies. *ApJ*, 742:20.

Wang, J., Bose, S., Frenk, C. S., Gao, L., Jenkins, A., Springel, V., and White, S. D. M. (2019a). Universality in the structure of dark matter haloes over twenty orders of magnitude in halo mass. *arXiv e-prints*, page arXiv:1911.09720.

Wang, M. Y. et al. (2019b). The Morphology and Structure of Stellar Populations in the Fornax Dwarf Spheroidal Galaxy from Dark Energy Survey Data. *ApJ*, 881(2):118.

Wang, M. Y., Fattahi, A., Cooper, A. P., Sawala, T., Strigari, L. E., Frenk, C. S., Navarro, J. F., Oman, K., and Schaller, M. (2017). Tidal features of classical Milky Way satellites in a Λ cold dark matter universe. *MNRAS*, 468(4):4887–4901.

Wang, M.-Y., Strigari, L. E., Lovell, M. R., Frenk, C. S., and Zentner, A. R. (2016). Mass assembly history and infall time of the Fornax dwarf spheroidal galaxy. *MNRAS*, 457(4):4248–4261.

Wang, W., Han, J., Cautun, M., Li, Z., and Ishigaki, M. N. (2020). The mass of our Milky Way. *Science China Physics, Mechanics, and Astronomy*, 63(10):109801.

Weinberg, M. D. and Katz, N. (2002). Bar-driven Dark Halo Evolution: A Resolution of the Cusp-Core Controversy. *ApJ*, 580:627–633.

Weisz, D. R., Dolphin, A. E., Skillman, E. D., Holtzman, J., Dalcanton, J. J., Cole, A. A., and Neary, K. (2013). Comparing the ancient star formation histories of the magellanic clouds. *Monthly Notices of the Royal Astronomical Society*, 431:364–371.

Weisz, D. R., Dolphin, A. E., Skillman, E. D., Holtzman, J., Gilbert, K. M., Dalcanton, J. J., and Williams, B. F. (2014). The Star Formation Histories of Local Group Dwarf Galaxies. I. Hubble Space Telescope/Wide Field Planetary Camera 2 Observations. *ApJ*, 789:147.

Wetzel, A. R., Hopkins, P. F., Kim, J.-h., Faucher-Giguère, C.-A., Kereš, D., and Quataert, E. (2016). Reconciling Dwarf Galaxies with ΛCDM Cosmology: Simulating a Realistic Population of Satellites around a Milky Way-mass Galaxy. *ApJL*, 827(2):L23.

White, S. D. M., Davis, M., Efstathiou, G., and Frenk, C. S. (1987a). Galaxy distribution in a cold dark matter universe. *Nature*, 330(6147):451–453.

White, S. D. M. and Frenk, C. S. (1991). Galaxy Formation through Hierarchical Clustering. *ApJ*, 379:52.

White, S. D. M., Frenk, C. S., and Davis, M. (1983). Clustering in a neutrino-dominated universe. *ApJl*, 274:L1–L5.

White, S. D. M., Frenk, C. S., Davis, M., and Efstathiou, G. (1987b). Clusters, Filaments, and Voids in a Universe Dominated by Cold Dark Matter. *ApJ*, 313:505.

White, S. D. M., Navarro, J. F., Evrard, A. E., and Frenk, C. S. (1993). The baryon content of galaxy clusters: a challenge to cosmological orthodoxy. *Nature*, 366(6454):429–433.

Wiersma, R. P. C., Schaye, J., and Smith, B. D. (2008). The effect of photo-ionization on the cooling rates of enriched, astrophysical plasmas. *MNRAS*, 393:99–107.

Wiersma, R. P. C., Schaye, J., Theuns, T., Dalla Vecchia, C., and Tornatore, L. (2009). Chemical enrichment in cosmological, smoothed particle hydrodynamics simulations. *MNRAS*, 399:574–600.

Wolf, J., Martinez, G. D., Bullock, J. S., Kaplinghat, M., Geha, M., Muñoz, R. R., Simon, J. D., and Avedo, F. F. (2010). Accurate masses for dispersion-supported galaxies. *MNRAS*, 406:1220–1237.

Wright, A. C., Brooks, A. M., Weisz, D. R., and Christensen, C. R. (2019). Reignition of star formation in dwarf galaxies. *MNRAS*, 482:1176–1189.

York, D. G. et al. (2000). The Sloan Digital Sky Survey: Technical Summary. *AJ*, 120(3):1579–1587.

Zhao, H. (1996). Analytical models for galactic nuclei. *MNRAS*, 278(2):488–496.

Zhu, L., van de Ven, G., Watkins, L. L., and Posti, L. (2016). A discrete chemo-dynamical model of the dwarf spheroidal galaxy sculptor: mass profile, velocity anisotropy and internal rotation. *MNRAS*, 463(1):1117–1135.

Zhu, Q., Marinacci, F., Maji, M., Li, Y., Springel, V., and Hernquist, L. (2016). Baryonic impact on the dark matter distribution in Milky Way-sized galaxies and their satellites. *MNRAS*, 458(2):1559–1580.

Zolotov, A. et al. (2012). Baryons Matter: Why Luminous Satellite Galaxies have Reduced Central Masses. *ApJ*, 761(1):71.

Zwicky, F. (1933). Die Rotverschiebung von extragalaktischen Nebeln. *Helvetica Physica Acta*, 6:110–127.

Colophon

This thesis is based on a template developed by Matthew Townson and Andrew Reeves. It was typeset with LaTeX 2$_{\varepsilon}$. It was created using the *memoir* package, maintained by Lars Madsen, with the *madsen* chapter style. The font used is Latin Modern, derived from fonts designed by Donald E. Kunith.